

Multiphase Synchronous Generators for DC Aircraft Power Systems

A thesis submitted to The University of Manchester for the degree of
Doctor of Philosophy
in the Faculty of Engineering and Physical Sciences

2013

Steven Jordan

School of Electrical and Electronic Engineering

Table of Contents

List of Figures	4
List of Tables	15
List of Abbreviations	18
Nomenclature	20
Abstract	24
Declaration	25
Copyright Statement	26
Acknowledgements.....	27
1 Introduction	28
1.1 Background	28
1.2 Research Aims and Objectives.....	30
1.3 Significance of Work	31
1.4 Thesis Structure	32
2 Literature Review	34
2.1 Introduction	34
2.2 More-electric Applications in Transport.....	35
2.3 Multiphase Machines	45
2.4 Prior Modelling Techniques.....	47
2.5 DC Distribution Networks	48
2.6 AC to DC Rectification	50
2.7 Summary	51
3 Dynamic Circuit Modelling and Simulation of a Synchronous Generator	53
3.1 Introduction	53
3.2 Three-phase Mathematical Model	54
3.3 Extension to Multiphase Model.....	63
3.4 Harmonic Modelling	67
3.5 Passive Rectification	70

3.6	Summary	94
4	Finite Element Modelling	96
4.1	Introduction	96
4.2	Background	97
4.3	The Synchronous Generator in Femm	98
4.4	Modelling the Three-phase Generator	103
4.5	Modelling the Five-phase Generator	109
4.6	Modelling the 15-phase Generator	112
4.7	Core Losses when Connected to an Uncontrolled Rectifier	116
4.8	Summary	125
5	Experimental Testing	127
5.1	Introduction	127
5.2	Experimental Set-up and Chapter Structure.....	128
5.3	Comparison of Experimental and Simulation Results.....	130
5.4	Comparison of Fully- and Short-pitched Generators.....	142
5.5	Generator Loading Comparison.....	150
5.6	Comparison of Fault Tolerance in Star-/Polygon-connected Generators	158
5.7	Summary	172
6	Conclusions and Future Work.....	174
6.1	Introduction	174
6.2	Review of Presented Work	174
6.3	Contribution to Knowledge.....	176
6.4	Further Work	178
6.5	Publications.....	181
	References.....	182
	Appendices	186

List of Figures

Figure 1.1: Reduction in Fuel Burn Compared with Comet 4 Commercial Jetliner (adapted from [4])	29
Figure 2.1: Load Power on Prominent Civil Aircraft (adapted from [11]).....	35
Figure 2.2: Comparison of Conventional and More-electric Engine Power Offtake (adapted from [13])	36
Figure 2.3: Integrated Drive Generator (adapted from [13])	37
Figure 2.4: Variable-speed Constant-frequency Starter/Generator System (adapted from [9])	38
Figure 2.5: Type 23 Frigate Power and Propulsion System (adapted from [21])	40
Figure 2.6: Series Hybrid Electric Drive Train Architecture (adapted from [34]).....	43
Figure 2.7: Parallel Hybrid Electric Drive Train Architectures (adapted from [34]).....	44
Figure 2.8: Split-phase Machine Stator Winding Phasor Representation	45
Figure 2.9: Symmetrical Multiphase Machine Stator Winding Phasor Representation	46
Figure 3.1: MATLAB Simulink Implementation	56
Figure 3.2: Constant Speed Drive Model	58
Figure 3.3: Simulation Model AVR	58
Figure 3.4: DeVised Model vs. SimPowerSystems Phase Current Output	61
Figure 3.5: DeVised Model vs. SimPowerSystems Short-circuit Phase Current Response	61
Figure 3.6: Experimental vs. Simulation Model Short-circuit Behaviour	62
Figure 3.7: Simulated AC Phase Voltage	66
Figure 3.8: Simulated AC Phase Current	66
Figure 3.9: Simulated 15-phase AC Phase Voltage	66
Figure 3.10: Simulated 15-phase AC Phase Current	66
Figure 3.11: FFT of Short-pitched (SP) and Fully-pitched (FP) Generator Back-emf.....	67
Figure 3.12: Harmonic Block Acting on Simulation Model Voltage	68
Figure 3.13: MATLAB Simulink Representation of Harmonic Model Block	69
Figure 3.14: Winding Arrangements for a Double-layer Winding (a) Series-star and (b) Series-delta	70
Figure 3.15: Simulation of Open-circuit Phase Fault	71
Figure 3.16: Ideal Voltage Source with Constant Current Load (adapted from [48]).....	72
Figure 3.17: Diagram of Differential (line-to-line) Voltages	73

Figure 3.18: Five-phase Voltage Phasor Diagram	73
Figure 3.19: DC Ripple Magnitude	74
Figure 3.20: Commutation between Phases.....	76
Figure 3.21: DC Voltage Formation with Commutation Effects.....	77
Figure 3.22: Phasor Quadrants and Polygon-connected Generator Greatest Voltage Differential	79
Figure 3.23: Polygon-connected Generator Current Path under Commutation	80
Figure 3.24: Five-phase (a) Star- and (b) Polygon-connected Generator with Rectifier and Constant Current Load.....	82
Figure 3.25: Star-connected Generator AC Currents.....	83
Figure 3.26: Star-connected Generator DC Voltages.....	83
Figure 3.27: Polygon-connected Generator AC Currents	84
Figure 3.28: Polygon-connected Generator DC Voltages	84
Figure 3.29: Star-connected Generator FFT of Currents Normalised to Three-phase Fundamental.....	85
Figure 3.30: Polygon-connected Generator FFT of Currents Normalised to Three-phase Fundamental.....	85
Figure 3.31: Star-connected Generator (a) Voltage Determination (b) Current Path.....	87
Figure 3.32: Three-phase Star-connected Simulated AC Voltage.....	87
Figure 3.33: Three-phase Star-connected Simulated AC Current.....	87
Figure 3.34: Three-phase Star-connected Simulated DC Voltage.....	88
Figure 3.35: Three-phase Star-connected Simulated DC Current.....	88
Figure 3.36: Five-phase Star-connected Simulated AC Voltage.....	88
Figure 3.37: Five-phase Star-connected Simulated AC Current.....	88
Figure 3.38: Five-phase Star-connected Simulated DC Voltage	89
Figure 3.39: Five-phase Star-connected Simulated DC Current	89
Figure 3.40: 15-phase Star-connected Simulated AC Voltage	89
Figure 3.41: 15-phase Star-connected Simulated AC Current	89
Figure 3.42: 15-phase Simulated DC Voltage.....	90
Figure 3.43: 15-phase Simulated DC Current.....	90
Figure 3.44: Polygon Connection (a) Voltage Determination (b) Current Path through Generator.....	90
Figure 3.45: Three-phase Delta-connected Simulated Line-to-line Voltage.....	91
Figure 3.46: Three-phase Delta-connected Simulated Generator with Diode Current.....	91

Figure 3.47: Three-phase Delta-connected Simulated DC Voltage	91
Figure 3.48: Three-phase Delta-connected Simulated DC Current	91
Figure 3.49: Five-phase Polygon-connected Simulated AC Voltage	92
Figure 3.50: Five-phase Polygon-connected Simulated Generator and Diode Current	92
Figure 3.51: Five-phase Polygon-connected Simulated DC Voltage	92
Figure 3.52: Five-phase Polygon-connected Simulated DC Current	92
Figure 3.53: 15-phase Simulated AC Line-to-line Voltage	93
Figure 3.54: 15-phase Simulated AC Generator Current	93
Figure 3.55: 15-phase Simulated AC Generator Current	93
Figure 3.56: 15-phase Simulated AC Diode Current	93
Figure 3.57: 15-phase Polygon-connected Simulated DC Voltage	94
Figure 3.58: 15-phase Polygon-connected Simulated DC Current	94
Figure 4.1: Current Definition in Finite Element Problems.....	98
Figure 4.2: VariCAD Drawing of BCI162G Synchronous Generator	99
Figure 4.3: FEM Representation of BCI162G Synchronous Generator including Mesh	99
Figure 4.4: Single Phase Coil, Concentric Winding.....	101
Figure 4.5: Phase Voltage using Equation (44)	106
Figure 4.6: Phase Voltage using Equation (45)	106
Figure 4.7: Aligned Rotor with Stator Field.....	107
Figure 4.8: Unaligned Rotor Position	107
Figure 4.9: Inductance Variation of Three-phase Generator through Rotation of Rotor....	108
Figure 4.10: Fourier Transform of Inductance Waveform	109
Figure 4.11: Back-emf for Fully-pitched Five-phase Generator	110
Figure 4.12: Five-phase Voltage Output for 36° Short-pitched Double Layer Windings.....	111
Figure 4.13: Inductance Variation for Five-phase Generator through Rotation of Rotor ...	112
Figure 4.14: Fully-pitched 15-phase Back-emf Waveform.....	113
Figure 4.15: Short-pitched 15-phase Back-emf Waveform	115
Figure 4.16: Inductance Waveform for 15-phase Generator	116
Figure 4.17: Core Loss against Flux Density for 50 Hz Operation	117
Figure 4.18: Simplified Diagram of Conduction Path used to Analyse Core Losses	118
Figure 4.19: Fully-pitched Star-connected Flux Density in Aligned Rotor Position	122
Figure 4.20: Fully-pitched Polygon-connected Flux Density in Aligned Rotor Position.....	122
Figure 4.21: Short-pitched Star-connected Flux Density in Aligned Rotor Position	123
Figure 4.22: Short-pitched Polygon-connected Flux Density in Aligned Rotor Position.....	123

Figure 5.1: Experimental Test-rig Schematic Set-up	128
Figure 5.2: Star- and Polygon-connected Generator Notation.....	129
Figure 5.3: Experimental Three-phase Short-pitched Star-connected Generator AC and DC Voltage and Current 58 Ω Load.....	131
Figure 5.4: Simulated Three-phase Short-pitched Star-connected Generator AC and DC Voltage and Current 58 Ω Load.....	131
Figure 5.5: Experimental Three-phase Fully-pitched Star-connected Generator AC and DC Voltage and Current 58 Ω Load.....	131
Figure 5.6: Simulated Three-phase Fully-pitched Star-connected Generator AC and DC Voltage and Current 58 Ω Load.....	131
Figure 5.7: Experimental Three-phase Fully-pitched Delta-connected Generator AC and DC Voltage and Current 58 Ω Load.....	132
Figure 5.8: Simulated Three-phase Fully-pitched Delta-connected Generator AC and DC Voltage and Current 58 Ω Load.....	132
Figure 5.9: Experimental Three-phase Short-pitched Delta-connected Generator AC and DC Voltage and Current 58 Ω Load.....	133
Figure 5.10: Simulated Three-phase Short-pitched Delta-connected Generator AC and DC Voltage and Current 58 Ω Load	133
Figure 5.11: Experimental Three-phase Fully-pitched Star-connected Generator Open- circuit Diode Fault 5 Ω Load	133
Figure 5.12: Simulated Three-phase Fully-pitched Star-connected Generator Open-circuit Diode Fault 5 Ω Load	133
Figure 5.13: Experimental Three-phase Fully-pitched Delta-connected Generator Open- circuit Diode Fault 5 Ω Load	134
Figure 5.14: Simulated Three-phase Fully-pitched Delta-connected Generator Open-circuit Diode Fault 5 Ω Load	134
Figure 5.15: Experimental Five-phase Fully-pitched Polygon-connected Generator 58 Ω Load.....	135
Figure 5.16: Simulated Five-phase Fully-pitched Polygon-connected Generator 58 Ω Load.....	135
Figure 5.17: Experimental Five-phase Fully-pitched Star-connected Generator 58 Ω Load	136
Figure 5.18: Simulated Five-phase Fully-pitched Star-connected Generator 58 Ω Load.....	136
Figure 5.19: Experimental Five-phase Fully-pitched Polygon-connected Generator Open- circuit Phase Fault 5 Ω Load	137

Figure 5.20: Simulated Five-phase Fully-pitched Polygon-connected Generator Open-circuit Phase Fault 5 Ω Load	137
Figure 5.21: Experimental Five-phase Fully-pitched Star-connected Generator Open-circuit Phase Fault 5 Ω Load	137
Figure 5.22: Simulated Five-phase Fully-pitched Star-connected Generator Open-circuit Phase Fault 5 Ω Load	137
Figure 5.23: Experimental 15-phase Short-pitched Star-connected Generator AC and DC Voltage and Current 5 Ω Load	138
Figure 5.24: Simulated 15-phase Short-pitched Star-connected Generator AC and DC Voltage and Current 5 Ω Load	138
Figure 5.25: Experimental 15-phase Fully-pitched Star-connected Generator AC and DC Voltage and Current 5 Ω Load	139
Figure 5.26: Simulated 15-phase Fully-pitched Star-connected Generator AC and DC Voltage and Current 5 Ω Load	139
Figure 5.27: Experimental 15-phase Short-pitched Polygon-connected Generator AC and DC Voltage and Current 58 Ω Load	140
Figure 5.28: Simulated 15-phase Short-pitched Polygon-connected Generator AC and DC Voltage and Current 58 Ω Load	140
Figure 5.29: Experimental 15-phase Short-pitched Polygon-connected Generator Open- circuit Phase Fault 58 Ω Load	140
Figure 5.30: Simulated 15-phase Short-pitched Polygon-connected Generator Open-circuit Phase Fault 58 Ω Load	140
Figure 5.31: Fully-pitched Stator Topology.....	143
Figure 5.32: Current Density Distribution in a Fully-pitched Winding.....	143
Figure 5.33: Short-pitched Stator Topology.....	143
Figure 5.34: Current Density Distribution in a Short-pitched Winding.....	143
Figure 5.35: Three-phase Fully-pitched Star-connected AC and DC Voltage and Current 58 Ω Load.....	144
Figure 5.36: Three-phase Short-pitched Star-connected AC and DC Voltage and Current 58 Ω Load.....	144
Figure 5.37: Three-phase Fully-pitched Delta-connected AC and DC Voltage and Current 58 Ω Load.....	145
Figure 5.38: Three-phase Short-pitched Delta-connected AC and DC Voltage and Current 58 Ω Load.....	145

Figure 5.39: Five-phase Fully-pitched Star-connected AC and DC Voltage and Current	
58 Ω Load.....	146
Figure 5.40: Five-phase Short-pitched Star-connected AC and DC Voltage and Current	
58 Ω Load.....	146
Figure 5.41: Five-phase Fully-pitched Polygon-connected AC and DC Voltage and Current	
58 Ω Load.....	147
Figure 5.42: Five-phase Short-pitched Polygon-connected AC and DC Voltage and Current	
58 Ω Load.....	147
Figure 5.43: 15-phase Fully-pitched Star-connected AC and DC Voltage and Current	
58 Ω Load.....	148
Figure 5.44: 15-phase Short-pitched Star-connected AC and DC Voltage and Current	
58 Ω Load.....	148
Figure 5.45: 15-phase Fully-pitched Polygon-connected AC and DC Voltage and Current	
58 Ω Load.....	149
Figure 5.46: 15-phase Short-pitched Polygon-connected AC and DC Voltage and Current	
58 Ω Load.....	149
Figure 5.47: Three-phase Fully-pitched Star-connected Generator AC and DC Voltage and Current 5 Ω Load	152
Figure 5.48: Three-phase Short-pitched Star-connected Generator AC and DC Voltage and Current 5 Ω Load	152
Figure 5.49: Five-phase Fully-pitched Star-connected AC and DC Voltage and Current	
5 Ω Load.....	153
Figure 5.50: Five-phase Short-pitched Star-connected AC and DC Voltage and Current	
5 Ω Load.....	153
Figure 5.51: 15-phase Fully-pitched Star-connected AC and DC Voltage and Current	
5 Ω Load.....	153
Figure 5.52: 15-phase Short-pitched Star-connected AC and DC Voltage and Current	5
Ω Load.....	153
Figure 5.53: Three-phase Fully-pitched Delta-connected AC and DC Voltage and Current	
58 Ω Load.....	154
Figure 5.54: Three-phase Fully-pitched Delta-connected AC and DC Voltage and Current	
5 Ω Load.....	154
Figure 5.55: Harmonic Content of Three-phase Fully-pitched Delta-connected Generator	
Current 58 Ω Load	154

Figure 5.56: Harmonic Content of Three-phase Fully-pitched Delta-connected Generator	
Current 5 Ω Load	154
Figure 5.57: Five-phase Fully-pitched Polygon-connected AC and DC Voltage and Current	
58 Ω Load.....	155
Figure 5.58: Five-phase Fully-pitched Polygon-connected AC and DC Voltage and Current	
5 Ω Load.....	155
Figure 5.59: Harmonic Content of Five-phase Fully-pitched Polygon-connected Generator	
Current 58 Ω Load	156
Figure 5.60: Harmonic Content of Five-phase Fully-pitched Polygon-connected Generator	
Current 5 Ω Load	156
Figure 5.61: 15-phase Fully-pitched Polygon-connected AC and DC Voltage and Current	
58 Ω Load.....	156
Figure 5.62: 15-phase Fully-pitched Polygon-connected AC and DC Voltage and Current	
5 Ω Load.....	156
Figure 5.63: Harmonic Content of Polygon-connected Generator 58 Ω Load.....	157
Figure 5.64: Harmonic Content of Polygon-connected Generator 5 Ω Load.....	157
Figure 5.65: Three-phase Star- and Delta-connected Generator and Diode Open-circuit	
Condition	159
Figure 5.66: Three-phase Fully-pitched Star-connected Generator Open-circuit Phase Fault	
58 Ω Load.....	159
Figure 5.67: Three-phase Fully-pitched Delta-connected Generator Open-circuit Phase Fault	
58 Ω Load.....	160
Figure 5.68: Three-phase Fully-pitched Delta-connected Generator Open-circuit Diode Fault	
58 Ω Load.....	160
Figure 5.69: Three-phase Fully-pitched Delta-connected Generator Open-circuit Phase Fault	
5 Ω Load.....	161
Figure 5.70: Three-phase Fully-pitched Delta-connected Generator Open-circuit Diode Fault	
5 Ω Load.....	161
Figure 5.71: Three-phase Fully-pitched Delta-connected AC Generator Currents with Open-	
circuit Diode Fault	161
Figure 5.72: Five-phase Generator Connection Methods and Open-circuit Fault Locations	
.....	163
Figure 5.73: Five-phase Fully-pitched Star-connected Generator Open-circuit Phase Fault	
58 Ω Load.....	163

Figure 5.74: Five-phase Fully-pitched Star-connected Generator Open-circuit Phase Fault 5 Ω Load.....	163
Figure 5.75: AC Currents for Five-phase Fully-pitched Star-connected Generator with Open- circuit Phase Fault	164
Figure 5.76: AC Generator Currents for Five-phase Fully-pitched Polygon-connected Generator with Open-circuit Phase Fault 58 Ω Load.....	165
Figure 5.77: Five-phase Fully-pitched Polygon-connected Generator Open-circuit Phase Fault 58 Ω Load.....	165
Figure 5.78: Five-phase Fully-pitched Polygon-connected Generator Open-circuit Phase Fault 5 Ω Load.....	165
Figure 5.79: Five-phase Fully-pitched Polygon-connected Diode Open-circuit 58 Ω Load .	166
Figure 5.80: Five-phase Fully-pitched Polygon-connected Diode Open-circuit 5 Ω Load ...	166
Figure 5.81: 15-phase Generator Connection Topologies and Open-circuit Fault Locations	167
Figure 5.82: 15-phase Fully-pitched Star-connected Generator Open-circuit Phase Fault 58 Ω Load.....	168
Figure 5.83: 15-phase Fully-pitched Star-connected Generator Open-circuit Phase Fault 5 Ω Load.....	168
Figure 5.84: 15-phase Fully-pitched Polygon-connected Generator Open-circuit Phase Fault 58 Ω Load.....	168
Figure 5.85: 15-phase Fully-pitched Polygon-connected Generator Open-circuit Phase Fault 5 Ω Load.....	168
Figure 5.86: 15-phase Fully-pitched Polygon-connected Generator Open-circuit Diode 58 Ω Load.....	169
Figure 5.87: 15-phase Fully-pitched Polygon-connected Generator Open-circuit Diode 5 Ω Load.....	169
Figure 5.88: 15-phase Short-pitched Polygon-connected Generator Open-circuit Phase Fault 58 Ω Load.....	170
Figure 5.89: 15-phase Short-pitched Polygon-connected Generator Open-circuit Phase Fault 5 Ω Load.....	170
Figure 5.90: Harmonic Content of 15-phase Short-pitched Polygon-connected Generator Currents with Open-circuit Phase Faults.....	171
Figure 7.1: DC Machine Connected to Synchronous Generator	188
Figure 7.2: Original BCI162G Generator Stator.....	188

Figure 7.3: Modified BCI162G Generator Stator (Under Construction)	188
Figure 7.4: Original Rotor with Brushless Excitation.....	189
Figure 7.5: Modified Rotor with Slip Rings	189
Figure 7.6: Testing of Rewound BCI162G Generator.....	189
Figure 7.7: Rewound Stator Housed in Original Casing with Spigot for Brushes.....	189
Figure 7.8: Protective Insert to Prevent Damage to Stator Laminations.....	189
Figure 7.9: Brushes in Situ.....	189
Figure 7.10: Cooling Fan Placement in Generator.....	190
Figure 7.11: Clearance between Fan and Windings	190
Figure 7.12: Front of Rewound Generator.....	190
Figure 7.13: Rear of Rewound Generator with DC Input Lead to Brushes	190
Figure 7.14: Multiphase Synchronous Generator in Situ.....	191
Figure 7.15: External Wiring Cabinet for Multiphase Terminals and Power Electronics.....	191
Figure 7.16: Experimental Test-rig in Operation.....	191
Figure 7.17: Equivalent circuit of a synchronous generator [53].....	199
Figure 7.18: Simulated slip test at 2990 rpm	203
Figure 7.19: Finite Element Simulated Inductances (Unexcited Rotor).....	204
Figure 7.20: d-q axis Inductances for Slip Test.....	205
Figure 7.21: Diagram of Short-circuit Test Conditions Applied to a Synchronous Generator	206
Figure 7.22: Experimental Short-circuit Current Transient at 250 V _{L-L}	207
Figure 7.23: Simulation (Datasheet Parameters) Short-circuit Current Transient at 250 V _{L-L}	208
Figure 7.24: Simulation Short-circuit Current Transient from Experimental Parameters ...	209
Figure 7.25: Calculation of Parameters from Short-circuit Response	210
Figure 7.26: MATLAB Simulink Model Overview	213
Figure 7.27: Harmonic Voltages from Winding Factors.....	214
Figure 7.28: Park Transform.....	215
Figure 7.29: Recombination of Fundamental d-q Values with Higher Order d-q Harmonic Pairs and Zero-sequence Components.....	216
Figure 7.30: Rectifier with SimPowerSystems Diode Models.....	217
Figure 7.31: Three-phase Open-circuit Diagram.....	220
Figure 7.32: Formation of Diode Current Path	221
Figure 7.33: Delta-connected Generator Voltage for 58 Ω Load.....	222

Figure 7.34: Delta-connected Generator Current with Open-circuit Phase Fault for 58 Ω Load.....	223
Figure 7.35: Diode and Generator Current with Open-circuit Phase Fault	223
Figure 7.36: Short-pitched Star-connected Generator Open-circuit Phase Fault 58 Ω Load	224
Figure 7.37: Star-connected Generator b-phase Open-circuit AC Voltage and Current	225
Figure 7.38: Three-phase Short-pitched Star-connected Generator Open-circuit Phase Fault 5 Ω Load.....	226
Figure 7.39: Three-phase Short-pitched Delta-connected Generator AC and DC Voltage and Current 58 Ω Load	226
Figure 7.40: Three-phase Short-pitched Delta-connected Generator AC and DC Voltage and Current 5 Ω Load	226
Figure 7.41: Three-phase Short-pitched Delta-connected Generator Open-circuit Phase Fault 58 Ω Load.....	227
Figure 7.42: Three-phase Short-pitched Delta-connected Generator Open-circuit Diode Fault 58 Ω Load.....	227
Figure 7.43: Three-phase Short-pitched Delta-connected Generator Open-circuit Phase Fault 5 Ω Load.....	227
Figure 7.44: Three-phase Short-pitched Delta-connected Generator Open-circuit Diode Fault 5 Ω Load.....	227
Figure 7.45: Five-phase Short-pitched Star-connected Generator Open-circuit Phase Fault 58 Ω Load.....	228
Figure 7.46: Five-phase Short-pitched Star-connected Generator Open-circuit Phase Fault 5 Ω Load.....	228
Figure 7.47: Five-phase Short-pitched Polygon-connected AC and DC Voltage and Current 58 Ω Load.....	229
Figure 7.48: Five-phase Short-pitched Polygon-connected AC and DC Voltage and Current 5 Ω Load.....	229
Figure 7.49: Five-phase Fully-pitched Polygon-connected Generator Diode Current 5 Ω Load.....	229
Figure 7.50: Five-phase Short-pitched Polygon-connected Generator Open-circuit Phase Fault 58 Ω Load.....	230
Figure 7.51: Five-phase Short-pitched Polygon-connected Generator Open-circuit Phase Fault 5 Ω Load.....	230

Figure 7.52: Five-phase Short-pitched Polygon-connected Diode Open-circuit 58 Ω Load	230
Figure 7.53: Five-phase Short-pitched Polygon-connected Diode Open-circuit 5 Ω Load ..	230
Figure 7.54: 15-phase Short-pitched Star-connected Generator Open-circuit Phase Fault 58 Ω Load.....	232
Figure 7.55: 15-phase Short-pitched Star-connected Generator Open-circuit Phase Fault 5 Ω Load.....	232
Figure 7.56: 15-phase Short-pitched Polygon-connected Generator Open-circuit Diode Fault 58 Ω Load.....	232
Figure 7.57: 15-phase Short-pitched Polygon-connected Generator Open-circuit Diode Fault 5 Ω Load.....	232

List of Tables

Table 3.1: Model Parameters used in Simulation.....	60
Table 3.2: Comparison of Simulation Model Outputs	61
Table 3.3: Mapping of Harmonics to d-q, x-y planes and Zero-sequence.....	69
Table 3.4: Comparison of AC and DC Simulation and Analysis Values	85
Table 4.1: Normalised Harmonic Content of Fully-pitched Five-phase Voltage.....	110
Table 4.2: Normalised Harmonic Content of 36° Short-pitched Five-phase Voltage	111
Table 4.3: Normalised Harmonic Content of Fully-pitched 15-phase Voltage	114
Table 4.4: Normalised FFT Voltages of Short-pitched Windings for 15-phase Generator ..	114
Table 4.5: THD of RMS Voltages for Short-pitching of 15-phase Generator	115
Table 4.6: Core Loss for Aligned, Fully-pitched Star-connected Generator at $2/3^{\text{rds}}$ Rated Current	119
Table 4.7: Core Loss for Aligned, Fully-pitched Star-connected Generator at Rated Current	120
Table 4.8: Core Loss for Aligned, Short-pitched, Star-connected Generator at $2/3^{\text{rds}}$ Rated Current	120
Table 4.9: Core Loss for Aligned, Short-pitched, Star-connected Generator at Rated Current	120
Table 4.10: Core Loss for Aligned, Fully-pitched, Polygon-connected Generator at $2/3^{\text{rds}}$ Rated Current.....	121
Table 4.11: Core Loss for Aligned, Fully-pitched, Polygon-connected Generator at Rated Current	122
Table 4.12: Core Loss for Aligned, Short-pitched, Polygon-connected Generator at $2/3^{\text{rds}}$ Rated Current.....	123
Table 4.13: Core Loss for Aligned, Short-pitched, Polygon-connected Generator at Rated Current	124
Table 4.14: Comparison of Core Losses	124
Table 5.1: Experimental and Simulated Results for Three-phase Fully-pitched Delta- connected Generator under Normal Operating Conditions with 58 Ω Load.....	132

Table 5.2: Experimental and Simulated Results for Three-phase Fully-pitched Generator under Open-circuit Diode Fault with 5 Ω Load	134
Table 5.3: Experimental and Simulation Results for Five-phase Fully-pitched Generator under Normal Operating Conditions 58 Ω Load	136
Table 5.4: Experimental and Simulated Results for Five-phase Fully-pitched Generator under Open-circuit Phase Fault with 5 Ω Load	138
Table 5.5: Fully-pitched and Short-pitched Star-connected Generator Experimental and Simulated Results for 5 Ω Load	140
Table 5.6: Short-pitched Polygon-connected Generator Experimental and Simulated Results for Normal and Open-circuit Phase Fault Conditions for 58 Ω Load	141
Table 5.7: Three-phase Star-connected Fully- and Short-pitched Normal Operating Conditions	144
Table 5.8: Three-phase Delta-connected Fully- and Short-pitched Normal Operating Conditions	145
Table 5.9: Five-phase Star-connected Fully- and Short-pitched Normal Operating Conditions	146
Table 5.10: Five-phase Polygon-connected Fully- and Short-pitched Normal Operating Conditions	147
Table 5.11: 15-phase Star-connected Fully- and Short-pitched Normal Operating Conditions	149
Table 5.12: 15-phase Polygon-connected Fully- and Short-pitched Normal Operating Conditions	149
Table 5.13: Loading of the Generator-Rectifier System	151
Table 5.14: Harmonic Content of Three-phase Delta-connected Generator Current	155
Table 5.15: Harmonic Content of Five-phase Polygon-connected Generator Current	156
Table 5.16: Harmonic Content of 15-phase Polygon-connected Generator Currents	157
Table 5.17: Three-phase Fully-pitched Generator Open-circuit Phase and Diode Faults ...	162
Table 5.18: Five-phase Fully-pitched Generator Open-circuit Phase and Diode Device Faults	166
Table 5.19: 15-phase Fully-pitched Generator Open-circuit Phase and Diode Device Faults	169
Table 7.1: Three-phase Winding Factors	194
Table 7.2: Five-phase Winding Factors	195
Table 7.3: 15-phase Winding Factors.....	196

Table 7.4: Experimental and Simulation Short-circuit Transient Currents	207
Table 7.5: Short-pitched Results	219
Table 7.6: Fully-pitched Results	219
Table 7.7: Three-phase Short-pitched Star- and Delta-connected Generator Open-circuit Faults.....	228
Table 7.8: Five-phase Short-pitched Star- and Polygon-connected Generator Open-circuit Faults.....	231
Table 7.9: 15-phase Short-pitched Generator Open-circuit Diode Fault.....	233

Word Count: 54,591

List of Abbreviations

AC	Alternating Current
AVR	Automatic Voltage Regulator
BLDC	Brushless Direct Current
CAD	Computer Aided Design
CODLAG	Combined Diesel Electric and Gas
DC	Direct Current
DOL	Direct-on-line
d-q	Direct-quadrature
ECS	Environmental Control System
EHA	Electro-hydrostatic Actuator
EMA	Electro-mechanical Actuator
emf	Electromotive Force
FDM	Finite Difference Method
FEA	Finite Element Analysis
FEM	Finite Element Modelling
FFT	Fast Fourier Transform
FP	Fully-pitched
FSDG	Fan-shaft Driven Generator
HVDC	High Voltage Direct Current
IDG	Integrated Drive Generator
IEPNEF	Intelligent Electrical Power Network Evaluation Facility
IGBT	Insulated Gate Bipolar Transistor
MMF	Magnetomotive Force
MEA	More-electric Aircraft
MEE	More-electric Engine

MOSFET	Metal-oxide-semiconductor Field Effect Transistor
PM	Permanent Magnet
POA	Power Optimised Aircraft
RMS	Root Mean Square
SP	Short-pitched
THD	Total Harmonic Distortion
TRU	Transformer Rectifier Unit
UAV	Unmanned Aerial Vehicle
VSCF	Variable Speed Constant Frequency

Nomenclature

<i>Symbol</i>	<i>Definition</i>	<i>S.I. Units</i>
A	Magnetic Vector Potential	$V \ s \ m^{-1}$
A_{slot}	Useful Copper Slot Area	m^2
$[A]$	State-space Matrix	-
α	Commutation Angle	<i>rads</i>
α_s	Short-pitch Angle	<i>rads</i>
B	Magnetic Flux Density	T
\hat{B}	Peak Magnetic Flux Density	T
$[B]$	State-space Matrix	-
β	Slot Pitch Angle	$^\circ$
D	Frictional Damping	$Nm \ s \ rad^{-1}$
D_1	Diode Number	-
e	Back-emf	V
e_{neg}	Negative Back-emf at DC side	V
e_{pos}	Positive Back-emf at DC side	V
E	Angular Dependent Induced Back-emf	V
E_q	q-axis Back-emf	V
f	Frequency	Hz
g	Air-gap Length	m
$[G]$	Matrix of Rotational Components	-
γ	Phase Displacement	<i>rads</i>
H	Magnetic Field Strength	$A-t \ m^{-1}$
i	Instantaneous Current	A
i_f'	Stator Referred Current	A

i_f^r	Rotor Referred Current	A
I	Current	A
I_n	Rated Current	A
J	Current Density	$A\ mm^{-2}$
J_r	Rotational Inertia	$kg\ m^2$
k	Phase Variable	-
k_{dn}	Distributed Winding Factor	-
k_e	Eddy Current Coefficient	-
k_h	Hysteresis Coefficient	-
k_{pn}	Short-pitch Factor	-
k_{wn}	Harmonic Winding Factor	-
k_{wr}	Rotor Winding Factor	-
k_{ws}	Stator Winding Factor	-
l	Length	m
L	Inductance	H
L_{ls}	Stator Leakage Inductance	H
L_{md}	d-axis Magnetising Inductance	H
m	Maximum Phase Number	-
m_c	Number of Coils per Phase Belt	-
μ	Permeability of Material	$H\ m^{-1}$
μ_0	Permeability of Free Space	$H\ m^{-1}$
n	Harmonic Number	-
n_k	Steinmetz Index	-
N	Number of Turns in Each Slot	-
N_c	Number of Windings per Coil	-
N_f	Number of Rotor Windings	-
N_s	Number of Stator Windings	-

N_{ss}	Number of Stator Slots	-
θ	Angular Rotation	<i>rads</i>
p	Pole Number	-
pp	Pole Pairs	-
ϕ	Phase Angle	<i>rads</i>
φ	Flux Linking a Single Coil	<i>Wb</i>
φ_d	d-axis Flux Linkage	<i>Wb</i>
φ_q	q-axis Flux Linkage	<i>Wb</i>
ψ	Flux Linking a Group of Coils	<i>Wb</i>
P_{loss}	Power Loss	<i>W</i>
R	Resistance	Ω
R_f	Field Winding Resistance	Ω
R_{kd}	d-axis Damper Winding Resistance	Ω
R_{kq}	q-axis Damper Winding Resistance	Ω
$[R]$	Matrix of Resistance	Ω
S_{base}	Base Rating	<i>VA</i>
T	Time Period	<i>s</i>
T_d'	d-axis Transient Time Constant	<i>s</i>
T_d''	d-axis Sub-transient Time Constant	<i>s</i>
T_q''	q-axis Sub-transient Time Constant	<i>s</i>
T_{em}	Electromagnetic Torque	<i>Nm</i>
T_{mech}	Mechanical Torque	<i>Nm</i>
τ	End of Time Period	<i>s</i>
v	Instantaneous Voltage	<i>V</i>
\hat{V}	Peak Voltage	<i>V</i>
V_{ab}	Voltage <i>a</i> Referenced to Voltage <i>b</i>	<i>V</i>
V_{an}	Voltage <i>a</i> Referenced to the Neutral Point	<i>V</i>

V_{base}	Base Voltage	V
V_{pn}	Positive DC Side Voltage Referenced to Neutral	V
V_{LL}	Line-to-line Voltage	V
V_{pk-pk}	Peak-peak Voltage	V
W_A	Turns per Path per Phase	-
ω	Line Frequency	$rads$
ω_{base}	Base Frequency	$rads$
ω_{rm}	Rotor Mechanical Speed	$rads^{-1}$
X	Reactance	Ω
X_d	d-axis Synchronous Reactance	Ω
X_d''	Sub-transient d-axis Synchronous Reactance	Ω
X_f	Field Winding Reactance	Ω
X_{kd}	d-axis Damper Winding Reactance	Ω
X_{kq}	q-axis Damper Winding Reactance	Ω
X_l	Leakage Reactance	Ω
X_{lf}	Field Winding Leakage Reactance	Ω
X_{lkd}	d-axis Damper Winding Leakage Reactance	Ω
X_{lkq}	q-axis Damper Winding Leakage Reactance	Ω
X_{md}	d-axis Magnetising Reactance	Ω
X_{mq}	q-axis Magnetising Reactance	Ω
X_q	q-axis Synchronous Reactance	Ω
x	Arbitrary Variable	-
Z_{base}	Base Impedance	Ω

Abstract

More-electric aircraft have been the focus of considerable development in recent years. Increased utilisation of electrical systems on-board the latest generation of aircraft has seen an increase in fuel efficiency, through improved electrical derivation from the gas turbine engine and weight savings from the replacement of mechanical and hydraulic transmission systems. The advancement of power electronic and DC breaker devices has led to the reconsideration of DC power distribution systems for standalone networks. Aircraft can benefit from this through the reduced transmission losses, improved controllability and intelligent networking.

Through the use of a multiphase synchronous generator, connected to a diode rectifier, a standalone DC network capable of providing power with redundancy can be produced. The aim of this research project is to investigate the effects that phase number, connection topology and winding pitch have on the behaviour of an AC generator connected to a passive diode rectifier. This thesis develops the methodology for determining the number of phases and the topology of the generator. Static and dynamic modelling is conducted through the use of computer finite element modelling and circuit simulation. The dynamic circuit simulation model is configured using parameters obtained from experimental data. The experimental test-rig, which is constructed to be reconfigurable in phase number, connection topology and winding pitch, is used to validate the simulation and provide detailed results on the steady-state operation of the generator-rectifier system. Open-circuit faults are introduced to assess the fault tolerance of the system and the effects of the inherent phase redundancy on the generator performance.

Declaration

No portion of the work referred to in the thesis has been submitted in support of an application for another degree or qualification of this or any other university or other institute of learning.

Copyright Statement

The author of this thesis (including any appendices and/or schedules to this thesis) owns certain copyright or related rights in it (the “Copyright”) and s/he has given The University of Manchester certain rights to use such Copyright, including for administrative purposes.

Copies of this thesis, either in full or in extracts and whether in hard or electronic copy, may be made **only** in accordance with the Copyright, Designs and Patents Act 1988 (as amended) and regulations issued under it or, where appropriate, in accordance with licensing agreements which the University has from time to time. This page must form part of any such copies made.

The ownership of certain Copyright, patents, designs, trade marks and other intellectual property (the “Intellectual Property”) and any reproductions of copyright works in the thesis, for example graphs and tables (“Reproductions”), which may be described in this thesis, may not be owned by the author and may be owned by third parties. Such Intellectual Property and Reproductions cannot and must not be made available for use without the prior written permission of the owner(s) of the relevant Intellectual Property and/or Reproductions.

Further information on the conditions under which disclosure, publication and commercialisation of this thesis, the Copyright and any Intellectual Property and/or Reproductions described in it may take place is available in the University IP Policy (see <http://documents.manchester.ac.uk/DocuInfo.aspx?DocID=487>), in any relevant Thesis restriction declarations deposited in the University Library, The University Library’s regulations (see <http://www.manchester.ac.uk/library/aboutus/regulations>) and in The University’s policy on Presentation of Theses

Acknowledgements

I would like to express my upmost gratitude to Dr Judith Apsley whose supervision has been unparalleled. The knowledge and expertise that she has imparted has been greatly appreciated and without her dedication, direction and foresight this project would not have been so rewarding.

I would like to thank the UK Engineering Physical Sciences Research Council, along with Rolls-Royce, for their financial input into this project. Furthermore, I wish to acknowledge the kind donation from Cummins Generator Technologies UK. Without such backing, the practical aspects and the opportunities to present this research work would not have been possible.

Acknowledgments are also paid to the expertise of Graham, David and the team at Quartzelec, Sheffield. The rewind of the generator was an integral part of this project and their professionalism in assisting my goals was greatly appreciated. Further mechanical aspects were completed in-house by Glyn Ireland whose contribution in the construction and assembly of a working test-rig was highly valued.

The Whitworth Society is deserving of special mention. Their contribution to my university studies helped me to achieve the highest possible grades and has shaped my future as an engineer.

I wish to thank my family for their patience, understanding and reassurance throughout the process; it would have been so much more difficult without it. To my friends, thank you for the welcome distractions, the excursions and the fun along the way. In particular, Drs Tuohy, Bryan, Feehally and Preece who have shared in this experience and have always been willing to listen and give sound advice.

Finally, special thanks to Denise who has been the unsung hero. The support, love and encouragement you have shown has been the foundation to this PhD.

1

Introduction

1.1 Background.....	28
1.2 Research Aims and Objectives	30
1.3 Significance of Work.....	31
1.4 Thesis Structure.....	32

1.1 Background

The first synchronous generator was developed through the work undertaken by a number of prominent scientists and engineers. However, it is Friedrich August Haselwander who is credited with the production of a prototype synchronous generator system in 1887 [1]. This comprised a three-phase stator and a wound salient pole rotor, providing 2.8 kW at a frequency of 32 Hz. Electrical distribution was, at the time, being sourced from the DC electrodyamo. The ability to change AC voltage and current levels for transmission using transformers changed the future of electric power distribution. In 1891, the first long distance transmission of three-phase electrical power took place using a synchronous generator at a hydroelectric plant to a location 175 km away. The generator had a power rating of 210 kW and an efficiency of 96.5 % [1], giving an indication to its future prevalence in power transmission networks. Since their inception, synchronous generators have undergone a number of design enhancements to improve their performance, output quality, reliability and efficiency [1]. The three-phase topology has standardised the power industry and today, the synchronous generator makes up the majority of the UK and world power distribution generation units [2].

Synchronous machines are versatile, capable of highly efficient power generation or acting to produce torque when motoring. As well as supplying power to the UK grid infrastructure, they can be found in a range of standalone applications where reliable power generation is critical, on-board aircraft, for example [3]. The ability to generate electricity efficiently in such an environment has proved beneficial in saving on construction and operating costs.

The re-design of the on-board power transmission network has led to a considerable reduction in weight which, coupled with the composite material used in the construction of modern aircraft, results in a reduction in fuel burn and, therefore, CO₂ emissions.

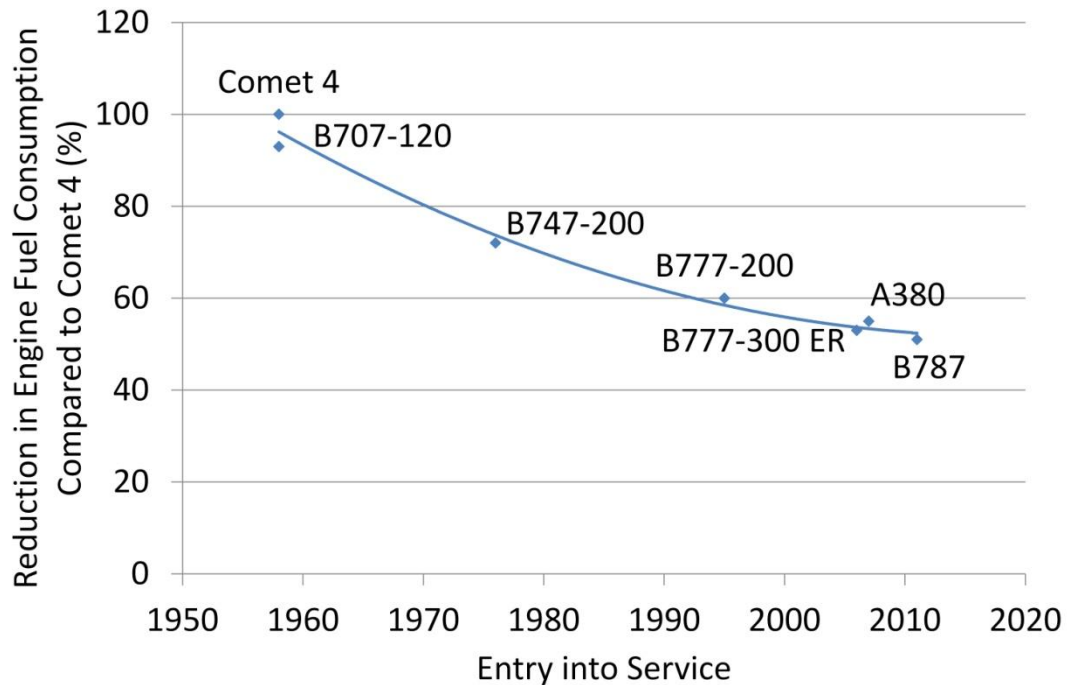


Figure 1.1: Reduction in Fuel Burn Compared with Comet 4 Commercial Jetliner (adapted from [4])

The Boeing 787 has the highest degree of electrification on-board any aircraft and benefits from a 50 % reduction in fuel burn compared with the Comet aircraft, observed in *Figure 1.1*. The electrical generation for the power systems is provided by synchronous generators that are located within the housing of the gas turbine engines underlining their suitability for aircraft. The placement of the generators can be modified as developments in material will allow them to be situated within the harsh environments of the gas turbine core [5]. This will have further benefits in the reduction of drag and fuel saving.

Although seen as a relatively recent advancement, multiphase topologies have been considered since before the 1960s with [6] generalising the m -phase machine. There was little interest in the multiphase machine since the three-phase topology was commonplace and, as a result, manufacturing was equipped for their production at minimal cost. Advancements in power electronic devices have opened up the possibility of increasing the number of phases. Multiphase topologies are starting to be considered for a number of applications, particularly in variable speed drive systems [7]. Furthermore, multiphase machines are being utilised by ALSTOM in marine applications where a 15-phase induction machine and its associated control are studied [8]. The increase in stator windings can lead

to several advantages in motors and generators, from greater torque production to better output power quality for a machine that is volumetrically the same as a conventional three-phase machine. A number of different topologies exist for exploiting the higher phase number with benefits in improved power quality reaching to the loads connected. The redundancy of multiphase machines is highly sought within the transport sector where a standalone distribution power system can continue to supply both an electric propulsion means and auxiliary equipment in the event of a generator phase fault [9].

For aircraft applications, it is imperative that the power system continues to operate correctly in the event of a fault. Therefore, multiphase technology is highly suited for use in improving the existing variable frequency, three-phase systems used in the modern more-electric aircraft. A fault in occurring in a three-phase machine will lead to an increase in load on the two remaining healthy phases. Increasing the phase number will allow a better load share across the remaining healthy phases, reducing the impact on the machine and the possible de-rating required.

The transmission of power around the aircraft is via three-phase cabling which contains a sizeable amount of conductive material and, therefore, adds weight. Significant savings could be made through the replacement of the multi-core AC cabling for single core DC cable. The losses incurred in transmitting DC power are reduced and complications with frequency affecting the cable sheath are removed. Direct-on-line (DOL) and transformer loads connected to the distribution system can be suitably sized since the variation in network frequency has been removed. On the load side of the conventional AC distribution network, localised power electronic devices are required to service DC loads, which are increasingly prevalent in next generation aircraft. Each conversion unit will have associated losses and as a collective this amounts to a considerable proportion of system losses. Therefore, the multiphase input, coupled with the DC output, can offer considerable performance increases in the electrical networks on-board aircraft.

1.2 Research Aims and Objectives

The aim of this research project is to investigate the effects that phase number, connection topology and winding pitch have on the behaviour of an AC generator connected to a passive diode rectifier. The novelty of this work lies in the approach of assessing a multiphase synchronous generator-rectifier system, its fault tolerance and the suitability of

such a system for use in the transportation sector, particularly on-board civil aircraft. The following objectives are set to define this research project:

- Development of a simulation model in order to predict and assess the behaviour of the integrated generator-rectifier system
- Finite element analysis of the generator behaviour under given conditions to ascertain the losses incurred and the back-emf developed at the output terminals. The latter will provide spacial harmonic information which can be used to improve the accuracy of the simulation model
- The construction of a test-rig enabling experimental results to be gathered to validate and inform the simulation model. The experimental test-rig will highlight areas where the simulation model requires further detail not contained in standard modelling techniques
- Direct comparisons for the best- and worst-case scenarios, regarding the power quality, between the results gathered from experimental testing and simulation to ascertain the impact that passive rectification has on both the AC and DC side of the system
- The investigation into the effect of open-circuit generator phase and diode device faults for both the star- and polygon-connected generator to allow the degradation in behaviour to be assessed

This thesis will consider a rewind generator for multiphase output to a diode rectifier unit. The considered stator configurations are for three-, five- and 15-phases with equal spacial displacement between consecutive phases. Configurations of the multiphase stator winding analysed in this thesis are the star-connection with a single neutral point and the polygon-connection: for the three-phase system, it is still referred to as the delta-connection. Fully- and short-pitched stator windings are also encompassed.

1.3 Significance of Work

This research project contributes to the advancement of power distribution systems on-board aircraft through the study of multiphase synchronous generator-rectifier systems. The behaviour that a passive rectification device has on a higher phase number machine is outlined for changes to the pitch angle of the stator windings and the connection topology of the generator.

The development of an accurate and robust dynamic multiphase synchronous generator model has been completed through the implementation of standard d-q modelling techniques. Finite element modelling is used for static solutions, informing the simulation model of the harmonic content of the armature windings for open-circuit conditions and establishing stator losses for a saturated generator delivering peak current.

The comparison across different phase number machines highlights the inherent problems when using a passive rectifier to derive DC power. The domination of commutation effects and uncontrolled switching events in high phase number machines leads to significantly reduced DC voltages under heavy loading conditions. Furthermore, the investigation into open-circuit phase and diode device faults quantifies the degradation of AC and DC power quality for the different connection topologies.

1.4 Thesis Structure

The thesis has been structured to provide relevant background information leading to the main body of the research work carried out and, finally, the conclusions drawn. A brief overview of each chapter is presented here:

Chapter 2: Literature Review provides information regarding the prior art for the electrification of aerospace, marine and automotive applications. Furthermore, multiphase machine topologies are discussed, focusing on two distinct variants of the multiphase architecture. The modelling techniques employed in simulating the dynamic behaviour of electric machines are briefly covered with attention paid toward the most efficient modelling methods for multiphase machines. The utilisation of DC distribution networks is also presented, underlining the current areas of implementation and specifications for system performance. This is followed by a short summary of the methods used to rectify AC power.

Chapter 3: Dynamic Circuit Modelling and Simulation of a Synchronous Generator details the dynamic circuit simulation of a synchronous generator-rectifier system. It briefly outlines the construction of a three-phase machine model in MATLAB Simulink, stating assumptions made, before verifying and validating it under steady-state and transient conditions against an industry standard model and physical generator. The extension of the model to a multiphase variant is presented and steady-state load results for the five- and 15-phase are shown. Passive rectification of the generator output is discussed for an increase in phase number with simulation results supporting analytical expressions as

phase number is increased and connection topology is changed. Furthermore, equivalent power transfer models are presented for fixed current loads on the DC side. Methods for the implementation of harmonic voltage sources are discussed for comparison against the multiphase experimental test-rig results in the experimental results chapter.

Chapter 4: Finite Element Modelling presents the background and development of the technique for solving complex models using finite elements. The electromagnetic design of the Cummins BCI162G generator is discussed covering the winding layout, the damper windings and the set-up of the finite element software. The three-, five- and 15-phase generator topologies are modelled and the results for the harmonic content of the open-circuit back-emf are analysed to establish the optimum short-pitching factor for experimental testing as well as enhancing the dynamic simulation model. Assumptions relating to the scaling of the inductances with the number of phases and the representation of saliency effects in the dynamic model are verified. Finally, the core losses for connection to an uncontrolled rectifier are calculated for the fully-pitched and short-pitched, star- and polygon-connected generator.

Chapter 5: Experimental Results presents detailed analysis of the results obtained from the experimental test-rig. This includes the system performance under normal operating conditions and with open-circuit generator phase and diode device faults. Some interesting cases are highlighted with more in-depth discussion of the behaviour. These are then compared with the enhanced simulation model results, identifying the validity of the dynamic circuit modelling.

Chapter 6: Conclusions and Future Work provides information regarding the outcome of this project. The work is summarised, with respect to the objectives set out, and key aspects are underlined. Recommendations are made for the future development of the project, building on the components of this thesis as well as unexplored areas of potential.

Literature Review

2.1 Introduction.....	34
2.2 More-electric Applications in Transport	35
2.3 Multiphase Machines	45
2.4 Prior Modelling Techniques	47
2.5 DC Distribution Networks.....	48
2.6 AC to DC Rectification	50
2.7 Summary	51

2.1 Introduction

The more-electric concept is becoming widely adopted across the transportation sector. Electrical systems are increasingly prevalent in all modes of transport where flexibility and efficiency is demanded. The constant drive to reduce operating costs whilst upholding targets for the reduced production of CO₂ [10] is facilitating this move toward the increased use of electrical systems.

Civil and defence aerospace require electrical generation for the purposes of essential aircraft functions such as navigational equipment and flight surface control. This extends to much larger load requirements for passenger comfort, cabin air conditioning, providing in-flight entertainment and galley services in civil aerospace. The marine sector has also benefitted from an increase in electrical systems on-board ships, for propulsion, passenger comfort and also weapon systems in defence applications. In marine, electrical power is typically derived from a number of distributed generators on an interconnected bus system. In aerospace, the electrical power is generated from the main prime mover, which may compromise the optimisation of propulsive power in order to maintain the electrical power network. Another area of development is electric road vehicles, which have a considerably different electrical architecture. There are two main types of vehicle design which encompass personal, commercial and commuter vehicles. Full electric vehicles use

batteries or fuel cells to provide the power for propulsion. Hybrid technology retains the traditional internal combustion engine but has an efficient electrical drive for low-range journeys.

This chapter reviews the advances of more-electric technologies across the transportation sector, looking at the generation techniques and the distribution systems currently employed, as well as future prospects. Multiphase machine technology research is also explored, underlining the potential for utilising this type of technology in identified applications. Finally, the rectification of current AC multiphase systems for the use of providing for, or feeding from, DC electrical networks are investigated with the power quality highlighted.

2.2 More-electric Applications in Transport

2.2.1 Civil Aerospace

Civil aerospace is now starting to experience the benefits of moving toward a greater utilisation of electrical power, underlined by the introduction into service of two next generation aircraft, the Boeing 787 and Airbus A380. The Boeing 787, in particular, shows a significantly high degree of electrical loading [11], highlighted in *Figure 2.1*.

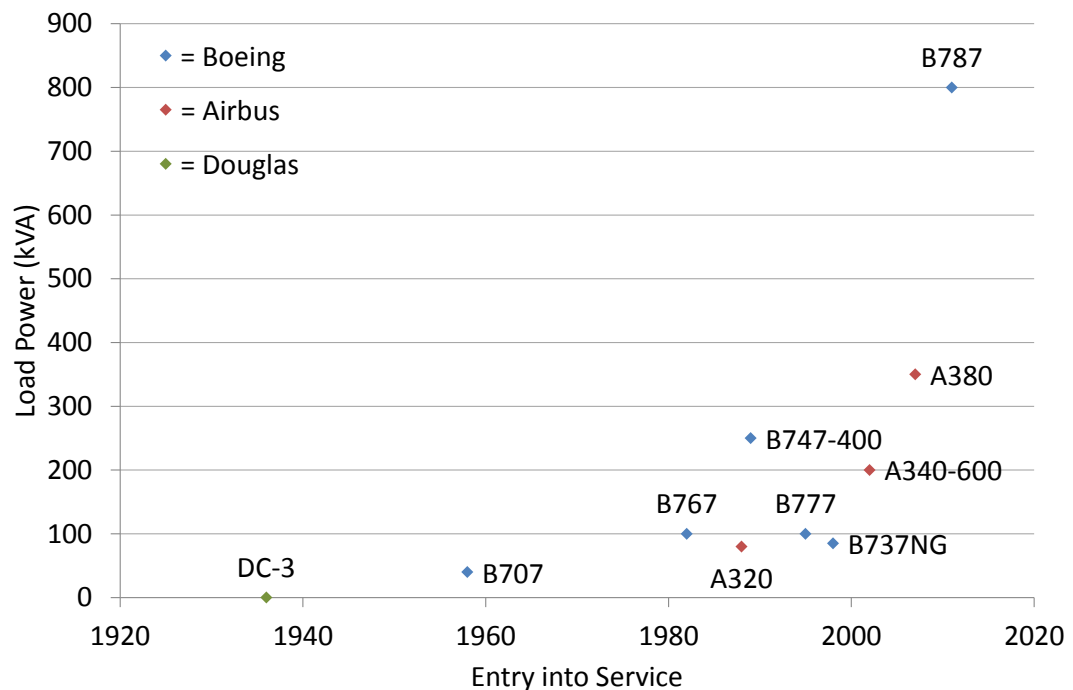


Figure 2.1: Load Power on Prominent Civil Aircraft (adapted from [11])

The step increase in loading on the Boeing 787 is because bleed air is no longer taken from the engine to be cooled and used for cabin air conditioning. The removal of this pneumatic

engine power offtake offers great advantage in increasing the efficiency of the gas turbine cycle. The next generation engines are high bypass, which provide a bypass ratio of close to 10:1, i.e. 10 times the amount of air bypasses the core to displace the air at the rear of the engine as that travelling through the core of the engine to power the turbofan. The pneumatic power offtakes have a greater effect on gas turbine efficiency as the bypass ratio increases and, therefore, their removal and replacement with electrical generation is highly sought. Fully-electric environmental control systems (ECS) are used to provide the cabin air, which is claimed to be less polluted [12] and better pressure regulated at a lower equivalent altitude [13], providing a more oxygen rich environment and imparting less altitude stress on the passengers. A comparison of the conventional and more-electric power offtake is shown in *Figure 2.2*.

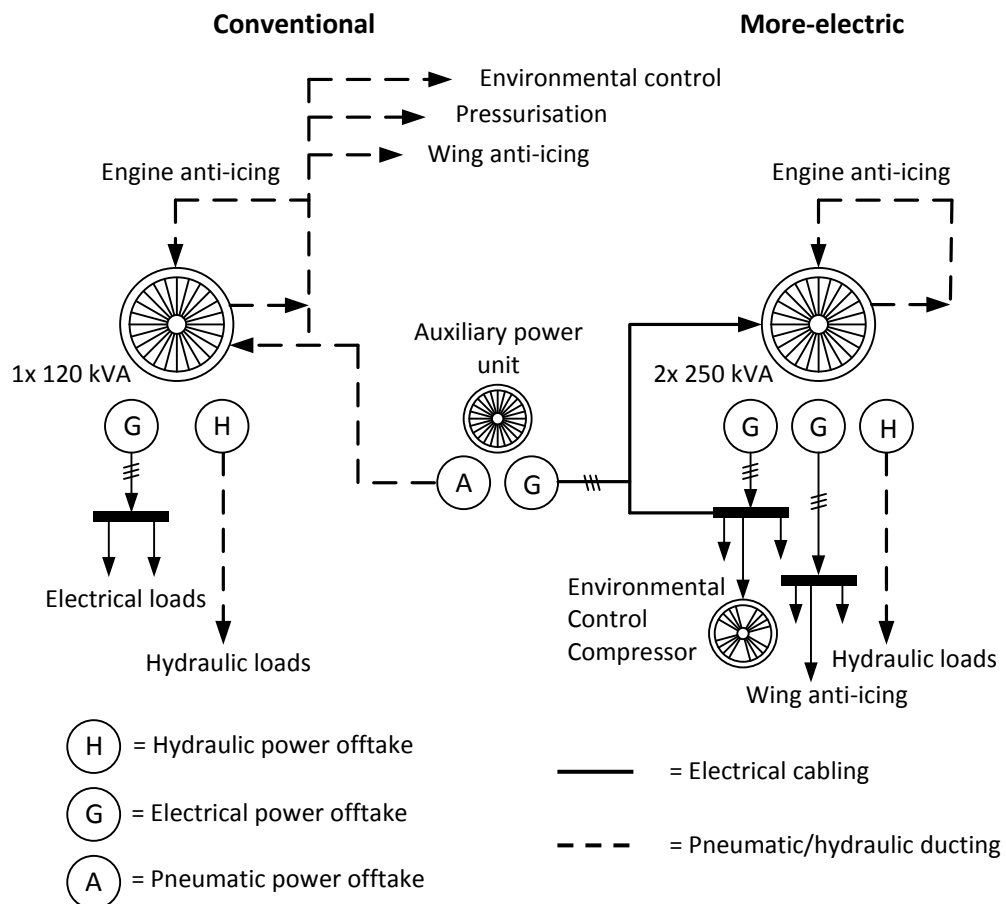


Figure 2.2: Comparison of Conventional and More-electric Engine Power Offtake (adapted from [13])

Reliable and efficient supply of power is critical for the modern aircraft. The current gas turbine engine architecture has the generator situated external to the engine core, mounted on the auxiliary gearbox. This creates a protrusion in the engine cowling leading

to aerodynamic drag and increasing fuel burn. The gearbox and associated driveshaft is prone to fatigue through mechanical vibration and requires maintenance to ensure its continued operation [14]. Its removal is, therefore, of benefit for the continued in-service operation of a civil aircraft and a reduced maintenance requirement.

The removal of the auxiliary gearbox would require the generator to be placed in an alternative location, perhaps embedded within the gas turbine core. This would impact directly on the identified problems associated with aerodynamic drag, removing the cowling protrusion and producing a smooth air surface, decreasing fuel-burn and increasing suitability for long-haul use. The Liebherr-Aerospace coordinated power optimised aircraft (POA) project [15] investigated two possible locations for electric machines. The first was a fan-shaft driven generator (FSDG) in the tail cone of the gas turbine, with associated power electronics mounted to the fan shaft casing and the second in the high pressure core [16]. The latter of the two machines was implemented as a starter/generator, a necessity as the bleedless engine [17] leaves no access point with which to pneumatically start the engine. Therefore, the starter/generator technology used for future aircraft must be able to provide sufficient torque to overcome the large inertia of a gas turbine spool to start the engine. It must also be rated to generate the required electrical load power.

Traditional aircraft generators provide AC power to the distribution network via a number of different means. The generator rotor speed can be fixed using a hydraulic coupling and generator as an integrated drive generator (IDG), shown in *Figure 2.3*.

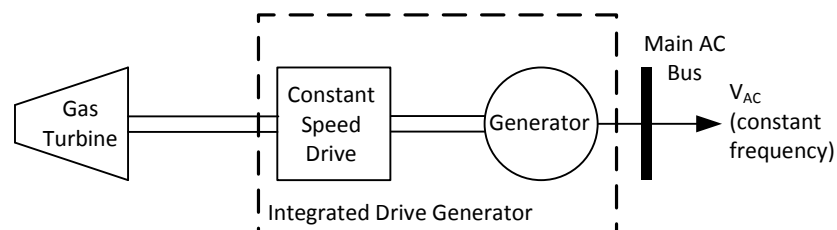


Figure 2.3: Integrated Drive Generator (adapted from [13])

The speed of the rotor can also be allowed to vary as in the variable speed constant frequency (VSCF) system, which utilises a complex power electronic converter to provide the constant frequency AC power, pictured in *Figure 2.4*. Both of these systems provide a constant 400 Hz frequency AC power regardless of the spool speed of the gas turbine engine.

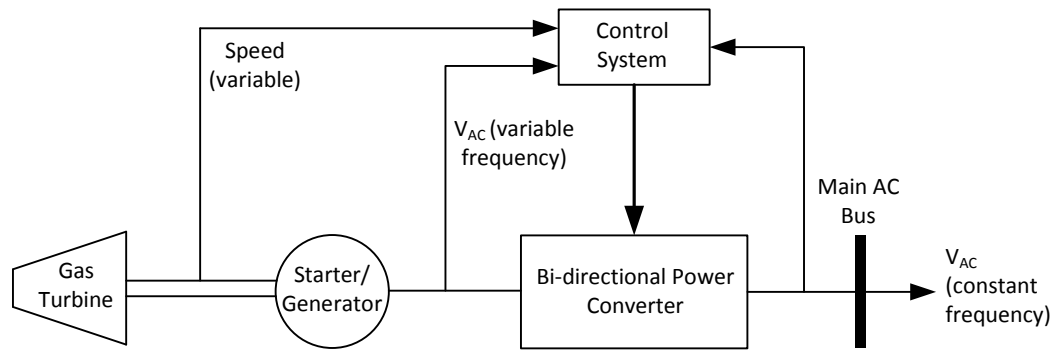


Figure 2.4: Variable-speed Constant-frequency Starter/Generator System (adapted from [9])

The Boeing 787 uses a more-electric engine which has a variable frequency wound-field starter/generator to provide the main aircraft AC distribution network with a frequency of between 380 – 760 Hz [13]. This system eliminates the power electronic converter of the VSCF system, with the voltage controlled using the field of the generator. However, the variable frequency approach leads to technical challenges when sizing electrical loads for such a wide ranging frequency, particularly sizing magnetic components, e.g. transformers. The reactive voltage drops throughout the distribution system change over the flight cycle leading to complexity when controlling the distribution system under varying load conditions. Direct-on-line (DOL) loads connected to the AC bus are affected by the change in frequency, which – in the case of the conventionally engine driven pumps – can lead to a change in machine flux and a fluctuation in drive pump speed. Although the most cost effective solution, it is clear the challenges that this variable frequency system imposes are significant and the complexity of the system architecture, and its control, is increased. The power electronic converter, in Figure 2.4, could be exchanged for a rectifier unit, capable of supplying a DC power distribution network. Similar to the VSCF system, this would provide a means of decoupling the speed of the rotor from the frequency of the power generated. This allows the gas turbine to be optimised for its most efficient propulsion mode without compromising the aircraft electrical power network. However, a passive rectification unit would remove the possibility of using the generator to start the engine.

Embedded generation is explored in [5], which underlines Rolls-Royce's commitment to developing this as a viable consideration for the future of more-electric engine technology. The proposed re-positioning of the generator unit shows a number of key benefits and architectural improvements. In particular, the resultant increase in efficiency for transferring power through the propulsion shafts. This would reduce the number of engine components, such as compressor stages or bleed valves, leading to a decrease in construction cost and weight.

The electrical machine itself must be carefully considered and it is well documented [3, 5] that individual generator units taking power from separate gas turbine spools is preferable. The proposed generator in [3] has a permanent magnet (PM) rotor, being cited as potentially more reliable than the wound-field variant. However, the cost of rare-earth magnetic materials is comparatively high and the manufacturing process for encapsulating the magnets to withstand the inertial forces experienced is considerable. The alternative wound rotor offers the possibility to control the rotor flux and, therefore, the terminal voltage in a variable speed application, without the need for armature field weakening. Through the disconnection of the field voltage, it also offers the potential to remove the generation capability in the event of a critical fault. The same engineering challenges remain in securing the rotor windings at high speed. Furthermore, a controlled thyristor converter is selected – over a diode rectification unit – to control the load power factor since the synchronous reactance is high (above 0.5 p.u.), limiting the machine's ability to deliver the required maximum power under passive rectification [3]. The design of the machine must, therefore, be carefully considered if a passive rectifier is to be utilised.

The major thermal challenges when embedding an electric machine within a gas turbine are being overcome through the development of high temperature superconducting machines [18]. Heat generated by operating the machine, combined with the ambient temperature within the gas turbine, can push temperatures up to and beyond 450 °C [19], dependant on the area of the gas turbine considered. Advancements in high temperature technologies allow current and future research to be considered as an option for embedded generation within an aircraft gas turbine. Alternatively, significant benefits can still be obtained through the implementation of new technology as a direct replacement for current AC generation techniques that remain connected to the auxiliary gearbox of the gas turbine.

2.2.2 Marine Power Systems

Shipboard power systems are undergoing a radical design change. Electrical technologies are being implemented to obtain the advantages that these efficient systems and propulsion means provide. Parallels can be drawn between the aerospace and marine sectors where maintenance issues are concerned and the removal of mechanical assemblies is sought. The marine sector endures longer service intervals whilst the turnaround time in the maintenance of aircraft is much more critical and, therefore, shorter as a result. The weight saving through the replacement of mechanical assemblies

with electrical systems is less restrictive than in aerospace, where fuel burn is increased as weight increases [5].

Traditional architectures for marine systems use separate prime movers for propulsion and generation. The Type 23 Frigate, developed in the 1980s, was the first to use a combined diesel electric and gas (CODLAG) propulsion configuration [20]. The diesel engine provides electrical power under general operation, with the gas turbine engine, connected through a gearbox, providing boost propulsion for high-speed manoeuvres. The gas turbine creates significant vibration, so the electrical components of the system are used for noise sensitive operation. The Type 23 infrastructure is diagrammatically shown in *Figure 2.5*.

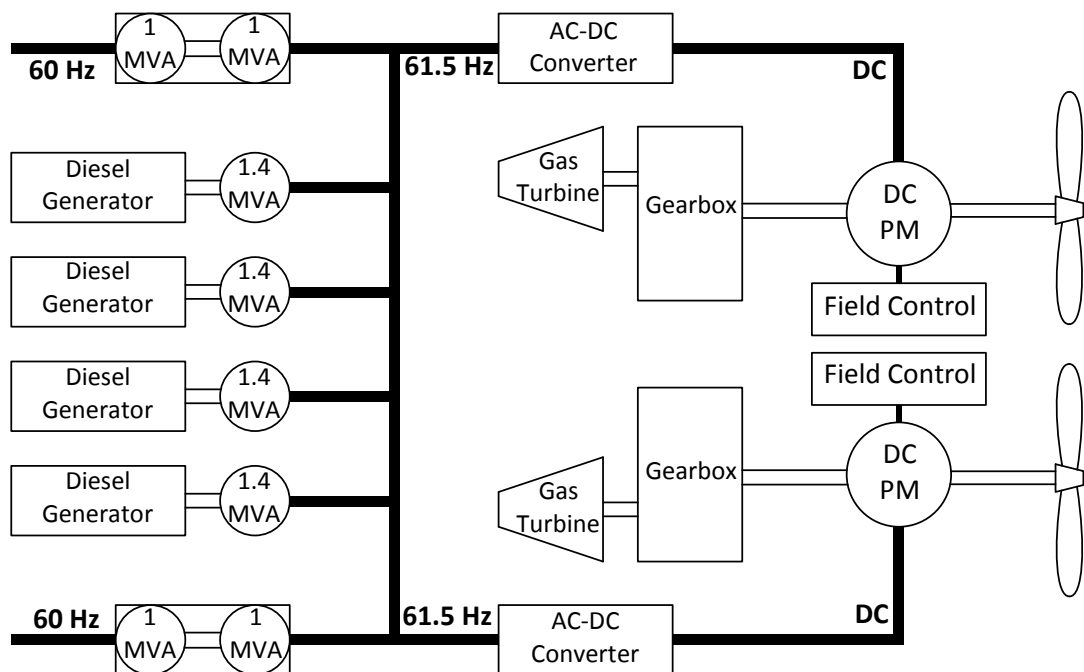


Figure 2.5: Type 23 Frigate Power and Propulsion System (adapted from [21])

The electricity generated from this system is AC, which is then rectified through a thyristor converter to provide a variable voltage DC power supply for the DC propulsion motors. The AC distribution network has a reduced efficiency with twice the amount of distribution losses than that of a DC distribution system [20].

Conventional ship architectures utilise AC distribution systems consisting of several generators connected to separate prime movers with a common AC bus network. This was brought about by the introduction of AC drives and podded propulsors [22] causing the implementation of technology to require such distribution networks. The power management system is complex for applications where these propulsors are exploited for dynamic positioning. The offshore drilling vessel, presented in [22], highlights the

complexity in the control of AC power systems. The diesel generation units are heavily loaded by the electrical system in order to maximise fuel efficiency and limit the fatigue exerted on mechanical couplings. There is little scope for faults due to the system running close to its design limit. DC distribution systems can provide better controllability due to the power electronic stage between the generator and electrical network allowing independent control of power drawn from each prime mover. Work presented in [23] details the performance of an integrated ship power system model. The 60 Hz, 450 V, AC distribution system is powered from two independent auxiliary gas turbine power plants, offering survivability. These are supplemented by two other gas turbine generator units that provide the main electrical propulsion. Both propulsion power trains are rectified and inverted with PWM control to provide variable speed operation. Similar to the Type 23 frigate discussed, there is also a DC bus network to serve the DC loads. As with the AC distribution system, there are two network buses, one on the port side and one on the starboard side of the ship. These provide the necessary redundancy in the event of a fault on either bus. The loads are connected to both of the buses and can be switched in independently to control the loading on each bus or continue operation under bus fault conditions.

Zonal power distribution systems are an area of current interest and they can be AC or DC. However, the future is perceived to be the widespread implementation of DC electrical networks on ships. The zonal networks act to provide separation and a degree of fault tolerance for survivability [24]. The zones are divided into watertight bulkheads [9], where the flexibility of the electrical network allows the loads and generators to be situated in the most suitable location, saving space for weaponry or payload. The benefit of the DC zonal architecture over traditional AC distribution networks is the removal of large switchgear and other magnetic components, which add considerable size and weight to the system. One study predicted the construction cost savings through the implementation in more-electric ships of \$1.4 million per ship for large naval vessels, with a significant proportion of that coming from savings in labour and materials [24].

Suitable generation methods for the DC zonal system are undefined, with many approaches available. Fault tolerance is a factor that affects the decision in selecting generator/motor topologies. Standard three-phase architectures can be designed with fault tolerance. However, the redundancy of such machines in more critical fault conditions is an issue. Several advantages for using a multiphase machine topology are outlined in [25], which

underline the high suitability for this technology in marine applications. For a high phase number induction machine, the torque reduction is considerably less when an open-circuit winding fault occurs. Some de-rating of the machine is required because the stator loss in the remaining healthy windings are increased but, again, as phase number is increased, the de-rating is comparatively much lower [26].

Electrical networks on-board ships remain similar to those of aerospace, with a wide number of technologies employed dependent on military or civil application. For instance, as previously identified, the Type 23 Frigate has a DC bus network but predominately uses the AC network for propulsion power, with localised rectification units providing the DC power to the PM machines. The exclusive use of DC power networks for future naval ships is proposed by [27] which provides experimental research into a testbed for a medium voltage (500 V) zonal DC power system on-board a ship. Both generators used in the system are synchronous machines, the higher power rated generator being wound-field. The ship propulsion system is emulated whilst a high peak power weapon system load is also incorporated. A multiphase synchronous generator would offer the same balanced system performance with the voltage droop from high peak power weaponry counteracted through the same control strategies. However, the torque rating for the propulsion and the fault characteristics can be improved. Under open-circuit fault conditions, a multiphase synchronous motor can still self-start with the loss of one or more phases (dependent on the total number of phases), where a three-phase variant would require an external means of starting [28]. An additional benefit of shipboard propulsion is the amount of torque that can be produced per RMS amp of current, which is moderately increased for the multiphase variant when compared with the volumetric equivalent three-phase generator [29].

As an example of the electrification of civil and defence marine vessels, the rim-driven electric thruster project commissioned by Rolls-Royce [30] was seen as a direct replacement to azimuth thrusters and enabled the removal of the axial driveshaft and gearbox. This project provides an insight into the cross-sector approach towards removing mechanical and hydraulic components in favour of electrical derivatives. Further parallels can be drawn with the aerospace sector as the move toward DC electrical distribution networks is made. This will eliminate reactive volt drops and allow the complexity of the distribution control system to be reduced. The weight savings are not limited to those made through the exchange of mechanical and hydraulic loads for electrical variants. The

connection of these devices through an electrical power distribution system has a reduced size transmission means. Moreover, the connection of a DC distribution network, compared to AC, allows further weight savings to be made through the reduction in cable cores and cross-sectional area required to transmit the same current.

2.2.3 Automotive Applications

Unlike aircraft or ships, the architecture for standard production motor vehicles has, as a whole, changed very little. The internal combustion engine remains dominant for means of propulsion even though it has a poor efficiency [31]. Electric motor drives are relatively under-used, however, hybrid variants are gaining a greater market share. Vehicles for commuter use, such as buses and taxis, have seen the most radical developments but no standard platform has been devised. The optimal motor and generator technology used for this application remains inconclusive [32] but the methods used have successfully reduced carbon dioxide emissions, with the Toyota Prius, for example, achieving a CO₂ output of 104 g/km [33] compared to the average 210 g/km produced by the cars which the Prius replaced.

There are two main architectures currently used in hybrid electric vehicles, although more complex variations of these configurations are being developed and implemented. The first is the series hybrid electric vehicle, which has an electric drive train providing power to the drive wheels, depicted in *Figure 2.6*.

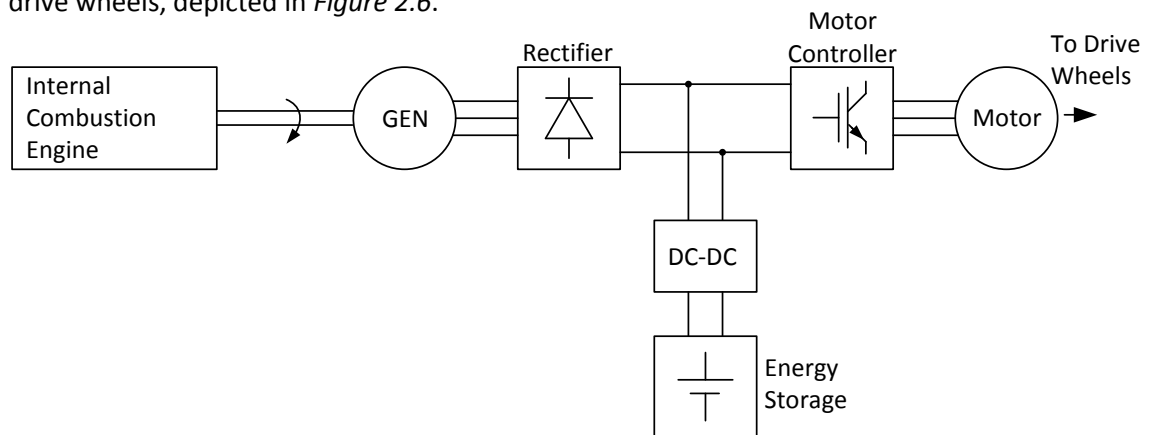


Figure 2.6: Series Hybrid Electric Drive Train Architecture (adapted from [34])

The series hybrid drive train operation depends on the driver input and driving cycle. For low-range, low load journeys, drive can be supplied from the energy storage unit (usually batteries). Under heavier load, the engine provides electrical power to drive the wheels and the stored energy is not utilised. At peak load, however, the electrical power derived from the engine and the energy storage are used together to power the motor. Under braking, energy can be recovered from the motor and stored. The energy storage can also

be topped up from the engine under low load conditions and also when plugged into a grid connection. The great benefit of this type of drive system is that the mechanical coupling is minimal and, as a result, weight and maintenance requirements can be reduced.

The second is the parallel hybrid, shown in *Figure 2.7*, which couples the mechanical and electrical drives to provide power, similar to the CODLAG system discussed earlier.

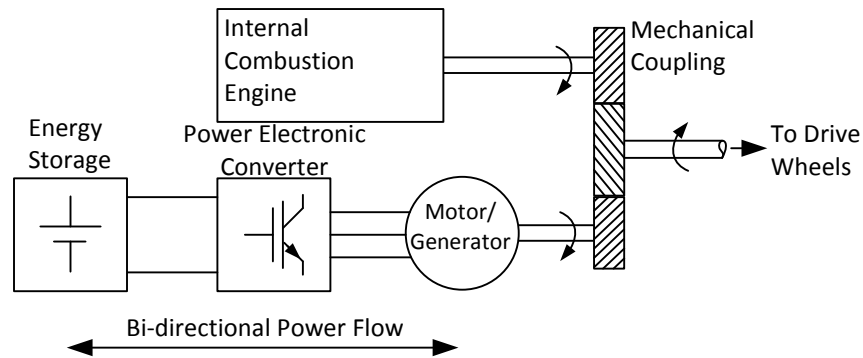


Figure 2.7: Parallel Hybrid Electric Drive Train Architectures (adapted from [34])

This type of architecture offers benefits over the series hybrid drive train through the utilisation of both the engine and electrical motor providing torque to the drive wheels and the compact design as a result of removing the separate generation module.

Generator technology currently utilised for hybrid electric vehicles mainly involves power dense, water cooled PM machines [32]. The torque per unit volume and efficiency provides a good solution for hybrid public service vehicles. However, as previously identified, the cost of rare-earth magnetic materials [35] is a major factor affecting the use of this technology. A wound-field synchronous machine could provide the generation and drive capabilities required in this application. The lower voltage, higher current demand of traction motors is ideally suited to multiphase machines. The wound-field can act to control the voltage level over a wide speed range in the series hybrid architecture, where the control of a PM machine for this purpose is complex. From a safety perspective, the ability to remove the field allows the generator to become passive in the event of a fault. Furthermore, the higher torque density of a multiphase machine would provide weight and space saving compared with the traditional three-phase variant but also offer cost savings in the converter ratings and a higher degree of redundancy.

2.3 Multiphase Machines

Multiphase machines are not a new technology, having been generalised in a number of textbooks [6, 36] and the focus of journal review [7, 28, 37]. The way in which the multiphase machines are presented differs, as described in the following sections.

2.3.1 Split-phase Machines

A split-phase machine is one of the most popular choices for multiphase machine topologies due to its relative simplicity in achieving a higher phase number from a standard machine topology. For instance, [38] describes a split-phase machine where groups of three-phase windings are separated, through their individual star points, within the generator to create a three-, six-, nine- or 12-phase generator, depicted in *Figure 2.8*. The slot distribution of the coils is asymmetrical, with the phase belt being split by 2, 3 and 4, arising in the 30° , 20° and 15° separation in each case, respectively.

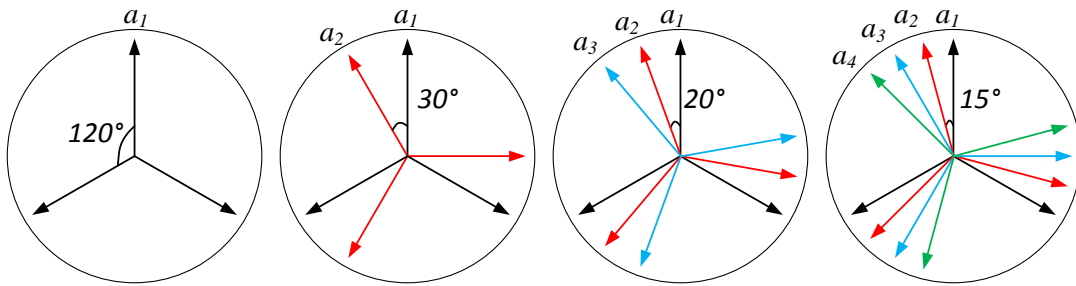


Figure 2.8: Split-phase Machine Stator Winding Phasor Representation

The split-phase machine offers some of the advantages of a multiphase machine, such as improved air-gap field and lower torque pulsations in rotor circuits [38, 39]. Each set of windings can supply, or feed from, a three-phase converter depending on the respective generating or motoring operation required [40]. The ratings for the power electronic components, and therefore cost, can be reduced with this type of machine topology, showing suitability for use in transportation applications. In the event of open-circuit phase faults on the generator or power converter, the split-phase architecture can switch out the remaining phases of that three-phase system to prevent excessive DC ripple magnitude, reducing the 12-phase machine to a nine-phase machine, for example. Work carried out in [41] assesses the normal operation and open-circuit fault performance of a split-phase generator comprising six output phases, for shipboard power systems. The effect of losing one diode in the three-phase rectifier unit has a profound effect on the generator performance, which feeds into the system as a whole, particularly the electromagnetic

torque ripple. For the six-phase generator supplying the input to the dual three-phase rectifier, the DC output side shows significant improvement under open-circuit diode fault conditions. The generator is dual star-connected, suggesting that an open-circuit fault in the generator would exhibit the same performance degradation as the open-circuit diode condition. The DC ripple voltage is considerable for both the three-phase and split-phase machine, a greater ripple reduction could be achieved through a further increase in phase number.

2.3.2 Symmetrical Multiphase Stator Machines

The other type of machine to feature an extension of the three-phase architecture is the symmetrical multiphase variant, which houses a single set of m -phases within the stator. There can be any number of windings present, however, the required rating and geometry of the machine usually governs what is cost effective and practical. The type of machine that can exploit a multiphase stator winding is not restricted, with induction, synchronous and variable reluctance all having been studied for multiphase operation [7, 37, 42].

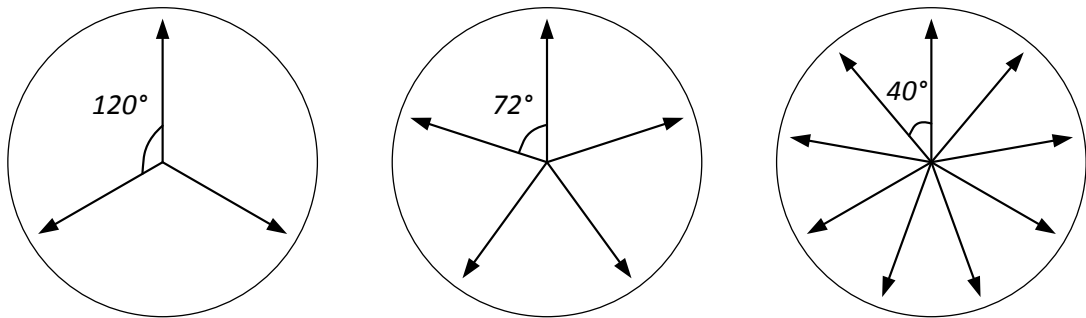


Figure 2.9: Symmetrical Multiphase Machine Stator Winding Phasor Representation

Multiphase Synchronous Generators

Synchronous generators are prevalent in the power generation industry where high efficiency and robust power generation is required. The use of multiphase synchronous generator units is not widely established due to the restrictive nature of the developed transmission infrastructure. However, as power electronic technology develops, the move from AC to DC, in particular HVDC transmission, can be facilitated and the benefits offered by multiphase synchronous generators, outlined in this section, can be exploited in new or replacement generation units.

Current areas where multiphase synchronous generators are utilised are limited, with the developments being described in Section 2.2. One area of technology currently being widely implemented and receiving UK government funding is renewable energy in the form of wind and tidal power. Since the connection of these devices is offshore, the transmission

method for near future applications is perceived to be HVDC. At present, the use of multiphase generators has been proposed to provide control to the offshore wind turbine array [43]. This paper also highlights that the power electronic converter device ratings can be greatly reduced since the current carrying capability is shared across more phases for the same power rated machine. In all applications, this will reduce acquisition cost, costs associated with the thermal control of devices and the improved longevity of the devices.

Work contained in [44] investigates the performance of a three- and five-phase permanent magnet generator for the production of DC power in wind applications. The generator is connected to a diode rectifier which has filter capacitance on the DC side and a resistor-inductor load connected to the output. Normal operation along with single and dual open-circuit phase faults are evaluated for torque ripple and the effects on the AC and DC behaviour. The faults occur in the phase windings only and the capacitance on the DC side helps to improve the pk-pk ripple characteristic. The simulation and finite element analysis (FEA) results are validated through experimental testing conducted on a low power 700 W machine. The capacitance required for the three-phase DC smoothing is considerably larger (2200 μF) than the five-phase generator-rectifier system (470 μF) under normal operating conditions. The efficiency of the system remains higher in the five-phase generator for both single and dual open-circuit faults when compared with the three-phase generator under a single open-circuit fault. Both machines are star-connected which will effectively open-circuit the diode path also. For both failure modes, the copper losses in the machine exceeded rated values and, therefore, de-rating of the generator would be required to sustain the fault over a period of time.

Comparisons are drawn in [45] on a machine that can be configured as a symmetrical 12-phase brushless DC (BLDC) PM synchronous machine or a double-star six-phase machine, both providing DC output. The double-star machine is full-wave rectified, whereas the 12-phase topology is only half-wave rectified, which would be unacceptable for aircraft applications [46]. The distinct advantage of the 12-phase machine is the reduction in diode losses at the expense of increased generator copper losses. However, the comparative savings in diode losses justify these increased copper losses.

2.4 Prior Modelling Techniques

Many of the papers discussed in this literature review contain some element of computer modelling in order to prove a concept. The approaches vary in modelling techniques,

assumptions and programs used. Many textbooks offer code [47, 48], MATLAB Simulink diagrams [49] or dedicated chapters detailing modelling techniques to provide a platform for the modelling of machines and systems [2, 50]. The two-phase equivalent d-q axis approach has been established as the most suitable method for the dynamic modelling of electrical machines since its inception in 1929 [51]. It is particularly efficient as the phase number increases beyond the typical three-phase architecture, retaining the time-stepped computation as a two-phase equivalent.

As computer programs have advanced, the ability to utilise other modelling techniques has become apparent. Three-dimensional, and time-stepped, finite element analysis provide highly detailed information on the internal distribution of the electric field, as well as the machine behaviour with a defined load connected. For example, in [45] the proposed 12-phase PM BLDC machine is configured in a finite element modelling package, whilst the dynamic circuit model is also simultaneously computed as the flux linking the stator varies with angle. This is a very data intensive approach, requiring substantial computing power and a detailed knowledge of the exact electromagnetic and geometric structure of the machine. As phase number increases, the memory requirements in this method of modelling become substantial. The flux linking each coil must be individually calculated as time elapses, making it inefficient for the study of reconfigurable multiphase machines.

The modelling of multiphase synchronous generators is usually application based with [52] providing a generic shipboard model for purposes of evaluation. The proposed generator is a split-phase design with a 12-phase generator being constructed from four, separated neutral, three-phase winding sets connected to four, three-phase rectifiers. For purposes of experimental validation, not undertaken in the paper, the use of four, three-phase diode bridge rectifiers is suitable because of their wide commercial availability. For utilisation in a reconfigurable multiphase system, the benefit of having separate three-phase diode packages reduces overall system cost for voltage and current ratings whilst maintaining the flexibility. In high current applications, and where the phase number has been reduced, the thermal constraints for the diode rectifier can be met by separating the generator output to individual diode packages.

2.5 DC Distribution Networks

The use of higher voltage DC electricity is making a return after the prolonged domination of AC electricity, particularly in transmission networks [53]. This move is facilitated by the

advancement in power electronic devices, being developed to withstand higher voltage and current levels demanded in modern applications, and the current development of technology capable of safely breaking high DC currents [54], which at present is at a voltage level suitable for aircraft. Technical challenges are still being faced in the breaking of DC current at high voltage levels.

The test system used in the POA project [15] was modelled using a 350 V DC power network from which the oil pump, fuel pump and inlet guide vane loads were powered [55]. Current DC electrical networks, found almost exclusively in the defence sector, are typically rated at 270 V DC [13] as a result of standard aerospace generator AC voltages being rated at 115 V. Work carried out in [56] outlines the performance of a DC distribution network in comparison with conventional systems. The results are evaluated against MIL-STD-704F [46], which specifies a +10 dB/decade distortion amplitude up to 1 kHz, -20 dB/decade beyond 1 kHz and -40 dB/decade after 50 kHz for harmonic distortion. The voltage droop characteristics of a 270 V DC aircraft power networks are specified to be within 250 to 280 V with a maximum ripple magnitude of 6 V. The system presented in [56] showed significant improvement in the mitigation of supply distortion. However, except for extremely high frequency amplitudes, the distortion was within MIL-STD-704F tolerances prior to the engagement of the technology.

The intelligent electrical power network evaluation facility (IEPNEF), developed at the University of Manchester in conjunction with Rolls-Royce, emulates an unmanned aerial vehicle (UAV) application and utilises a 540 V DC bus [57]. In comparison to the POA developed test-rig, the IEPNEF has a gas turbine emulation, with the LP spool and HP spools represented by different motor topologies. The generator unit, used to provide the DC bus network, is a five-phase PM machine rated at 70 kW. The generator output is rectified using single phase H-bridge converter units. This ensures that the current drawn from the generator is sinusoidal and allows the DC bus to be controlled. This approach guarantees the power quality of the DC bus network whilst maintaining efficiency in the generator. However, the problems associated with the control of power electronic devices can be exacerbated in extreme environments [58]. Switching signals are highly susceptible to noise and the proposed environment of a gas turbine engine will incur electromagnetic interference.

2.6 AC to DC Rectification

In the previous sections, the move towards the electrification of aerospace, marine and automotive vehicles has been discussed. Much of the technology being developed and implemented relies on input power being rectified from AC to DC locally, for example aircraft electro-mechanical actuators (EMA), used on the A380, require local rectification for the DC drive. It is clear that there is a requirement for the conversion of AC electrical power to DC and there are a number of techniques available.

Diode rectification is the most common and cheapest solution in the conversion of power from AC to DC. As voltage and current handling capabilities increase, the diodes become more expensive. However, they require no form of control, thus saving on the cost of a separate control unit necessary for thyristors and other controllable semiconductor devices. On-board aircraft, diode rectifiers are used in the transformer rectifier unit (TRU) [13] to provide a stepped down 28 V DC supply for auxiliary control and avionics. These TRUs produce a large amount of heat, since they are specified to provide large amounts of current. Methods are presented in [59] to provide improved diode rectified TRUs for use in converting AC voltage from 115 V to DC at a level of 270 V. This would better utilise the TRU but require a DC-DC converter to provide a 28 V DC power offtake. Diode rectifiers can also be found in almost all automotive vehicles since the on-board alternator must provide DC power to charge the battery and supply power to auxiliary equipment after starting.

Switchable devices such as thyristors, insulated gate bipolar transistors (IGBT) or metal-oxide-semiconductor field effect transistors (MOSFET) all have very different characteristics due to their semiconductor construction, not explored here. These devices can be beneficial compared to diodes depending on their application. In automotive applications, energy recovery is used during reverse power flow, under deceleration, for example. This requires a bi-directional power flow and diodes cannot support this, whereas using a number of switchable devices can allow power to flow in both directions. The charging and discharging of the battery must be carefully regulated to avoid deep cycling and overheating issues occurring. Work presented in [60] shows a number of modes where an IGBT converter provides or accepts power from the DC link.

2.7 Summary

This literature review has identified areas within the transportation sector where adaptation and improvement of current more-electric technologies can be applied. It is evident that the efficiency, maintenance and cost can be improved upon through the use of electrical systems in aerospace, marine and automotive applications. Civil aerospace has already made the move toward more-electric aircraft (MEA) with current and future electrical generation systems outlined as electrical loading on-board aircraft increases. In marine applications, the more-electric ship is undergoing constant review as technology matures. The type of electrical machine employed is still open for consideration and there is ample evidence to support the use of torque dense multiphase machines. Automotive applications can also exploit the multiphase machine, where lower voltages and higher currents are required for traction drives. The speed range over which some of these systems can be operated can be improved through the use of wound-field machines, allowing control of the voltage level.

The types of multiphase machines available were discussed with comparisons drawn against the technologies. Split-phase machines provide a multiphase output through a multiple of three-phase winding sets. However, under fault conditions it is common to switch out healthy phases in order to maintain the DC performance. The symmetrical multiphase machine offers the best method of providing redundancy and power density for use in safety critical applications such as aircraft but incur greater construction costs as a result of the non-standard construction methods.

The computer modelling of electrical machines can be undertaken through a number of methods and with a number of programs available. It has been identified that time-stepped finite element modelling would be very slow for a reconfigurable multiphase generator and, as such, standard circuit modelling techniques will be used to ascertain the generator dynamic performance. Static finite element modelling can be advantageous in the investigation of the internal flux distribution of the generator and losses occurring for given load conditions.

The proliferation of DC power networks has been briefly discussed. The advancement of technologies used in high-voltage DC (HVDC) transmission has had wide reaching benefits across a number of sectors. Standards and requirements for the use of DC power in

defence aerospace applications were presented. The process of achieving DC power from an AC system was also presented, highlighting the technology currently used.

Taking into consideration the findings of the literature review, there are sections where there is scope for development. Although there is considerable literature available concerning the modelling, construction and use of multiphase motors, there is very little regarding generators, in particular synchronous generators. This type of machine, in its three-phase form, is used extensively in industry for the reliable generation of power and it is clear that there are significant benefits to be gained from increasing the phase number. In aerospace applications, synchronous machines are widely used and already certified. Compared with a PM generator, a wound-field machine would provide voltage regulation over a wide speed range and offers a means of removing the generation capability in the event of a critical fault. In order to move toward DC power distribution systems on-board aircraft, and in marine applications, the ability to convert the AC power must be realised. The most cost effective way of achieving this is through the use of power diodes, which would have a reduced rating and increased longevity in multiphase systems. Diode rectification also offers simplicity, with no need for associated control and gate drive circuits. This thesis studies a multiphase synchronous generator with diode rectification to ascertain how phase number, connection topology and winding design affect DC power quality and generator losses for use, primarily, on-board aircraft.

3

Dynamic Circuit Modelling and Simulation of a Synchronous Generator

3.1 Introduction.....	53
3.2 Three-phase Mathematical Model.....	54
3.3 Extension to Multiphase Model	63
3.4 Harmonic Modelling.....	67
3.5 Passive Rectification	70
3.6 Summary	94

3.1 Introduction

Mathematical modelling provides an opportunity to design and simulate a component or system based on envisaged or tangible data: ‘A model is a representation of a theory that can be used for prediction and control’ [49]. At present there are a plethora of computer programs available that use established techniques to model all aspects of engineering. Some programs have the capability to model mechanical and electrical systems within the same environment, allowing the electro-mechanical interactions to be evaluated. However, most programs exist to provide highly detailed information on some aspect of a system design, finite element analysis (FEA) detailed later in Chapter 4, for example.

Modelling the internal electrical behaviour of a generator, discussed in Chapter 4, can quantify the electromagnetic components through a fixed current solution based on the geometry of the machine. However, it is often required that a full system is dynamically

modelled, including input, control and output elements. Components connected on the output side can have their behaviour affected by the intrinsic qualities of the electric generator. However, they can also have a significant effect on the generator itself, drawing non-sinusoidal current due to switching effects, for example. Unlike finite element modelling (FEM), the circuit model provides a time varying solution through fixed magnetic circuits. The dynamic modelling of the entire system is required to allow the effects of components connected at the output side to be evaluated.

Generalised machine theory is based on the differential equations that describe a machine's electrical circuits. The equations are consistent in textbooks in the three-phase domain. However, the mathematical modelling techniques are defined with some variation in conventions [2, 49, 50]. The key difference, in terms of computing power and execution time, is the choice to resolve the differential equations to a two axis equivalent, converting a three-phase system to an effective two-phase reference frame. This reference frame does not physically exist on the stator side and, therefore, the three-phase stationary reference frame is preferred for directly comparing simulation and experimental results. The fundamental benefit of applying this method, however, is the ability to reduce the complexity of the system by decreasing the number of differential equations that require computation. Furthermore, the ability to resolve the new two-phase coordinate system to a synchronous reference frame removes the angular dependence of the inductance involved in the machine equations. The methodology employed in the mathematical modelling of the synchronous generator utilises the two-axis theory and is detailed in this chapter.

This chapter covers the development of a dynamic simulation model in MATLAB Simulink, including the verification and validation of the simulation output for the three-phase machine, before extending to higher phase numbers. Each generator model can then be expanded upon to include a passive power electronic converter to rectify the AC power output. Validation results are based on tests carried out on a Cummins BCI162G generator whose parameters are given in Appendix 7.4. Testing of the system is covered in Chapter 5.

3.2 Three-phase Mathematical Model

3.2.1 Introduction

The three-phase synchronous generator is well documented due to its popularity in power generation, owing largely to its high efficiency and reliability [61]. The mathematical

modelling principles remain the same for generators in the 10 – 100 kW range as those for large scale generation, 10s of MW. However, the per unit parameters for large scale generators differ from the smaller scale units, requiring careful consideration of simulated tests to enable the data output to be evaluated. Large generators, with a higher pole number, have a longer sub-transient time constant under short-circuit fault conditions, allowing them to be fully characterised [53]. However, as the physical size of the generator is reduced, the relative resistance increases, giving faster transient effects resulting in difficulty in measuring the sub-transient time constant.

3.2.2 Construction of the Simulation Model

Construction of the generator dynamic circuit model was carried out in MATLAB Simulink (version 7.5), a platform extension to the general purpose MATLAB (R2010 version 7.10) software, which is capable of mathematically representing a system from any engineering domain. Modelling a synchronous generator requires no specialist toolboxes to be installed since the dynamic behaviour can be fully described with the mathematical equations linking flux, voltages and currents within the machine windings. The Simulink platform provided the advantage of a visual approach, with each section of the model well defined for purposes of evaluation. The electrical equation that describes the generator, in its simplest form, is shown in Equation (1).

$$v = [R]i + \frac{d}{dt}[\varphi] \quad (1)$$

where v and i are the instantaneous values of voltage and current, respectively, $[R]$ is the matrix of resistances and $[\varphi]$ is the matrix of time-dependent flux linkages.

The dimensions of the matrices involved are dependent on whether the stator variables are retained as three-phase variables, as discussed in [2, 49, 50], or transformed to the d-q axis reference frame. Further simplification can be made by referring the transformed variables to the synchronous (rotational) reference frame, removing the angular dependence of the inductance terms in the machine equations.

The mathematical model is configured to provide a current output from a voltage input, therefore, re-arrangement of the machine equations is required to facilitate this. The matrices are separated into their respective derivative and rotation dependant component parts, which leaves two current vectors, one of which is in derivative form. To avoid

algebraic loops and maintain accuracy, the matrices are further arranged into integral form with the state-space representation providing a suitable solution, shown in Equation (2).

$$\begin{aligned} \underline{v} &= [A]\underline{i} + [B]\frac{d}{dt}\underline{i} \\ \underline{i} &= \int ([B]^{-1}\underline{v} - [B]^{-1}[A]\underline{i})dt \end{aligned} \quad (2)$$

where a vector column is denoted by the embellishment \underline{x} (x is an arbitrary variable) and the construction of matrices $[A]$ and $[B]$, which can be observed in *Figure 3.1*, are provided in Appendix 7.7.

The manipulation of the matrices into the form of Equation (2) is facilitated by separating the component parts. The B matrix comprises the constant inductance coefficients which can be implemented as a MATLAB pre-processor script, allowing the inversion to be done as a single instruction. The A matrix is more complex and requires information regarding the angular speed of the rotor. Consisting of the rotational matrix, G , and the resistance matrix, R , the values were input as a MATLAB script and multiplied out in Simulink as shown in *Figure 3.1*, reducing the required computational power for simulation.

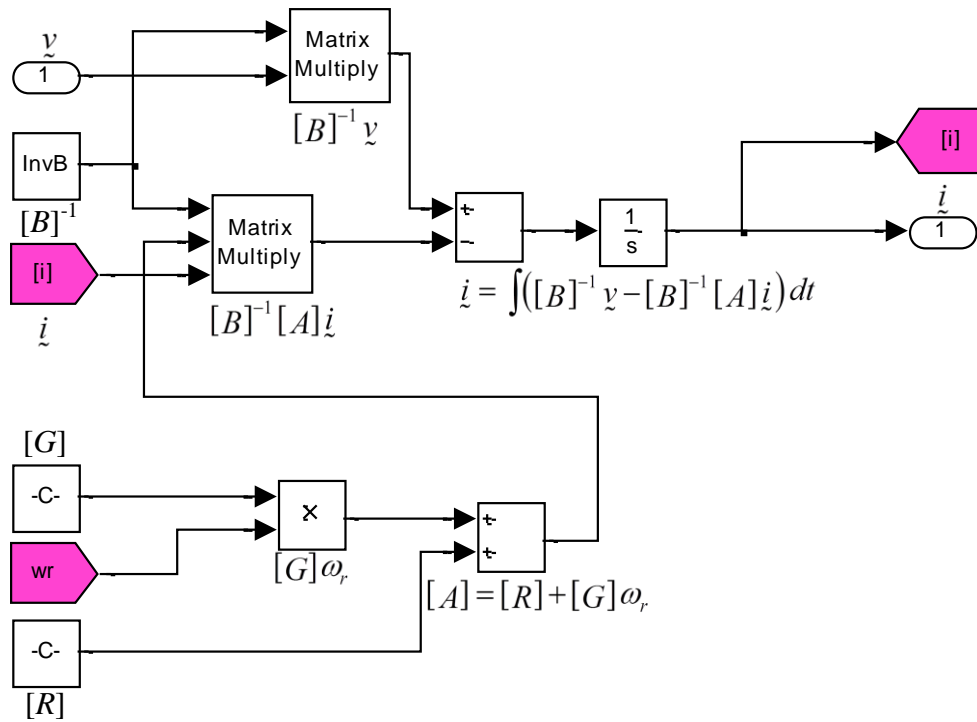


Figure 3.1: MATLAB Simulink Implementation

The output current is responsible for the development of electromagnetic torque, which relates the electrical model to the mechanical rotational input.

The electromagnetic torque is calculated using the d- and q-axis currents to satisfy Equation (3).

$$T_{em} = pp \times (\varphi_d i_q - \varphi_q i_d) \quad (3)$$

The mechanical model is simplified to the main equation of motion to determine speed, which in turn is fed back to the state-space model to determine the current generated and thus the electromagnetic torque. Equation (4) rearranges this in integral form, as used in the model.

$$\begin{aligned} T_{mech} &= -T_{em} + D\omega_{rm} + J_r \frac{d\omega_{rm}}{dt} \\ \omega_{rm} &= \frac{1}{J_r} \int (T_{mech} + T_{em} - D\omega_{rm}) dt \end{aligned} \quad (4)$$

where T_{mech} is the mechanical torque, D is the frictional damping, T_{em} is the electromagnetic torque developed, J_r is the rotor inertia and ω_{rm} is the rotor mechanical speed.

The negative sign of the electromagnetic torque in Equation (4) shows that the machine is acting as a generator. In the simulation, the mechanical torque is linked to the speed through a proportional-integral controller which acts to best maintain the input shaft at synchronous speed, shown in *Figure 3.2*. In aircraft applications, the mechanical torque to the generator would be provided by the gas turbine engine, which would have its own dynamic behaviour. For full system simulation, the gas turbine's dynamic spool behaviour could be incorporated at this stage to fully model the interactions between the generator and the gas turbine. For simulated slip and short-circuit transient testing, the speed of the rotor was allowed to vary. For all other simulated conditions, the speed control loop was removed and fixed, synchronous speed was imposed. Experimental torque measurements were not recorded due to the absence of a working torque transducer on the test-rig. This has been identified for future investigation.

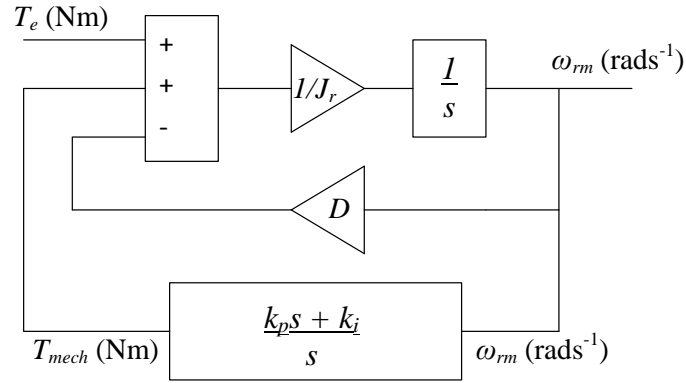


Figure 3.2: Constant Speed Drive Model

The automatic voltage regulator (AVR) is an electrical control algorithm that acts to keep the output voltage of the generator at a constant value. This is implemented as an electronic controller on the physical generator, which uses the terminal voltage magnitude as an input signal and compares with a reference value before modifying the field voltage to maintain the terminal voltage level. The AVR is implemented in the simulation model as a proportional-integral control to maintain the field voltage level, shown in *Figure 3.3*. This is not a full representation of the physical AVR and does not represent the dynamics of the system. Under experimental test conditions, the AVR was disabled and the field was supplied with a constant voltage source through slip rings.

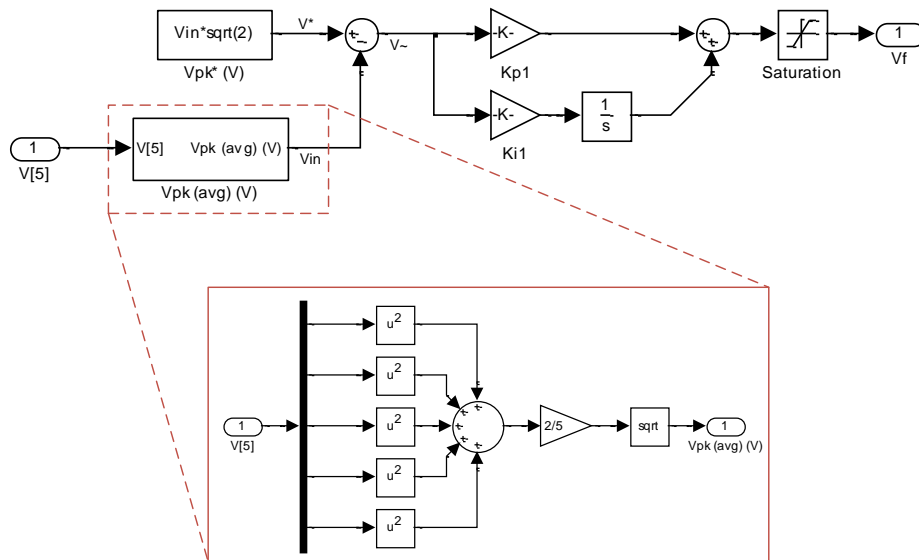


Figure 3.3: Simulation Model AVR

The full simulation model can be found in Appendix 7.6.

3.2.3 Model Assumptions and Final Model Equations

The mathematical modelling is limited by the detail describing the electromagnetic interactions. In order to ensure performance and accuracy when modelling the synchronous generator, the following assumptions were made:

- Magnetic saturation effects are assumed negligible, allowing superposition to be applied to the magnetic circuits within the machine model. A linear flux-current relationship is therefore assumed
- Stator and rotor windings are assumed to be sinusoidally distributed, ignoring winding harmonics
- The saliency of the machine takes into account the 2θ terms but not higher order terms
- Rotor self-inductances are assumed constant, neglecting variation of rotor inductances with angular position
- Model parameters are assumed to be the same for fully- and short-pitched topologies

These assumptions are explored in the following chapter, see Section 4.4.

The final model equations relating the d-q voltages, currents and inductances are shown in Equation (5) in the synchronous reference frame. The matrix is split into its component parts with the A matrix consisting of the resistances and rotational components and the B matrix comprising the constant inductance coefficients, described in Appendix 7.7 and depicted in *Figure 3.1*. The three-phase variables are transformed to d-q coordinates through the Clarke transform using the constant power convention, which is available in textbooks [50, 62].

$$\begin{bmatrix} V_{ds} \\ V_{qs} \\ V_{kd} \\ V_{kq} \\ V_f \end{bmatrix} = \begin{bmatrix} R_D + L_D p & -L_Q \omega_r^e & L_{md} p & -L_{mq} \omega_r^e & L_{md} p \\ L_D \omega_r^e & R_Q + L_Q p & L_{md} \omega_r^e & L_{mq} p & L_{md} \omega_r^e \\ L_{md} p & 0 & R_{kd} + L_{kd} p & 0 & L_{md} p \\ 0 & L_{mq} p & 0 & R_{kq} + L_{kq} p & 0 \\ L_{md} p & 0 & L_{md} p & 0 & R_f + L_f p \end{bmatrix} \begin{bmatrix} i_{ds} \\ i_{qs} \\ i_d \\ i_q \\ i_f \end{bmatrix} \quad (5)$$

where subscripts ds and qs are the d- and q-axis stator variables in the synchronous reference frame, respectively, kd and kq are the rotor damper windings, f is the field winding and p is the operator d/dt .

The parameters used in the three-, five- and 15-phase dynamic circuit models contained in this chapter are shown in *Table 3.1*.

Table 3.1: Model Parameters used in Simulation

			Three-phase	Five-phase	15-phase
Stator Resistance	R_D, R_Q	Ω	0.4316	0.2590	0.0863
d-axis Damper Resistance	R_{kd}	Ω	0.1560	0.0936	0.0312
q-axis Damper Resistance	R_{kq}	Ω	0.1731	0.1038	0.0346
Field Resistance	R_f	Ω	0.3050	0.1830	0.0610
d-axis Stator Inductance	L_D	H	0.0711	0.0427	0.0142
q-axis Stator Inductance	L_Q	H	0.0348	0.0209	0.0070
d-axis Magnetising Inductance	L_{md}	H	0.0691	0.0414	0.0138
q-axis Magnetising Inductance	L_{mq}	H	0.0328	0.0197	0.0066
d-axis Damper Inductance	L_{kd}	H	0.0702	0.0421	0.0140
q-axis Damper Inductance	L_{kq}	H	0.0337	0.0202	0.0067
Field Inductance	L_f	H	0.0746	0.0447	0.0149

3.2.4 Verification against Standard Models

Prior to undertaking the modelling of a multiphase synchronous generator, the three-phase model was verified using an industry standard modelling package and later validated against the physical output of the machine that the model replicated. Some comparisons can be drawn from the characterisation tests undertaken, covered in Appendix 7.4, which were also simulated. These highlighted the similarities in the machine's performance under transient conditions with the simulated prediction of its behaviour.

The SimPowerSystems toolbox in MATLAB allows the modelling of generation, transmission and distribution networks and contains a standard model of a three-phase synchronous generator. The model in Section 3.2.2 differs from the SimPowerSystems standard model, which uses different conventions on machine parameters and input connections to define the underlying mathematical model. Both models were configured in the same manner for the characterisation test, as described in Appendix 7.4, as they were for the loading tests described herein. The mathematical model and SimPowerSystems model could be simulated simultaneously and the outputs transferred to Excel for post-processing.

The load utilised in the simulation was based on a bank of resistors available for laboratory testing, connected in parallel to give a total 13 Ω resistance. Both machine models provide

a current output from a voltage input, therefore, a gain block was used to compute the voltage drop across the load resistance. The same AVR was used in both cases and was set to provide a terminal voltage of 380 V. The results from both models are displayed in *Figure 3.4* and *Figure 3.5* under steady-state and transient effects, respectively.

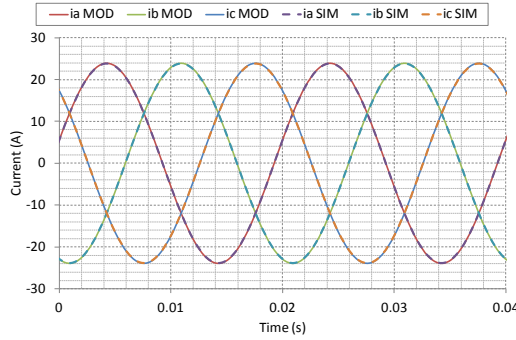


Figure 3.4: DeVised Model vs. SimPowerSystems Phase Current Output

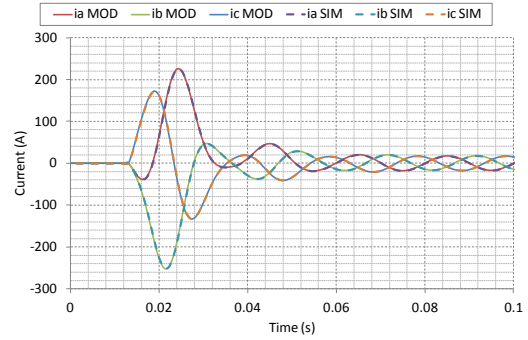


Figure 3.5: DeVised Model vs. SimPowerSystems Short-circuit Phase Current Response

The steady-state currents drawn from both models are consistent for the 13 Ω load applied. The steady-state voltage and, therefore, power drawn by the load, also match as shown in *Table 3.2*.

Table 3.2: Comparison of Simulation Model Outputs

	Simulation Model	SimPowerSystems Model
Current (A_{pk})	23.875	23.872
Voltage (V_{pk})	310.369	310.335
Three-phase Power (kW_{RMS})	11.116	11.114
Field Voltage (V_{pk})*	17.92	14.63
Field Current (A_{pk})*	35.51	28.99
Speed (rpm)	314.159	314.159
Torque (Nm)	36.370	36.362

**Note: The field voltages and currents differ by a factor of $\sqrt{3/2}$ due to the use of the constant magnitude convention in the SimPowerSystems model.*

The SimPowerSystems synchronous generator model is developed using the American standard for defining the two-axis theory, where the q-axis is aligned with the a -phase. The result of this is that the d-q model outputs are separated by 90° , which can be corrected for by subtracting $\pi/2$ from the angle applied to the Clarke transform.

Evaluating the devised model against an industry standard model provided confidence in the configuration and implementation of the mathematical model for the three-phase case.

SimpowerSystems does not provide a multiphase model. Prior to extending the devised model to a multiphase case, validation that it could accurately predict the physical behaviour of the laboratory machine was required.

3.2.5 Validation against Experimental Results

Open-circuit and generator loading tests showed close correlation between results sets, confirming those presented in *Table 3.2*. Further experimental characterisation results are given in Appendix 7.4. The dynamic behaviour of the experimental machine differed slightly under test conditions, highlighted in *Figure 3.6*. The simulated peak values for the short-circuit transient test were initially lower than that achieved in experimental testing. The assumption is made that this is due to linear magnetic circuits in the model. There is, however, good correlation between the sub-transient and transient decays to steady-state, underlining the reactances being correctly estimated from Appendix 7.4.

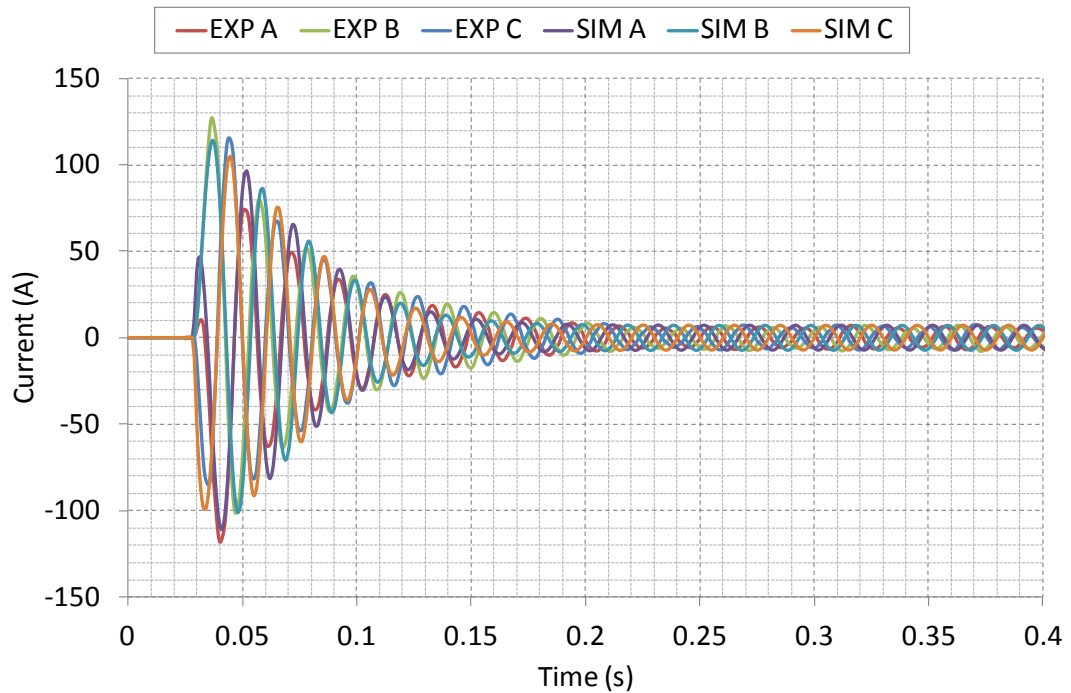


Figure 3.6: Experimental vs. Simulation Model Short-circuit Behaviour

The agreement between results from the steady-state and transient fault behaviour of the generator provided confidence in the dynamic circuit model to proceed with extending it to a multiphase model. Further characterisation results for the three-phase model can be found in Appendix 7.4, where tests highlight the model performance under transient conditions. Accurate representation of the transient behaviour is important for recreating the commutation effects in the diode rectifier.

3.3 Extension to Multiphase Model

3.3.1 Introduction

The three-phase model was extended to create a multiphase synchronous generator model. The principles involved in creating a multiphase model were fundamentally the same, transforming m -phases to a two-phase equivalent, described in further detail in [6]. This greatly simplifies the mathematics involved in inverting the inductance matrix, which, again, can be completed prior to simulation in a MATLAB m-file script.

Applying the Clarke transform, the three-phase model simplified to the fundamental d- and q-axis components with a zero sequence component present, where supply harmonics map to the fundamental or zero-sequence. Extending to more than three phases creates higher order d-q sets, and supply harmonic components map to the fundamental, third, fifth, etc. in d-q pairs. Under balanced load operating conditions, the harmonic content of a synchronous machine supplying an AC network is minimal. However, when considering non-linear loads and machine faults, it is necessary to examine the harmonics as they can create losses and pulsating torque, affecting the behaviour of the machine. Since the generator will be connected to a rectification stage, the load experienced by the generator will appear non-linear due to the switching elements, giving rise to non-sinusoidal voltages and currents. The extended Clarke transform retains the advantage of being defined in a pre-processor script and can, therefore, be embedded in Simulink for matrix multiplication.

$$\begin{bmatrix} V_d \\ V_q \\ V_{x1} \\ V_{y1} \\ V_{x2} \\ \vdots \\ V_0 \end{bmatrix} = \sqrt{\frac{2}{m}} \begin{bmatrix} \cos(0) & \cos(\gamma) & \cos(2\gamma) & \cdots & \cos((m-1)\gamma) \\ \sin(0) & \sin(\gamma) & \sin(2\gamma) & \cdots & \sin((m-1)\gamma) \\ \cos(0) & \cos(2\gamma) & \cos(4\gamma) & \cdots & \cos(2(m-1)\gamma) \\ \sin(0) & \sin(2\gamma) & \sin(4\gamma) & \cdots & \sin(2(m-1)\gamma) \\ \cos(0) & \cos(3\gamma) & \cos(6\gamma) & \cdots & \cos(3(m-1)\gamma) \\ \vdots & \vdots & \vdots & \ddots & \vdots \\ \frac{1}{\sqrt{2}} & \frac{1}{\sqrt{2}} & \frac{1}{\sqrt{2}} & \cdots & \frac{1}{\sqrt{2}} \end{bmatrix} \begin{bmatrix} V_a \\ V_b \\ V_c \\ V_d \\ V_e \\ \vdots \\ V_m \end{bmatrix} \quad (6)$$

where γ is the phase displacement $2\pi/m$, m being the phase number.

It can be observed from Equation (6) that the power invariant form has been used for an odd number of phases. The power in the multiphase reference frame is the same as that in the d-q reference.

Implementation in MATLAB Simulink is relatively straightforward when extending from an established three-phase model. The extended Clarke transform, described above, is used to create the fundamental d-q axis voltages and higher order harmonic d-q pairs in the x - y plane. The fundamental elements are used, along with the damper winding and field voltage components, as the input for the state-space model, detailed in Section 3.2.2, after undergoing the Park transform [51] to remove the angular dependence of the inductances. The harmonic and zero sequence parts do not undergo this rotational transformation and therefore require separate computation. Balanced harmonics other than those of order $2m \pm 1$ that are present in the system, map to the x - y planes and follow the leakage path, described by Equation (7).

$$\dot{\tilde{i}} = \frac{1}{[L_{ls}]} \int (\tilde{v} - [R]\tilde{i}) dt \quad (7)$$

where L_{ls} is the leakage inductance, R is the stator resistance and \tilde{v} and \tilde{i} are the higher order voltages and currents up to, and including, the zero sequence, respectively.

The output of the state-space model gives the fundamental d-q currents, damper winding currents and also the field winding current based on the assumption that the machine is sinusoidally wound. These outputs must be combined with the harmonic currents calculated through Equation (7) to provide the full solution. In order to recombine the output currents, the fundamental currents must be transformed back into the stationary reference frame through the inverse Park transform. Concatenating to form a single column vector of fundamental and harmonic currents, they are fed into the inverse of the extended Clarke transform, which transforms the d-q values back into multiphase values. Once in the multiphase domain, the output can be fed into a resistive load or a non-linear load such as a diode rectifier, providing application based results. The full MATLAB Simulink model is shown in Appendix 7.6.

The stator leakage calculation in Equation (7) is based on the overall leakage, which will change for phase number, machine pitching and higher order harmonics. The slot leakage comprises the conductor losses into the slot face, which for double layer windings will have the two conductor losses plus a mutual coupling between them. This mutual coupling

component will change depending on the pitching of the machine arising in a different leakage value for the fully- and short-pitched windings. The calculation of such effects is a time intensive process, discussed in [63], and is beyond the scope of this project. Testing could be carried out on the three-phase machine for a fully- and short-pitched configuration and the leakage component found through the techniques discussed in Appendix 7.3 and 7.4. The end-windings have a considerable effect on the leakage and machines are designed to maintain short end-winding lengths through the use of concentric windings. The multiphase generator used for experimental testing is wound such that the end-windings are of a similar length and, therefore, the contribution to the leakage path remains unchanged. For higher order harmonic effects, the leakage will be different. However, as phase number increases, the difference between the fundamental leakage path and resultant harmonic paths is negligible, therefore, the same value of leakage was used.

3.3.2 Five-phase Resistor Loaded Generator Results

The three-phase model has been rigorously tested through characterisation, verification and validation methods culminating in a model that proved dynamically sound. The five-phase generator was simulated with a fixed $58\ \Omega$ per phase resistive load to match experimental testing in the laboratory. The load bank available for experimental testing was rated at that resistance. The model assumes sinusoidally distributed windings and constant shaft speed input. The parameters for the simulation model are scaled according to the phase number, highlighted in Appendix 7.5. The connection method exhibits no difference in machine performance for a steady-state load such as this and, therefore, only the star-connected generator will be considered.

As stated in Section 3.2.3, the model will reflect fundamental winding behaviour only and not the distortion in voltages and currents when the generator windings are not sinusoidally distributed. Chapter 4 underlines the effects of pitching the double layer windings and will be investigated further in Chapter 5.

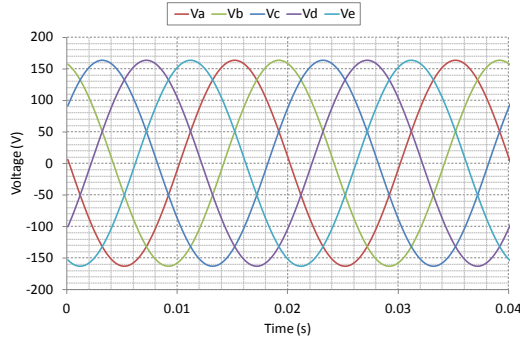


Figure 3.7: Simulated AC Phase Voltage

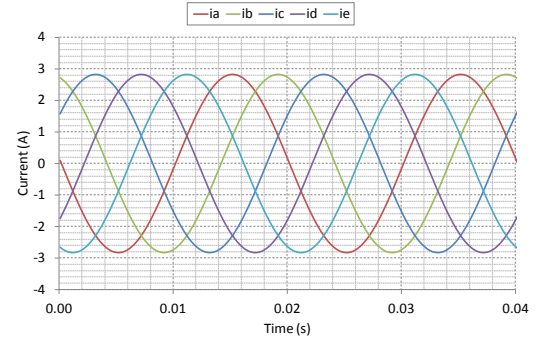


Figure 3.8: Simulated AC Phase Current

The voltages and currents, depicted in *Figure 3.7* and *Figure 3.8*, respectively, are sinusoidal in nature due to the model not taking into account the stator winding effects. The voltage developed at the generator terminals is lower due to the reduction in phase winding turns and the current through the external resistance is linearly scaled. The dynamic model gives a good indication of the voltage and current levels that can be achieved when loading the machine. The simulation results of the full system, including rectifier, are compared with experimental test results detailed for selected cases in Chapter 5.

3.3.3 Fifteen-phase Resistor Loaded Generator Results

Further extending the generator model from five-phases to incorporate the maximum permissible 15-phases yields the simulated results contained in this section. Again, the parameters were scaled to reflect the changes in the generator with the increase in phase number, shown in Appendix 7.5. This is a simple AC resistor load simulation in order to verify the model extension before connecting a non-linear rectification device at the output.

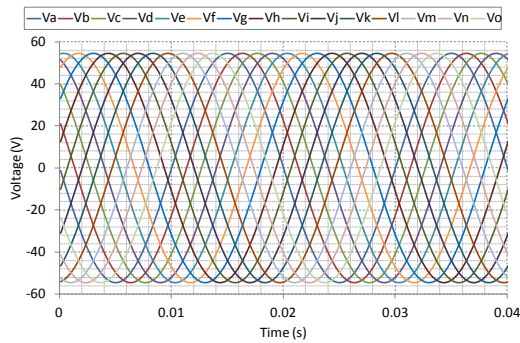


Figure 3.9: Simulated 15-phase AC Phase Voltage

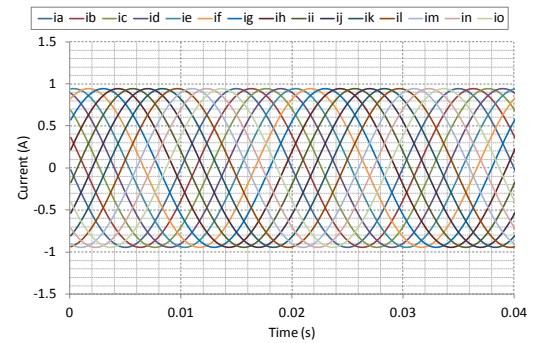


Figure 3.10: Simulated 15-phase AC Phase Current

The voltages and currents shown in *Figure 3.9* and *Figure 3.10* are ideal values and thus have a perfect sinusoidal shape. The phase voltage magnitude has reduced for the same load resistance due to the machine being designed to have a constant rated power output.

The 15-phase machine voltage is reduced to 20 % of the original three-phase voltage output. As a result of the reduced voltage across the same resistance, the current must also decrease.

3.4 Harmonic Modelling

The sinusoidal assumption made in the simulation modelling is proven to be valid for cases where near sinusoidal back-emf is developed by the generator. However, as the FEA shows in Chapter 4, and the experimental work of Chapter 5 highlights, as the phase number increases, the sinusoidal approximation is no longer valid, particularly for the fully-pitched generator. To address this problem, the spacial harmonic content can be evaluated by using the FEA to extract the harmonic data from the open-circuit back-emf characteristics.

Before being rewound, the generator used for experimental testing originally housed a double layer three-phase concentric winding. The specification for the rewound generator was as close to the original machine as practicable. Therefore, for ease during the rewind process the double layer winding was retained, allowing short-pitching to be considered to reduce harmonic content in the air-gap flux. The pitch factor was determined from the equations discussed in Appendix 7.2. Predominantly, the lower order harmonics were selected to be cancelled to allow the production of sinusoidal voltages at the generator terminals. The three-phase machine was pitched by 60° as per the original machine to remove triplen harmonics. The five- and 15-phase generator pitch factors were chosen based on the minimisation of total harmonic distortion, discussed in Chapter 4.

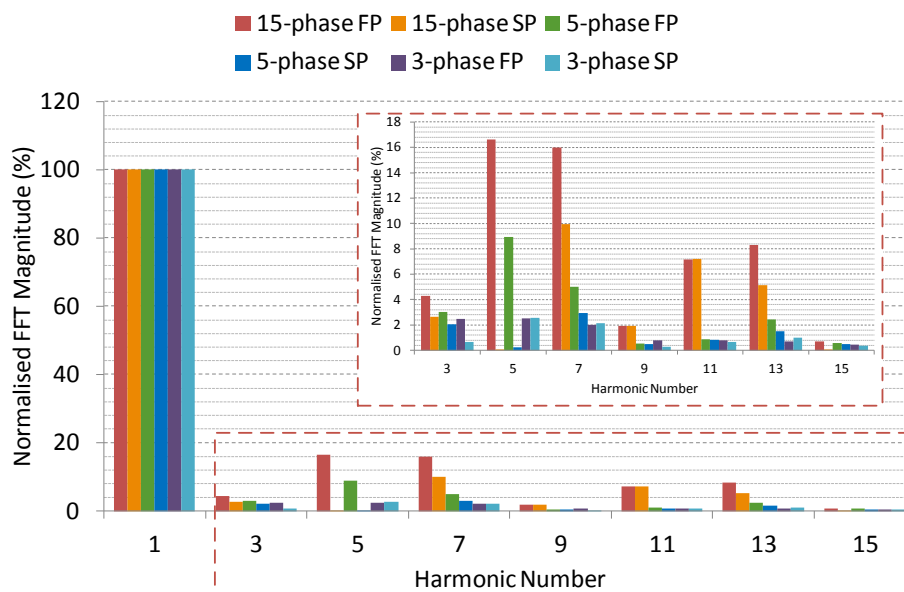


Figure 3.11: FFT of Short-pitched (SP) and Fully-pitched (FP) Generator Back-emf

Performing an FFT on both the fully- and short-pitched machine topology open-circuit voltage waveforms, shown from Section 4.4 to 4.6, provides the information required to implement the harmonic content in the simulation model. It is clear from *Figure 3.11* that a number of topologies contain a considerable amount of space harmonics, particularly the 15-phase fully-pitched topology. To incorporate the harmonic effects into the dynamic simulation model, a separate harmonic block was created.

The space harmonics are usually considered at the machine design stage, where the winding layouts can be altered to remove or reduce contributing components. For example, many three-phase commercial generators are wound to remove the triplen harmonics (3^{rd} , 9^{th} , 15^{th} , etc.) [62].

The voltage developed across the load in the simulation model, acts as the input to the state-space model, described earlier in this chapter. The space harmonics will act to distort this voltage and, as a result, the voltage is modified.



Figure 3.12: Harmonic Block Acting on Simulation Model Voltage

In *Figure 3.12*, each phase is separated in order to match the higher order harmonics with the phase of the fundamental, underlined in Equation (8).

$$V_k = V_{k0} + V_{k1} \sin(\omega t) + V_{k3} \sin\left(3\omega t + 3\frac{2\pi}{m} - 3\phi\right) + V_{k5} \sin\left(5\omega t + 5\frac{2\pi}{m} - 5\phi\right) + \dots \quad (8)$$

where subscript k denotes an arbitrary phase, m is the number of generator phases and ϕ is the phase angle.

Implementing this in MATLAB Simulink provides the model depicted in *Figure 3.13* for the a -phase only.

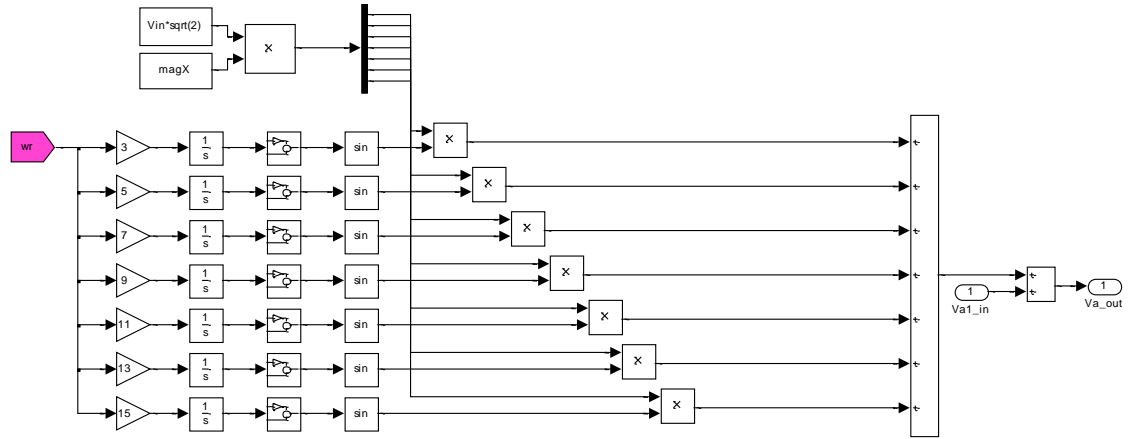


Figure 3.13: MATLAB Simulink Representation of Harmonic Model Block

The fundamental phase voltage is combined with the higher order harmonic phase voltages that are scaled by the percentage FFT magnitudes from the fully-pitched and short-pitched back-emf results. The angle at which they are applied to the fundamental is modified to provide the best match in voltage and current behaviour.

Since the voltages supplied to the model input are no longer sinusoidal, the higher order harmonic content maps to the x - y planes of the extended Clarke transform shown in Equation (6). Which plane the respective harmonics map to is determined by the number of phases and the harmonic order. This mapping is shown in Table 3.3 with general expressions identified in [7] for determining the harmonic content of the x - y planes.

Table 3.3: Mapping of Harmonics to d - q , x - y planes and Zero-sequence

	Three-phase	Five-phase	15-phase
d-q	$1^{\text{st}}, 5^{\text{th}}, 7^{\text{th}}, 11^{\text{th}}, 13^{\text{th}}$	$1^{\text{st}}, 9^{\text{th}}, 11^{\text{th}}$	$1^{\text{st}}, 29^{\text{th}}$
x_1 - y_1	-	$3^{\text{rd}}, 7^{\text{th}}, 13^{\text{th}}$	$13^{\text{th}}, 17^{\text{th}}$
x_2 - y_2	-	-	$3^{\text{rd}}, 27^{\text{th}}$
x_3 - y_3	-	-	$11^{\text{th}}, 19^{\text{th}}$
x_4 - y_4	-	-	$5^{\text{th}}, 25^{\text{st}}$
x_5 - y_5	-	-	$9^{\text{th}}, 21^{\text{st}}$
x_6 - y_6	-	-	$7^{\text{th}}, 23^{\text{rd}}$
Zero-sequence	$3^{\text{rd}}, 9^{\text{th}}, 15^{\text{th}}$	$5^{\text{th}}, 15^{\text{th}}$	15^{th}

3.5 Passive Rectification

3.5.1 Connection Topology

The connection of three-phase generators and motors to passive rectification devices, such as diode bridges, is well documented in textbooks [2, 48, 64]. However, as phase number increases, the rectifier and generator behave differently, depending on connection method. A star-connected generator provides a neutral point, which acts as a reference for the voltage across each phase winding; each winding is independent. Delta- or, for higher phase number machines, polygon-connected generators do not have this common connection point and the voltage is, therefore, referenced to the adjacent phases, highlighted in *Figure 3.14*.

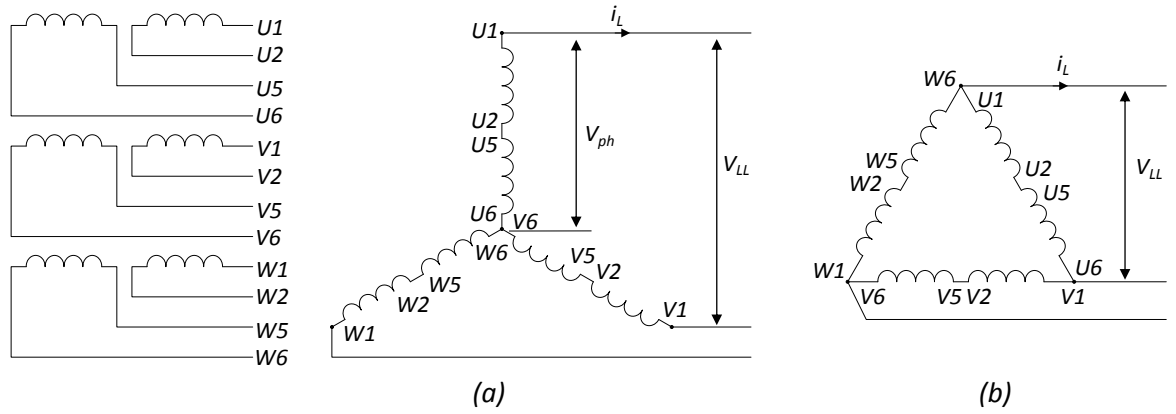


Figure 3.14: Winding Arrangements for a Double-layer Winding (a) Series-star and (b) Series-delta

where U, V and W (1, 2, 5 and 6) are the single coil ends. These are brought out of the stator into the generator housing, enabling a number of connection topologies to be achieved.

In order to facilitate the investigation into the effects that a passive rectifier has on a generator, the three-, five- and 15-phase simulation models must be extended to include the switching components.

This section focuses on the differences in AC and DC power quality when the generator is star-connected and polygon-connected. The effects of the non-linear rectifier load are investigated experimentally at higher power as the generator approaches rated current levels in Chapter 5. The saturation of the generator magnetic path will lead to a different voltage output waveform and, therefore, alter the commutation effects. This is not modelled since the assumptions made include superposition of the magnetic circuits, neglecting saturation effects.

3.5.2 Simulation of an Open-circuit Fault

In order to fully assess the performance of the system, the open-circuit testing outlined in the project objectives must be simulated for comparison with the experimental results in Chapter 5. This section details the approach taken in simulating the open-circuit generator phase and diode device faults.

The open-circuit diode device fault is relatively straightforward to implement through an increase in diode resistance. The nominal on-state resistance is 1 m Ω , which in the faulted device is increased to 1 M Ω . This prevents current from flowing in that path and acts as an open-circuit condition.

The open-circuit phase fault requires a proportional-integral control loop to act in driving the current source, supplied to the rectifier, to zero, depicted in *Figure 3.15*.

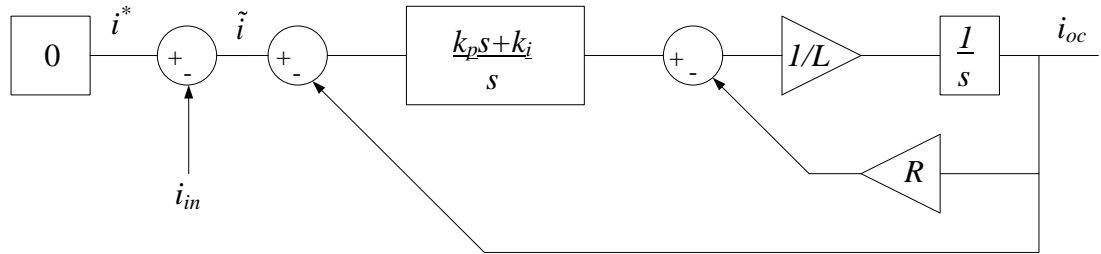


Figure 3.15: Simulation of Open-circuit Phase Fault

The zero setpoint value was compared with the input current and the gain controls were set to provide an output current, i_{oc} , of zero. The output from *Figure 3.15* was connected to a current source block that enabled the Simulink results to be interpreted by the SimPowerSystems rectifier model. At this point, the connection method could be configured to allow the simulation of a star- or polygon-connected generator for comparison. The results are presented in Section 5.3.

3.5.3 Analysis of Synchronous Generator with Diode Rectifier

The diode is a semiconductor switching device that conducts current when the forward voltage exceeds the threshold voltage. Conduction continues until the current reaches zero. However, in practice reverse recovery effects prevent the diode device turning off when the current reaches zero [48]. Connected in an array, a diode rectifier can be constructed as a passive device to convert AC voltage to DC through these uncontrolled switching events. This method of rectification negates the need for any complex control schemes but can cause a reduction in system efficiency when connected to a transformer

or machine. With a greater number of machine phases, and the resultant increase in the number of diode devices, the effect that the rectifier has on AC system supplying it changes. Mathematical analysis can be performed on the three-, five- and 15-phase rectifier and compared with the results from the simulation model for a multiphase synchronous generator connected to a diode rectifier.

Assumptions that are made in the analysis are listed here:

- Ideal voltage sources behind an impedance, representative of back-emf developed in a synchronous generator
- Resistive IR drops are neglected
- Constant current is drawn on the DC side, simplifying the analysis
- Voltage drops across the diode and threshold voltage are ignored
- Diode recovery effects are ignored

Star-connected Generator

Ideal Voltage Source

With an ideal source, the biggest voltage difference between the phases will determine which diodes are conducting current to the DC side. Ignoring commutation effects, the DC ripple voltage will be ascertained from the envelope of the phase voltage referenced to the neutral point.

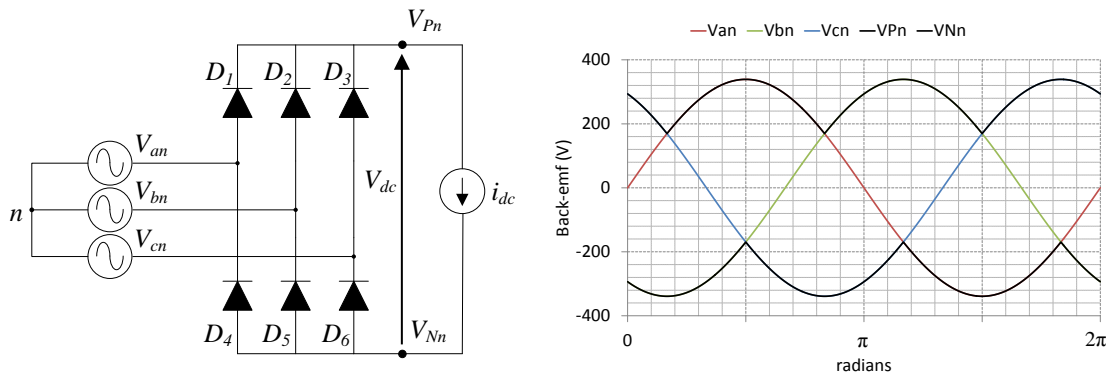


Figure 3.16: Ideal Voltage Source with Constant Current Load (adapted from [48])

As the a -phase voltage increases, diode D_1 is forward conducting whilst the b -phase, at its most negative, impresses a reverse voltage across diode D_5 . Diode D_1 stays forward conducting and, as the c -phase becomes its most negative, diode D_6 reverse conducts, as demonstrated in Figure 3.16. The resulting DC voltage is shown in Figure 3.17.

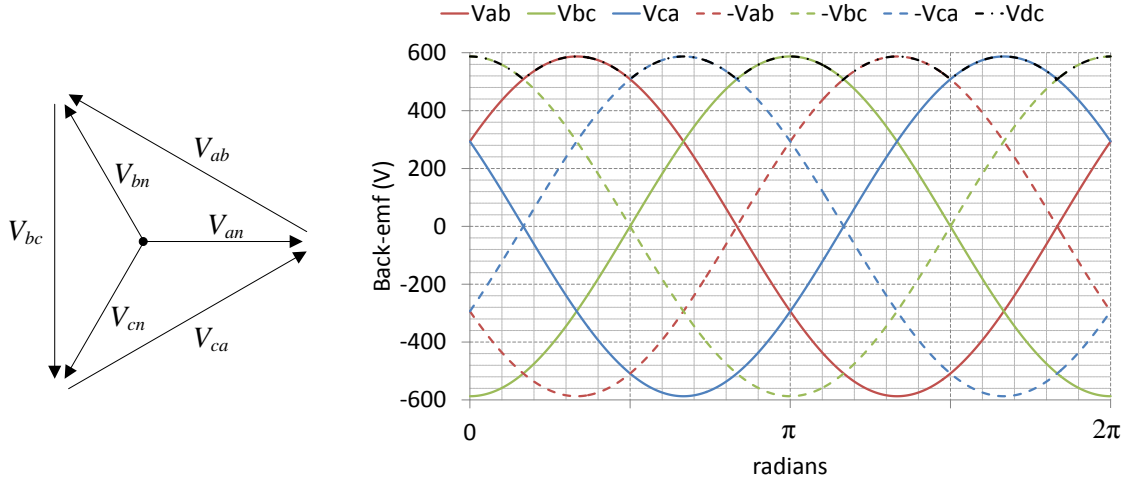


Figure 3.17: Diagram of Differential (line-to-line) Voltages

The experimental test-rig generator is capable of three-, five-, and 15- phase operation. Therefore, analysis will be performed on odd phase number generators only, allowing comparison with simulation model results in Section 3.5.4.

For a symmetrical multiphase star-connected generator, the greatest voltage differentials exist between the opposite phases, illustrated by the phasor diagram in Figure 3.18.

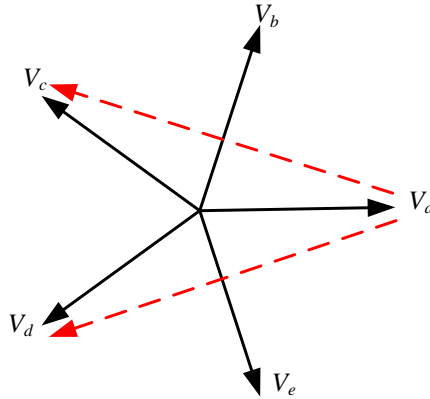


Figure 3.18: Five-phase Voltage Phasor Diagram

This gives the general equation:

$$V_{dc} = V_x - V_{x + \frac{(m \pm 1)}{2}} \quad (9)$$

where V_x is the reference phase, x is an arbitrary phase and m is the total number of generator phases.

In the five-phase example, taking V_a as the reference phase V_x , the voltages with the greatest difference to the reference will be V_c and V_d , respectively, shown in Figure 3.18.

For a set of voltages, travelling forward in time:

$$\begin{aligned} V_1 &= \hat{V}_{ac} \cos(\omega t) \\ V_x &= \hat{V}_{ac} \cos(\omega t - (x-1)\gamma) \end{aligned} \quad (10)$$

where $\gamma = \frac{2\pi}{m}$

So for the greatest voltage differential between phasors, the following equation shows the general form:

$$\begin{aligned} V_1 - V_{\frac{(m+1)}{2}} &= \hat{V}_{ac} \left[\cos(\omega t) - \cos\left(\omega t - \left(\frac{m+1}{2}\right)\gamma\right) \right] \\ &= 2\hat{V}_{ac} \sin\left[\left(\frac{m-1}{2m}\right)\pi\right] \sin\left[\omega t - \left(\frac{m-1}{2m}\right)\pi\right] \end{aligned} \quad (11)$$

As phase number increases (assume m tends to infinity), Equation (11) can be simplified:

$$\sin\left[\left(\frac{m-1}{2m}\right)\pi\right] \Rightarrow \sin\left(\frac{\pi}{2}\right) \Rightarrow 1 \quad (12)$$

Therefore, for high phase numbers, the peak voltage differential can be approximated to $2\hat{V}_{ac}$.

Observing the DC side, the ripple frequency is governed by the phase number, such that the DC ripple frequency is $2mf$. Under ideal conditions, the ripple is repetitive for $2m$ times across one cycle. Therefore, for analysis it can be split down to investigate one section.

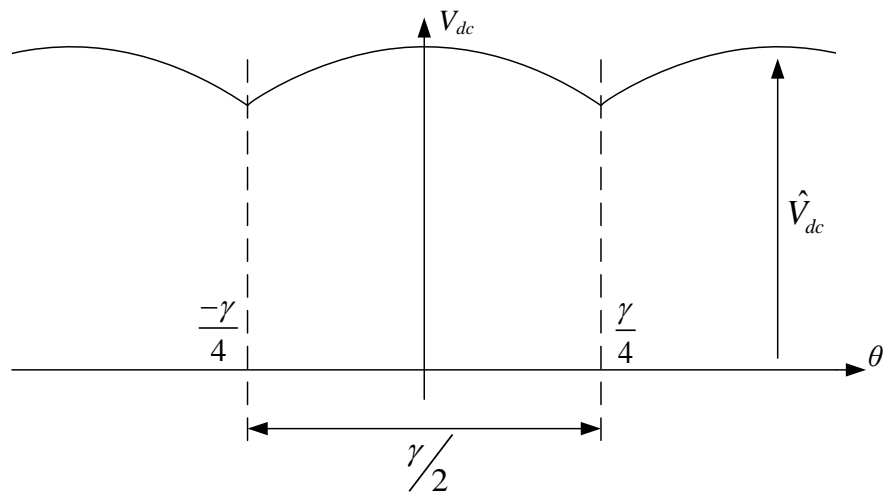


Figure 3.19: DC Ripple Magnitude

The peak DC voltage is dependent on the phase number for the star-connected generator and can be described through Equation (13).

$$\hat{V}_{dc} = 2\hat{V}_{ac} \sin \left[\left(\frac{m-1}{2m} \right) \pi \right] \quad (13)$$

The average voltage can be found by integrating the section between the two limits, shown in *Figure 3.19*:

$$\begin{aligned} AVG V_{dc} &= \frac{\hat{V}_{dc}}{\left(\frac{\gamma}{2} \right)} \int_{-\gamma/4}^{\gamma/4} \cos(\theta) d\theta \\ &= \frac{2\hat{V}_{dc}}{\gamma} \left[\sin(\theta) \right]_{-\gamma/4}^{\gamma/4} \\ &= \frac{2m}{\pi} \hat{V}_{dc} \sin \left(\frac{\pi}{2m} \right) \end{aligned} \quad (14)$$

Again, as the phase number, m , increases, the approximation tends toward the peak value, since $\sin \left(\frac{\pi}{2m} \right)$ tends toward $\left(\frac{\pi}{2m} \right)$.

$$AVG V_{dc} \Rightarrow \hat{V}_{dc} \quad (15)$$

The pk-pk ripple voltage can be found from the difference between the peak DC voltage and the point at which the ripple is the lowest, $\pm \frac{\gamma}{4}$.

$$\begin{aligned} V_{dc(pk-pk)} &= \hat{V}_{dc} \left[1 - \cos \left(\pm \frac{\gamma}{4} \right) \right] \\ &= \hat{V}_{dc} \left[1 - \cos \left(\frac{\pi}{2m} \right) \right] \end{aligned} \quad (16)$$

Inclusion of Source Inductance

The ideal behaviour is not representative of a real diode rectifier where, under commutation, the conducting diodes will only turn off when their current reduces to zero. This can provide a scenario where more than two diodes conduct at any one time. The equations describing the rectifier behaviour become more complex when commutation effects are included. *Figure 3.20* shows how the current transfers from the a - to the b -phase, with a constant current I being supplied to the load.

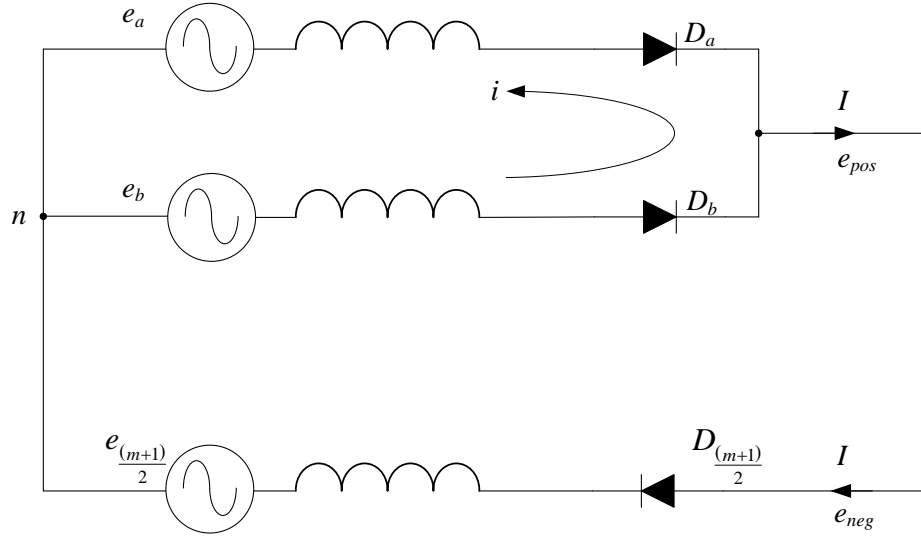


Figure 3.20: Commutation between Phases

At the start of commutation, $i = 0$ and $e_a = e_b$, $i_a = I$ and $i_b = 0$. At the end of commutation, $i = I = i_b$, $i_a = 0$ and $e_a \neq e_b$. Applying Kirchhoff's voltage law (voltages are defined with respect to the star point n):

$$\begin{aligned}
 e_{pos} &= e_a - L \frac{di}{dt} = e_b + L \frac{di}{dt} \\
 e_a - e_b &= 2L \frac{di}{dt} \\
 L \frac{di}{dt} &= \frac{1}{2}(e_a - e_b) \\
 e_{pos} &= e_a - \frac{1}{2}(e_a - e_b) = \frac{1}{2}(e_a + e_b) \\
 e_{pos-neg} &= e_{pos} - e_{neg} = \frac{1}{2}(e_a + e_b) - e_{\frac{(m+1)}{2}}
 \end{aligned} \tag{17}$$

where e_{pos} is the positive and e_{neg} is the negative back-emf at the DC side, respectively, and $e_{pos-neg}$ is the difference.

With reference to Figure 3.20, Equation (17) shows that, during commutation, the voltage across diode D_a is reduced to the average between the two most positive voltages compared with the most negative. This is denoted as $t = 0$ in Figure 3.21. It then follows this average voltage until the current i reduces to zero at $t = \tau$, where the voltage across diode D_b now reaches maximum.

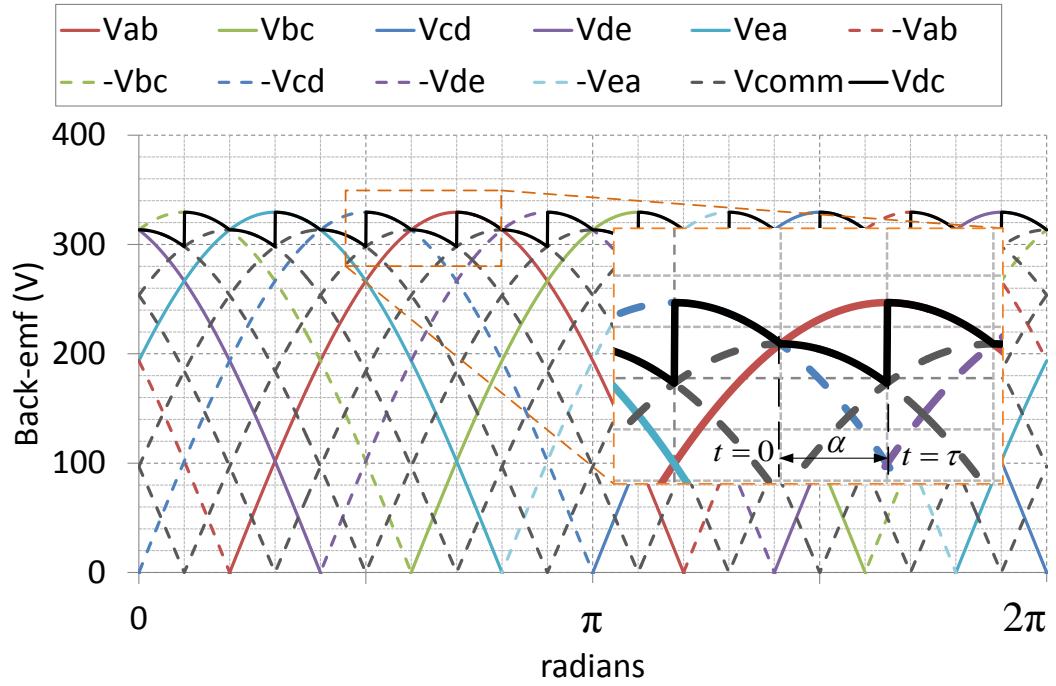


Figure 3.21: DC Voltage Formation with Commutation Effects

The effects of commutation can be seen on both the AC and DC side. It can be observed, from Figure 3.21, that the pk-pk ripple voltage is increased but the peak DC voltage remains unchanged. The average DC voltage reduces as a result of the increased ripple magnitude.

During commutation, the current in the loop can be described through:

$$\begin{aligned}
 (e_a - e_b) &= 2L \frac{di}{dt} \\
 (e_a - e_b) &= \hat{V}_{ac} \left[\cos \omega t - \cos \left(\omega t + \frac{2\pi}{m} \right) \right] \\
 &= 2\hat{V}_{ac} \sin \left(\omega t + \frac{\pi}{m} \right) \sin \left(\frac{\pi}{m} \right)
 \end{aligned} \tag{18}$$

Starting at $I = 0$, where $e_a - e_b = 0$, therefore, angle function $\alpha = 0$.

$$\hat{V}_{ac} \left(\sin \frac{\pi}{m} \right) \sin(\theta) = -L \frac{di}{dt} \quad \text{between} \quad \begin{cases} i = 0 & \text{at } \theta = 0 \\ i = I & \text{at } \theta = \alpha \end{cases} \tag{19}$$

where $\theta = \omega t$

Integrating between the two limits:

$$\begin{aligned}
\int_0^\alpha \left(\sin \frac{\pi}{m} \sin(\omega t) \right) d\omega t &= \frac{L\omega}{\hat{V}_{ac}} \int_0^I di \\
[\cos(\omega t)]_0^\alpha &= \frac{-\omega LI}{\hat{V}_{ac} \sin\left(\frac{\pi}{m}\right)} \\
(1 - \cos \alpha) &= \frac{\omega LI}{\hat{V}_{ac} \sin\left(\frac{\pi}{m}\right)}
\end{aligned} \tag{20}$$

Equation (20) shows that the commutation angle, α , increases with load current, source inductance, frequency and the number of phases. The average DC voltage will be modified to include the commutation angle where the average DC voltage is the sum of the two distinct points from the peak to the end of α . Equation (14) becomes:

$$AVG V_{dc} = \frac{m}{\pi} \hat{V}_{dc} \sin\left(\frac{\pi}{2m}\right) [1 + \cos(\alpha)] \tag{21}$$

The pk-pk ripple voltage can be found between the peak voltage and the end commutation point, where $\theta = \alpha$.

$$V_{pk-pk} = \hat{V}_{dc} \left[1 - \cos\left(\frac{\pi}{2m}\right) \cos \alpha \right] \tag{22}$$

Polygon-connected Generator

The polygon-connected generator offers a different analysis since there is no neutral connection point. Therefore, an arbitrary neutral point has been defined to carry out the analysis.

$$\begin{aligned}
V_{an} &= e_a \\
V_{bn} &= e_a + e_b \\
V_{cn} &= e_a + e_b + e_c \\
V_{(m-1)n} &= e_a + e_b + e_c + \dots = -e_m \\
V_{mn} &= 0
\end{aligned} \tag{23}$$

It can be observed that the greatest voltage differential is, therefore, the sum of all the phases in the positive two quadrants for a phasor diagram, depicted in *Figure 3.22*.

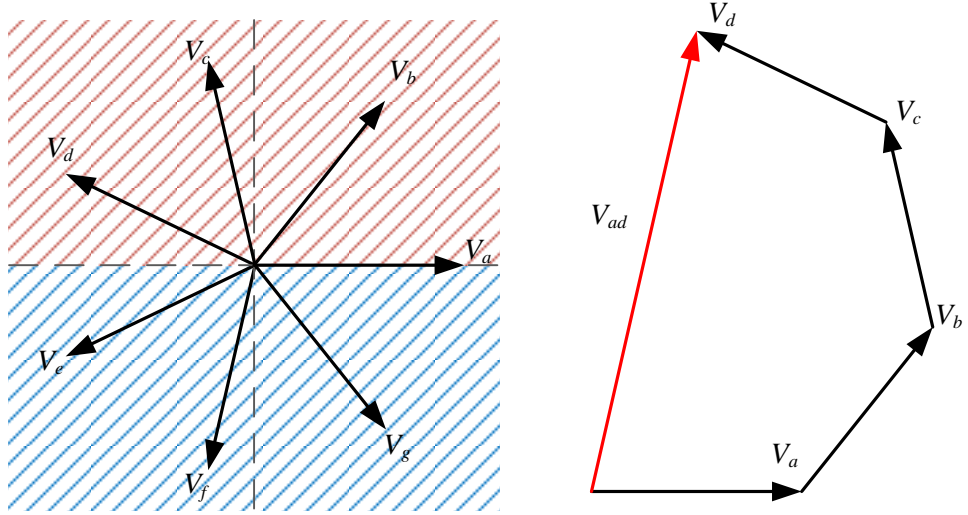


Figure 3.22: Phasor Quadrants and Polygon-connected Generator Greatest Voltage Differential

This gives the point at which all the voltages must be summed to provide the greatest voltage differential, represented by the variable k .

$$\hat{V}_{xk} = \hat{V}_{ac} \sum_{x=1}^k \cos(\omega t + (x-1)\gamma) \quad (24)$$

where $k = \frac{m+1}{2}$

$$\begin{aligned} \hat{V}_{xk} &= \hat{V}_{ac} \sum_{x=1}^k \frac{e^{j(\omega t + (x-1)\gamma)} + e^{-j(\omega t + (x-1)\gamma)}}{2} \\ &= \hat{V}_{ac} \cos \left[\omega t + \left(\frac{k-1}{2} \right) \gamma \right] \sin \left(\frac{k\gamma/2}{\sin(\gamma/2)} \right) \\ &= \hat{V}_{ac} \cos \left[\omega t + \left(\frac{m-1}{2m} \right) \pi \right] \frac{\sin \left(\frac{m+1}{m} \frac{\pi}{2} \right)}{\sin(\pi/m)} \end{aligned} \quad (25)$$

$$\begin{aligned} \sin \left(\frac{m+1}{m} \frac{\pi}{2} \right) &= \sin \left(\frac{\pi}{2} + \frac{\pi}{2m} \right) = \cos \left(\frac{\pi}{2m} \right) \\ \sin \left(\frac{\pi}{m} \right) &= 2 \sin \left(\frac{\pi}{2m} \right) \cos \left(\frac{\pi}{2m} \right) \\ \hat{V}_{xk} &= \frac{\hat{V}_{ac} \cos \left[\omega t + \left(\frac{m-1}{2m} \right) \pi \right]}{2 \sin \left(\frac{\pi}{2m} \right)} \end{aligned} \quad (26)$$

Since the peak DC voltage is a fixed value with no angular dependence, it can be equated to the peak differential voltage where the \cos term in Equation (26) is 1.

$$\hat{V}_{dc} = \frac{\hat{V}_{ac}}{2 \sin\left(\frac{\pi}{2m}\right)} \quad (27)$$

If commutation is neglected, the equations for the pk-pk and average DC voltage are the same as for the star-connected generator. Taking into account the inductance of the polygon-connected generator will alter the values obtained from analysis due to the commutation angle being different between the connection topologies.

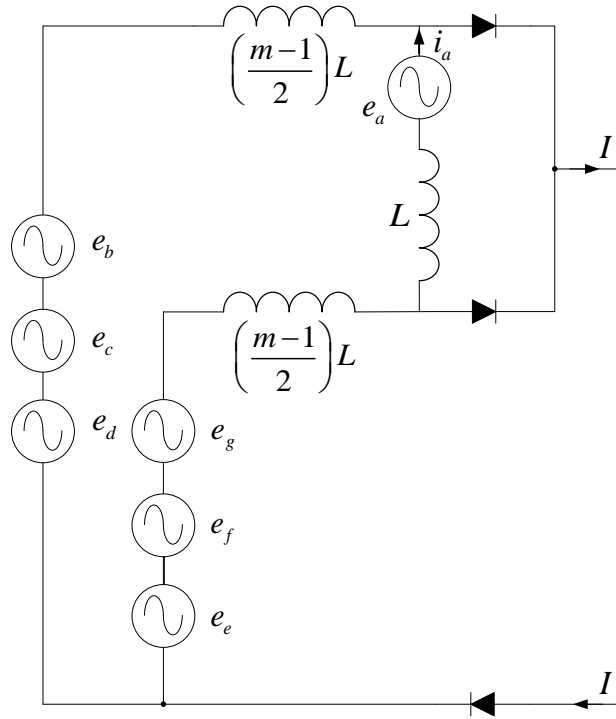


Figure 3.23: Polygon-connected Generator Current Path under Commutation

Ignoring the IR drops, the commutation angle, α , affecting the diode conduction can be described from the current path shown in Figure 3.23.

$$\begin{aligned}
e_a - L \frac{di_a}{dt} &= 0 \\
\Delta i_a &= \frac{1}{L} \int_0^T e_a dt \\
&= \frac{\hat{V}_{ac}}{L} \int_0^T \sin(\omega t) dt = -\frac{\hat{V}_{ac}}{\omega L} [\cos(\omega t)]_0^T \\
&= \frac{\hat{V}_{ac}}{\omega L} [1 - \cos \alpha]
\end{aligned} \tag{28}$$

At the start of commutation, $t = 0$, the current i_a provides a portion of the positive DC current. As time elapses, the current reduces until the next phase conducts and the a -phase becomes part of the return path for the negative DC current.

$$\begin{aligned}
t = 0, \quad i_a &= I_{dc} \left(\frac{m-1}{2m} \right) \\
t = T, \quad i_a &= -I_{dc} \left(\frac{m-1}{2m} \right) \\
\Delta i_a &= 2I_{dc} \left(\frac{m-1}{2m} \right)
\end{aligned} \tag{29}$$

Substituting the difference in the current i_a from Equation (29) into Equation (28) yields the commutation angle.

$$(1 - \cos \alpha) = \frac{\omega L}{\hat{V}_{ac}} I_{dc} \left(\frac{m-1}{m} \right) \tag{30}$$

Again, as m tends to infinity, for higher phase number machines, the final term in the equation tends to unity.

Equivalent Power Transfer

In order to understand the difference in the performance of a star- or polygon-connected generator connected to a passive rectifier, it is necessary to evaluate it under the same conditions as the phase number is increased. To facilitate this, a constant current load is simulated across the output terminals of the rectifier device. The magnitude of the current drawn on the output side is altered to reflect the phase number and connection method. For example, the five-phase generator-rectifier is shown in *Figure 3.24* for both star- and polygon-connected configurations. For the star-connection, the current drawn to the DC side is provided for by the two windings that are connected to the diodes that are in their

on-state. As the phase number is increased, the current on the DC side must also be increased due to the reduction in DC side voltage. The polygon-connection windings all provide a current path, therefore, the constant current load on the DC side does not scale with phase number to account for the reduction in phase voltage. The DC power remains approximately constant in all cases. The three-, five- and 15-phase topologies were investigated to gain an understanding of how the magnitudes of the harmonic content compare.

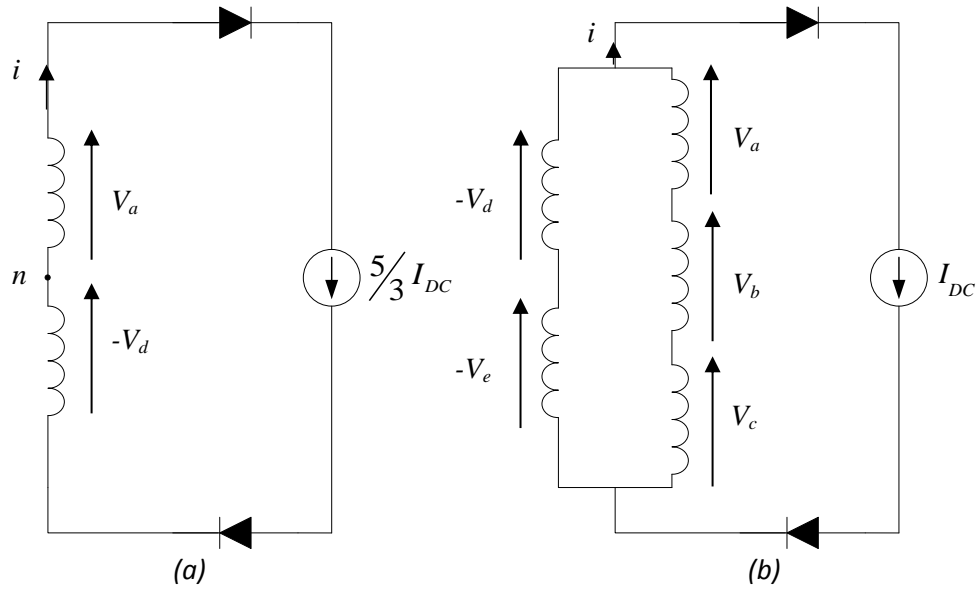


Figure 3.24: Five-phase (a) Star- and (b) Polygon-connected Generator with Rectifier and Constant Current Load

As phase number increases, a higher peak current is drawn from the star-connected generator to supply the constant current demand on the DC side, demonstrated in Figure 3.25. The commutation time is increased as the angle is increased due to its dependence on the load current, shown in Equation (20). This increase in commutation time limits the current that can be drawn from the generator. The currents exhibit a high peak value and a reduced on-time. This results in considerable harmonic content in the generator as a result of the time harmonics imposed by the rectifier. The high peaks will cause saturation in the generator stator-core material, leading to higher losses and increased generator heating as a result.

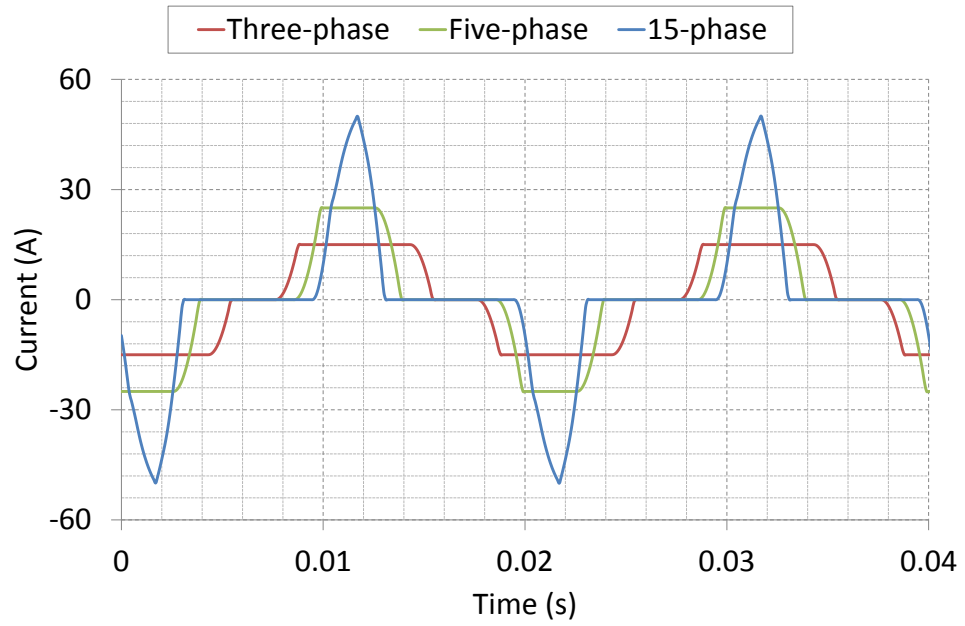


Figure 3.25: Star-connected Generator AC Currents

On the DC side, the voltage is noticeably reduced as the phase number is increased. Since the AC side voltage must be reduced to keep the rated power produced by the machine constant as phase number increases then it follows that the DC side voltage must also decrease, shown in *Figure 3.26*. However, the ripple voltage magnitude is also reduced, important in the application to aircraft where the removal of filter capacitance is highly desirable.

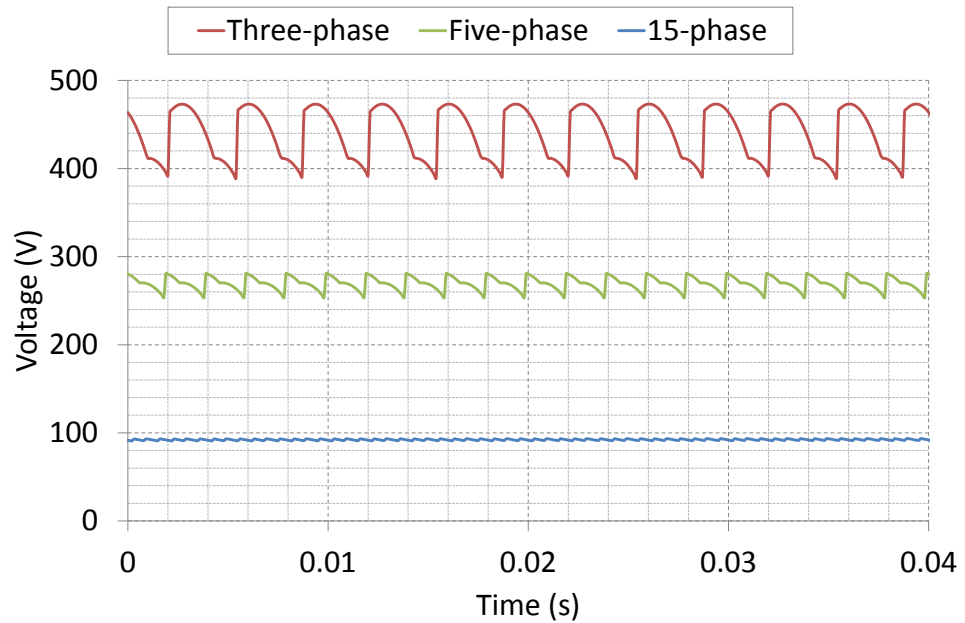


Figure 3.26: Star-connected Generator DC Voltages

The polygon-connected generator performs much better overall due to the utilisation of all the current carrying paths available, underlined in *Figure 3.27*. This lowers the peak current and, therefore, prevents the machine from entering saturation.

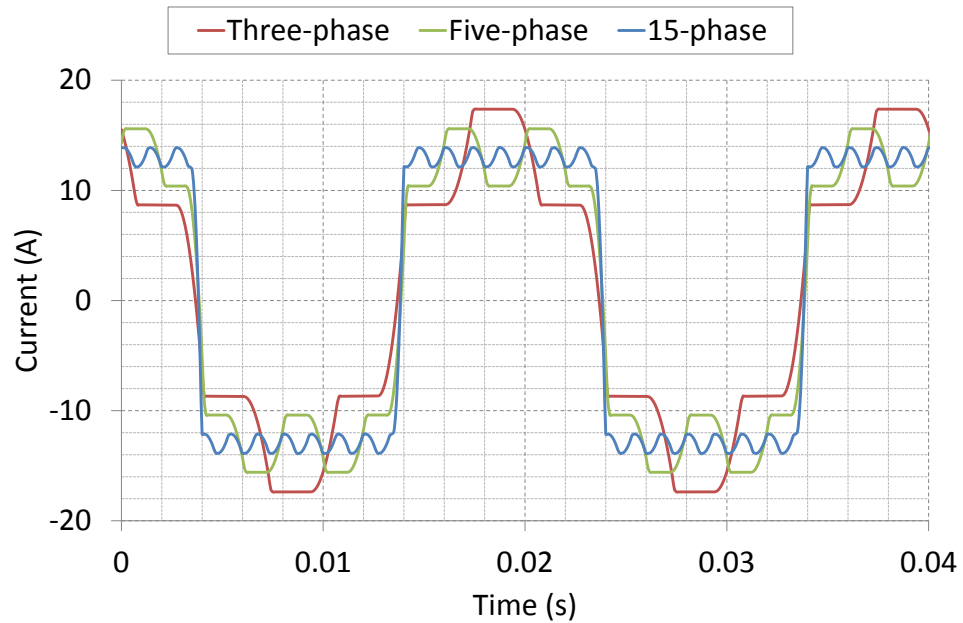


Figure 3.27: Polygon-connected Generator AC Currents

The AC voltage, still reduced to keep the generator rated power output, is similar to that of the star-connected generator. However, as phase number is increased the DC voltage remains the same. Since the current output of the machine to the DC side doesn't change, the DC voltage must also remain consistent to provide the same power on the DC side, observed in *Figure 3.28*.

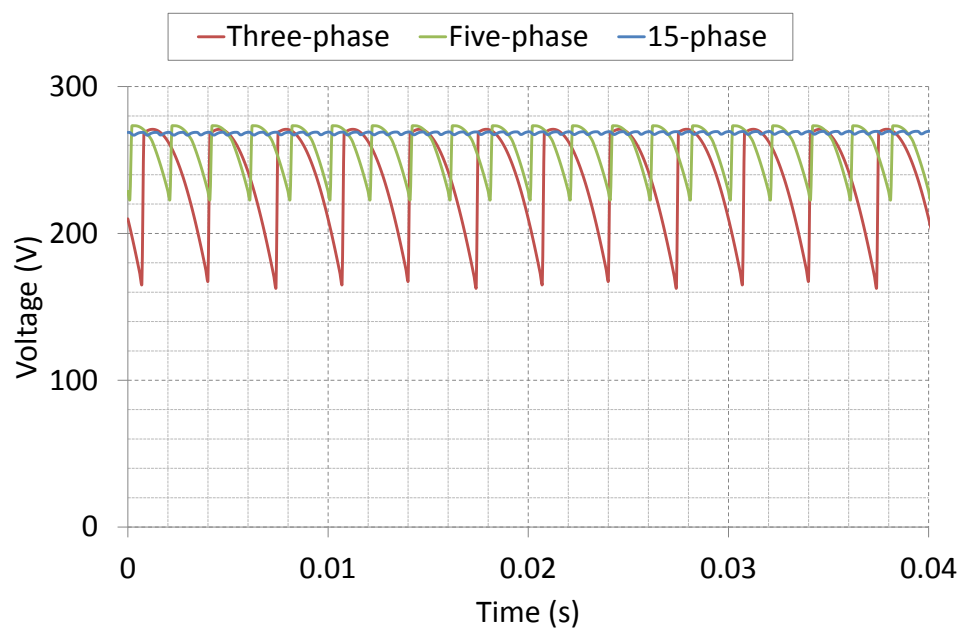


Figure 3.28: Polygon-connected Generator DC Voltages

The currents drawn from the AC generator for both connection topologies can be compared to establish the best topology for minimising the harmonic losses in the generator. Taking an FFT of the generator currents, shown in *Figure 3.29* and *Figure 3.30*, it is clear that the polygon-connected generators perform better.

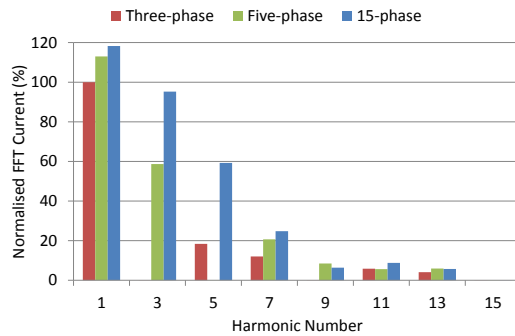


Figure 3.29: Star-connected Generator FFT of Currents Normalised to Three-phase Fundamental

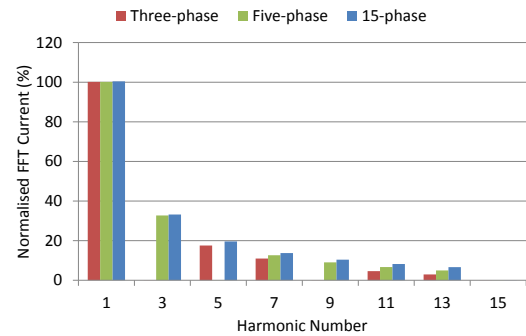


Figure 3.30: Polygon-connected Generator FFT of Currents Normalised to Three-phase Fundamental

3.5.4 Comparison of Analysis and Simulation

The simulation of the constant current demand can be compared with the analysis carried out from the equations described in the Section 3.5.3. This will show the validity of the mathematics and highlight problems when commutation effects become significant as phase number increases.

Table 3.4: Comparison of AC and DC Simulation and Analysis Values

		STAR			POLYGON		
Phase Number		Three	Five	15	Three	Five	15
Peak AC Current (A)	S	15.001	25.001	50.104	17.378	15.595	13.879
	A	15.000	25.000	75.000	17.321	15.588	13.856
RMS AC Current (A)	S	11.969	15.107	19.283	11.942	12.462	12.800
	A	12.247	15.811	27.386	12.247	12.728	12.961
Peak DC Voltage (V)	S	473.542	280.841	94.179	271.019	273.313	270.587
	A	471.527	310.694	108.298	272.236	264.292	260.442
AVG DC Voltage (V)	S	439.959	269.165	92.595	238.954	257.755	268.985
	A	441.275	300.359	105.850	255.442	255.331	255.237
Pk-pk Ripple (% of AVG)	S	19.23	10.18	3.62	45.09	19.45	1.39
	A	18.02	8.44	4.80	17.49	8.58	4.25
Commutation Angle (rads)	S	0.35	0.38	-	0.28	0.28	-
	A	0.28	0.26	0.29	0.26	0.27	0.27
Stator Copper Loss (W)	S	185.5	295.5	481.5	184.7	201.1	212.1
	A	194.2	323.7	971.1	194.2	209.8	217.5

S = Simulated A = Analysis

The comparison between the simulation and analysis values, shown in *Table 3.4*, provides an insight into the validity of the mathematic analysis and highlights areas where it is unsuitable. All of the polygon-connected results show good agreement except for the pk-pk ripple values. The three-phase star-connected generator shows good agreement between simulated and predicted results. However, for higher phase number machines, the analysis and simulation do not tie up. For example, the analysis predicts that the peak current for the star-connected 15-phase generator should be approximately 75 A. However, the simulation results show only 50 A is achieved as the full phase current transfer does not take place before commutation to the next phase occurs. This is due to the commutation time increasing as a result of the load current.

The pk-pk DC voltage for the simulated polygon-connected generator provides some disparity between analysis and simulation results. The three-phase case is particularly high even though the peak and average DC voltage values are a good match and commutation is taken into account. The pk-pk ripple voltage is approximately 107 V, which is in excess of the predicted value and the star-connected generator pk-pk ripple of 80 V. The percentage of the average DC voltage is comparatively greater due to the lower peak DC voltage value.

The analysis has shown that it is useful when generalising for three phases or more. It has been observed that the analysis underlines the simulation, acting to verify the simulation model. However, some higher phase number cases are more suited to simulation since the analysis doesn't take into account the increase in commutation time.

3.5.5 Star-connected Generator Connected to Diode Rectifier

The star-connected synchronous generator is the most common topology in industrial and commercial applications. When connected to an uncontrolled rectifier, as proposed here, the current drawn from the generator is no longer sinusoidal, impacting on the generator performance by inducing time varying harmonics.

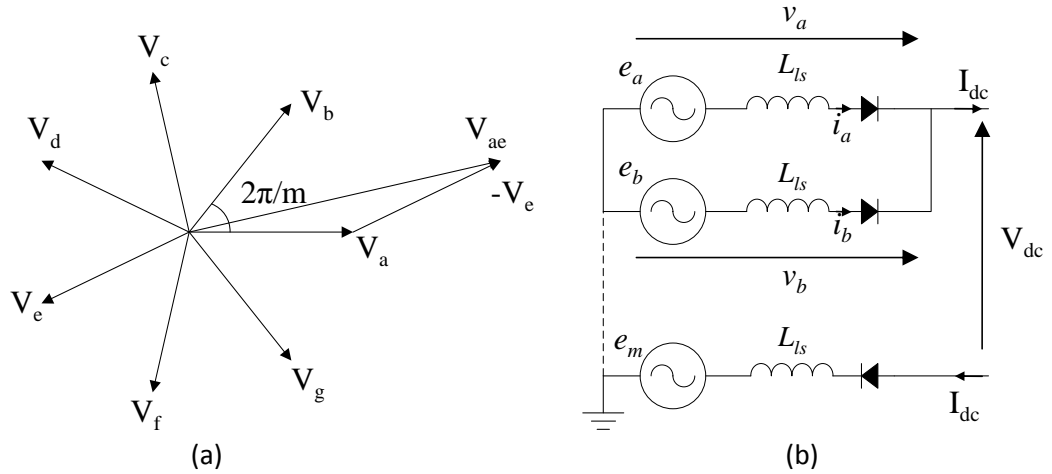


Figure 3.31: Star-connected Generator (a) Voltage Determination (b) Current Path

Modelling the three-phase star-connected machine with a diode rectifier, along with the same 58Ω fixed resistive load utilised in the AC generator testing of the previous section, yields the voltage waveform depicted in Figure 3.32 and the current, in Figure 3.33.

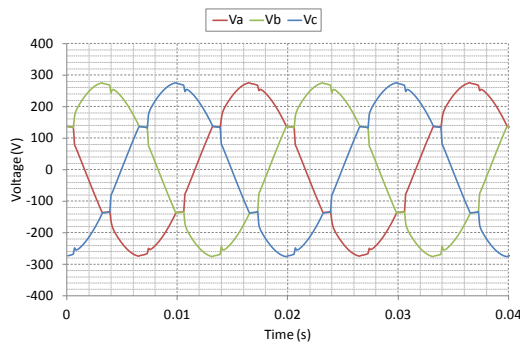


Figure 3.32: Three-phase Star-connected Simulated AC Voltage

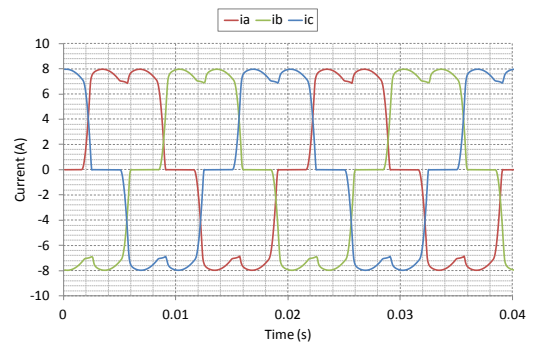


Figure 3.33: Three-phase Star-connected Simulated AC Current

The simulation output can be readily compared with the short-pitched experimental testing results in Section 5.4. The commutation effects can be seen in the Figure 3.32, where notching occurs in the voltage.

Observing the DC side of the rectifier, the voltage and current ripples are as described in Section 3.5.3 from their typical behaviour. The average DC voltage can be found from consideration of the six distinct segments per cycle, each one lasting for $\pi/3$ radians. As can be seen in Figure 3.34, the inductance of the synchronous generator has an effect on the waveform shape and the average DC voltage reduces with the inclusion of commutation.

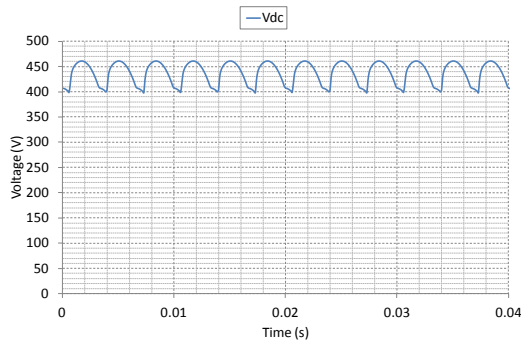


Figure 3.34: Three-phase Star-connected Simulated DC Voltage

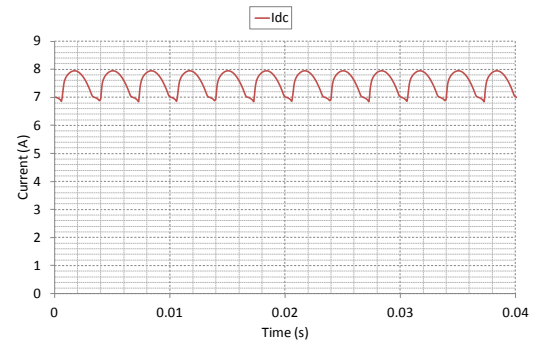


Figure 3.35: Three-phase Star-connected Simulated DC Current

With a resistive load, the DC current ripple, depicted in Figure 3.35, is the same as the DC voltage ripple, at approximately 15 % of the average DC value. This would require filter capacitance to reduce the ripple magnitude to within the allowed limits by the standards. Using the MIL-STD704F [46] as reference, the acceptable ripple voltage for an aircraft DC electrical network is 7.4 % under and 3.7 % over the nominal 270 V system, equating to an 11 % ripple overall.

Increasing the number of stator phases to five will result in a reduction in voltage as a result of maintaining the same rated power output for all topologies and the same rotor flux. Details of the winding designs are discussed in Sections 4.4 to 4.6, for the three-, five- and 15-phase machines. Since the same resistive load is being applied at the rectifier output terminals, for purposes of comparison with experimental test results, the current drawn to the DC side will also reduce as a result of the DC voltage being lower. The AC generator output is presented in Figure 3.36 and Figure 3.37.

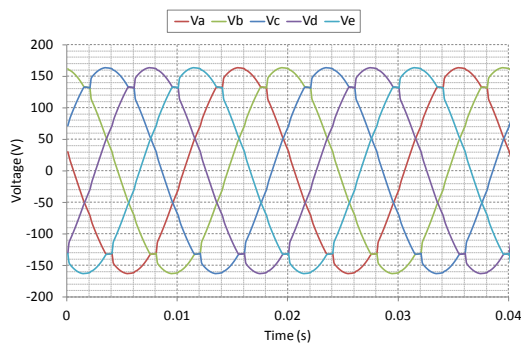


Figure 3.36: Five-phase Star-connected Simulated AC Voltage

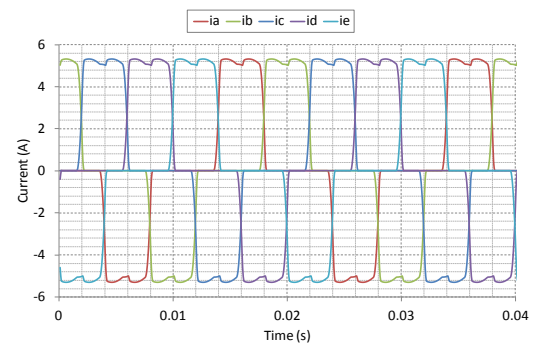


Figure 3.37: Five-phase Star-connected Simulated AC Current

The simulation model reflects little distortion in the generator voltage output, maintaining a sinusoidal characteristic but including notching effects under switching transients. The current exhibits the same shape as the three-phase model but with a reduced AC pk-pk magnitude of 10.6 A.

The five-phase generator provides a better DC side performance than the three-phase model with a reduced DC ripple voltage of 5.65 % of the average DC voltage, depicted in *Figure 3.38*.

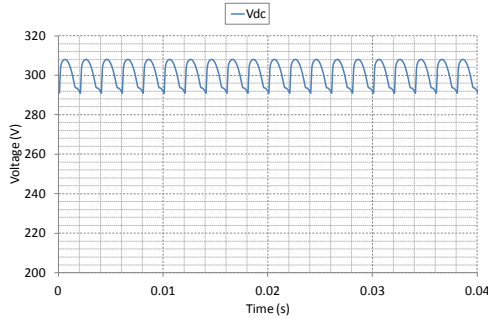


Figure 3.38: Five-phase Star-connected Simulated DC Voltage

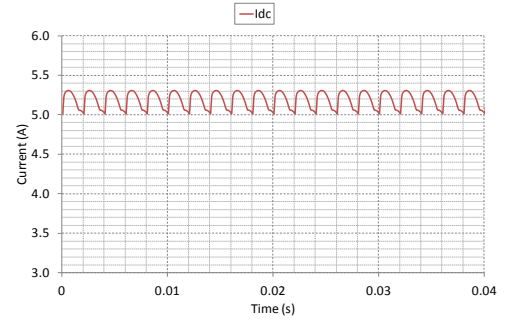


Figure 3.39: Five-phase Star-connected Simulated DC Current

There is a reduction in the voltage magnitude on the DC side, shown in *Figure 3.38*, since the voltage on the AC side is reduced, as depicted in *Figure 3.36*.

The 15-phase star-connected generator is the final topology to be investigated. This is the physical limit to the experimental test system and provides validation of the importance of commutation effects on high phase number machines connected to uncontrolled rectification devices. The current drawn from the generator will, again, be non-sinusoidal and will have a lower magnitude for the same value of resistive load. The AC current has a high harmonic content that will reduce the efficiency of the machine. Core losses arising from this are calculated in Chapter 4. However, the simulation model retains the assumption that the generator is sinusoidally wound, and therefore the output voltage will be approximately sinusoidal. The voltage and current waveforms are displayed in *Figure 3.40* and *Figure 3.41*, respectively.

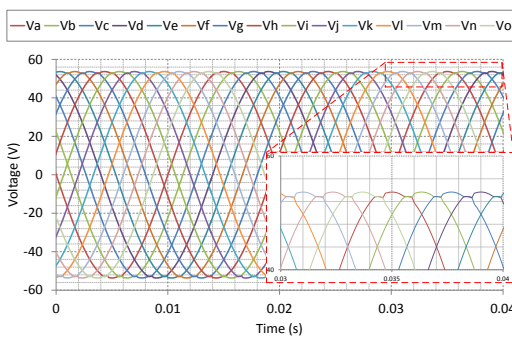


Figure 3.40: 15-phase Star-connected Simulated AC Voltage

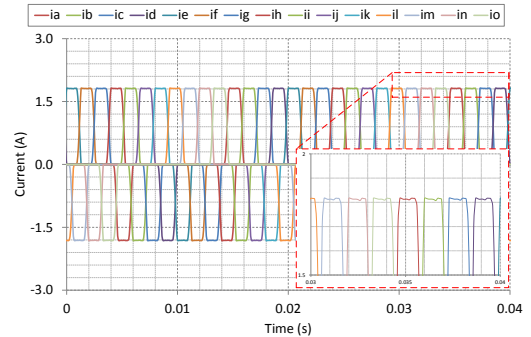


Figure 3.41: 15-phase Star-connected Simulated AC Current

The commutation notches are less obvious but still exist and are greater in number, occurring 30 times per cycle where the three-phase topology has only six commutation events. The effect of this is best demonstrated by observing the DC side in *Figure 3.42* and *Figure 3.43*.

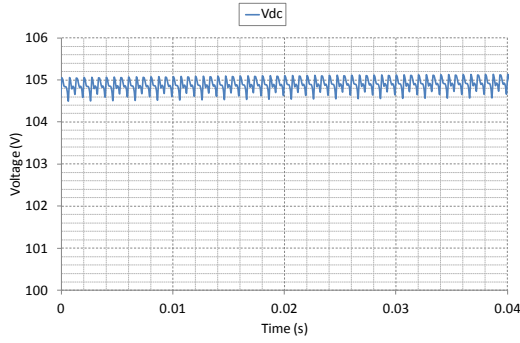


Figure 3.42: 15-phase Simulated DC Voltage

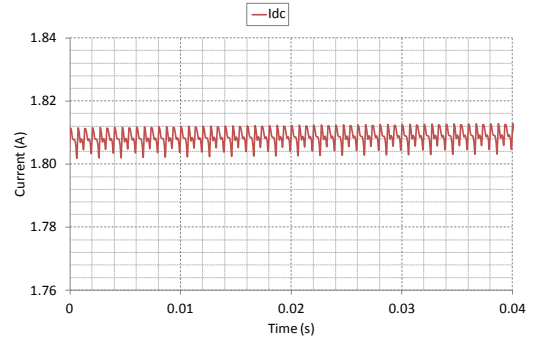


Figure 3.43: 15-phase Simulated DC Current

The 15-phase DC output waveforms clearly demonstrate the increase in ripple frequency to 30 times the fundamental and a reduced peak to peak ripple magnitude of less than 1 % of the average DC voltage.

3.5.6 Polygon-connected Generator Connected to Diode Rectifier

The waveforms for a delta-connected three-phase generator are significantly different to those seen in the star-connected machine. The connection method allows for continuous current to be achieved, where the phase windings contribute to the DC output at all times. It can be observed, from *Figure 3.44*, that with the removal of the star point, the formation of the differential voltages controlling the diode switching gives a much higher peak than across phases.

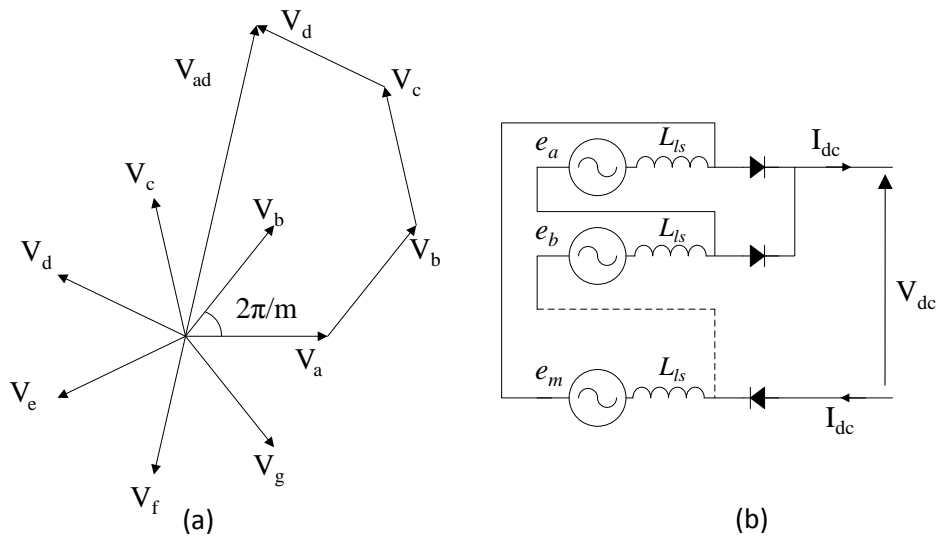


Figure 3.44: Polygon Connection (a) Voltage Determination (b) Current Path through Generator

In the delta-connected model, two currents are shown in *Figure 3.46* for comparison, the generator current and the diode current, or line current. The voltage measurement in *Figure 3.45* is taken line-to-line since the neutral point no longer exists to gain phase measurements. The same $58\ \Omega$ fixed resistance is used as the load on the DC side.

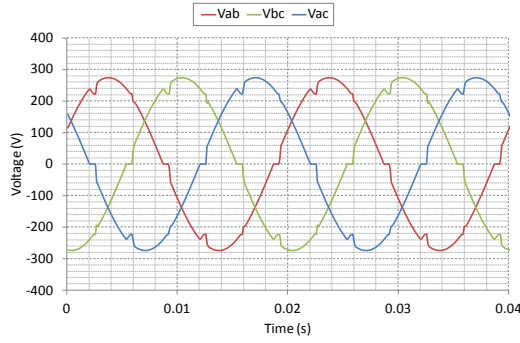


Figure 3.45: Three-phase Delta-connected Simulated Line-to-line Voltage

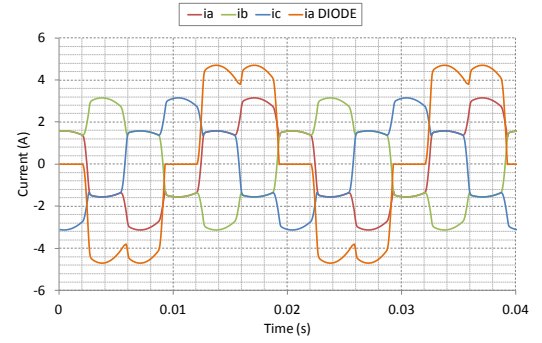


Figure 3.46: Three-phase Delta-connected Simulated Generator with Diode Current

It is clear from *Figure 3.46* that all the phases conduct current to contribute toward the line current. Unlike the star-connected system, there is no off-period and the magnitude of the phase current drawn from the generator is much lower. The improved form factor of the current is expected to give lower generator losses, calculated from the finite element modelling in Section 4.7.

The output of the rectifier will be very similar in shape to that of the star-connected generator since the rectifier operates on the difference between line-to-line voltages.

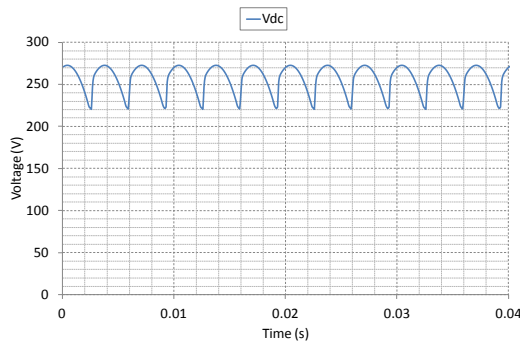


Figure 3.47: Three-phase Delta-connected Simulated DC Voltage

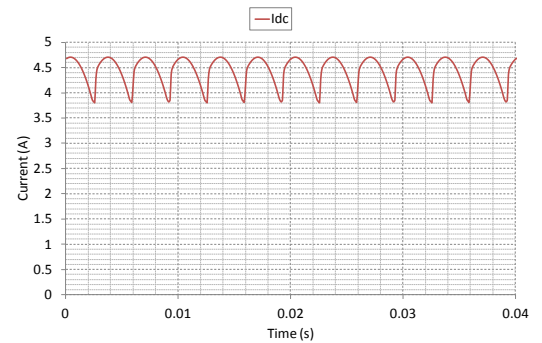


Figure 3.48: Three-phase Delta-connected Simulated DC Current

The DC side peak voltage is shown, in *Figure 3.47*, to be considerably lower than for the star-connected system. The line-to-line voltage, in the case of the delta-connected generator, is $\sqrt{3}$ lower than that of the star-connected generator.

The five-phase polygon-connected generator further highlights the greater utilisation of the synchronous generator, explored in greater detail in the equivalent power transfer section.

The line-to-line voltages, in *Figure 3.49*, remain sinusoidal for the mathematical model and the commutation effects are less pronounced. The current drawn from the generator shows the distinct contribution of the phase windings to the diode current, which maintains a higher magnitude than the generator currents in *Figure 3.50*.

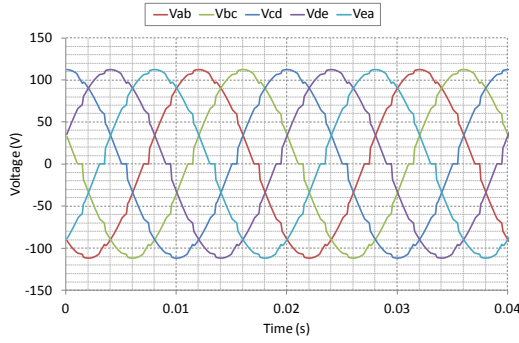


Figure 3.49: Five-phase Polygon-connected Simulated AC Voltage

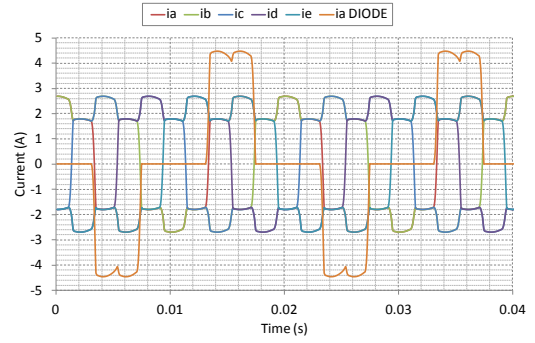


Figure 3.50: Five-phase Polygon-connected Simulated Generator and Diode Current

Compared to the star-connected generator, the delta connection provides an approximately constant average DC voltage as phase number increases, shown in *Figure 3.51*. The AC voltage has scaled, as a result of the machine design for higher phase numbers, discussed earlier. However, the DC voltages and currents remain around the same value for the five-phase case as for the three-phase.

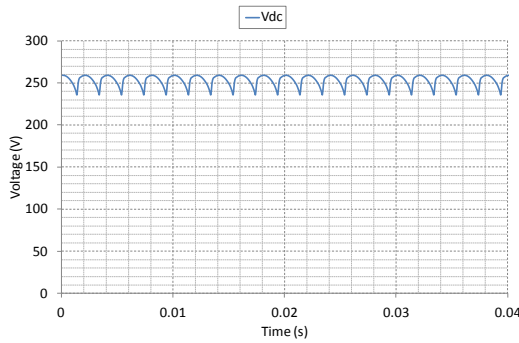


Figure 3.51: Five-phase Polygon-connected Simulated DC Voltage

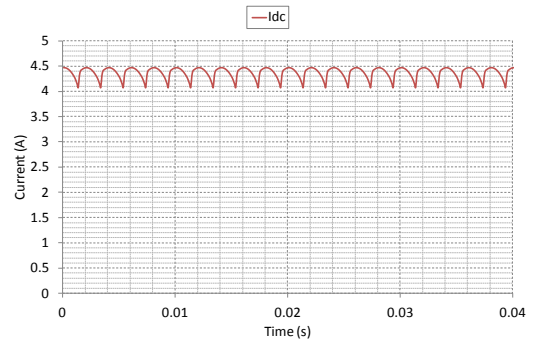


Figure 3.52: Five-phase Polygon-connected Simulated DC Current

The 15-phase generator has the same fixed resistive load applied to the DC side as for the three- and five-phase simulations.

The AC voltage, in *Figure 3.53*, shows the line-to-line voltage between adjacent phases. However, for ease of reading here, the legend does not show the reference phase.

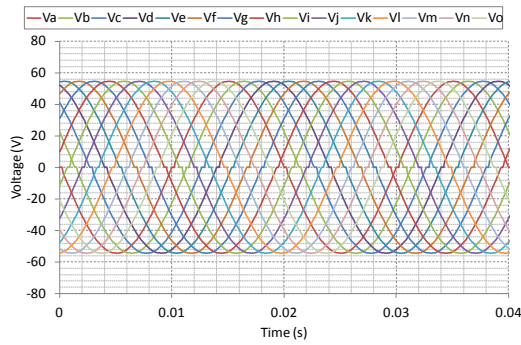


Figure 3.53: 15-phase Simulated AC Line-to-line Voltage

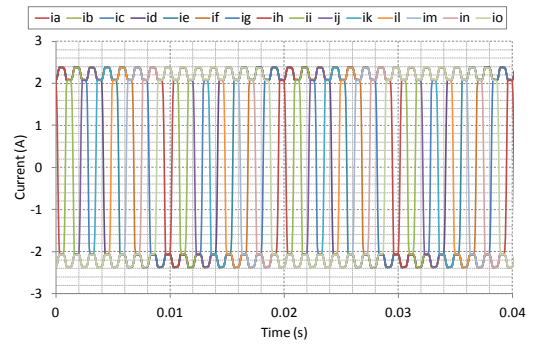


Figure 3.54: 15-phase Simulated AC Generator Current

The generator current, in Figure 3.54, is particularly interesting. A single waveform is shown in comparison with the diode current in Figure 3.55 and Figure 3.56, below.

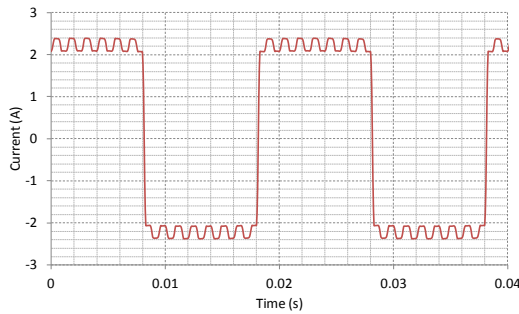


Figure 3.55: 15-phase Simulated AC Generator Current

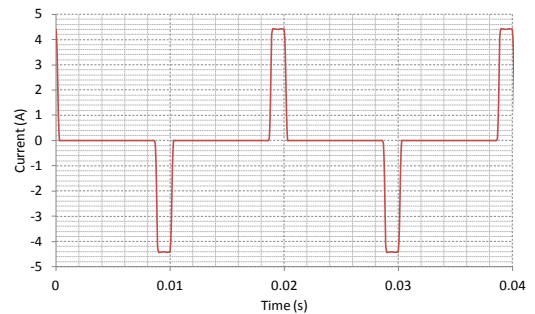


Figure 3.56: 15-phase Simulated AC Diode Current

The current drawn from the generator phase winding is distinctly different in both magnitude and duty. The shape of the waveform is a result of the generator connection method passing current through each phase winding before the rectifier. The combined effect of all the generator currents is to provide a line current that has a greater magnitude than the single corresponding phase winding provides. In Figure 3.56, the peak of the AC line current waveform is approximately flat-topped. On the DC side, the current ripple is 0.52 % of the peak value when compared to the three-phase DC ripple of approximately 20.32 %.

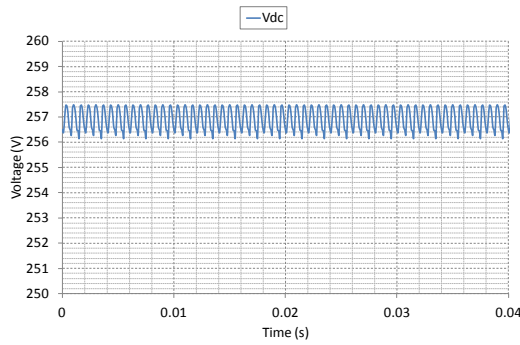


Figure 3.57: 15-phase Polygon-connected Simulated DC Voltage

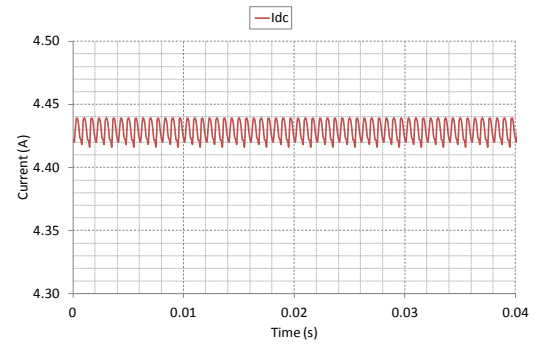


Figure 3.58: 15-phase Polygon-connected Simulated DC Current

The DC output voltage of the 15-phase rectifier connected to polygon configured machine is notable for retaining the DC voltage magnitude at around 260 V. The voltage and current shapes, in Figure 3.57 and Figure 3.58, respectively, are consistent with the three- and five-phase delta- and polygon-connected waveforms. The voltage commutation is different when compared with the star-connected generator. The commutation angle is visibly shorter, indicating a consistent rectifier performance when connected to a polygon configured generator.

3.6 Summary

This chapter has detailed the construction of a simulation model for the synchronous generator with a diode rectifier. The three-phase generator model was created to represent the dynamic circuit behaviour of a three-phase synchronous generator, which was then tested and verified. The validated model was extended to encompass a higher number of phases before the system was completed with the addition of a rectifier load.

Analysis was performed to establish the ideal behaviour of a synchronous generator connected to a passive rectifier. This allowed the simulation model to be checked and identified areas for which the analysis became too complicated. It was apparent from finite element modelling, and the experimental testing that followed, that the simulation model required information regarding the harmonic content of spacial flux. As such, the addition of winding harmonic behaviour was necessary to increase the accuracy of the model.

This chapter has demonstrated the implementation of harmonic back-emf in the circuit model. It has also identified high generator currents in the star-connected case and made assumptions on the dynamic behaviour of the machine. The following chapter uses finite element analysis to check the assumptions made in the dynamic circuit model, establish

the magnitude and phase of the harmonic content of the open-circuit voltages developed from the back-emf of the different winding topologies and calculate the core losses for a synchronous generator connected to a diode rectifier.

4

Finite Element Modelling

4.1	Introduction.....	96
4.2	Background.....	97
4.3	The Synchronous Generator in Femm ...	98
4.4	Modelling the Three-phase Generator	103
4.5	Modelling the Five-phase Generator ...	109
4.6	Modelling the 15-phase Generator.....	112
4.7	Core Losses when Connected to an Uncontrolled Rectifier	116
4.8	Summary	125

4.1 Introduction

Modelling of electric machines has become commonplace as programs and computers have advanced. Techniques to simulate the dynamic behaviour are well documented in textbooks and journal publications. However, the most recent advancements have allowed the modelling of the internal electromagnetic fields of electric machines to be evaluated readily. Finite element modelling (FEM) is based on the numerical solution of boundary condition problems, where a set of differential equations are solved to reveal the field distribution. Finite element analysis (FEA) is now widely used to evaluate electromagnetic, electrostatic, fluid and thermal problems within a number of different engineering disciplines.

In this chapter, FEA is used to determine the open-circuit voltage waveforms for the three-, five- and 15-phase generator with the windings connected in either a fully- or short-pitched topology. The core losses are also evaluated for both winding topologies for a star- or polygon-connected synchronous generator connected to a rectifier.

4.2 Background

Preceding FEM, the finite difference method (FDM), developed in the 1920s by Alexander Thom and later published [65], had similar characteristics to the techniques used today. FDM involved a fixed grid system overlaid onto the problem which was then solved using the grid reference. This led to limitations when dealing with complex shapes. The history of the finite element method is described in detail in [66], starting from its development as a method for solving structural stress calculations in continuous solids, through to its more recognisable modern format. The development of such a method had a significant impact on electrical engineering as electric machines could have their internal stresses modelled.

Encompassing all facets of engineering, Poisson's equation is the underlying equation used to solve finite element problems. For electrical engineering, there are two main types of problem: electrostatic and electromagnetic. The former is relatively straightforward since potential is a scalar quantity related to Coulomb's electric field. Magnetic potential, used to solve electromagnetic problems, is introduced here along with the mathematical methods that exist to enable its use. The magnetic vector potential, A , can be processed using the curl function, a mathematical measure of the tendency for a contour to spiral, turn or curl around a point. The curl function applied to A gives the magnetic flux density, B , in Equation (31). The equations discussed are adapted from [47].

$$\text{Curl}A = B \quad (31)$$

Magnetic flux density and magnetic field strength, H , are linked through the permeability of the material such that:

$$B = \mu H \quad (32)$$

where μ is the permeability of a material.

Applying Ampère's law:

$$\text{Curl}H = J \quad (33)$$

This condition is true when a stationary magnetic condition exists (its time derivative is null) then:

$$\text{Curl}B = \mu J \quad (34)$$

And:

$$\text{CurlCurl}A = \mu J \quad (35)$$

The relationships described enable the use of the magnetic vector potential in the solution of finite element problems through Poisson's equation (in 2D form):

$$\frac{\delta^2 A}{\delta x^2} + \frac{\delta^2 A}{\delta y^2} = -\mu J \quad (36)$$

Potential A is a vector and, therefore, has components in three-dimensions. However, if it is used in two-dimensional simulations, where current flows only in the z -direction and B is in the x - y plane, illustrated in *Figure 4.1*, then the z -directed component can be assumed to be the magnetic vector potential, making it a scalar value. The complexity of the problem is greatly reduced and allows the finite element solver to find the unknown magnetic potentials for the given current density distribution with known boundary conditions.

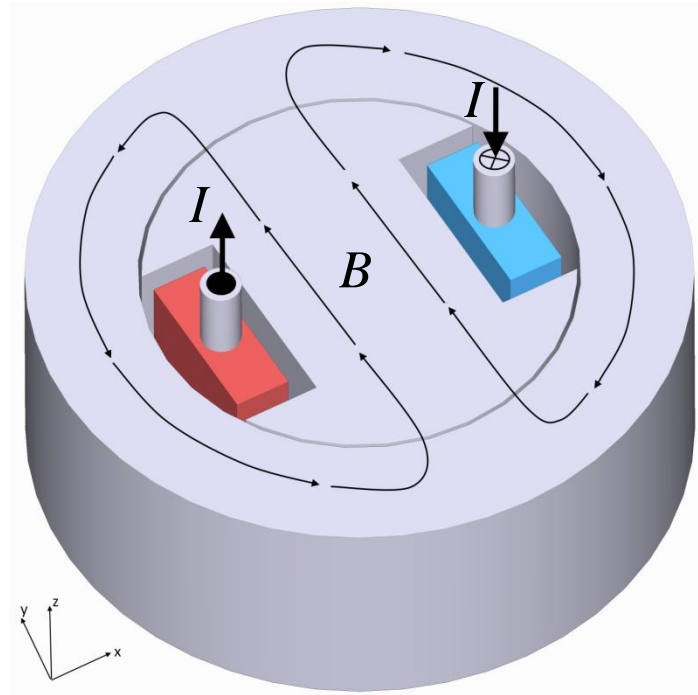


Figure 4.1: Current Definition in Finite Element Problems

4.3 The Synchronous Generator in Femm

A three-phase synchronous generator can be modelled in finite element software packages through its physical geometric measurements. The most straightforward implementation of

the generator design was to create a computer aided design (CAD) drawing which could then be transferred to the finite element software environment. The key benefit behind this was the ability to modify the model within the technical drawing package, VariCAD, whilst retaining the accuracy of the geometric dimensions of the machine. Most information regarding the mechanical dimensions of the machine could be found through the manufacturer's technical drawings. However, some aspects required physical measurements such as the internal stator bore size and the salient rotor dimensions. The accuracy of these measurements was cross-checked with the original technical drawings and the machine specification supplied by the manufacturer. *Figure 4.2* shows the BCI162G synchronous generator in the CAD environment and *Figure 4.3* transferred to the finite element software package.

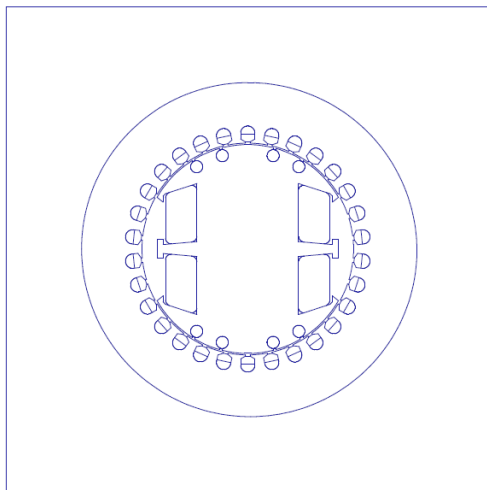


Figure 4.2: VariCAD Drawing of BCI162G Synchronous Generator

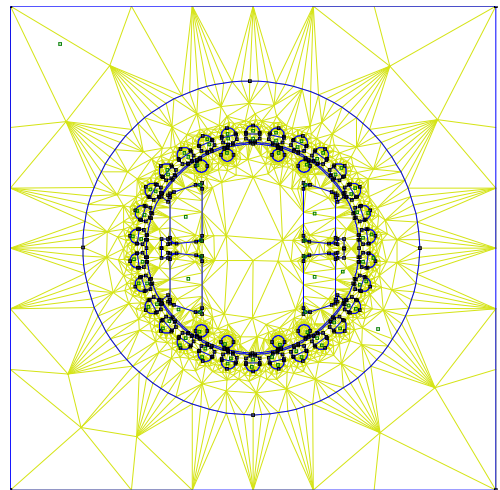


Figure 4.3: FEM Representation of BCI162G Synchronous Generator including Mesh

The program used for the FEA, highlighted in *Figure 4.3*, was the free software package Femm [67]. Built around Wolfram's Mathematica platform, Femm provides a minimal complexity environment in which to build, solve and analyse finite element problems. The software is split into three distinct sections:

- *pre-processor* is the base problem environment of the software, where the model is defined with respect to its geometric sizing, current carrying conductors and boundary conditions
- *processor* refers to the solver used to step through mesh elements and solve the potentials at each node
- *post-processor* is the solution environment allowing values to be drawn from specific points of the model, variations across a contour or distribution across a surface

The definition of the model within the pre-processor environment must be accompanied by information regarding the boundary conditions. Complex models can be reduced down to a single segment if there is sufficient symmetry within the problem. The three types of boundary conditions are well described in textbooks [47, 66] but their differences are briefly discussed here.

- **Dirichlet boundary:** ensures that the potential at the boundary is a constant value, either zero or a predetermined constant
- **Neumann boundary:** utilises the derivative of the potential - potential gradient - where the potential lines are orthogonal to the boundary
- **Periodic boundary:** requires the periodic conditions to be defined within at least two of the boundary lines. The problem is reduced to a fundamental solution that is then mirrored to form the full solution

For the application of FEM to the BCI162G synchronous generator, the complexity of the problem did not allow the detailed segment modelling through use of a periodic boundary, regardless of the symmetry within the problem. Since it is a two-pole generator, it is easiest to model the entire geometry of the machine. The Dirichlet boundary was the most obvious choice, holding the potential at the external boundary at zero. The stator of the machine acts as a natural boundary condition, with all the flux contained within the structure, however, any defects within the model show up as fringing effects extending toward the boundary.

4.3.1 Electrical Design of the Generator

The BCI162G synchronous generator is wound such that the double layer windings of the stator act to reduce the harmonics induced in the air-gap magnetic field. This is true of most synchronous generators, short-pitching by a factor of $2/3^{\text{rds}}$, which removes the triplen harmonics from the supply generated. The removal of triplen harmonics is important for a standalone generator configured in a star connection to the neutral point with an unbalanced load, since this would allow circulating third harmonic currents to flow. This is true for a three-phase machine but increased phase number machines require the consideration of the higher harmonics in order to produce a near sinusoidal voltage output. The winding factor gives an indication of the magnitude of the higher order harmonics induced in the machine, dependent on the short-pitching topology. Equations described in textbooks [50, 62, 68] allow the calculation of the winding factor. For a two-pole machine, the winding factor can be described through Equation (37).

$$\begin{aligned}
k_{dn} &= \frac{\sin\left(\frac{m_c n \beta}{2}\right)}{m_c \sin\left(\frac{n \beta}{2}\right)} \\
k_{pn} &= \cos\left(\frac{n \alpha_s}{2}\right) \\
k_{wn} &= k_{dn} k_{pn}
\end{aligned} \tag{37}$$

where, k_{wn} is the harmonic winding factor, k_{dn} is the distributed winding factor, k_{pn} is the short-pitch factor, m_c is the number of coils per phase belt, n is the harmonic number, β is the slot pitch and α_s is the short-pitch angle.

The stator and rotor winding factors for the three-, five- and 15-phase fully-pitched and short-pitched generators can be found in Appendix 7.2.

4.3.2 Winding Layout

The original three-phase BCI162G generator is wound such that the coils effectively loop around to create a concentric winding, illustrated in *Figure 4.4*.

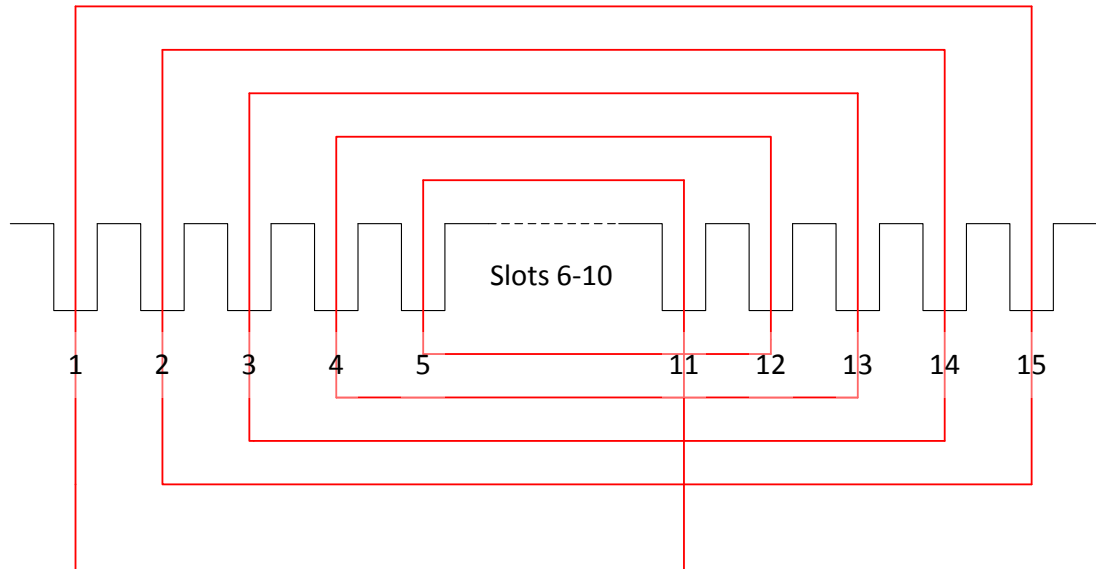


Figure 4.4: Single Phase Coil, Concentric Winding

The concentric winding reduces the size of the end-windings, which are responsible for an increase in leakage inductance and axial force acting on the rotor. As a standalone generator, the multiphase variant could be wound in the same way. However, with the multiphase generator being a single unit and encompassing three-, five- and 15-phase configurations, concentric winding cannot be achieved due to the fixed slot displacement of each coil. In Femm, the type of winding layout is not important since the flux linkage is

calculated for each individual stator slot and, therefore, disregards the current path through the end windings.

4.3.3 Damper Windings

The BCI162G, like any synchronous machine, contains damper windings or damper bars to create pull-in torque under non-synchronous operation. These are usually constructed from a solid alloy bar short-circuited at the ends to form a squirrel-cage arrangement but they can also be wound from thinner gauge material [50]. The existence of these damper windings fundamentally provides the ability for a synchronous generator to maintain synchronous speed, guaranteeing the supply frequency at the output terminals. The design specification accompanying the generator did not specify any details about the rotor damper bars. Therefore, the material was based on those commonly used in the construction of synchronous machines, since its main effect will be related to the starting and pull-in torque values, which are not of critical importance in this project. The brass material commonly used has a permeability similar to that of copper, therefore the relative permeability of 1.05 Hm^{-1} was found from the average of suitable brass materials given in the Nondestructive Testing Collaboration's copper alloy conductivity list [69].

4.3.4 Pre-Processor Lua Scripting

Taking into account all of this information, it was possible to find the flux linkage in the generator, amongst other parameters, through FEA. A pre-processor script was constructed to facilitate the data capture from this process by means of a Lua script. This is a scripting language developed to allow the execution of commands related to all manner of programs by embedding it within the program structure. The results were stored as a text file, which could be plotted in Excel, to allow further computation and presentation herein.

4.3.5 Problem Definition

The model was configured to represent the physical machine, providing the solver with information regarding the depth of the generator, through which the current sheet is distributed, the precision to which the solver must comply and the minimum angle that the triangular mesh can take. The latter is of particular importance in avoiding long, thin triangular sliver elements which can lead to erroneous results. The length of the triangle should be kept to a size that would be consistent with an equilateral variant, in order to prevent the magnetic vector potential changes being overlooked across its surface area. Completion of the problem definition allowed the model to be meshed, where the

software chooses the dimensions of the mesh to fill the area based on the problem definition, so that sufficient detail can be gathered from the solution.

4.4 Modelling the Three-phase Generator

4.4.1 Rotor Field Energised

The first case to consider using FEA was the stator windings in the open-circuit condition, the damper windings carrying no current (indicating synchronous operation) and with the rotor field energised. This configuration was the simplest, allowing the flux linkage within the machine to be calculated and harmonic content of the open-circuit back-emf developed at the terminals of the stator windings to be derived.

The model was configured so that the stator windings contained phase coil groups. How the Femm software package handled that was not obvious and, therefore, the coil group was broken down to a constituent part for verification before continuing to process the model. The Femm solution for one coil in two half-stator slots – since it is a double layer concentric winding – is shown in Equation (38).

$$\begin{aligned}\varphi_{A1_1+} &= 0.002194 \\ \varphi_{A1_1-} &= -0.011844 \\ \varphi_{A1_1} &= \varphi_{A1_1+} - \varphi_{A1_1-} = 0.014038 \text{ Wb}\end{aligned}\tag{38}$$

where φ_{A1} refers to the flux linking the phase coil A in the first layer and the subscript $1+$ and $1-$ denotes the first coil current carrying direction in the phase group.

Checking this against information calculated – the magnetic vector potential and flux density across that area, using Equations (39) and (40), respectively – the flux linkage for a single coil can be compared with the solution directly sourced from Femm.

$$\begin{aligned}\varphi_{A1_1} &= (A_{A1_1+} - A_{A1_1-})lN \\ \varphi_{A1_1} &= (0.0019506 + 0.001484) \cdot 0.28 \cdot 16 \\ \varphi_{A1_1} &= 0.015387 \text{ Wb}\end{aligned}\tag{39}$$

where φ_{A1_1} is the flux linking the first coil of phase a in the first layer winding with the rotor field, A is the magnetic vector potential, l is the axial length through the generator (ignoring the end windings) and N is the number of turns in each slot.

$$\begin{aligned}
\varphi_{A1_1} &= \int B \cdot dl \cdot w \\
\varphi_{A1_1} &= 0.409472 \cdot 0.278471 \cdot 0.14 \\
\varphi_{A1_1} &= 0.015964 \text{ Wb}
\end{aligned} \tag{40}$$

where B is the average flux density over the contour length, l is the contour length and w is the axial length.

Summating all of the individual coil flux linkages across the phase band, the total flux linking the first layer of phase a is close to that given by Femm for the overall phase band.

$$\begin{aligned}
\text{Femm } \psi_{A1\pm} &= 0.0629995 \text{ Wb} \\
\text{Calc } \psi_{A1\pm} &= 0.0629107 \text{ Wb}
\end{aligned} \tag{41}$$

where ψ is the flux linking a group of coils, i.e. a phase winding.

This confirms that the Femm software package will calculate the flux linkage for the phase band considering all coils rather than taking the average flux crossing the centre of the phase band, which would lead to erroneous data in later calculations.

The rotor was configured to carry a 4 A DC current since, for open-circuit conditions, the dynamic circuit model devised simulates a current of 14.71 A for the stator referred field current. Mathematically, this can be checked by considering the q-axis stator voltage relationship to the field current, shown in Equation (42). Since the d-q axis model is power invariant and uses reference frame quantities, at steady-state operation the q-axis voltage can be equated to the line-to-line RMS output voltage of the generator.

$$\begin{aligned}
E_q &= \omega L_{md} i'_f \\
332.5 &= 2\pi \cdot 50 \cdot 0.0721 i'_f \\
i'_f &= 14.679 \text{ A}
\end{aligned} \tag{42}$$

where E_q is the q-axis voltage developed from the excitation path, ω is the line-frequency, L_{md} is the d-axis magnetising inductance (taken from experimental testing) and i'_f is the stator referred field current.

Calculating the current actually contained within the rotor winding requires scaling through the turns ratio, as demonstrated in Equation (43) adapted from [49]. This must be consistent with the reference frame convention used, i.e. the retention of power invariance.

$$\begin{aligned}
i_f' &= \sqrt{\frac{2}{3}} \left(\frac{N_f}{N_s} \right) \left(\frac{k_{wr}}{k_{ws}} \right) i_f^r \\
14.71 &= \sqrt{\frac{2}{3}} \left(\frac{390}{70} \right) \left(\frac{0.6538}{0.8285} \right) i_f^r \\
i_f^r &= 4.098 \text{ A}
\end{aligned} \tag{43}$$

where i_f^r is the rotor referred field current, N_s is the number of stator windings, N_f is the number of rotor field windings, k_{ws} is the fundamental stator winding factor and k_{wr} is the rotor winding factor (see Appendix 7.2).

If the three-phase model is to accurately represent the physical generator, the double layer windings must be displaced by the pitching factor quoted in the datasheet. Pitching the machine stator windings reduces harmonics induced in the air-gap magnetic field as a result of the pseudo square wave MMF field created by the windings. The distribution and pitching of the windings for the two-pole generator are discussed and calculated earlier in this chapter, Section 4.3.1.

Post-processing in Excel allows the data to be evaluated, enabling the open-circuit stator voltages to be found through two different methods, Equations (44) and (45).

$$E(\theta) = 2\pi N_c k_{ws} f \psi(\theta) \tag{44}$$

$$E(\theta) = \omega \frac{d\psi}{d\theta} \tag{45}$$

where E is the angular dependent induced voltage, N_c is the number of windings per coil, k_{ws} is the stator winding factor, f is the frequency and θ is the angle in radians.

The first method of calculation, Equation (44), is relatively straightforward. However, the number of windings per coil, N_c , and the winding factor, k_{ws} , are taken into account in the solution of the problem and thus were set to 1 when calculating the voltage. The resulting waveform is depicted in *Figure 4.5*.

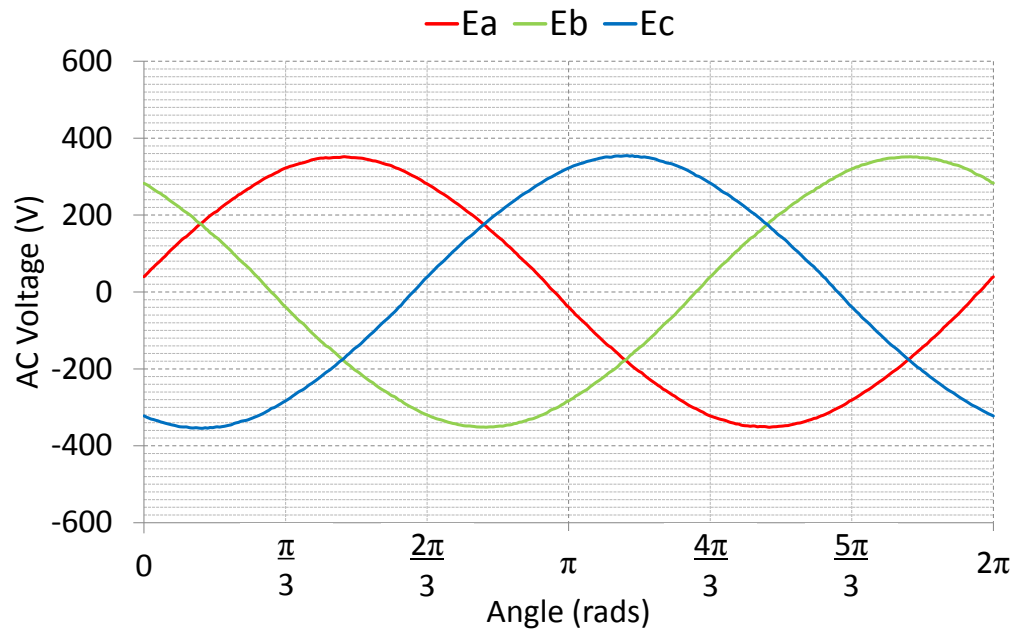


Figure 4.5: Phase Voltage using Equation (44)

The figure highlights the sinusoidal output expected from a three-phase generator. However, Femm does overestimate the output voltage, equating to an RMS voltage of 248 V. Since the end-windings have not been modelled their effects on this value cannot be taken into account in the solution, this assumes that there is no flux linking the end-windings.

The second method of calculating the open-circuit voltage can be observed in Figure 4.6.

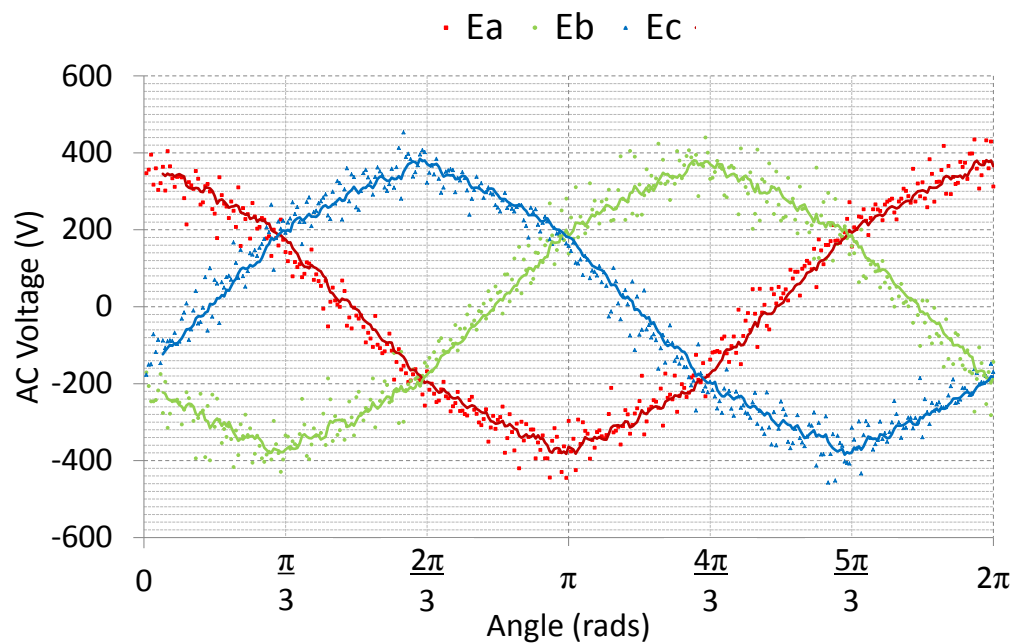


Figure 4.6: Phase Voltage using Equation (45)

This means of calculating the open-circuit voltage leads to discrete data points reliant on the previous value, as the relation between the flux linkage changes with the angle. Since the angle is also dependent on time, one mechanical revolution being one wave cycle, there is a phase shift present compared with *Figure 4.5*. A moving-average trend line provides the smooth sinusoidal waveform with which to interpret the results.

4.4.2 Stator Windings Energised

Removing the DC excitation on the rotor side and, instead, configuring the model with currents in its stator windings will allow d- and q-axis parameters to be observed. Taking the instantaneous three-phase currents and applying the Clarke transform, as discussed previously in Chapter 3, it was possible to find the d- and q-axis currents. These values were put into the model to find the static solution of the flux as the rotor position was varied from its aligned to unaligned position, as depicted in *Figure 4.7* and *Figure 4.8*.

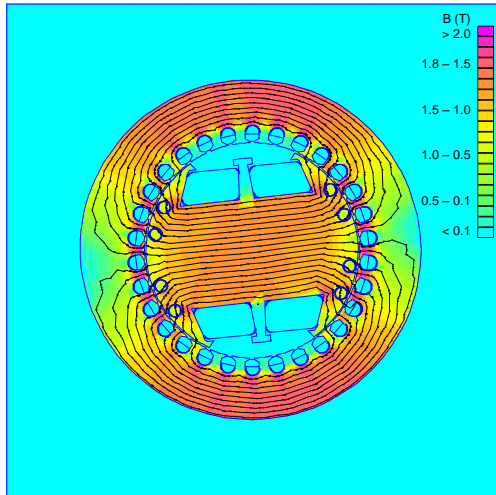


Figure 4.7: Aligned Rotor with Stator Field

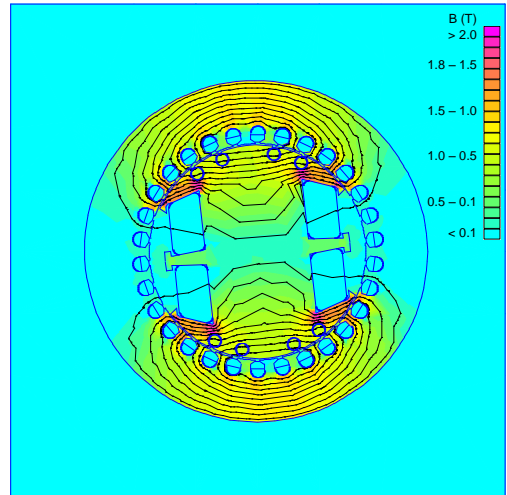


Figure 4.8: Unaligned Rotor Position

The model is configured with full current in the stator windings, which leads to the saturated areas of the stator iron in the aligned position. The flux linking the rotor in this aligned position gives the peak inductance through the flux linkage relationship to the d-axis current, underlined in Equation (46).

$$L_d = \frac{\varphi_d}{i_d} \quad (46)$$

where L_d is the d-axis inductance, φ_d is the d-axis flux linkage and i_d is the d-axis current.

The minimum inductance corresponds to the unaligned position and indicates the q-axis inductance value. Again, post-processing of the data was completed using Excel to calculate the inductance as the rotor position varied, depicted in *Figure 4.9*.

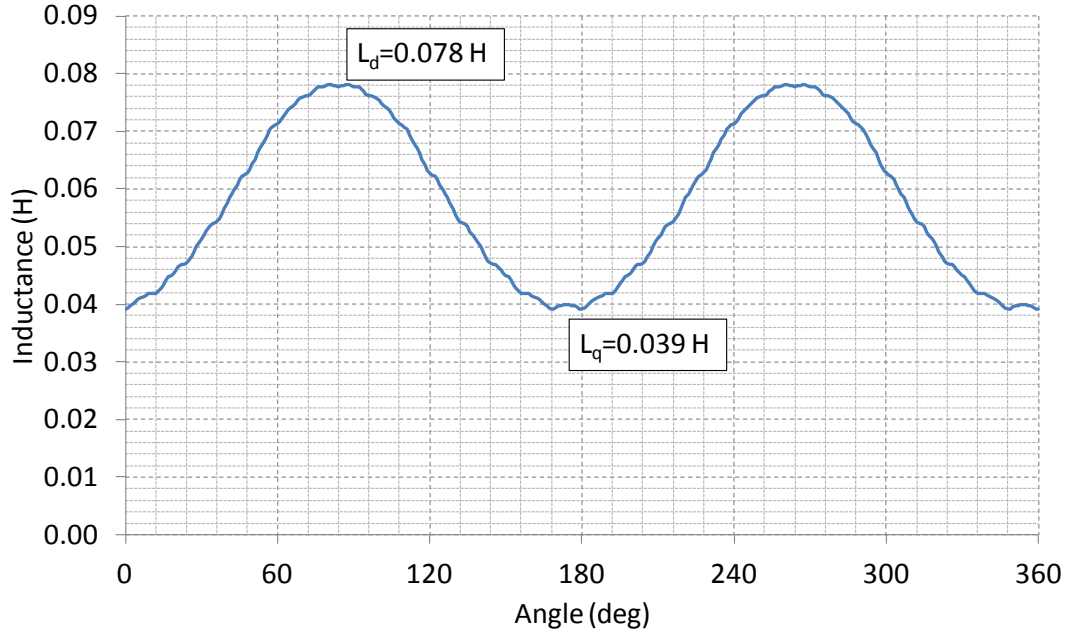


Figure 4.9: Inductance Variation of Three-phase Generator through Rotation of Rotor

The d- and q-axis inductances are an over estimate of those supplied within the generator datasheet, see Appendix 7.5. However, the data from the FEA correlates with that achieved from short-circuit testing carried out in laboratory conditions on the BCI162G generator, as discussed in Appendix 7.4.

Referring back to the mathematical modelling and dynamic machine behaviour simulated in Chapter 3, assumptions were made regarding the loss mechanisms and level of detail in the modelling of the generator. One of the assumptions states that saliency terms of greater than twice line frequency can be neglected. This can be assessed by taking a FFT of the waveform, depicted in *Figure 4.9*, and checking that no harmonic components are present at higher than twice line frequency, i.e. 100 Hz. The Fourier transform in *Figure 4.10* verifies that the assumption made when mathematically modelling the generator was valid. The transform provides information relating to the DC offset magnitude, consistent with *Figure 4.9*, and the higher harmonic contribution. It can be observed that above the second harmonic, there is very little contributing to the air-gap magnetic field.

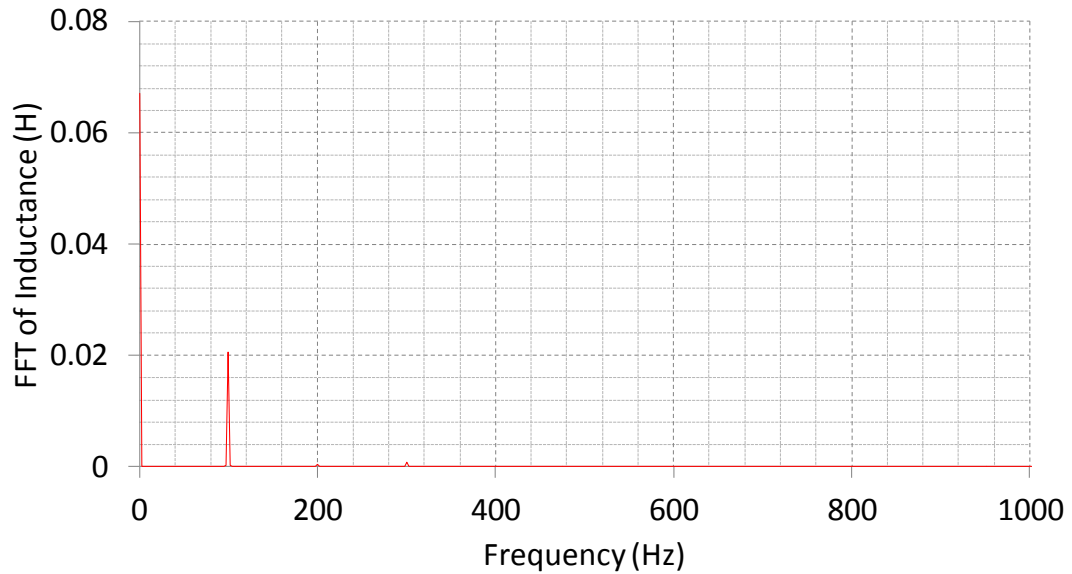


Figure 4.10: Fourier Transform of Inductance Waveform

4.5 Modelling the Five-phase Generator

The multiphase extension to the Femm model involves the same principles as for the three-phase generator. However, consideration must be made toward the pitching of the generator in order to reduce the harmonic content of the output. In the three-phase generator, the second layer windings are pitched at 60° mechanical to the origin, each phase belt takes 5 slots separated mechanically by 12° . The pitching of the windings is similar for the five-phase topology but, due to the fixed volume of the machine, the number of slots per phase belt must be reduced. There are 30 stator slots which will give three slots per positive phase and three per negative phase. This means that, if the second layer of windings is pitched at 36° mechanical, this will cancel the 5th harmonic currents. FEA is subsequently carried out on the fully pitched and 36° short-pitched topologies.

4.5.1 Rotor Field Energised

Utilising the same methods as for the three-phase case, the DC rotor field was again energised with a 4 A DC current. The flux linkage and the resultant shape of the back-emf could then be observed for the two winding pitch configurations.

The first case examined was the fully-pitched topology and the back-emf, calculated from Equation (45), can be observed in Figure 4.11.

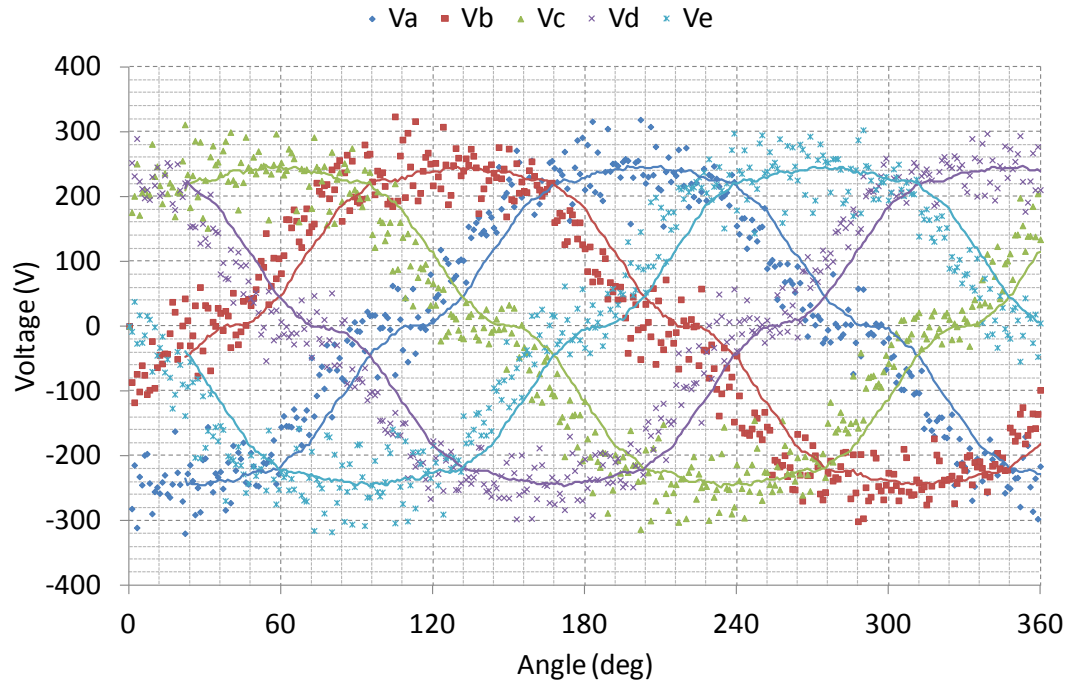


Figure 4.11: Back-emf for Fully-pitched Five-phase Generator

Taking the FFT of one of the back-emf waveforms would suggest the presence of higher order harmonics due to the flattening of the wave around the peak and zero cross-over point. This is confirmed in *Table 4.1*, where the normalised higher order harmonic content shows a significant contribution of 3rd, 5th and 7th harmonics.

Table 4.1: Normalised Harmonic Content of Fully-pitched Five-phase Voltage

Harmonic	1	3	5	7	9	11	13	15
Freq. (Hz)	50	150	250	350	450	550	650	750
Magnitude	1.0000	0.0303	0.0894	0.0500	0.0052	0.0086	0.0241	0.0057
(%)	100.00	3.03	8.94	5.00	0.52	0.86	2.41	0.57

This would indicate that utilising fully-pitched windings for the five-phase generator would result in an increased harmonic content of the voltage.

Short-pitching the windings by three slots will remove the 5th harmonic, shown in *Table 7.2* of Appendix 7.2. Other winding harmonic factors are also reduced, reducing the voltage THD. The fundamental voltage is reduced by 6 % as a result of short-pitching the windings. The waveforms for the short-pitched windings, shown in *Figure 4.12*, can be directly compared with that of *Figure 4.11*.

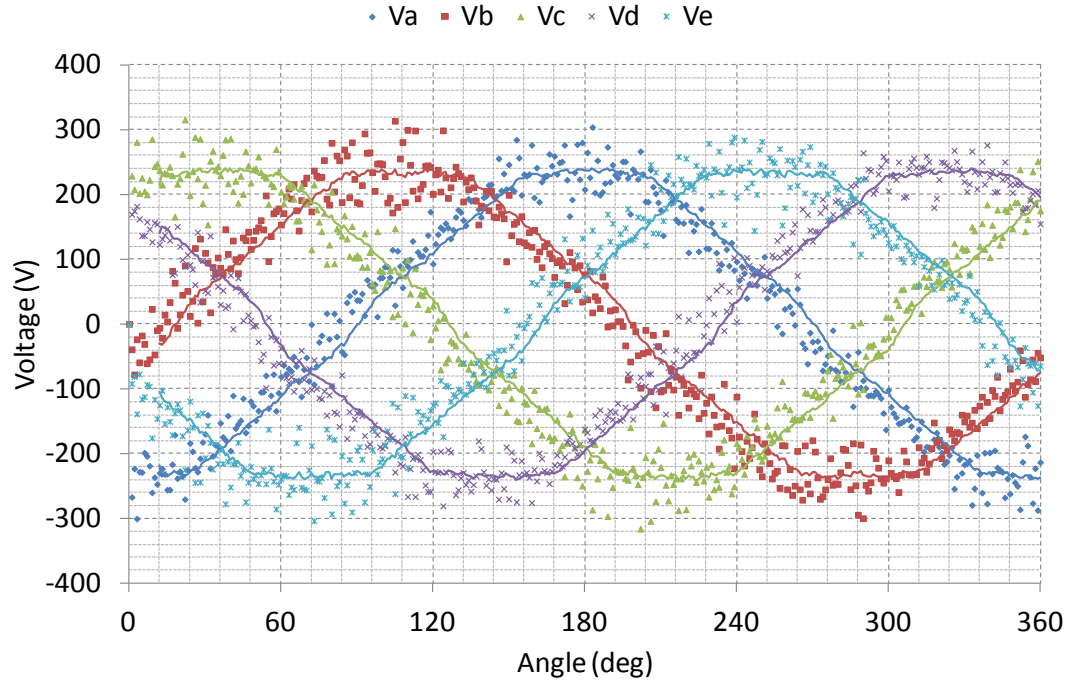


Figure 4.12: Five-phase Voltage Output for 36° Short-pitched Double Layer Windings

The waveform is more sinusoidal in shape due to the considerable reduction of the 5th harmonic contribution to the waveform structure. The FFT of this highlights the increase in machine performance achieved by short-pitching the double-layer windings toward cancelling the 5th harmonic, illustrated in Table 4.2.

Table 4.2: Normalised Harmonic Content of 36° Short-pitched Five-phase Voltage

Harmonic	1	3	5	7	9	11	13	15
Freq. (Hz)	50	150	250	350	450	550	650	750
Magnitude	1.0000	0.0536	0.0195	0.0230	0.0104	0.0096	0.0088	0.0061
(%)	100.00	5.36	1.95	2.30	1.04	0.96	0.88	0.61

Although the fully-pitched windings give reasonable generator performance, providing a back-emf waveform with a low harmonic content, the short-pitched winding clearly performs better.

4.5.2 Stator Windings Energised

As with the three-phase generator, the five-phase generator also simplifies to a d-q axis reference system. The phase currents contribute to the d- and q-axis dependent on the Clarke transform, in this case the extended Clarke transform, as highlighted in Chapter 3. FEA is conducted to find the d- and q-axis inductance. As the rotor is rotated through 360°, the maximum and minimum flux values will indicate the d- and q-axis inductances,

respectively. The simulation modelling assumes that increasing the number of phases from three to five, by reducing the number of coils per phase group, will result in an inductance scaling factor of $3/5^{\text{th}}$.

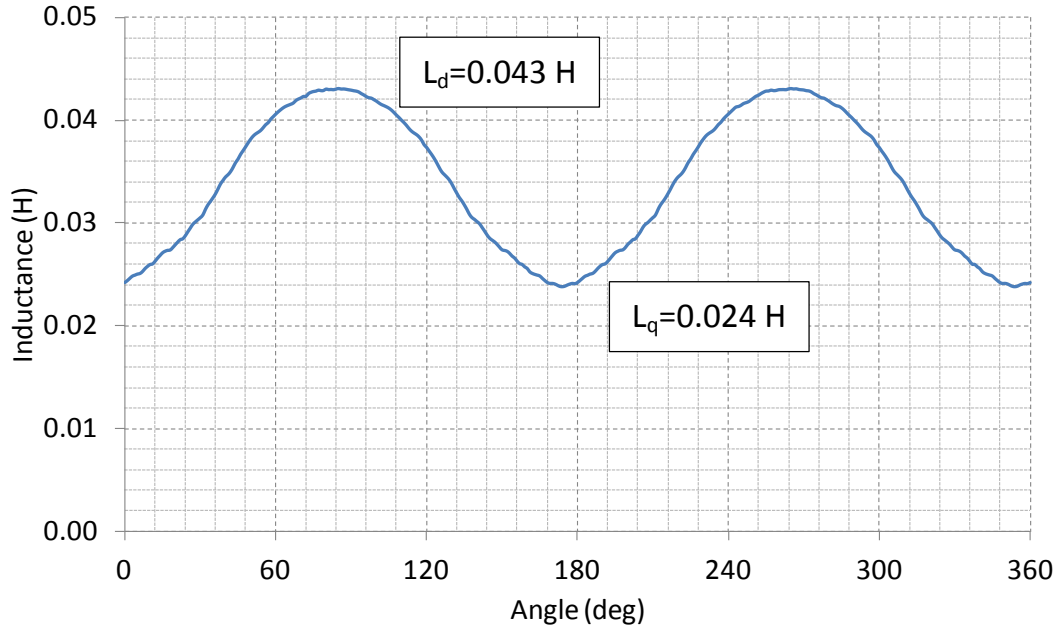


Figure 4.13: Inductance Variation for Five-phase Generator through Rotation of Rotor

As highlighted in Figure 4.13, the d- and q-axis inductance values equate to 55.1 % and 61.5 % of the three-phase generator inductance values, respectively, which is approximately $3/5^{\text{th}}$, so the scaling factor on the inductance is valid. The FFT of the inductance for the five-phase generator follows the same principles as for the three-phase variant. Figure 4.13 shows that the inductance follows a sinusoidal pattern with a DC offset and twice line frequency oscillation. The assumption that the higher order harmonics are negligible is valid.

4.6 Modelling the 15-phase Generator

The 15-phase topology is the physical limit on the number of windings that can be achieved for the number of slots in the machine. Fractional slot windings offer the potential to increase the phase number further but incur a high de-rating of the generator output as a result [62]. Simulation of the dynamic behaviour of the generator, discussed in Chapter 3, would suggest that beyond a certain number of phases, the passive rectification becomes limited by the commutation time between devices turning on or off. A 15-phase generator is, therefore, deemed a suitable number to investigate and justify the effects of passive rectification on a higher phase number machine.

When pitched at 12° , the winding factor for the fifteen-phase generator indicates the removal of the 15th harmonic from the back-emf waveform. However, the 3rd, 5th and other higher order harmonics remain to govern the waveform shape. This short-pitching does not offer much improvement over the fully-pitched windings and would contain greater quantities of higher order harmonic magnitudes than a simple distributed winding. *Table 7.3* (in Appendix 7.2) highlights the winding factor for the 15-phase generator.

4.6.1 Rotor Field Energised

The Femm software is configured to run with the same current within the rotor field as used in the previous topologies. The fully-pitched windings were the starting point, where the double layer phase windings are aligned. The back-emf waveform, shown in *Figure 4.14*, exhibits a large amount of distortion. This will have a greater effect on the losses in the generator since there will be an increased presence of higher order space harmonics in the machine flux. The data points are not displayed as in previous cases due to the number of phases being plotted. Therefore, the 12-point moving averages of these data points are plotted only.

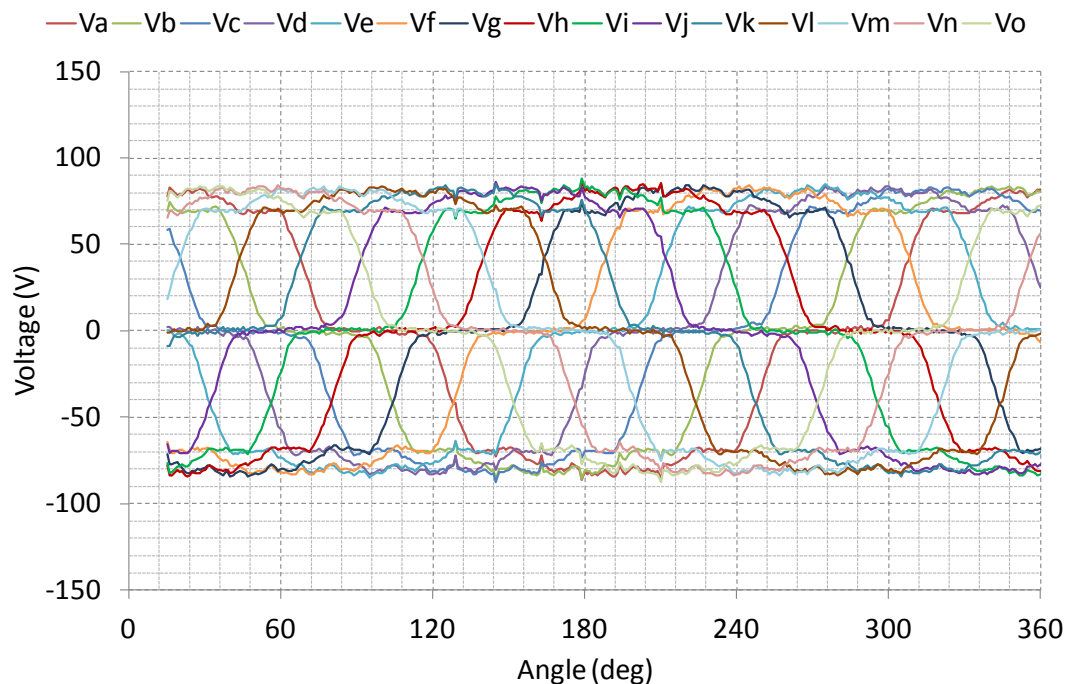


Figure 4.14: Fully-pitched 15-phase Back-emf Waveform

Analysing the waveform by performing a FFT on a single phase shown yields the results in *Table 4.3*.

Table 4.3: Normalised Harmonic Content of Fully-pitched 15-phase Voltage

Harmonic	1	3	5	7	9	11	13	15
Freq. (Hz)	50	150	250	350	450	550	650	750
Magnitude	1.0000	0.0787	0.1134	0.0523	0.0049	0.0112	0.0165	0.0175
(%)	100.00	7.87	11.34	5.23	0.49	1.12	1.65	1.75

The higher order harmonics are much greater than those created by fully-pitched windings in the five-phase generator. This is to be expected for the fifteen-phase generator, where there is only a single coil per phase per layer to carry the current.

The short-pitching of the second-layer windings for the fifteen-phase generator, therefore, becomes particularly interesting since there is only one coil per slot. The movement of the coils through the 12° mechanical slot pitch can have a significant effect on the harmonic content of the back-emf developed. Furthermore, the shape of the waveform produced will be considerably altered as a result. The generator was short-pitched in steps of one slot from 0° to 60° . The results are displayed in Table 4.4.

Table 4.4: Normalised FFT Voltages of Short-pitched Windings for 15-phase Generator

Harmonic	1	3	5	7	9	11	13	15
Frequency	50	150	250	350	450	550	650	750
Mag. (0°)	1.0000	0.0787	0.1134	0.0523	0.0049	0.0112	0.0165	0.0175
Mag. (12°)	1.0000	0.0763	0.0985	0.0331	0.0061	0.0046	0.0047	0.0015
Mag. (24°)	1.0000	0.0667	0.0537	0.0073	0.0033	0.0091	0.0166	0.0153
Mag. (36°)	1.0000	0.0578	0.0119	0.0566	0.0237	0.0159	0.0202	0.0199
Mag. (48°)	1.0000	0.0663	0.0339	0.0765	0.0277	0.0194	0.0157	0.0158
Mag. (60°)	1.0000	0.0849	0.0682	0.0561	0.0105	0.0063	0.0202	0.0267

Equation (37) specifies that short-pitching the windings by 60° should lead to the mitigation of triplen harmonics. However, as Table 4.4 shows, the harmonic content for those triplen values is higher than for the three- and five-phase machines and enough to distort the voltage considerably. The most suitable solution would be to use the 36° short-pitching. However, checking the total harmonic distortion (THD), observed in Table 4.5, suggests that the 24° short-pitching would also have been a viable option if fundamental voltage drop was of critical importance.

Table 4.5: THD of RMS Voltages for Short-pitching of 15-phase Generator

Harmonic	1	3	5	7	9	11	13	15	THD (%)
$V_{\text{RMS}} (0^\circ)$	57.042	4.487	6.469	2.982	0.279	0.639	0.943	0.998	11.591
$V_{\text{RMS}} (12^\circ)$	56.955	4.347	5.612	1.888	0.346	0.263	0.266	0.083	10.556
$V_{\text{RMS}} (24^\circ)$	56.142	3.742	3.014	0.410	0.184	0.512	0.930	0.857	7.623
$V_{\text{RMS}} (36^\circ)$	55.585	3.213	0.660	3.147	1.316	0.884	1.125	1.103	7.557
$V_{\text{RMS}} (48^\circ)$	54.485	3.613	1.850	4.168	1.510	1.057	0.854	0.863	9.098
$V_{\text{RMS}} (60^\circ)$	52.523	4.458	3.581	2.945	0.553	0.329	1.059	1.402	10.021

The THD is higher for the single slot, 12° short-pitched generator when compared with short-pitching by two, three or four slots. Short-pitching by 36° offers the least THD and, crucially, contains the least third harmonic component. Furthermore, the fundamental voltage only drops by 2.55 % compared with the fully-pitched windings. The 36° short-pitching offers the best machine performance and will be used herein for the short-pitching of the 15-phase generator.

The voltage waveform created by short-pitching the generator windings can be observed in Figure 4.15.

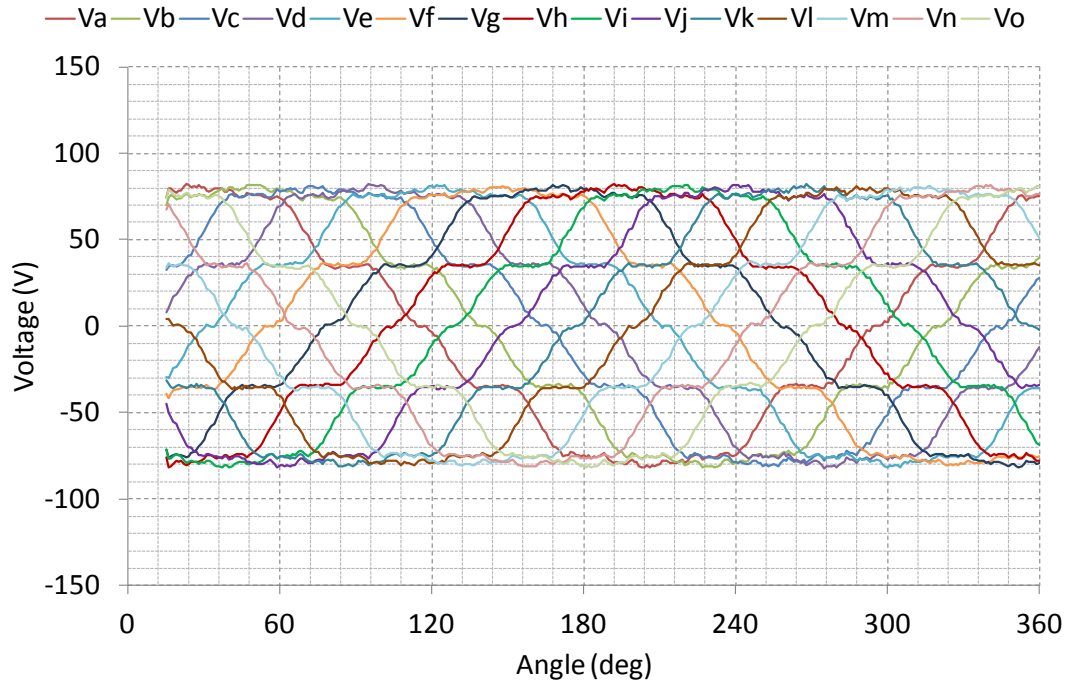


Figure 4.15: Short-pitched 15-phase Back-emf Waveform

Comparing with Figure 4.14, the short-pitched back-emf shows a marked difference in waveform shape, notably the removal of the sustained zero section.

4.6.2 Stator Windings Energised

Energising the stator windings will allow the inductances to be found for the d- and q-axis. The resolution of the inductances to two axes allows the comparison across the three topologies discussed. The fifteen-phase generator should have d- and q-axis inductances equivalent to $1/5^{\text{th}}$ the magnitude of the three-phase generator.

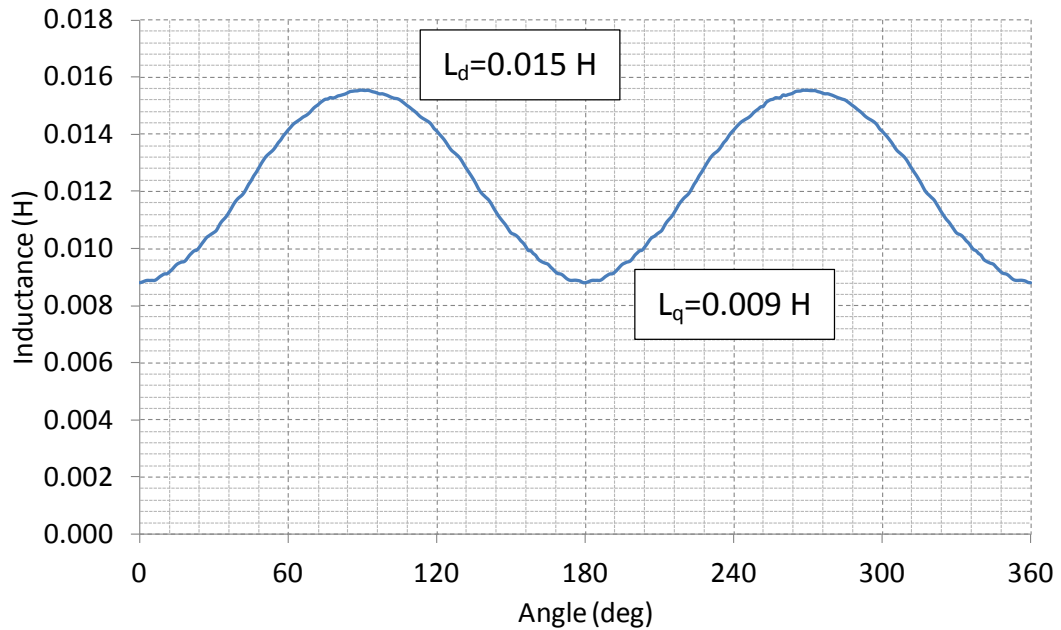


Figure 4.16: Inductance Waveform for 15-phase Generator

The d- and q-axis inductances, shown in Figure 4.16, verify that the values are $1/5^{\text{th}}$ the original three-phase values obtained from FEA.

4.7 Core Losses when Connected to an Uncontrolled Rectifier

Core losses are associated with the material properties used to construct both the stator and rotor magnetic circuits. Since these components are responsible for creating the path through which the flux can link the electric circuits, they play a particular importance in the performance of the machine. The BCI162G synchronous generator is designed to produce a sinusoidal output. However, connecting a rectifier to the generator output terminals causes it to behave differently depending on the method of connection used.

The two generator winding configurations considered were the series-star and series-polygon topologies which, for multiphase machines, both offer different advantages, explained earlier in Chapter 3. The effect this has on the generator core losses can be quantified by replicating the current distribution in Femm, for the five-phase generator.

The FE model was split into regions so that the losses for the stator back-iron, stator tooth and tooth-tip could be evaluated with respect to their mass. This gives the core losses in the typically quoted W/kg format. The characteristic of the losses for increasing flux density is shown in *Figure 4.17*.

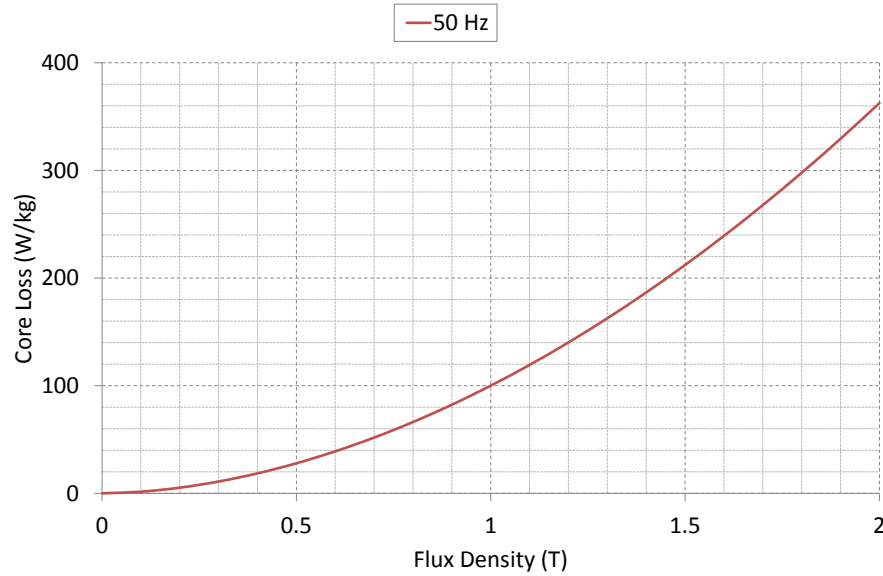


Figure 4.17: Core Loss against Flux Density for 50 Hz Operation

The stator back-iron makes up the majority of the stator mass, highlighted in Equation (47). The stator tooth and tooth-tip mass can be calculated in the same manner, enabling the losses in the rotor aligned position to be analysed, shown in *Table 4.6*.

$$\begin{aligned}
 \text{Mass} &= \text{Volume} \times \text{Density} \\
 \text{Mass} &= 3.824 \times 10^{-3} \times 7650 \\
 \text{Mass} &= 29.254 \text{ kg}
 \end{aligned}
 \tag{47}$$

The value used for the material density is taken from the Product Data Bulletin published by AK Steel Corporation for a 3 % silicon steel [70].

The model is set-up to reflect the conditions at one point during the power transfer through the rectifier, unlike previous analysis where energising the rotor and rotating it through 360° would result in the back-emf developed in the generator. Observing the back-emf would require knowledge of the change in the current in each winding, this could be achieved based on the simulation output for connection to a passive rectifier. However, it would require considerable programming and assumes that the simulation output is accurate. It was most suitable to experimentally verify the effects of short-pitching the generator on the back-emf waveform shape, which can be found in Chapter 5.

The flux density can be found in Femm by taking the integral of B throughout the volumetric section. This gives the summation of the average flux density for each meshed element as an x- and y-coordinate, given in units Tm^3 . To find the power loss, the flux density alone is required. Therefore, the answer given by the post-processor is divided by the block volume. The flux density magnitude can be found by taking the root of the sum of the squared x- and y-coordinate values. The power loss is typically calculated using Equation (48).

$$P_{loss} = k_h B^{n_k} f + k_e B^2 f^2 \quad (48)$$

where P_{loss} is the power loss in the stator material, k_h and k_e are hysteresis and eddy current coefficients, respectively, B is the flux density, superscript n_k is the Steinmetz index and f is the frequency. The hysteresis and eddy current coefficients are neglected here since the power loss does not require splitting into its component parts.

4.7.1 Fully-pitched Star-connected Generator

For the star-connected generator, the stator currents were set such that only two phases conducted at any point in time, in this case phases a and c shown in *Figure 4.18*. The nature of the star-connected diode rectifier holds all other phases in an open-circuit condition for a balanced five-phase system except under commutation. To avoid saturation of the generator, the current level was first set to approximately $2/3^{\text{rds}}$ the generator rated current output before later being configured to the full rating.

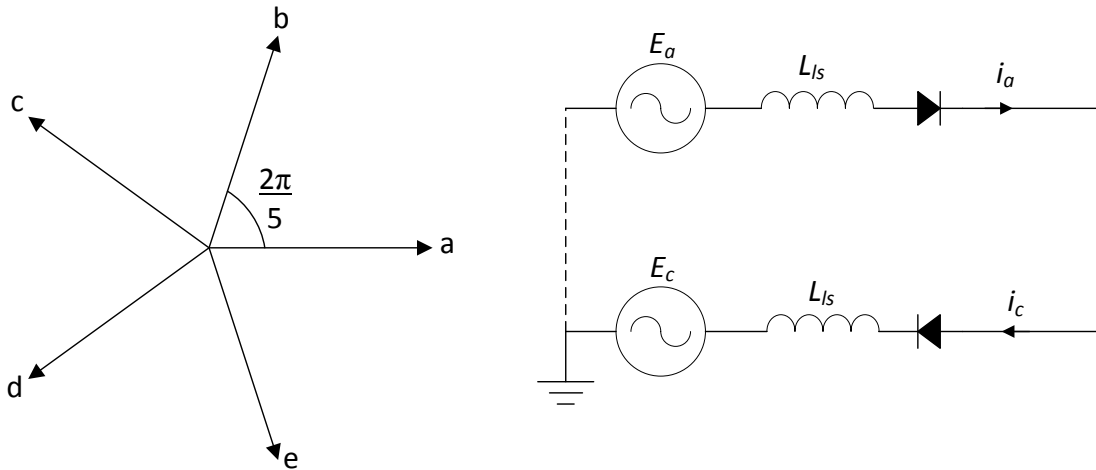


Figure 4.18: Simplified Diagram of Conduction Path used to Analyse Core Losses

Table 4.6: Core Loss for Aligned, Fully-pitched Star-connected Generator at $2/3^{rd}$ Rated Current

	Flux Density (T)	Power Loss (W)	Mass (kg)	Core Loss (W/kg)
Stator back-iron	0.554	33.6	29.3	1.15
Stator tooth	0.693	50.8	0.141	361.4
Stator tooth-tip	0.431	21.2	0.015	1386
Total loss	-	105.7	-	-

The data for the stator tooth and tooth-tip, shown in *Table 4.6*, gives the average value around the generator since some teeth will be saturated whilst others have little, if any, flux through them in the rotor aligned position. The tooth-tip results show a high core loss quoted due to the relatively small fraction this volumetric component has on the composition of the whole generator. This considers the fundamental loss component only and does not consider the minor flux loops around the slots since this is too time intensive to model. The average flux density remains relatively high throughout this area since the tooth-tip is the point at which flux enters and leaves the stator and rotor material. The air-gap magnetic flux is concentrated by the constrained width of the stator tooth leading to a higher degree of saturation within that area and, therefore, a greater power loss component. The total stator power loss is in *Table 4.6* for comparison with other generator topologies.

For this particular application, the tooth-tip saturation was not of great importance. The generator has been rewound in such a way that it will not exceed the limits set out in the original manufacturer design criteria. However, it is necessary, when designing a generator, to consider this part separately in order to evaluate the areas of peak loss and ensure that the stator material can accept the electrical and thermal stresses.

Repeating the test for the generator at rated current provided a better understanding of the saturation effects experienced by the stator material. The results are displayed in *Table 4.7* and it can be observed that the power loss considerably increases as the machine is pushed further into saturation.

Table 4.7: Core Loss for Aligned, Fully-pitched Star-connected Generator at Rated Current

	Flux Density (T)	Power Loss (W)	Mass (kg)	Core Loss (W/kg)
Stator back-iron	0.669	47.7	29.3	1.63
Stator tooth	0.821	69.5	0.141	494.1
Stator tooth-tip	0.521	30.1	0.015	1967
Total loss	-	147.2	-	-

4.7.2 Short-pitched Star-connected Generator

As previously stated, short-pitching the generator by three slots (36° mechanical) is designed to reduce the harmonics providing a more sinusoidal output voltage. However, the flux density pattern through the stator will change the stator core losses. With the same current distribution as that used in the fully-pitched topology, the short-pitching provides a more even flux density distribution within the generator material, reducing the peak flux linking the rotor in the aligned position.

Table 4.8: Core Loss for Aligned, Short-pitched, Star-connected Generator at $2/3^{\text{rds}}$ Rated Current

	Flux Density (T)	Power Loss (W)	Mass (kg)	Core Loss (W/kg)
Stator back-iron	0.538	31.9	29.3	1.09
Stator tooth	0.669	47.7	0.141	338.9
Stator tooth-tip	0.424	20.6	0.015	1346
Total loss	-	100.2	-	-

Comparing fully- and short-pitched results, the short-pitched generator incurs 5.2 % less core losses at $2/3^{\text{rds}}$ rated current.

Table 4.9: Core Loss for Aligned, Short-pitched, Star-connected Generator at Rated Current

	Flux Density (T)	Power Loss (W)	Mass (kg)	Core Loss (W/kg)
Stator back-iron	0.672	48.0	29.3	1.64
Stator tooth	0.810	67.8	0.141	481.9
Stator tooth-tip	0.525	30.5	0.015	1994
Total loss	-	146.3	-	-

It is clear from the results displayed in *Table 4.9* that short-pitching the generator has no significant difference in core losses when driven into saturation. Therefore, under heavy loading conditions, the generator will experience similar power losses regardless of the winding topology.

4.7.3 Fully-pitched Polygon-connected Generator

This section will show that the polygon-connected generator incurs lower core losses, indicating an increase in generator performance due entirely to the connection method at the generator output side. As presented in Chapter 3, all stator windings carry current using this topology, unlike the star-connected system. The polygon-connected generator, therefore, has a much lower peak current resulting in a reduced average flux density throughout the stator material. Since all phases are conducting, the rotor aligned position is different when compared with the alignment for the star-connected system. The current distribution within the model was again set to $2/3^{\text{rds}}$ the rated current and repeated for full current rating.

Table 4.10: Core Loss for Aligned, Fully-pitched, Polygon-connected Generator at $2/3^{\text{rds}}$ Rated Current

	Flux Density (T)	Power Loss (W)	Mass (kg)	Core Loss (W/kg)
Stator back-iron	0.496	27.4	29.3	0.938
Stator tooth	0.611	40.3	0.141	286.8
Stator tooth-tip	0.368	15.9	0.015	1039
Total loss	-	83.7	-	-

Comparing *Table 4.10* with the results gained from the fully-pitched star-connected generator in *Table 4.6*, the core losses are approximately 21 % lower. The generator magnetic material experiences a lower average flux density. However, for the fully-pitched polygon-connected generator, the peak flux density value – measured at the stator core-back face as a closed contour – is higher, as highlighted in the comparison of *Figure 4.19* and *Figure 4.20*.

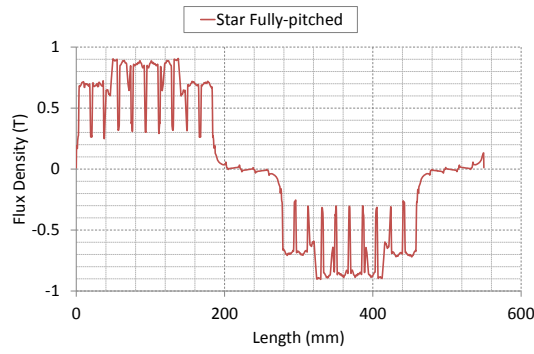


Figure 4.19: Fully-pitched Star-connected Flux Density in Aligned Rotor Position

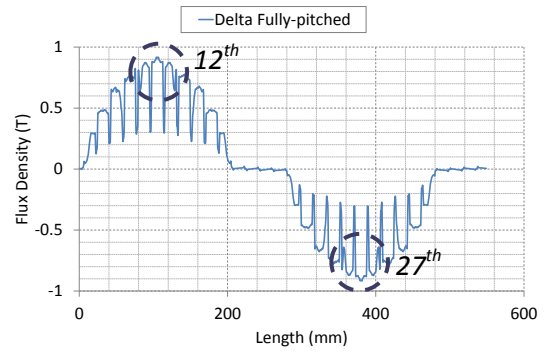


Figure 4.20: Fully-pitched Polygon-connected Flux Density in Aligned Rotor Position

The star-connected generator has a high concentration of flux density over a large contour length of the generator, spanning approximately 10 stator slots. However, the polygon-connected generator has a higher peak flux density due to the concentration of flux through the 12th and 27th stator teeth. The rotor is aligned with the flux path for the α - and e -phases, which are the phases with the greatest amount of current flowing causing the peak in the waveform of Figure 4.20 as the flux is constricted through the stator teeth.

Again, pushing the generator into saturation by simulating at rated current, the results are shown in Table 4.11, which compare with Table 4.7 for the fully-pitched star-connected case.

Table 4.11: Core Loss for Aligned, Fully-pitched, Polygon-connected Generator at Rated Current

	Flux Density (T)	Power Loss (W)	Mass (kg)	Core Loss (W/kg)
Stator back-iron	0.661	46.6	29.3	1.59
Stator tooth	0.777	62.7	0.141	446.2
Stator tooth-tip	0.488	26.7	0.015	1745
Total loss	-	136.0	-	-

The polygon-connected generator shows 7.6 % less total power loss in the stator material due to the connection method providing a better flux density distribution but the differences are less significant than for the 2/3rd current case.

4.7.4 Short-pitched Polygon-connected Generator

For the polygon-connected case, short-pitching the generator by three slots will offset the two phase windings that are carrying the peak current magnitude, leading to a reduction in peak flux density in the aligned position. The average flux through the generator core

material is more evenly distributed giving rise to 9.4 % lower core losses than the fully-pitched case.

Table 4.12: Core Loss for Aligned, Short-pitched, Polygon-connected Generator at 2/3rds Rated Current

	Flux Density (T)	Power Loss (W)	Mass (kg)	Core Loss (W/kg)
Stator back-iron	0.468	24.7	29.3	0.844
Stator tooth	0.584	37.1	0.141	263.5
Stator tooth-tip	0.344	14.1	0.015	921.2
Total loss	-	75.8	-	-

The data in *Table 4.12* shows the reduced core losses as a result of short-pitching the machine by 36°. Compared with the short-pitched star-connected generator in *Table 4.10*, there is a significant reduction in back-iron and stator tooth losses as a result of a lower flux density. The flux density waveforms for the star-connected and polygon-connected cases can be observed in *Figure 4.21* and *Figure 4.22*, respectively.

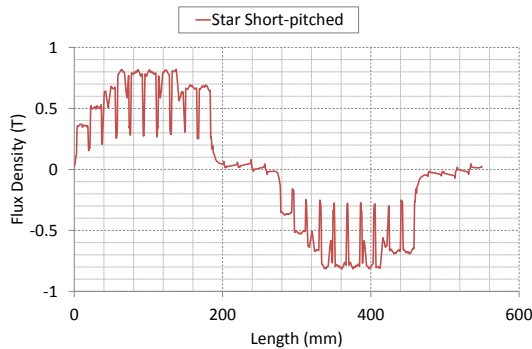


Figure 4.21: Short-pitched Star-connected Flux Density in Aligned Rotor Position

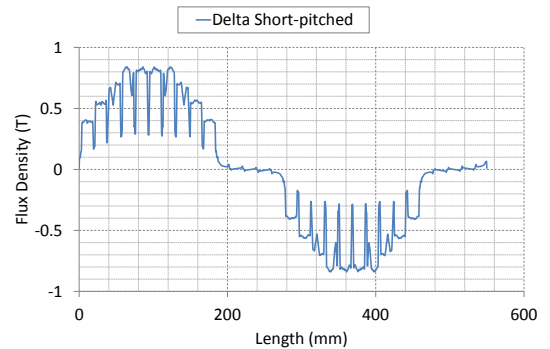


Figure 4.22: Short-pitched Polygon-connected Flux Density in Aligned Rotor Position

Again, the star-connected flux density shows the same peak flux across a number of slots. Both the star- and polygon-connection methods now exhibit a lower flux density at the stator slot than that observed in fully-pitched topology.

Table 4.13: Core Loss for Aligned, Short-pitched, Polygon-connected Generator at Rated Current

	Flux Density (T)	Power Loss (W)	Mass (kg)	Core Loss (W/kg)
Stator back-iron	0.643	44.3	29.3	1.52
Stator tooth	0.762	60.6	0.141	430.8
Stator tooth-tip	0.471	25.0	0.015	1634
Total loss	-	129.9	-	-

The short-pitched results in Table 4.13 shows a 4.5 % reduction in total core loss when compared with the fully-pitched case.

4.7.5 Core Loss Summary

Compiling all of the results into one table for comparison, Table 4.14 highlights the respective power loss magnitudes within the generator stator material dependent on the winding topology and the output connection method. The three-phase generator case is also included for completion.

Table 4.14: Comparison of Core Losses

		Star		Polygon	
		Fully-pitched	Short-pitched	Fully-pitched	Short-pitched
Three-phase 2/3 ^{ds}	(W)	207.937	203.573	162.416	138.971
Three-phase Rated	(W)	225.440	221.389	177.646	143.599
Five-phase 2/3 ^{ds}	(W)	105.688	100.191	83.666	75.828
Five-phase Rated	(W)	147.235	146.283	135.999	129.887

The fully- and short-pitched, polygon-connected generator have consistently lower core loss compared with the star-connection, approximately 19 % lower at rated current. Short-pitching the generator lowers the core losses but this is less obvious when the generator is operated toward its saturation region. The five-phase generator exhibits approximately half of the magnitude core losses when compared with the three-phase generator particularly in the lower current case.

4.7.6 Rotor Core Losses

The rotor is a complex geometric shape but, through the magnetic coupling, it will still have a loss component associated with it. The rotor is modelled using the same material as the stator and is laminated using the measured thickness of 0.64 mm. The rotor shaft is not

modelled as it is assumed that the laminations of the rotor make up the majority of the electromagnetic path. However, since the rotor is travelling at synchronous speed, it will not experience the same 50 Hz fundamental frequency component that contributes to the stator losses. The rotor has a DC component and some higher order harmonic components that exist as losses on the rotor surface. Due to the complex nature of these losses and the relatively small contribution to power loss, the rotor core losses are neglected.

4.8 Summary

The methods used in the design of electric machines have changed significantly with the proliferation of software programs capable of modelling their electromagnetic properties. This chapter has served to highlight some of the benefits of utilising FEA for the purposes of establishing the expected internal behaviour of the generator when extending beyond three-phases and quantifying core losses.

Consideration was made toward the software calculation, ensuring that the grouped coil method was acceptable for quantifying the flux linkage for the concentric winding featured in the three-phase generator. Methods for calculating the back-emf were also compared to verify the magnitudes calculated from the flux linkage given by FEA were consistent with the manufacturer's quoted generator output. Confirmation allowed the multiphase variants to be developed and modelled with confidence.

The inductance was found in all cases by considering the rated stator current and rotating the rotor through 360°. The results provided a sinusoidal flux linkage output which could be analysed to find the d- and q-axis inductances from the maxima and minima, respectively. The assumption made in the simulation modelling that inductances scaled by a factor of $3/m$ – when using the three-phase generator as a reference and ignoring end-winding effects – were proven to be correct as the phase number is increased. The assumption that saliency effects above the 2nd harmonic could be neglected has also been verified.

The harmonic content of the generator has been investigated, to establish the effect that short-pitching the double layer windings will have on the multiphase variants with particular attention paid to the 15-phase generator. The stator of the generator is fixed at 30 stator slots, therefore, for a 15-phase machine, each phase winding will take up one slot. It has been shown that short-pitching the generator can reduce the THD of the open-circuit back-emf developed by 4 % compared with the fully-pitched topology. The harmonic

content of the back-emf was determined from the FEA for use in the dynamic circuit model simulation in Section 3.4.

Further work has been carried out to investigate and quantify the iron losses within the generator when it is connected to an uncontrolled rectifier. The three- and five-phase generators were modelled to provide an understanding of what effects star- and polygon-connected generator topologies have on the power loss and how short-pitching also affects this. The results highlight a better utilisation of the generator when connected in a delta or polygon configuration.

This chapter has presented FEA of the connection method. The next chapter uses experimental testing to validate the modelling methods used. Further investigation into the system behaviour is considered and the optimal connection method for purposes of fault tolerance and DC ripple voltage is sought.

5

Experimental Testing

5.1	Introduction.....	127
5.2	Experimental Set-up and Chapter Structure.....	128
5.3	Comparison of Experimental and Simulation Results	130
5.4	Comparison of Fully- and Short-pitched Generators.....	142
5.5	Generator Loading Comparison	150
5.6	Comparison of Fault Tolerance in Star- and Polygon-connected Generators.....	158
5.7	Summary	172

5.1 Introduction

In order to validate the analysis and simulation performed in Chapter 3, experimental testing is conducted using the purpose-built test-rig. The multiphase synchronous generator has been wound to allow access to the stator coils, enabling the reconfiguration of phase number and, since it is a double layer winding, the pitching of the machine. Furthermore, the connection of the generator to the diode rectifier can be either a star- or polygon-connected configuration. This allows for the full appraisal of generator AC and output DC characteristics for a range of connection methods and machine topologies as phase number increases. The validation of the simulation model, through this testing, will allow it to be used to study applications that are beyond the limits of the test equipment, representative aircraft loads or 400 Hz operation, for example.

This chapter details the simulation model results which are compared with the experimental test results for selected normal operating and open-circuit fault cases in order to validate the model performance. Further experimental results are presented through the effects of generator pitching under normal operating conditions before analysis on the differences in loading conditions. Finally, the connection method ascertains the generator-rectifier behaviour under open-circuit fault conditions. Conclusions will be drawn about the performance of the generator and rectifier, including the accuracy of the simulation model.

5.2 Experimental Set-up and Chapter Structure

The experimental set-up is pictured in schematic form in *Figure 5.1* and further construction information can be found in Appendix 7.1. The test-rig DC drive machine armature was powered from a motor-generator set and a local DC power supply unit provided the rotor field voltage to control the speed. The multiphase synchronous generator, being a two-pole machine, required a synchronous speed of 3000 rpm, the DC motor being rated to provide the correct rotor speed. An emergency break switch was situated between the armatures of the two DC machines, removing the armature power source and allowing the DC motor to be stopped in the case of a field supply fault. The field for the synchronous generator was provided by another DC power supply unit, which replaced the AVR and was connected to the rotor through brushes and slip-rings. The stator winding output from the multiphase synchronous generator was brought out into an external cabinet where the diode rectifier was also situated. The winding connections were hard wired into a series of stud terminals, allowing the reconfiguration of the stator for different phase combinations, winding pitches and connection topologies. Cabinet wiring details can be found in Appendix 7.1.

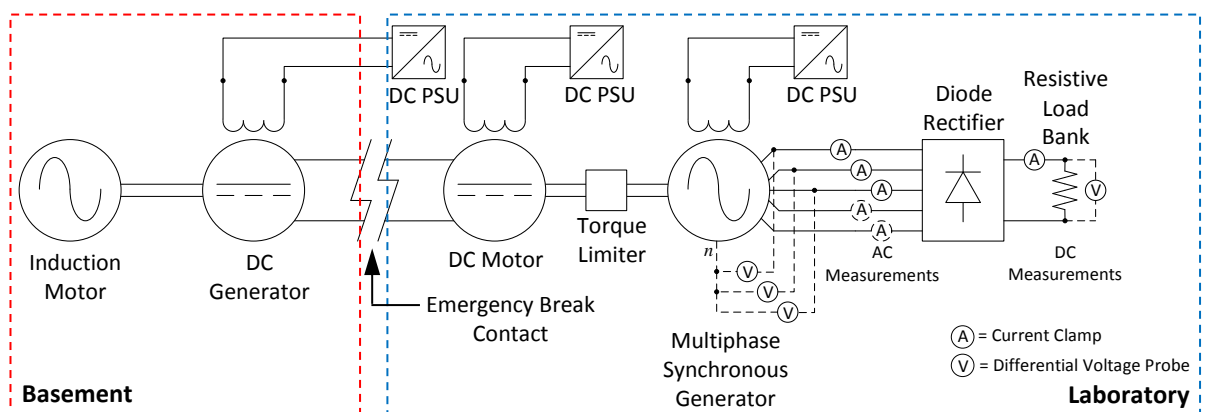


Figure 5.1: Experimental Test-rig Schematic Set-up

The diode rectifier used was an off-the-shelf three-phase bridge rectifier, rated to 60 A. Five of these units were used to provide 15-phase rectification. However, they were not the fast recovery type, which would have potentially provided better results in the experimental testing.

5.2.1 Loading the System

The generator used for testing was a rewound Cummins BCI162G wound-field synchronous generator, which was originally rated at 22.5 kVA. In the rewound machine the number of turns per coil was reduced from 8 to 7 due to the physical constraints of the stator slots limiting the number of turns that could fit into the slot. The field voltage was set to energise the rotor to provide the same magnetic field density as the original machine, giving a no-load phase voltage that was $7/8^{\text{th}}$ the original rated voltage of 220 V. Generator rating data are given in Appendix 7.5. The resistive load bank was configured to provide two different network loads. The first configuration was a $58\ \Omega$ fixed resistance in order to limit the current drawn from the machine and ascertain the generator performance in a lightly loaded state. The second configuration used the resistors in parallel to provide a minimum $5\ \Omega$ resistance, leading to a higher current drawn from the generator and increasing saturation in the stator. The effects that loading has on the generator-rectifier system are explored later in Section 5.5.

5.2.2 Notation for Diagrams

The results contained in this chapter are presented graphically for qualitative analysis. The notation used in labelling the phase quantities is shown in *Figure 5.2* and corresponds to the legends of the plots.

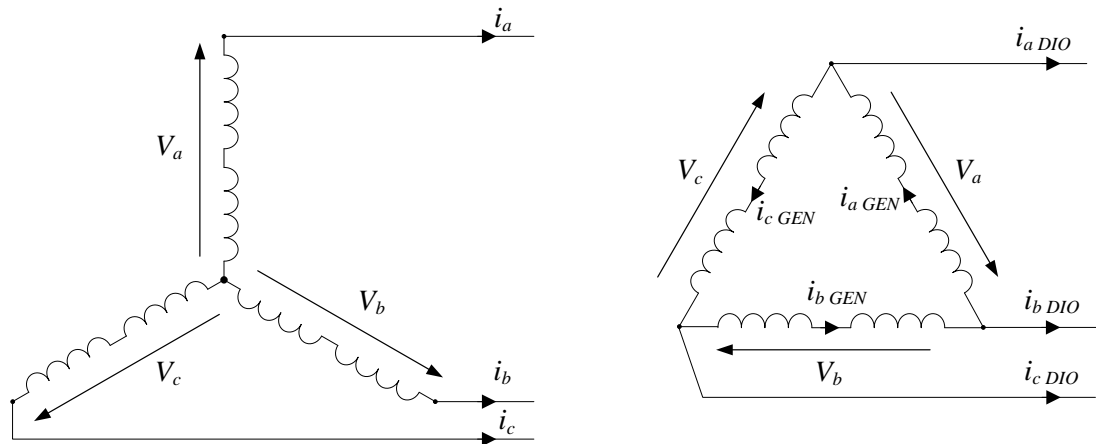


Figure 5.2: Star- and Polygon-connected Generator Notation

5.2.3 Structure of Chapter

Quantitative and qualitative analysis is performed through the comparison of magnitudes and waveform shapes on both the AC and DC side. The key measurements for the DC side are the average voltage level and the ripple magnitude. Fixed field current is used to observe the drop in DC voltage level for increased load conditions. For the AC side, the main quantitative measurement is the peak AC current and the effect that this has on the losses, explored in Chapter 3 and Chapter 4. Qualitative analysis is performed on the current sharing between phases, which will affect the de-rating under fault conditions and torque ripple production for non-balanced currents.

5.3 Comparison of Experimental and Simulation Results

The simulation model, from Chapter 3, has been configured with parameters based on data from open-circuit, slip, short-circuit, and fixed resistive load tests carried out on the three-phase generator, shown in Appendix 7.4. However, in order to fully validate the simulation results, the model must accurately represent the multiphase generator under normal operating and open-circuit fault conditions. The simulation results for the best and worst case generator-rectifier scenarios are compared and presented here. For completeness, tables of data in Appendix 7.8 detail the values of AC and DC quantities not shown graphically.

5.3.1 Three-phase Generator

For the three-phase generator, the simulation showed good agreement with the experimental results in a number of cases, but particularly when the generator was short-pitched to best approximate a sinusoidal output and minimise harmonic distortion. The short-pitched, star-connected generator is shown in *Figure 5.3* and *Figure 5.4* for the experimental and simulation results, respectively. The results displayed for the short-pitched, star-connected generator under light load and normal operating conditions show good agreement in terms of peak values and waveform shape.

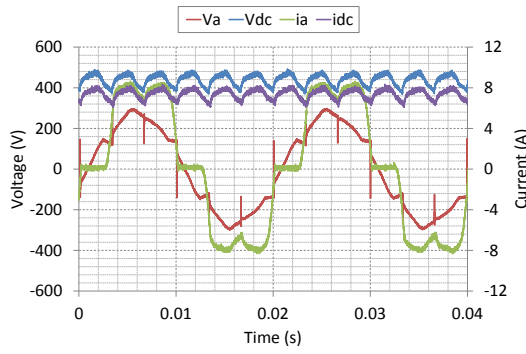


Figure 5.3: Experimental Three-phase Short-pitched Star-connected Generator AC and DC Voltage and Current 58 Ω Load

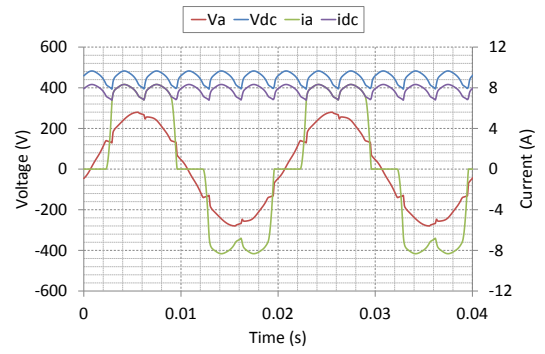


Figure 5.4: Simulated Three-phase Short-pitched Star-connected Generator AC and DC Voltage and Current 58 Ω Load

The fully-pitched generator tests the assumption of sinusoidally distributed windings that is made in the simulation as well as the harmonic voltage model estimation. However, as Figure 5.5 and Figure 5.6 show, the simulation and experimental results agree well, except for the AC voltage which exhibits a higher peak in the experimental results that is not present in the simulation results.

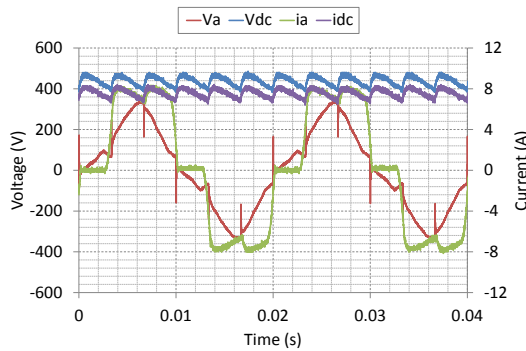


Figure 5.5: Experimental Three-phase Fully-pitched Star-connected Generator AC and DC Voltage and Current 58 Ω Load

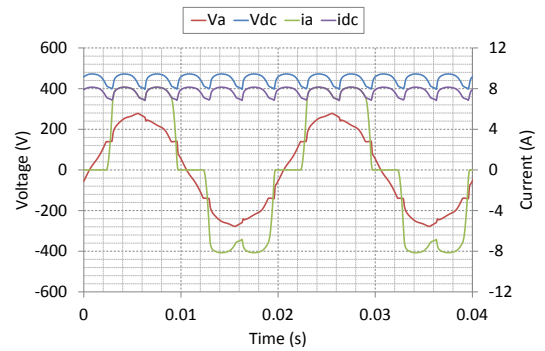


Figure 5.6: Simulated Three-phase Fully-pitched Star-connected Generator AC and DC Voltage and Current 58 Ω Load

Comparing the experimental and simulated results for the fully-pitched, delta-connected generator, displayed in Figure 5.7 and Figure 5.8, shows a good match for both AC and DC quantities, particularly in the peak magnitudes. The switching effects, in the form of commutation notching, are reflected in both the experimental and simulated voltage waveforms but the diode recovery effects are only visible in the experimental results, which is neglected in the simulated diodes. The AC generator current shows the presence of circulating third harmonic currents and their out-of-phase relationship with the fundamental waveform, correctly represented by the simulation. This is common in delta-connected transformers and machines, where the current created by the third-harmonic, for the three-phase case, does not flow into the line output. Instead, it remains in the windings, circulating with time as the connection topology acts as a current divider. The DC

side pk-pk voltage ripple is slightly overestimated in the simulation due to the AC voltage waveform having a less sinusoidal characteristic around its peak.

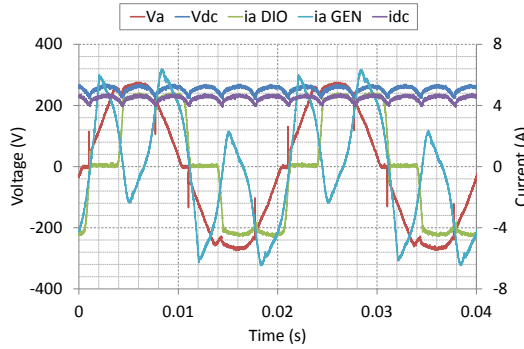


Figure 5.7: Experimental Three-phase Fully-pitched Delta-connected Generator AC and DC Voltage and Current 58 Ω Load

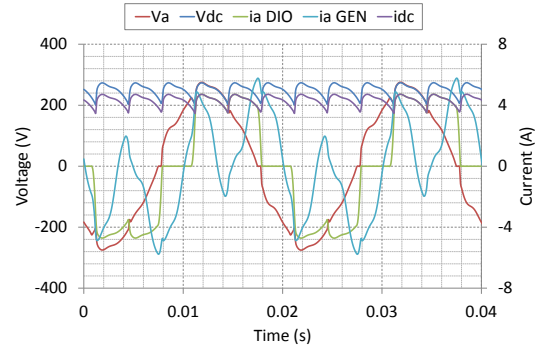


Figure 5.8: Simulated Three-phase Fully-pitched Delta-connected Generator AC and DC Voltage and Current 58 Ω Load

The peak values for both the fully-pitched star- and delta-connections are presented in Table 5.1 for comparison. The simulation results show a good match with the experimental results in both the star- and delta-connected configuration under normal operating conditions.

Table 5.1: Experimental and Simulated Results for Three-phase Fully-pitched Delta-connected Generator under Normal Operating Conditions with 58 Ω Load

		V_{AC} (V_{pk})	I_{DIO} (A_{pk})	I_{GEN} (A_{pk})	V_{dc} (V_{pk})	I_{dc} (A_{pk})	V_{DC} Ripple (% of AVG)
STAR	EXP	345.6	8.48	-	486.4	8.41	24.9
	SIM	277.9	8.14	-	472.1	8.14	16.7
DELTA	EXP	275.2	4.86	6.53	272.0	4.80	20.2
	SIM	276.1	4.74	5.78	274.6	4.73	29.1

The circulating harmonic currents that are observed in the experimental and simulated results for the fully-pitched, delta-connected generator are eliminated in the short-pitched generator, shown in Figure 5.9 and Figure 5.10.

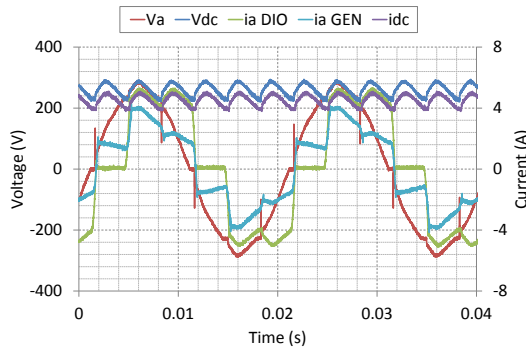


Figure 5.9: Experimental Three-phase Short-pitched Delta-connected Generator AC and DC Voltage and Current 58 Ω Load

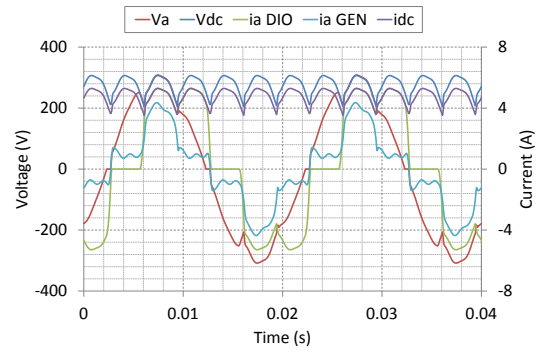


Figure 5.10: Simulated Three-phase Short-pitched Delta-connected Generator AC and DC Voltage and Current 58 Ω Load

Under normal operating conditions, the simulation has been shown to accurately portray the results observed from experimental testing. Investigating the open-circuit diode fault under high loading, the experimental results, depicted in Figure 5.11, show the effects of the third harmonic on the voltage waveform. This is not observed in the simulated star-connected system in Figure 5.12. However, the simulation still shows a good approximation of the AC current and DC side quantities. Taking an FFT of both voltage waveforms shows an 86 % lower third harmonic voltage content in the simulation.

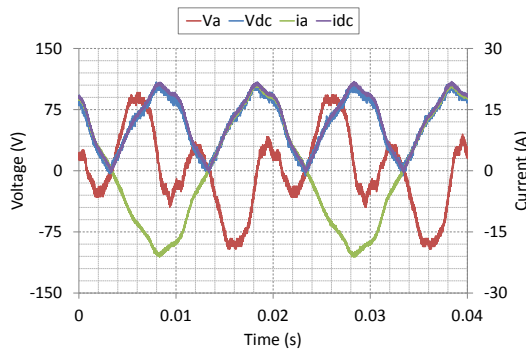


Figure 5.11: Experimental Three-phase Fully-pitched Star-connected Generator Open-circuit Diode Fault 5 Ω Load

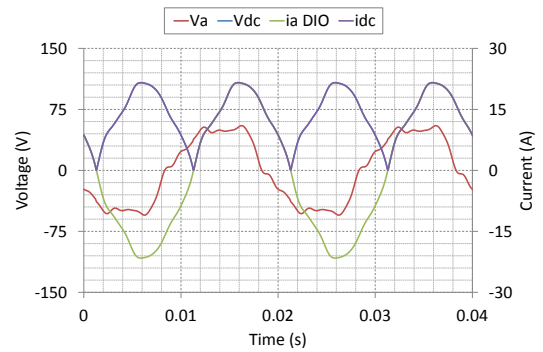


Figure 5.12: Simulated Three-phase Fully-pitched Star-connected Generator Open-circuit Diode Fault 5 Ω Load

Changing the connection topology to a delta configuration and retaining the diode device open-circuit fault, the simulation continues to offer a good approximation of the DC side experimental results, observed in Figure 5.13 and Figure 5.14.

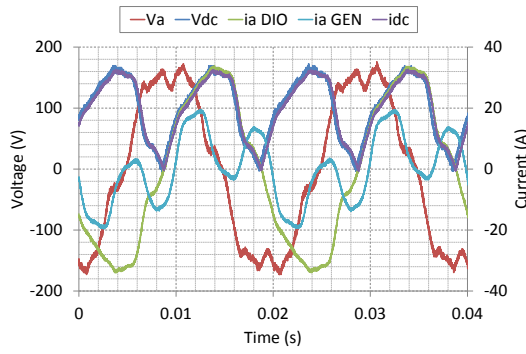


Figure 5.13: Experimental Three-phase Fully-pitched Delta-connected Generator Open-circuit Diode Fault 5 Ω Load

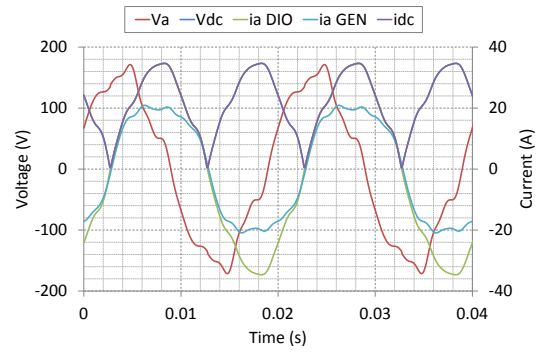


Figure 5.14: Simulated Three-phase Fully-pitched Delta-connected Generator Open-circuit Diode Fault 5 Ω Load

Under the open-circuit diode fault condition, the generator current drawn from the delta-connected machine differs between the experimental and the simulated results. The circulating third harmonic currents are expected in the fully-pitched winding as the generator is in a healthy state. They have been observed in the simulation of the fully-pitched, delta-connected generator under normal operating conditions. However, they are not being accounted for here.

Both of these star- and delta-connected cases highlight an area of the simulation that requires further development to accurately model the harmonic content present in the generator-rectifier system.

Table 5.2: Experimental and Simulated Results for Three-phase Fully-pitched Generator under Open-circuit Diode Fault with 5 Ω Load

		V_{AC}	I_{DIO}	I_{GEN}	V_{dc}	I_{dc}	V_{DC} Ripple
		(V_{pk})	(A_{pk})	(A_{pk})	(V_{pk})	(A_{pk})	(% of AVG)
STAR	EXP	95.996	21.439	-	105.596	21.311	143.02
	SIM	54.943	21.572	-	107.860	21.572	158.93
DELTA	EXP	175.993	33.919	19.519	172.793	32.799	178.70
	SIM	171.321	34.669	20.919	173.344	34.669	156.01

The comparison of data, presented in Table 5.2, shows that the simulation agrees with the peak AC current and DC quantities measured from the star-connected generator. However, the peak AC voltage is underestimated as a result of the missing third harmonic. The delta-connected generator peak values also match despite the circulating harmonics not being included.

5.3.2 Five-phase Generator

The five-phase generator model is set-up and described as per Chapter 3. Similar to the three-phase generator, the short-pitched machine simulated and experimental results showed good agreement in both waveform shape and peak magnitudes for both the star- and polygon-connected cases. The fully-pitched simulation results also show good agreement with the experimental results. However, there are some differences which are highlighted here.

Under normal operation, with a $58\ \Omega$ fixed resistive load on the DC output side, the AC and DC waveforms recorded from the experimental test-rig compare well with the simulation. This should be expected since the generator is not saturated and, as a result, the simulation retains the accuracy to model the lightly loaded case. For a polygon configuration, the AC voltage in *Figure 5.16* shows a slight offset in the zero period when compared with the experimental results of *Figure 5.15*.

The simulated AC generator current also presents a mismatch in the phase relationship with the fundamental waveform when compared with the experimental results due to the phase relationship of the harmonic content. The simulated AC generator current is overestimated, possibly due to inaccuracy in the leakage inductance value used in the simulation, which was derived from experimental testing. The presence of the fifth harmonic, in both the experimental and simulated results, signifies that the simulation is correctly accounting for the circulating harmonic currents that flow in a polygon-connected generator apart from a slight mismatch. This could be refined by changing the rotor angle which is applied in the d-q axis conversion.

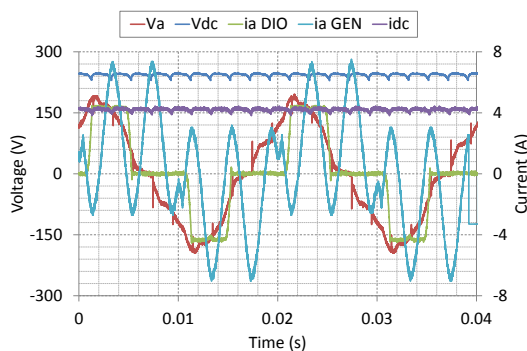


*Figure 5.15: Experimental Five-phase Fully-pitched Polygon-connected Generator
58 Ω Load*

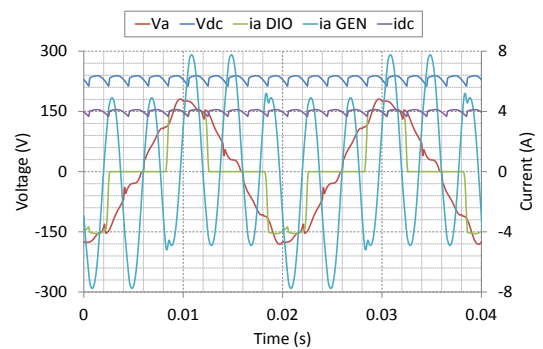


*Figure 5.16: Simulated Five-phase Fully-pitched Polygon-connected Generator
58 Ω Load*

The fully-pitched star-connected generator shows agreement in waveform shape between the experimental and simulated data in *Figure 5.17* and *Figure 5.18*, respectively. Observing

the DC side in particular, the ripple magnitude is greater and shows the commutation pattern more clearly than in the simulation. There is a 6.65 % difference in the average DC voltages, which follows from the lower peak voltage in the simulated results. There is also a difference in the AC voltages, with the simulated data showing the more typical fully-pitched behaviour, with the flatter peak previously seen in Chapter 4, suggesting the presence of out-of-phase third harmonic.

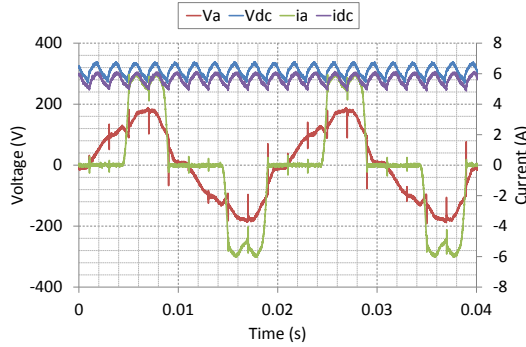


Figure 5.17: Experimental Five-phase Fully-pitched Star-connected Generator 58 Ω Load

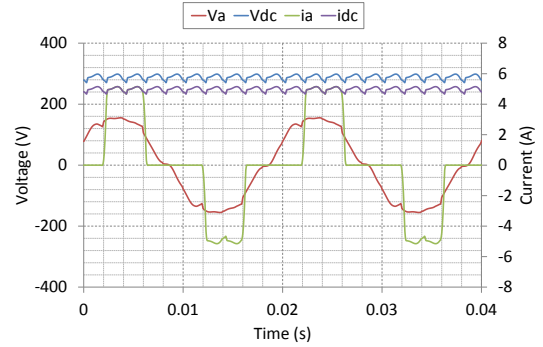


Figure 5.18: Simulated Five-phase Fully-pitched Star-connected Generator 58 Ω Load

The data for the normal operating conditions is shown in Table 5.3. The simulated waveform shapes show good approximation to the generator and rectifier behaviour. However, the numerical data highlights the differences.

Table 5.3: Experimental and Simulation Results for Five-phase Fully-pitched Generator under Normal Operating Conditions 58 Ω Load

		V_{AC}	I_{DIO}	I_{GEN}	V_{dc}	I_{dc}	V_{DC} Ripple
		(V_{pk})	(A_{pk})	(A_{pk})	(V_{pk})	(A_{pk})	(% of AVG)
STAR	EXP	188.793	6.008	-	339.187	6.144	22.76
	SIM	155.228	5.150	-	298.650	5.149	9.56
POLYGON	EXP	195.193	4.540	7.040	248.278	4.800	7.88
	SIM	180.663	4.117	7.743	238.775	4.117	10.88

In order to fully assess the five-phase generator-rectifier model, the open-circuit condition behaviour must be evaluated. The worst case scenario for the simulation is the fully-pitched, polygon-connected generator with an open-circuit phase fault and high DC current. The model must take into account the missing phase and accurately portray the dynamic system behaviour.

The polygon-connected generator experimental and simulated results are shown in Figure 5.19 and Figure 5.20, respectively. The peak AC values are well approximated by the

simulation and there is also a good prediction of DC voltage ripple. The AC voltages exhibit a similar shape, correctly predicting the second voltage spike. However, the simulation has a lower peak value, approximately 30 V lower, and a higher second voltage pulse measured. The key differences are in the waveform shapes of the current drawn from the generator and the diode line current. The AC generator current is shown to be constantly conducting but is not the case in the experimental results, whilst the diode line current shows no overlap in phases in the simulation results.

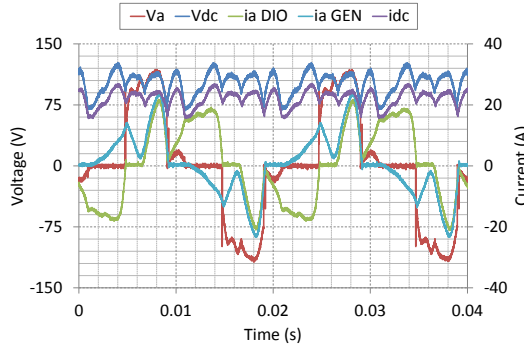


Figure 5.19: Experimental Five-phase Fully-pitched Polygon-connected Generator Open-circuit Phase Fault 5 Ω Load

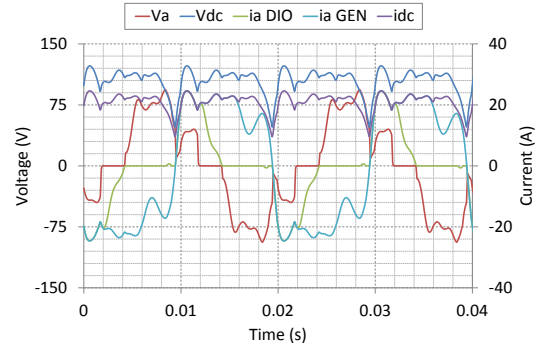


Figure 5.20: Simulated Five-phase Fully-pitched Polygon-connected Generator Open-circuit Phase Fault 5 Ω Load

The star-connected generator shows a greater degree of accuracy on the AC side in Figure 5.21 and Figure 5.22. However, the AC voltage is still inconsistent between the experimental and simulated results but shows some of the key traits, indicative of a difference in the harmonic content due to the rectifier. The DC side comparison shows a good match in the dynamic behaviour but as the voltage is more stable in the simulation, the pk-pk ripple is much lower, around half that measured in the experimental testing, displayed in Table 5.4.

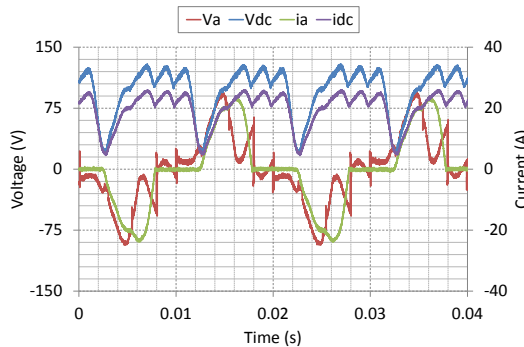


Figure 5.21: Experimental Five-phase Fully-pitched Star-connected Generator Open-circuit Phase Fault 5 Ω Load

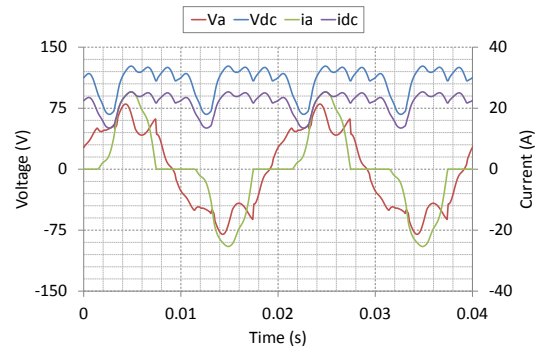


Figure 5.22: Simulated Five-phase Fully-pitched Star-connected Generator Open-circuit Phase Fault 5 Ω Load

Table 5.4: Experimental and Simulated Results for Five-phase Fully-pitched Generator under Open-circuit Phase Fault with 5 Ω Load

		V_{AC} (V_{pk})	I_{DIO} (A_{pk})	I_{GEN} (A_{pk})	V_{dc} (V_{pk})	I_{dc} (A_{pk})	V_{DC} Ripple (% of AVG)
STAR	EXP	94.4	23.6	-	129.6	26.0	115.3
	SIM	80.1	25.4	-	126.8	25.4	54.5
POLYGON	EXP	118.4	21.8	23.8	126.4	27.1	58.1
	SIM	93.9	24.6	24.6	123.0	24.6	72.3

5.3.3 15-phase Generator

Compared with the three- and five-phase simulation models, the 15-phase model was the most computationally intensive in terms of simulation time, in particular under fault conditions, due to the high number of diode switching devices, 30 in total, requiring a reduced time step. Because of the small differences between phase voltages, parasitic effects in the experimental test-rig such as connection resistances and small changes in inductances can alter the way that the rectifier behaves. The simulation model is, therefore, expected to provide a more ideal picture of the way that the generator responds under normal operation and open-circuit fault conditions.

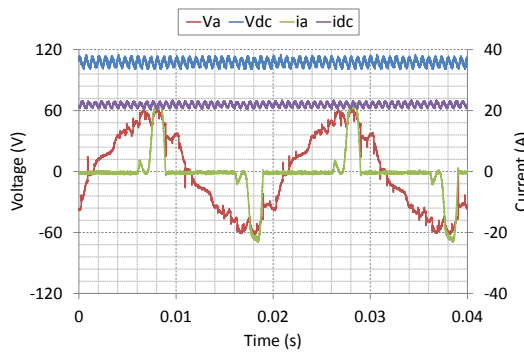


Figure 5.23: Experimental 15-phase Short-pitched Star-connected Generator AC and DC Voltage and Current 5 Ω Load

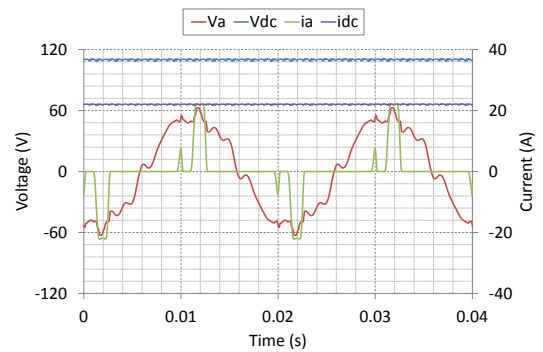


Figure 5.24: Simulated 15-phase Short-pitched Star-connected Generator AC and DC Voltage and Current 5 Ω Load

The short-pitched generator has the best match between experimental and simulated results, shown in Figure 5.23 and Figure 5.24, respectively. The AC voltage shows a good prediction of the waveform shape and peak magnitude. The AC current also shows a good match with the simulation through the peak magnitude and the inclusion of the two conduction periods. There is a less good match for the DC values in terms of pk-pk ripple, detailed in Table 5.5.

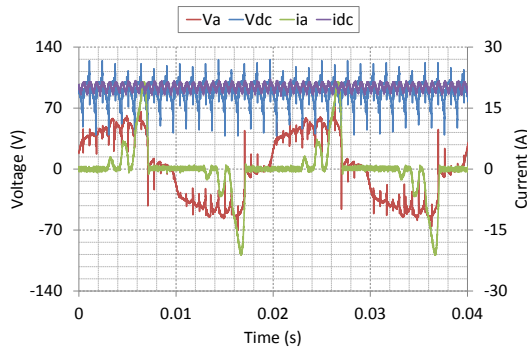


Figure 5.25: Experimental 15-phase Fully-pitched Star-connected Generator AC and DC Voltage and Current 5 Ω Load

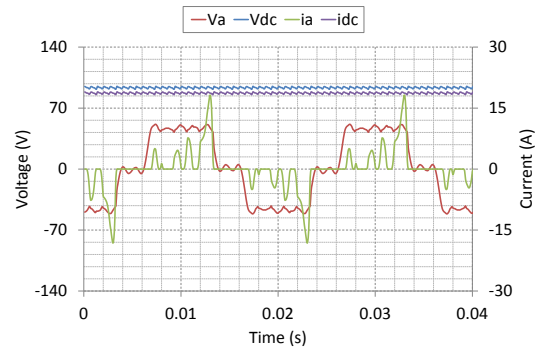


Figure 5.26: Simulated 15-phase Fully-pitched Star-connected Generator AC and DC Voltage and Current 5 Ω Load

The higher loading case for the normal operation of the 15-phase, fully-pitched, star-connected generator highlights the continuation of the trends between simulation prediction and experimental results. The AC characteristics show good matches between result sets in both peak magnitudes and the trend in current conduction pulses, observed in Figure 5.25 and Figure 5.26. The average DC values are also closely approximated.

Differences exist between what can be achieved in a physical system and what is expected from simulation results. The experimental results show the switching effects reflected in the AC and DC voltage waveforms. This causes considerable distortion to the pk-pk values presented in Table 5.5. The AC current can be observed to have multiple conduction periods, which indicates a number of diodes conducting simultaneously and reduces the overall peak magnitude of the current drawn from the generator. The simulation shows a more ideal AC voltage waveform which results in there being more phases conducting simultaneously over the period. The DC voltage is particularly interesting, showing a ripple frequency of 750 Hz instead of the expected 1.5 kHz. This may be caused by the overlapping in the line-to-line voltage providing little to differentiate between the phases. The commutation takes place based on the differences in these voltages; therefore, such a high degree of overlap will cause the diodes to remain in their on-states for a longer period.

Table 5.5: Fully-pitched and Short-pitched Star-connected Generator Experimental and Simulated Results for 5 Ω Load

		V_{AC} (V_{pk})	I_{DIO} (A_{pk})	I_{GEN} (A_{pk})	V_{dc} (V_{pk})	I_{dc} (A_{pk})	V_{DC} Ripple (% of AVG)
Fully-	EXP	67.8	22.1	-	125.6	20.9	99.9* (26.7)
Pitched	SIM	51.4	18.2	-	94.8	18.9	3.39
Short-	EXP	62.7	23.3	-	107.3	23.5	14.9
pitched	SIM	62.9	22.2	-	111.4	22.3	2.82

* = pk-pk ripple value is affected by the switching transients, () = Filtered value

Changing the connection topology, the polygon-connected generator shows good consistency between the experimental, *Figure 5.27*, and simulated results, *Figure 5.28*. The AC and DC side results show a good match, with the improved pk-pk voltage ripple magnitude that is expected for a high phase number machine.

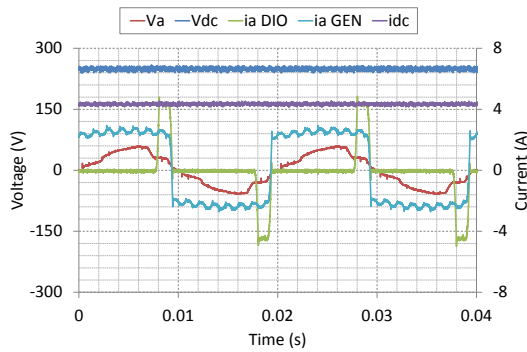


Figure 5.27: Experimental 15-phase Short-pitched Polygon-connected Generator AC and DC Voltage and Current 58 Ω Load

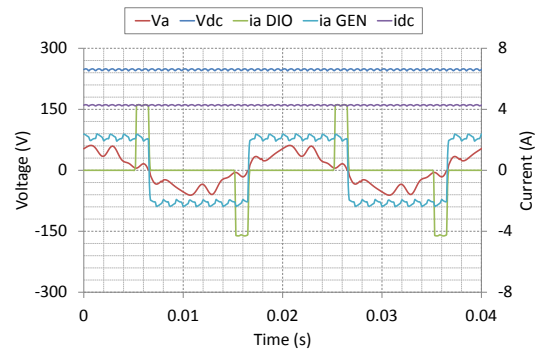


Figure 5.28: Simulated 15-phase Short-pitched Polygon-connected Generator AC and DC Voltage and Current 58 Ω Load

Introducing an open-circuit phase fault to the Polygon-connected generator yields the results shown in *Figure 5.29* and *Figure 5.30*.

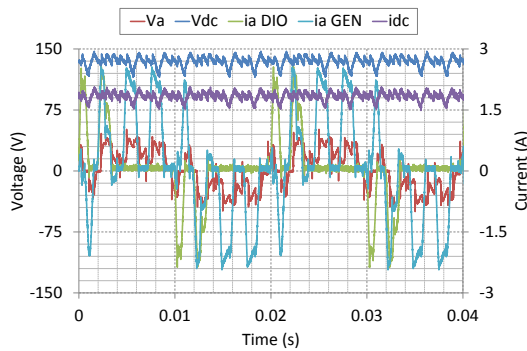


Figure 5.29: Experimental 15-phase Short-pitched Polygon-connected Generator Open-circuit Phase Fault 58 Ω Load

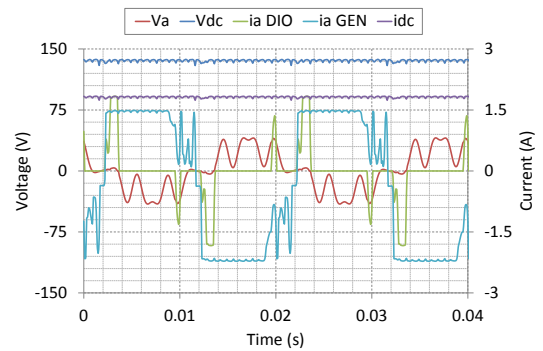


Figure 5.30: Simulated 15-phase Short-pitched Polygon-connected Generator Open-circuit Phase Fault 58 Ω Load

The AC voltage is closely approximated by simulation, showing the same peak magnitude and trend with the formation of the diode current also showing the correct traits but with some variation in peak value. The average DC voltage is a good match. The parasitic effects present in the experimental results, through the external connections of the generator, provide enough of an effect on the small variations in the AC voltages to change the order in which the diodes switch. The DC output is adversely affected as a result, showing considerable distortion. This underlines the complex switching pattern across the healthy phases as a result of the small variations in differential voltages. The simulation assumes that the path to each diode leg is the same and, therefore, switching takes place on a formulaic basis. This is highlighted by the DC voltage and current, which show the expected two events per cycle in the presence of a generator single phase open-circuit fault. The data for the experimental and simulated results is presented in *Table 5.6*.

Table 5.6: Short-pitched Polygon-connected Generator Experimental and Simulated Results for Normal Operation and Open-circuit Phase Fault Conditions for 58 Ω Load

		V_{AC} (V_{pk})	I_{DIO} (A_{pk})	I_{GEN} (A_{pk})	V_{dc} (V_{pk})	I_{dc} (A_{pk})	V_{DC} Ripple (% of AVG)
Normal	EXP	59.5	5.17	2.91	259.2	4.61	7.70
	SIM	61.1	2.37	2.37	249.5	4.30	2.06
Gen O/C	EXP	51.2	2.56	2.59	147.2	2.06	23.8
	SIM	40.6	1.49	1.49	137.2	1.84	5.57

5.3.4 Summary of Comparison of Experimental and Simulation Results

The comparison of experimental and simulation results highlighted the performance of the simulation model for selected best and worst case scenarios. The simulation assumes that the magnetic circuits in the dynamic circuit model are linear and that no saturation occurs. It also assumes that all winding resistances are equal and that diode devices are identical. Commutation will therefore take place between adjacent phases based on the voltage differentials being equivalent between each set of phases. Experimental testing has shown that this is not always valid. However, with the inclusion of harmonic modelling, particularly under normal operating conditions, the simulation model has shown, visually and quantitatively, accurate representation of the experimental system.

The simulation showed that for short-pitched, lightly loaded, cases it could accurately predict the system behaviour for the three-, five- and 15-phases under normal operating conditions, allowing it to be used in future study to investigate any number of phases. For the fully-pitched generator, simulating the generator with this winding configuration poses significant challenges since most dynamic circuit modelling is carried out under the assumption that the windings are sinusoidally distributed. The simulation demonstrated validity for waveform shape but under the higher load conditions showed some loss of accuracy in numerical data, highlighted in *Table 5.2* to *Table 5.5*.

The experimental testing of the polygon-connected generator showed the presence of circulating harmonic currents in the winding, which was also observed in the simulation for healthy cases. However, the phase relationship for the harmonic content in the simulation was not accurate. Under diode fault conditions, the simulated polygon-connection didn't account for the harmonic content present in the healthy generator.

The simulation doesn't always accurately predict the diode commutation, particularly for the higher phase, fully-pitched generator cases. However, the average DC voltage and current levels are well approximated. These selected cases show areas where assumptions made in the dynamic circuit modelling of the multiphase generator-rectifier system is suitable and where further research is required to improve the model with accurate harmonic information, for example.

5.4 Comparison of Fully- and Short-pitched Generators

5.4.1 Introduction

As stated in Chapter 4, the generator can be short-pitched to minimise total harmonic distortion in the back-emf generated. The short-pitching has been considered to improve the performance of the generator through the removal of harmonics. However, the fully-pitched generator is also considered to assess the performance of the AC side – when it is less sinusoidal – and the resultant effects on the DC ripple.

The fully-pitched generator has the coils of the same phase located above each other in the double layer slots, resulting in a particularly concentrated circumferential current density distribution around the stator, as seen in *Figure 5.31* and *Figure 5.32*. This will impact the back-emf developed since the winding is concentrated around that area, leading to a greater interval of zero change in flux linking the phase winding.

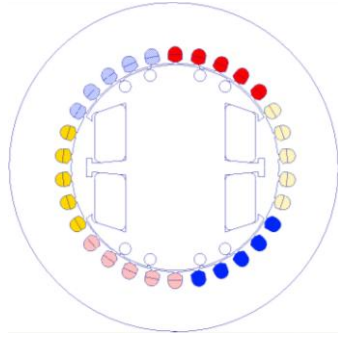


Figure 5.31: Fully-pitched Stator Topology

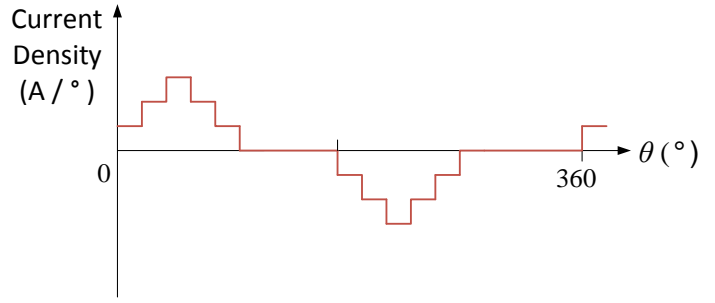


Figure 5.32: Current Density Distribution in a Fully-pitched Winding

The short-pitching of the coils in the machine can be seen in Figure 5.33 with an example of the current density distribution developed shown in Figure 5.34. It is clear that in comparison to the fully-pitched topology, the current density distribution around the stator is more sinusoidal in nature with a greater circumferential span and a shorter zero period as the rotor approaches 180°.

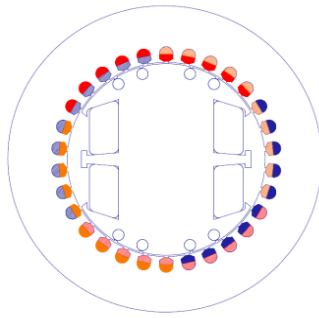


Figure 5.33: Short-pitched Stator Topology

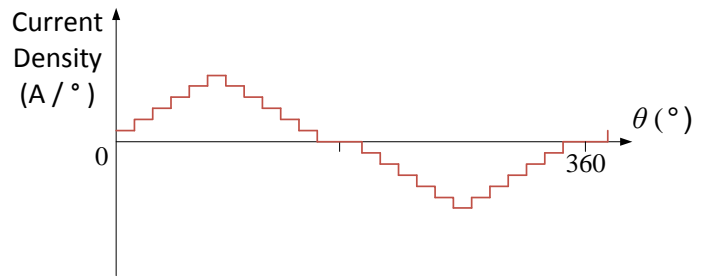


Figure 5.34: Current Density Distribution in a Short-pitched Winding

In this section, the fully-pitched generator is compared against the short-pitched generator topology to ascertain the potential benefits to the star- or polygon-connection type. The comparison is performed for the healthy generator case only. The mechanical pitching of the windings does not offer significant benefits in reducing the impact of open-circuit fault conditions, however, testing has been carried out for both topologies and results are contained in Section 5.6 and Appendix 7.9. The example shows the three-phase generator short-pitched by 60°. The short-pitching for the five- and 15-phase machines is detailed in Chapter 4.

5.4.2 Three-phase Generator

The fully-pitched three-phase generator is configured with both phase coil sets aligned in the double layer winding across five stator slots, as depicted in Figure 5.31. Short-pitching by 60° mechanical provides cancellation of the third harmonic, which presents significant

distortion to the back-emf in the fully-pitched case. The results for the three-phase, star-connected generator are shown in *Figure 5.35* (FP) and *Figure 5.36* (SP).

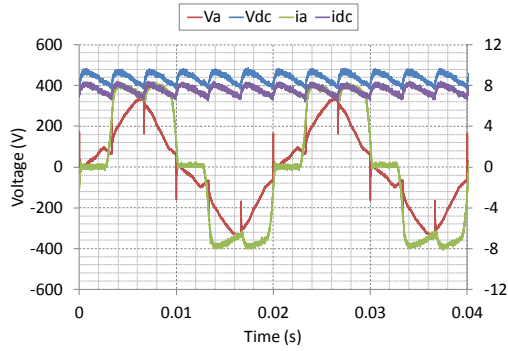


Figure 5.35: Three-phase Fully-pitched Star-connected AC and DC Voltage and Current 58 Ω Load

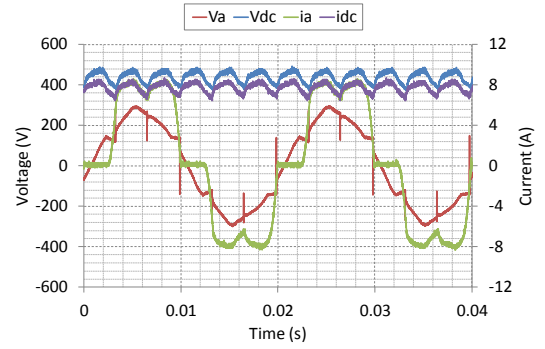


Figure 5.36: Three-phase Short-pitched Star-connected AC and DC Voltage and Current 58 Ω Load

The AC phase voltage, in *Figure 5.35*, shows a sinusoidal approximation with a high peak distorted by commutation notching and short-transient diode switching events. The AC current drawn from the generator, and the DC ripple following the commutation waveform, is typical for a resistive load connected to the rectifier [48].

The short-pitched generator, shown in *Figure 5.36*, is similar to the performance of the fully-pitched generator observed in *Figure 5.35*. The AC voltage shows a lower peak value as a result of the better sinusoidal output. The AC current is comparable and the DC side demonstrates the commutation pattern in the DC ripple that is discussed in Section 3.5.3. The effects of pitching are numerically displayed in *Table 5.7*, which highlights the difference in behaviour for the same fixed resistive load value. The peak AC voltage in the fully-pitched generator has been observed to be approximately 50 V higher for the same flux density. However, the lower AC voltage in the short-pitched machine provides a higher peak DC voltage. The current drawn from both winding topologies is comparable.

Table 5.7: Three-phase Star-connected Fully- and Short-pitched Normal Operating Conditions

		V_{AC} (V_{pk})	i_{AC} (A_{pk})	V_{DC} (V_{pk})	i_{DC} (A_{pk})	V_{DC} (V_{pk-pk})	V_{DC} Ripple (% of AVG)
Fully-pitched	58 Ω	345.6	8.48	486.4	8.41	108.8	24.9
Short-pitched	58 Ω	297.6	8.32	492.8	8.34	121.6	27.7

The delta-connected generator shows a significant performance increase from short-pitching the generator windings, as observed in *Figure 5.37* and *Figure 5.38*.

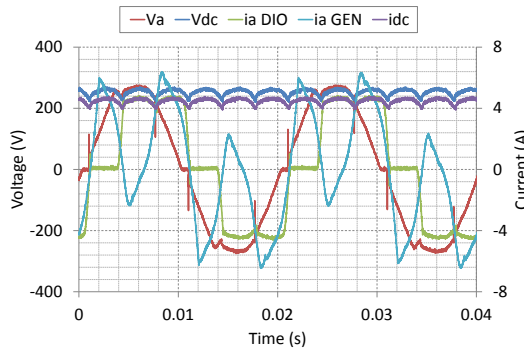


Figure 5.37: Three-phase Fully-pitched Delta-connected AC and DC Voltage and Current
58 Ω Load

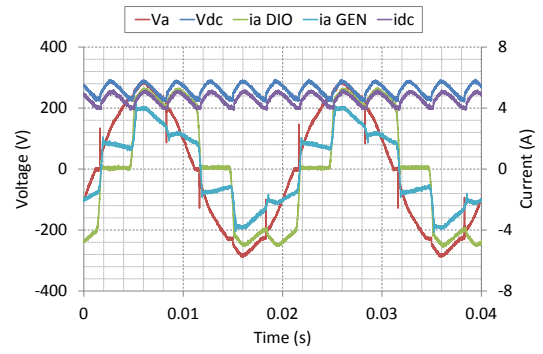


Figure 5.38: Three-phase Short-pitched Delta-connected AC and DC Voltage and Current
58 Ω Load

The fully-pitched winding topology shows third harmonic currents circulating in the delta-connected generator windings that are not transferred to the diode line current. This is cancelled by short-pitching the stator windings. However, the generator current now approximates the six-step waveform expected from Chapter 3 as a result of the diode rectifier connected to the output terminals.

Table 5.8: Three-phase Delta-connected Fully- and Short-pitched Normal Operating Conditions

		V_{AC} (V_{pk})	i_{AC} (A_{pk})	V_{DC} (V_{pk})	i_{DC} (A_{pk})	V_{DC} (V_{pk-pk})	V_{DC} Ripple (% of AVG)
Fully-pitched	58 Ω	275.2	6.40	272.0	4.78	51.2	20.2
Short-pitched	58 Ω	291.2	4.35	294.4	5.09	73.6	28.2

N.B.: i_{AC} refers to the current drawn from the generator, in the delta-connected this is the AC generator current $i_a GEN$

The results in Table 5.8 show that the short-pitched windings provide a better performance on the AC side of the generator-rectifier system. The peak generator current is much lower as a result of cancelling the circulating third harmonic current. However, the less smooth AC voltage gives a greater peak DC voltage but also a larger pk-pk ripple magnitude.

5.4.3 Five-phase Generator

The fully-pitched topology remains the same as that of the three-phase variant. However, instead of having a phase band that spans five stator slots, the phase band now spans three stator slots. The air-gap current density distribution is circumferentially shorter than the three-phase generator and, as a result, the phase voltages have increased periods where zero back-emf is developed at the terminals.

Short-pitching the generator by 36° gives a greater circumferential span of the stator, reducing the periods of zero back-emf developed at the generator terminals, leading to an improved generator performance through the minimisation of THD, as seen in Chapter 4. This results in a reduction in losses.

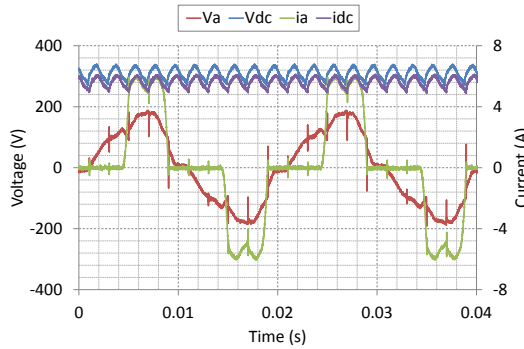


Figure 5.39: Five-phase Fully-pitched Star-connected AC and DC Voltage and Current $58\ \Omega$ Load

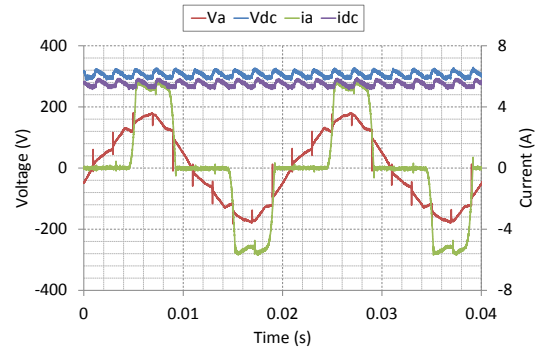


Figure 5.40: Five-phase Short-pitched Star-connected AC and DC Voltage and Current $58\ \Omega$ Load

The AC voltage and current waveforms of Figure 5.39 show the same trends as for the five-phase, fully-pitched, star-connected generator as the three-phase analysis and results. The peak AC voltage has reduced from approximately 330 V to around 200 V, which equates to the $3/5^{\text{th}}$ scaling expected from the reduction in coils per phase. The notching effects and zero back-emf periods are clearly visible as are the switching transient spikes.

Short-pitching the generator, shown in Figure 5.40, improves the AC voltage to the same extent as the three-phase generator, providing a more sinusoidal output. The peak AC current is lower than the fully-pitched generator and the average DC current is reduced also. However, unlike the three-phase case, the ripple magnitude as a percentage of the average is also lower at nearly half of the fully-pitched value. Full results are contained in Table 5.9.

Table 5.9: Five-phase Star-connected Fully- and Short-pitched Normal Operating Conditions

		V_{AC} (V_{pk})	i_{AC} (A_{pk})	V_{DC} (V_{pk})	i_{DC} (A_{pk})	V_{DC} (V_{pk-pk})	V_{DC} Ripple (% of AVG)
Fully-pitched	$58\ \Omega$	188.8	6.01	339.2	5.94	70.4	22.8
Short-pitched	$58\ \Omega$	180.8	5.76	329.6	5.76	41.6	13.6

Observing the fully-pitched, polygon-connected generator, shown in Figure 5.41, the AC voltage shows a good sinusoidal shape and the diode current is as expected. However, the generator current is distorted by circulating fifth harmonic currents which will contribute to

the losses within the generator. The DC side quantities show low ripple and compare well with the short-pitched case presented in *Figure 5.42*.

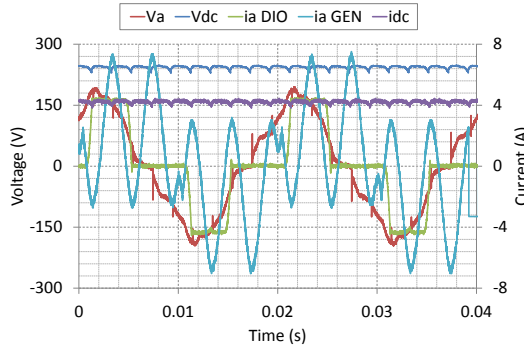


Figure 5.41: Five-phase Fully-pitched Polygon-connected AC and DC Voltage and Current 58 Ω Load

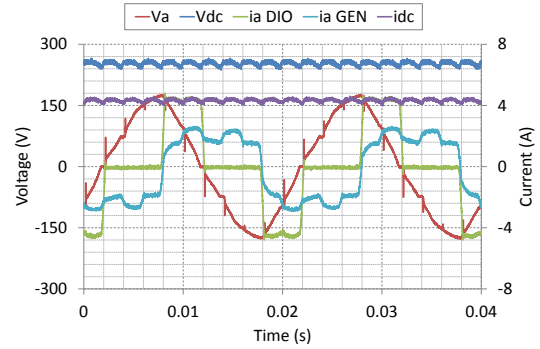


Figure 5.42: Five-phase Short-pitched Polygon-connected AC and DC Voltage and Current 58 Ω Load

For the short-pitched generator, the AC voltage, shown in *Figure 5.42*, is similar to that developed by the fully-pitched winding but shows a much smoother waveform shape, indicating that the short-pitched windings are providing harmonic cancellation of the flux linking the stator windings. The diode current and the current drawn from the generator exhibit expected behaviour, with a much lower peak current drawn from the generator than that of the fully-pitched topology.

The comparison of the change in winding topology is presented in *Table 5.10*, which highlights the key differences between the two pitch factors.

Table 5.10: Five-phase Polygon-connected Fully- and Short-pitched Normal Operating Conditions

		V_{AC}	i_{AC}	V_{DC}	i_{DC}	V_{DC}	V_{DC} Ripple
		(V_{pk})	(A_{pk})	(V_{pk})	(A_{pk})	(V_{pk-pk})	(% of AVG)
Fully-pitched	58 Ω	195.2	7.04	248.3	4.45	19.2	7.89
Short-pitched	58 Ω	177.6	3.71	265.6	4.61	28.8	11.4

Comparing with the three-phase generator case, similar results are observed for the polygon-connected generator. The peak AC current drawn from the generator is significantly reduced through short-pitching of the windings. However, the pk-pk ripple deteriorates, showing a much greater voltage differential on the DC side.

5.4.4 15-phase Generator

The fully-pitched generator topology is similar for the 15-phase generator as that of the three- and five-phase generators except there is now only one coil per phase band. The phase coils for the double layer winding are located in the same slot. Since the maximum

phase number has been achieved for this 30 stator slot generator, one phase resides in two slots spanning 180° mechanical, i.e. phase a will be located in slots 1 and 16.

Under normal operating conditions, the 15-phase, star-connected generator AC behaviour follows the trend of the three- and five-phase results for the $58\ \Omega$ resistance value, shown in *Figure 5.43*. The AC phase voltage shows a rough sinusoidal approximation with distinct periods of zero back-emf being generated at the terminals. The AC current drawn from the generator is a quasi-square-wave with a high harmonic distortion due to the non-linear load, affecting the copper losses in the generator. The DC side shows a much improved ripple characteristic, exhibiting a low pk-pk ripple magnitude and minimal switching transient behaviour.

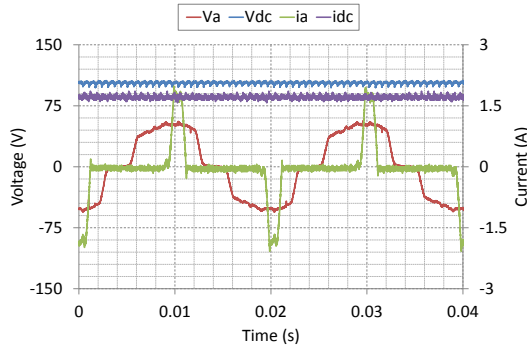


Figure 5.43: 15-phase Fully-pitched Star-connected AC and DC Voltage and Current $58\ \Omega$ Load

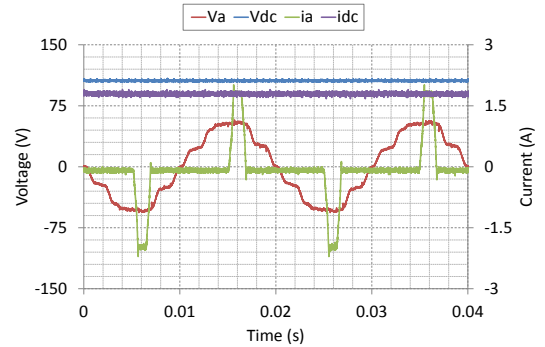


Figure 5.44: 15-phase Short-pitched Star-connected AC and DC Voltage and Current $58\ \Omega$ Load

The 15-phase short-pitched generator, shown in *Figure 5.44*, offers the same performance increase as the three- and five-phase generator topologies. The short-pitching at 36° mechanical provided minimum THD and, therefore, a more sinusoidal back-emf, as highlighted in Section 4.6.1. An improvement in AC voltage can be observed, reducing the zero back-emf period and producing a better sinusoidal approximation. The AC current remains quasi-square-wave and the peak is higher, giving an increased peak DC current and, since the ripple is reduced with phase number, a higher average value. The DC voltage ripple magnitude is greatly reduced as a result of the generator short-pitching, to around half of that achieved in the fully-pitched winding topology, highlighted in *Table 5.11*.

Table 5.11: 15-phase Star-connected Fully- and Short-pitched Normal Operating Conditions

		V_{AC} (V_{pk})	i_{AC} (A_{pk})	V_{DC} (V_{pk})	i_{DC} (A_{pk})	V_{DC} (V_{pk-pk})	V_{DC} Ripple (% of AVG)
Fully-pitched	58 Ω	56.9	1.98	106.1	1.86	8.96	8.72
Short-pitched	58 Ω	57.2	2.21	108.9	1.89	5.12	4.84

The polygon-connected generator shows the same low AC voltage as a result of the reduction in coils per phase. It has been observed that the three- and five-phase, fully-pitched topologies have both suffered from harmonic distortion in the generator current. However, the AC current drawn from the generator shows the typical 15-phase ripple that is expected for a polygon-connection.

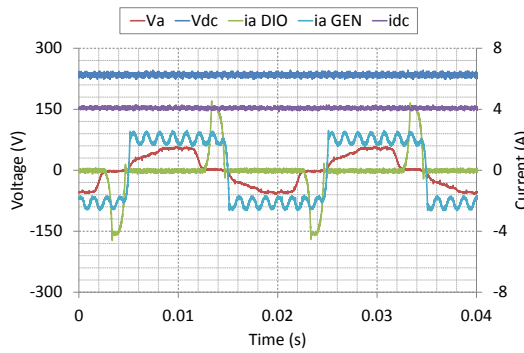


Figure 5.45: 15-phase Fully-pitched Polygon-connected AC and DC Voltage and Current
58 Ω Load

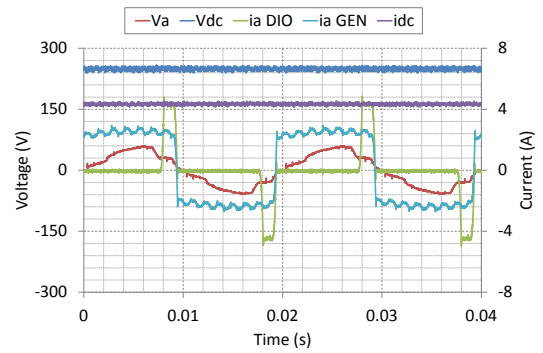


Figure 5.46: 15-phase Short-pitched Polygon-connected AC and DC Voltage and Current
58 Ω Load

The short-pitched results, depicted in Figure 5.46, show a slightly higher peak AC generator current with a reduced ripple. The current sharing in the windings of the short-pitched generator gives a smaller difference in the current magnitudes, resulting in a reduced AC current ripple. This also provides a better square-wave approximation diode current, giving a higher peak DC current value and a better DC side ripple quality, underlined in Table 5.12.

Table 5.12: 15-phase Polygon-connected Fully- and Short-pitched Normal Operating Conditions

		V_{AC} (V_{pk})	i_{AC} (A_{pk})	V_{DC} (V_{pk})	i_{DC} (A_{pk})	V_{DC} (V_{pk-pk})	V_{DC} Ripple (% of AVG)
Fully-pitched	58 Ω	58.2	2.61	246.4	4.29	22.4	9.52
Short-pitched	58 Ω	59.5	2.91	259.2	4.54	19.2	7.70

5.4.5 Summary of Comparison of Fully- and Short-pitched Generators

The three-, five- and 15-phase generator have been shown to demonstrate differences in AC and DC performance when the stator windings are short-pitched under normal operating conditions. Short-pitching the generator draws a lower AC current for the three- and five-phase machines. However, the DC ripple magnitude is reduced by utilising a fully-pitched winding in the lower phase number machines. The 15-phase generator exhibits the inverse of this behaviour, drawing a higher peak AC current for the short-pitched winding but a lower DC ripple for the fully-pitched topology.

Under short-pitching, the polygon-connected machine shows a reduced AC current ripple due to the current distribution in the windings providing a lower harmonic content. The reduction of circulating harmonic currents in the polygon configuration in lower phase number machines is particularly important.

The pitching has, therefore, demonstrated that for the 15-phase generator, short-pitching of the stator windings is considerably beneficial in the reduction of DC side ripple voltage. For the removal of filter capacitance that is necessary in three-phase systems, this is a critical step. However, further consideration should be made toward the pitch factor to ensure that lower order harmonics are not present in the case of a faulted system.

5.5 Generator Loading Comparison

5.5.1 Introduction

The previous section compared the fully- and short-pitched winding topologies and the effects that they have on the generator behaviour as the phase number increases. The loading was restricted to 58Ω , which allowed the generator characteristics to be observed without saturation effects. This section explores the effects that a change in load has on the behaviour of the system.

The nominal loading for an increase in generator phase number can be seen in *Table 5.13*, which includes information from the rectifier analysis carried out in Section 3.5.3. The table shows the difference that the loading is expected to have on the connection topology as the phase number increases.

Table 5.13: Loading of the Generator-Rectifier System

		Three-phase		Five-phase		15-phase	
		Star	Delta	Star	Polygon	Star	Polygon
No-load AC Voltage (V)		192.5	192.5	115.5	115.5	38.5	38.5
AVG No-load Rectifier DC Voltage (V)		440	255	300	255	105	255
Apparent DC Current (A)	58 Ω	7.59	4.40	5.17	4.40	1.81	4.40
	5 Ω	88	51	60	51	21	51
AC On-state Current (A)	58 Ω	7.59	2.80	5.17	2.80	1.81	2.80
	5 Ω	88	32.5	60	32.5	21	32.5
On-state/Rated Current (%)	58 Ω	20	7	14	7	5	7
	5 Ω	232	85	158	85	55	85

The rated current of the generator is approximately 38 A. The three- and five-phase star-connected generators show excessive nominal current on the DC side. The result in practice is that the voltage dropped across the internal impedance of the generator leads to a reduction in current output from the machine. *Table 5.13* shows that for the polygon-connection the same apparent current is drawn regardless of the phase number, so the comparison of load cases is valid. However, the star-connected system is not comparable as phase number increases due to the DC voltage level changing significantly. The results presented here show some of the effects that the different load values have on the system as a whole.

5.5.2 Star-connected Generator

The three-phase generator, observed previously in *Figure 5.35* (Section 5.4.2), shows near ideal sinusoidal AC voltage developed by the generator and behaviour that is expected from Chapter 3 for a three-phase generator connected to a diode rectifier. However, as the current drawn to the load side increases, the AC voltage is distorted by harmonic content, observed in *Figure 5.47*. The distortion is caused by third harmonic, which is 20 % greater in magnitude than the fundamental and is in-phase. The DC voltage follows the envelope of the line-to-line voltage, which has a lower peak than the phase voltage due to the cancellation of the third harmonic in the line-to-line voltages.

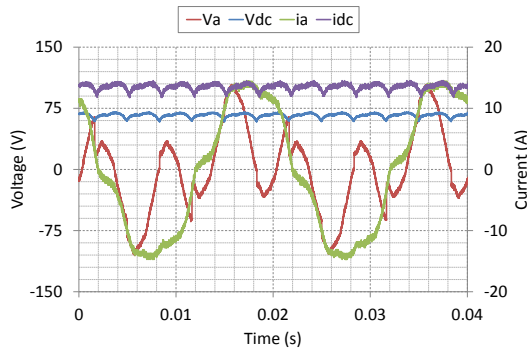


Figure 5.47: Three-phase Fully-pitched Star-connected Generator AC and DC Voltage and Current 5 Ω Load

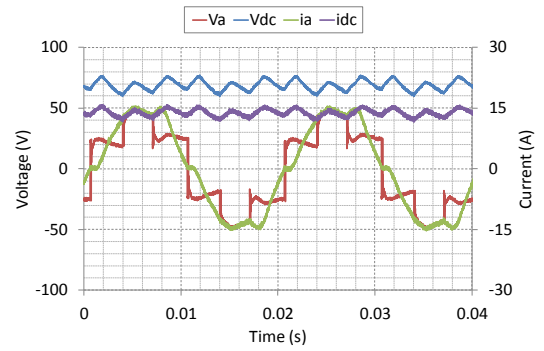


Figure 5.48: Three-phase Short-pitched Star-connected Generator AC and DC Voltage and Current 5 Ω Load

The short-pitched generator, presented in *Figure 5.48*, shows a distinctly different AC voltage to the sinusoidal voltage drawn under low load conditions, seen in *Figure 5.36*. As a result of diode commutation, the voltage is distorted with fifth harmonic components. The transfer of current between phases takes longer due to the higher level of current drawn. The voltages are clamped whilst commutation takes place until the AC current falls to zero and the next phase conducts.

The five-phase generator-rectifier system was subjected to the same fixed resistive loads on the DC side as used for the three-phase case. The fully- and short-pitched, star-connected generators, under light loading conditions, exhibit expected behaviour for a synchronous generator connected to a diode rectifier, as seen previously in *Figure 5.39* and *Figure 5.40*.

Increasing the loading on the DC side has a significant effect on the behaviour of the generator, particularly the AC voltage developed, as can be observed in *Figure 5.49* and *Figure 5.50*. The fully-pitched topology shows 60 % third, 38 % fifth – as a percentage of the fundamental – and higher order harmonic content. The short-pitching shows a suppression of the fifth harmonic, which is reduced to a magnitude of 2 %. However, the third and ninth harmonics are approximately 36 % and 23 % of the fundamental, respectively, causing significant distortion of the voltage waveform.

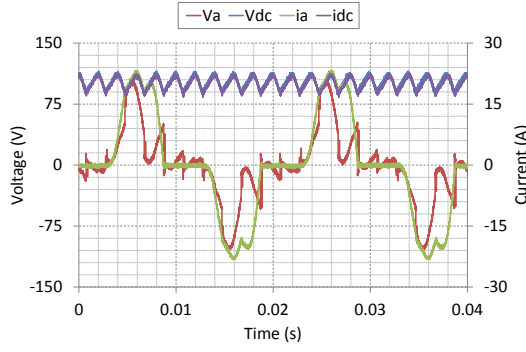


Figure 5.49: Five-phase Fully-pitched Star-connected AC and DC Voltage and Current 5 Ω Load

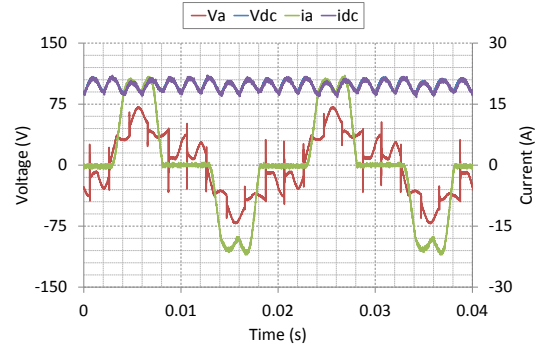


Figure 5.50: Five-phase Short-pitched Star-connected AC and DC Voltage and Current 5 Ω Load

The increase in DC side load current results in an increase in DC voltage ripple magnitude over the lightly loaded case. The fully-pitched topology incurs a 7 % increase whilst the short-pitched is up 9 %.

The 15-phase fully-pitched, star-connected generator with increased load current drawn to the DC side, observed in *Figure 5.51*, was discussed earlier in Section 5.3.3. The simultaneous diode conduction results in a reduction in peak current magnitude drawn from the generator when compared with short-pitched star-connected generator depicted in *Figure 5.52*. Diode recovery effects are clearly visible in the voltage waveform which transfers to the DC side but filtering these high frequency components is possible. This is not observed in the short-pitched generator in *Figure 5.52*.

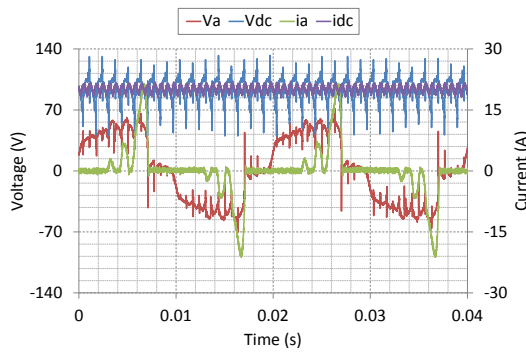


Figure 5.51: 15-phase Fully-pitched Star-connected AC and DC Voltage and Current 5 Ω Load

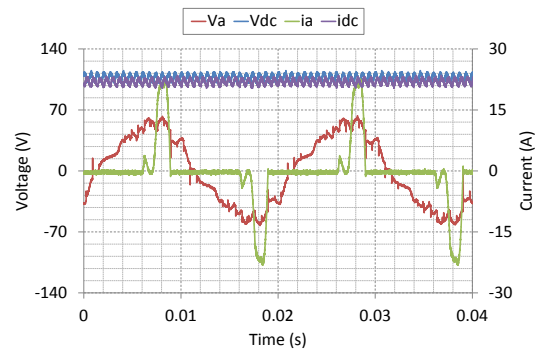


Figure 5.52: 15-phase Short-pitched Star-connected AC and DC Voltage and Current 5 Ω Load

5.5.3 Polygon-connected Generator

The fully-pitched, delta-connected generator presents a different behaviour to that seen in the star-connected generator for the different loading cases, displayed in *Figure 5.53* and *Figure 5.54* for the 58 Ω and 5 Ω resistive loads, respectively. Here, *Figure 5.53* is a reproduction of *Figure 5.37* for the purposes of comparison.

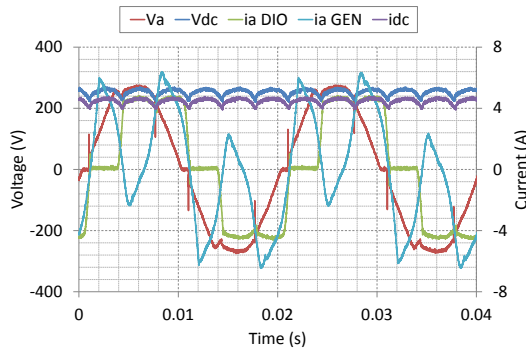


Figure 5.53: Three-phase Fully-pitched Delta-connected AC and DC Voltage and Current
58 Ω Load

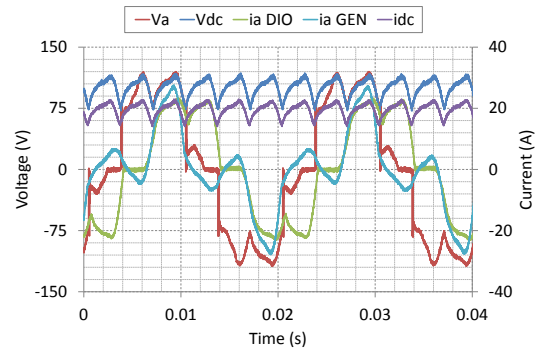


Figure 5.54: Three-phase Fully-pitched Delta-connected AC and DC Voltage and Current
5 Ω Load

The behaviour of the fully-pitched, delta-connected generator in Figure 5.53 is discussed in Section 5.4.2. Increasing the load changes the harmonic phase relationship with the generator current waveform, observed in Figure 5.54. The third harmonic circulating current is now in-phase and boosts the peak magnitude whilst suppressing the region close by. The line-to-line AC voltage shows a similar waveform to the short-pitched, star-connected generator AC line-to-line voltage under heavy loading. The ripple magnitude increases as a result of the increased loading.

Taking a FFT of the fully-pitched (FP) generator currents, and comparing it with the current expected from the three-phase simulated constant current waveform in Section 3.5.3, the results are shown in Figure 5.55 and Figure 5.56 for the 58 Ω and 5 Ω fixed resistive loads, respectively. The short-pitched (SP) experimental results are shown for comparison.

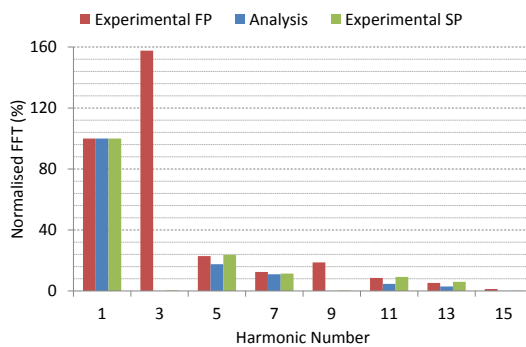


Figure 5.55: Harmonic Content of Three-phase Fully-pitched Delta-connected Generator Current 58 Ω Load

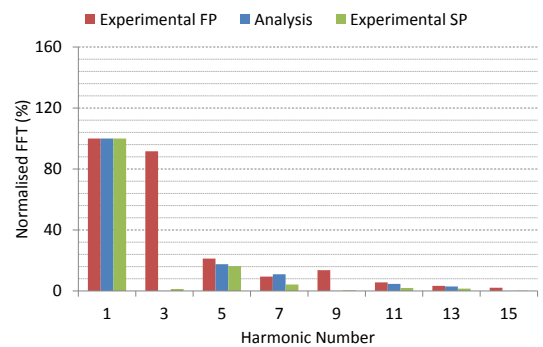


Figure 5.56: Harmonic Content of Three-phase Fully-pitched Delta-connected Generator Current 5 Ω Load

The current waveform that would be expected from the analysis shows no third harmonic current due to the assumption of ideal sinusoidal sources with no harmonic emfs. However, the fully-pitched experimental results show considerable third harmonic magnitude with different phase angles to the fundamental, highlighted in Table 5.14. The short-pitched

results agree with the analysis indicating that the short-pitched generator can be modelled as a sinusoidal source connected to the rectifier.

Table 5.14: Harmonic Content of Three-phase Delta-connected Generator Current

	Harmonic	1	3	5	7	9	11	13	15
DELTA 58 Ω	FFT (%)	100.000	157.626	22.833	12.484	18.724	8.550	5.269	1.299
	Angle (°)	-153.33	-43.22	-48.69	6.00	159.13	107.36	163.97	-73.56
DELTA 5 Ω	FFT (%)	100.000	91.133	20.977	9.423	13.520	5.477	3.266	2.131
	Angle (°)	115.39	137.68	-153.88	126.77	120.25	168.74	125.87	117.54

Further results for the three-phase, short-pitched generator can be found in Appendix 7.9.3.

The five-phase, polygon-connected generator shows the behaviour expected for a generator connected to a diode rectifier under light loading. The fully-pitched generator showed, in *Figure 5.41* (repeated here in *Figure 5.57* for comparison), that circulating harmonic currents were a significant problem for this winding topology. Short-pitching the stator windings eliminated these circulating harmonic currents. Decreasing the value of the resistive load on the DC side results in the harmonic current having a phase shift, shown in *Figure 5.58*.

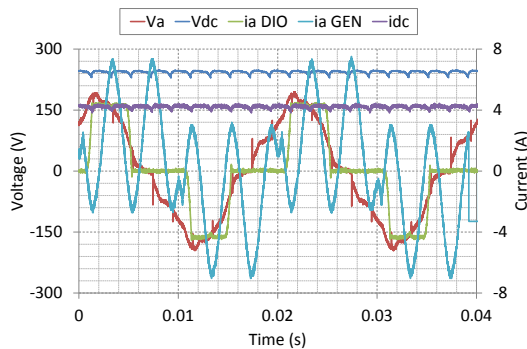


Figure 5.57: Five-phase Fully-pitched Polygon-connected AC and DC Voltage and Current 58 Ω Load

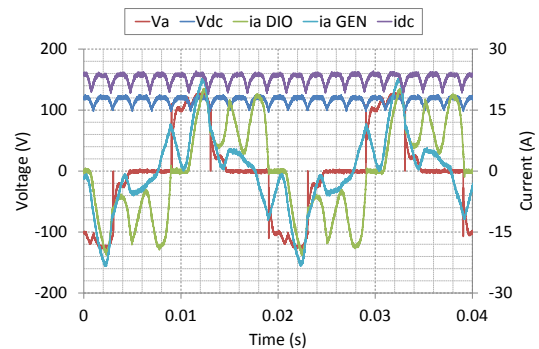


Figure 5.58: Five-phase Fully-pitched Polygon-connected AC and DC Voltage and Current 5 Ω Load

Taking an FFT of the generator currents from both load configurations yields the results presented in *Figure 5.59* and *Figure 5.60*.

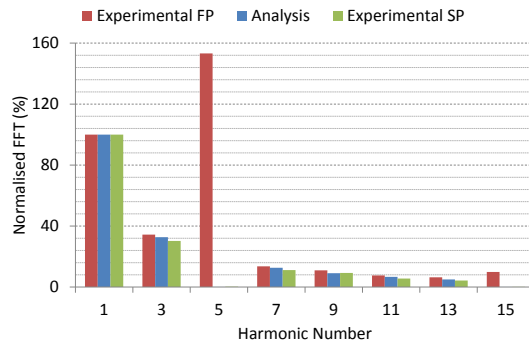


Figure 5.59: Harmonic Content of Five-phase Fully-pitched Polygon-connected Generator Current 58 Ω Load

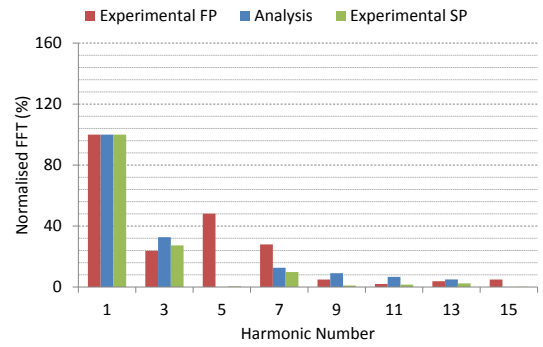


Figure 5.60: Harmonic Content of Five-phase Fully-pitched Polygon-connected Generator Current 5 Ω Load

The magnitude of the fifth harmonic remains approximately the same under high load conditions as in the lightly loaded case. However, due to the increase in the fundamental, the fifth harmonic is reduced to 1/3rd of the lightly loaded value as a percentage of the fundamental and there is a relative phase shift, highlighted in Table 5.15.

Table 5.15: Harmonic Content of Five-phase Polygon-connected Generator Current

	Harmonic	1	3	5	7	9	11	13	15
POLYGON	FFT (%)	100.000	34.373	153.268	13.600	10.930	7.621	6.375	9.886
58 Ω	Angle (°)	-18.24	-54.46	68.35	-130.24	-160.35	159.12	122.73	77.70
POLYGON	FFT (%)	100.000	23.766	48.154	27.959	4.915	2.002	3.807	4.907
5 Ω	Angle (°)	51.55	-19.58	-127.20	179.03	-143.61	-124.33	-112.85	156.26

The behaviour of the 15-phase, fully-pitched, polygon-connected generator is discussed earlier together with Figure 5.45. It is repeated here in Figure 5.61 for comparison.

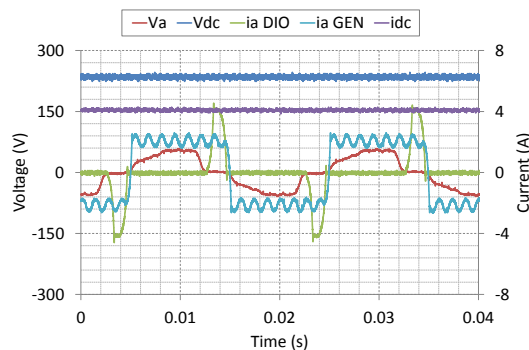


Figure 5.61: 15-phase Fully-pitched Polygon-connected AC and DC Voltage and Current 58 Ω Load

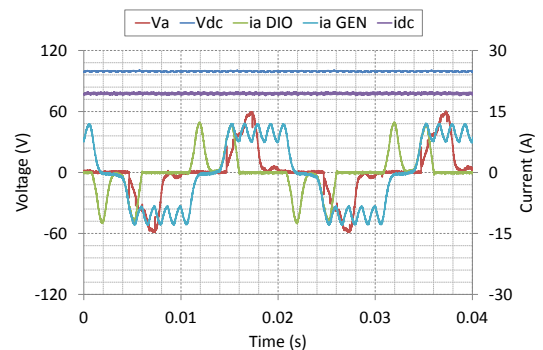


Figure 5.62: 15-phase Fully-pitched Polygon-connected AC and DC Voltage and Current 5 Ω Load

The higher loading case, depicted in Figure 5.62, exhibits a difference in the current drawn from the generator due to a change in the diode current waveform. The rectifier leg

conducts twice per half period, reducing its peak magnitude to equal the AC generator current. Periods of zero current being measured in the winding arise from the parallel paths created by the diodes conducting current, removing that portion of the generator winding from the current path.

Taking an FFT of both polygon-connected load cases will allow the examination of harmonic currents present in the generator.

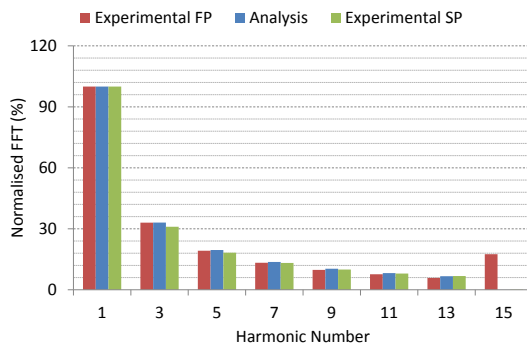


Figure 5.63: Harmonic Content of Polygon-connected Generator 58 Ω Load

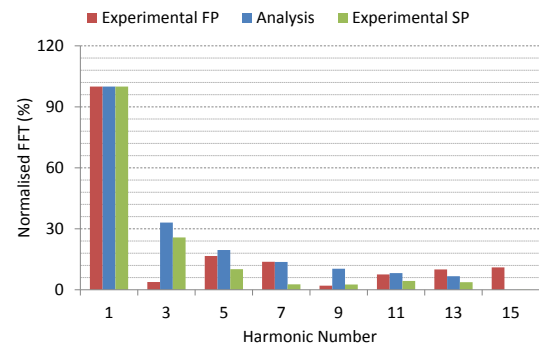


Figure 5.64: Harmonic Content of Polygon-connected Generator 5 Ω Load

The FFT results in Figure 5.63 show a good match between the lightly loaded system and the analysis for a constant current load, apart from the presence of the 15th harmonic. However, due to its high frequency and phase relation to the fundamental, it is small compared with the third and fifth. For a higher current drawn on the DC side, the harmonic content of the waveform is reduced overall with the 15th harmonic remaining but at a lower magnitude also, highlighted in Table 5.16. The short-pitched results show a performance similar to the analysis under both load conditions, showing a better harmonic behaviour in Figure 5.64 due to the increased fundamental to which the results are normalised.

Table 5.16: Harmonic Content of 15-phase Polygon-connected Generator Currents

	Harmonic	1	3	5	7	9	11	13	15
POLYGON	FFT (%)	100.000	33.041	19.203	13.286	9.770	7.645	5.836	17.523
58 Ω	Angle (°)	-87.29	97.40	-78.04	107.09	-68.70	113.76	-60.41	79.61
POLYGON	FFT (%)	100.000	3.832	16.639	13.759	2.032	7.556	10.016	11.031
5 Ω	Angle (°)	129.27	26.38	104.08	1.49	-98.80	-27.65	-132.78	-61.99

The data in Table 5.16 shows significant third, fifth and 15th harmonic under light conditions which is to be expected for a square-wave approximation. However, increasing the load

reduces the harmonics in the generator current, in particular the third harmonic which is reduced to half the magnitude when compared with the lightly loaded result.

5.5.4 Summary of Generator Loading Comparison

This section provided an insight into the behaviour of the generator-rectifier system as phase number increased and the load connected on the DC side was changed. The star-connected generator results for an increase in phase number were not comparable for the fixed resistive loads, as highlighted in *Table 5.13*. The current drawn on the DC side for the three- and five-phase generator cases were significantly beyond the machine rating. The results did show that AC voltage distortion increased whilst DC voltage reduced due to extended commutation time and internal volt drops increasing across the generator impedances. The polygon-connected generator had a comparable load imposed on it as phase number increased. The AC voltage demonstrated an extended zero period due to commutation across a number of windings, but reduced peak current drawn from the generator. There was also the presence of circulating harmonic currents in the fully-pitched windings which exhibited a change in phase relationship as the load increased.

5.6 Comparison of Fault Tolerance in Star- and Polygon-connected Generators

5.6.1 Introduction

When using the generator-rectifier system in an application such as aircraft or ships, it is important to appraise the system performance under fault conditions. Star- and polygon-connected generators provide different current paths through the generator windings and, therefore, alter the fault handling capabilities of the system. This section investigates open-circuit faults occurring in the generator and diode rectifier for both a star- and polygon-connection. Only steady-state open-circuit fault behaviour will be investigated, the onset of the fault is not considered.

5.6.2 Three-phase Generator

In the laboratory, open-circuiting a phase winding is accomplished through the removal of the link between the two coils in the double layer winding. The generator, in this three-phase case, has the *b*-phase winding open-circuited, as shown in *Figure 5.65*. For the open-circuit diode device fault, the input connection is removed from that leg and, again, it is the *b*-phase that is removed. The rectifier circuit behaviour is explained for each type of fault in Appendix 7.9.2.

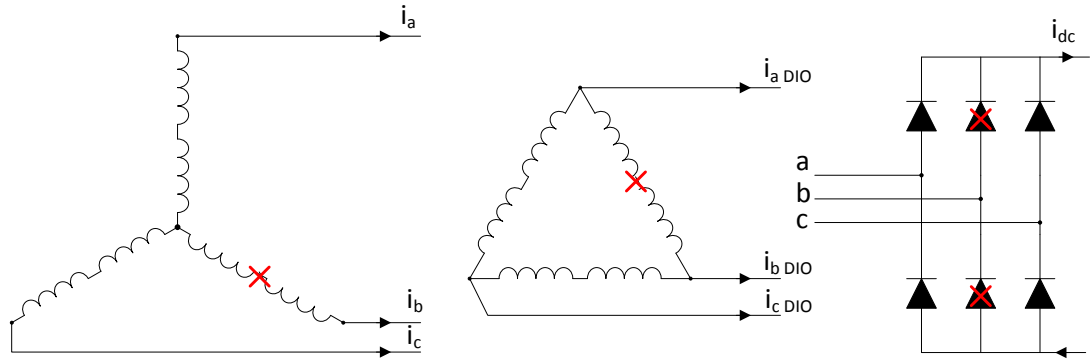


Figure 5.65: Three-phase Star- and Delta-connected Generator and Diode Open-circuit Condition

The effect of open-circuit conditions on the AC and DC side differs dependent on phase number, connection method and source of fault being the generator or diode device. Considering the star-connected case, the results for the generator phase and diode leg open-circuit faults can be seen in Figure 5.66. The connection method would indicate that the same current path is effectively removed, but at a different point in the system. As a result, there is no discernible difference in the performance of the generator and rectifier under open-circuit phase and diode device fault conditions. Only the generator open-circuit phase fault is presented throughout for the star-connected case. The diode open-circuit condition is for the less likely case of an open-circuit diode leg fault. The limitation of the hardware prevented the more probable scenario of a single open-circuit diode device fault and this has been identified for future work in Section 6.4.

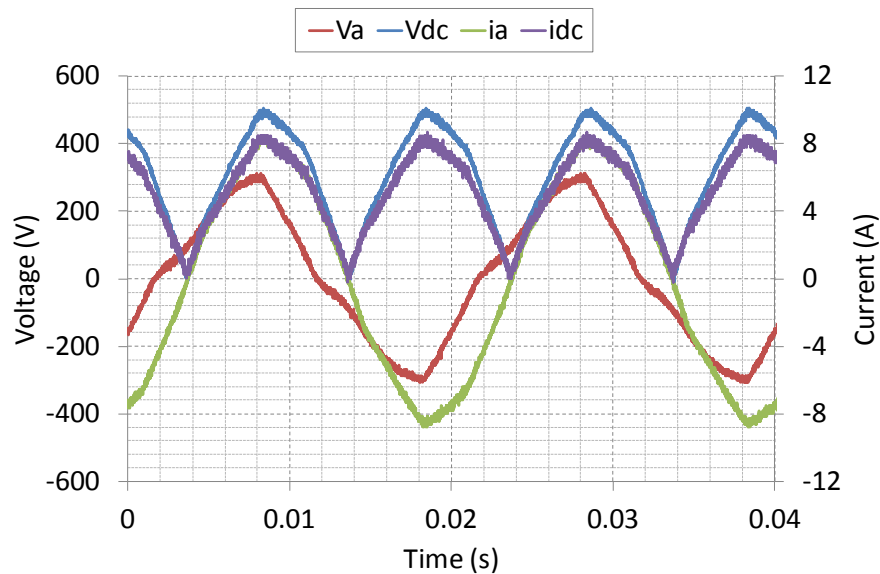


Figure 5.66: Three-phase Fully-pitched Star-connected Generator Open-circuit Phase Fault 58 Ω Load

The generator AC voltages and currents are approximately sinusoidal whilst the DC output now has a 100 Hz ripple; under normal operating conditions it would be six times the line-frequency, 300 Hz. The phase shift is caused by the rectifier acting as a H-bridge, explored

in Appendix 7.9.2. The DC voltage follows the rectified line-to-line voltage between the two healthy phases, resulting in full peak DC ripple magnitude.

Investigating the second available connection topology, the delta-connected generator has no neutral reference point so the voltage is measured across phases. The removal of the common reference point also affects the current path and the AC generator behaviour is very different from that of the star-connected generator.

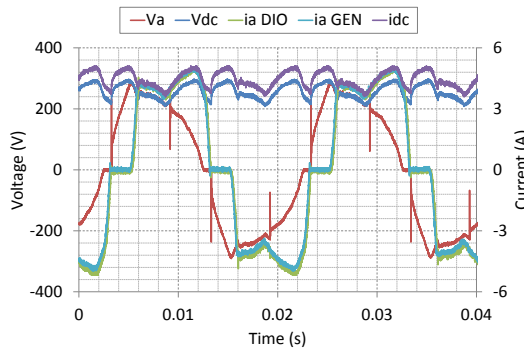


Figure 5.67: Three-phase Fully-pitched Delta-connected Generator Open-circuit Phase Fault 58 Ω Load

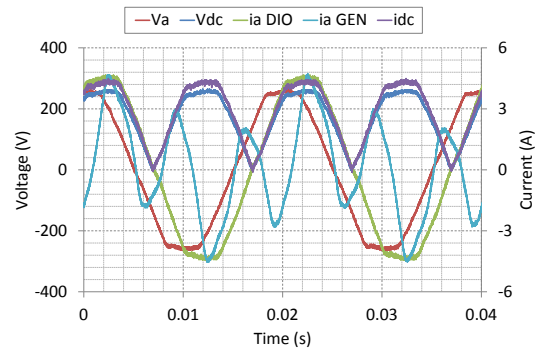


Figure 5.68: Three-phase Fully-pitched Delta-connected Generator Open-circuit Diode Fault 58 Ω Load

The generator open-circuit condition, shown in Figure 5.67, presents a much better DC side power quality than the star-connected case, observed in Figure 5.66, with the DC ripple voltage following the envelope of the distorted phase voltages. A full description of the circuit operation is given in Appendix 7.9. The AC characteristic is also much better than the healthy generator condition, shown in Figure 5.37, due to the removal of the circulating third harmonic current but current loading is higher in the two remaining healthy phases.

Comparing the delta-connected generator diode open-circuit fault, presented in Figure 5.68, with the star-connected generator results in Figure 5.66, the AC generator voltages are similar, except that Figure 5.68 exhibits a flat top to the waveform indicating some low magnitude harmonic interaction. This is also observed in the diode current. With the machine in its healthy condition the generator current shows a large degree of circulating third harmonic current interacting at a different phase angle to that depicted under normal operation in Figure 5.37. The AC diode current is of opposite sign in the two remaining healthy diode legs which connect the generator to the DC side. This leads to a full pk-pk ripple on the DC side at twice line frequency as the diode rectifier acts as a single H-bridge in the presence of the fault.

When a higher load current is drawn, for the open-circuit phase fault shown in Figure 5.69, the AC voltage distortion increases and the effects of the missing phase become more

apparent. This gives increased DC voltage ripple compared with both normal operating conditions and when the generator has moderate current drawn from it.

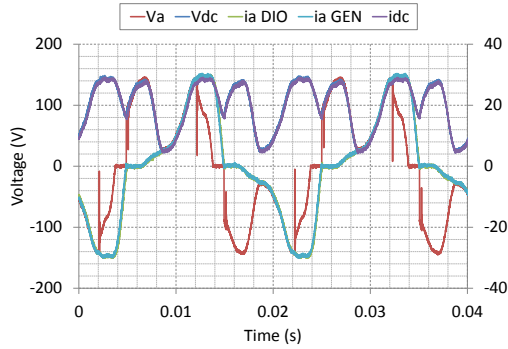


Figure 5.69: Three-phase Fully-pitched Delta-connected Generator Open-circuit Phase Fault 5 Ω Load

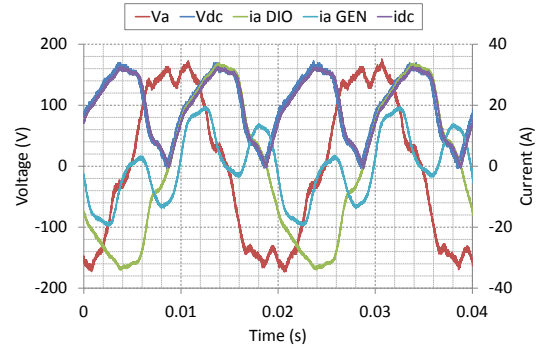


Figure 5.70: Three-phase Fully-pitched Delta-connected Generator Open-circuit Diode Fault 5 Ω Load

The DC side ripple performance remains better for the generator open-circuit phase fault than the diode open-circuit fault condition, shown in Figure 5.70. Circulating third harmonic currents are present in the fully-pitched windings. The removal of the diode line path results in the b -phase winding passing the current to the a - and c -phase diode lines, again the rectifier is acting as a single H-bridge. This results in a higher measured generator current in the b -phase winding, shown in Figure 5.71. The higher RMS current in the b -phase winding causes thermal stress on the phase winding due to the increased copper losses, and will limit the rating of the machine.

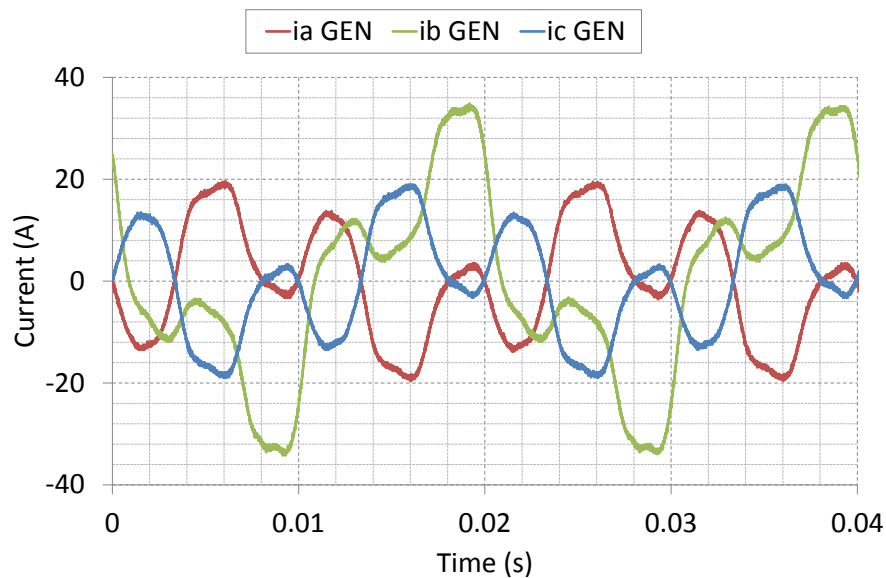


Figure 5.71: Three-phase Fully-pitched Delta-connected AC Generator Currents with Open-circuit Diode Fault

The behaviour of the star-connected generator and rectifier under an open-circuit phase or diode device fault remains similar when a higher load current is drawn. The AC voltage is

more distorted at higher load but the AC current drawn is a good sinusoidal approximation, similar to the normal operating conditions observed in *Figure 5.47*. The DC voltage ripple magnitude remains a critical problem with full pk-pk ripple and underlines the unsuitability of the standard star-connected, three-phase architecture for a fault tolerant aircraft DC power system.

The fault handling capability is not improved by short-pitching and, therefore, further results are contained in Appendix 7.9.3. These show a more sinusoidal waveform shape for the AC side quantities, offering a better performance in the presence of an open-circuit fault. The effects of the harmonics in the AC voltage for a star-connected generator are reduced by the short-pitched winding and the circulating harmonic currents for the delta-connection (*Figure 5.70*) are eliminated. This indicates that the generator losses will be reduced.

The comparison data, presented in *Table 5.17*, shows a significant improvement in the DC side power quality when using the delta-connected generator under open-circuit phase fault conditions but higher current loadings are present in the remaining healthy phases. It is apparent that the system behaviour is greatly affected by a failure in the rectifier regardless of connection topology. The delta-connected generator now exhibits less appreciable benefits when compared with the star-connected generator due to the losses associated with the circulating harmonic currents.

Table 5.17: Three-phase Fully-pitched Generator Open-circuit Phase and Diode Faults

			V_{AC}	i_{AC}	V_{DC}	i_{DC}	V_{DC}	V_{DC} Ripple
			(V_{pk})	(A_{pk})	(V_{pk})	(A_{pk})	(V_{pk-pk})	(% of AVG)
Star-	Gen/Dio	58 Ω	319.9	8.80	505.6	8.32	518.4	170.7
connected	O/C	5 Ω	89.6	21.2	102.4	22.3	105.6	186.1
Delta-	Gen	58 Ω	291.2	5.12	297.6	5.12	89.6	34.8
Connected	O/C	5 Ω	145.6	30.4	148.8	29.1	126.4	125.2
Delta-	Dio	58 Ω	265.6	4.74	265.6	4.49	272.0	161.0
Connected	O/C	5 Ω	176.0	19.5	172.8	32.8	179.2	178.7

5.6.3 Five-phase Generator

Increasing the number of phases, from three to five, will affect the behaviour of the generator under open-circuit fault conditions. The connection topologies and location of the open-circuit faults are shown in *Figure 5.72*.

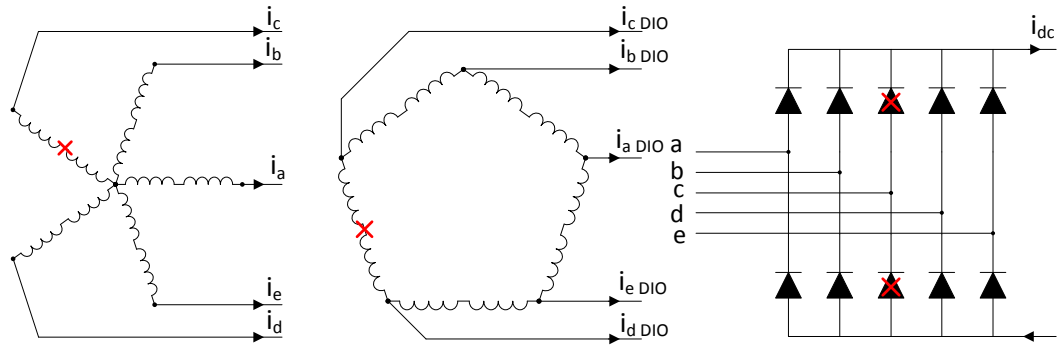


Figure 5.72: Five-phase Generator Connection Methods and Open-circuit Fault Locations

An open-circuit phase fault in the five-phase generator was achieved using the same technique described in Section 5.6.1. For this test, the generator and diode leg c -phase was chosen as the open-circuit. The effects on the performance of the generator, for both star- and polygon-connection, are outlined here.

The fully-pitched, star-connected generator with a $58\ \Omega$ fixed resistance load on the output DC side, is shown in Figure 5.73. The AC phase voltage is a relatively smooth sinusoid across the four healthy phases.

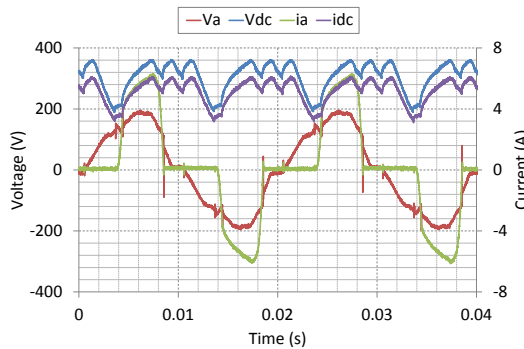


Figure 5.73: Five-phase Fully-pitched Star-connected Generator Open-circuit Phase Fault $58\ \Omega$ Load

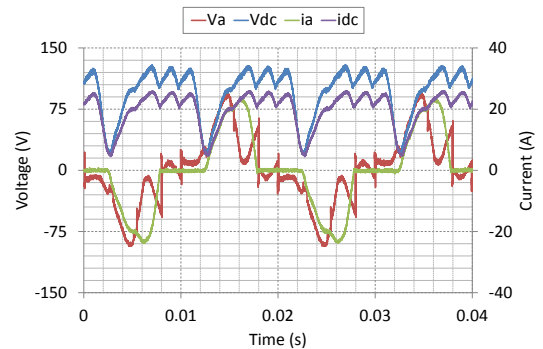


Figure 5.74: Five-phase Fully-pitched Star-connected Generator Open-circuit Phase Fault $5\ \Omega$ Load

The AC currents are uneven as a result of the missing phase. The a - and e -phase currents have approximately the same on-time as the healthy machine, where the b - and d -phases show an extended duty to cover the open-circuited c -phase, depicted in Figure 5.75. The copper losses in the b - and d -phase will be higher as a result of the extended duty increasing the RMS current. Under light loading conditions, the losses are not significant. However, as the load current is increased, de-rating would be required. The DC current follows the peak AC current and a significant improvement in voltage ripple is seen over the three-phase system.

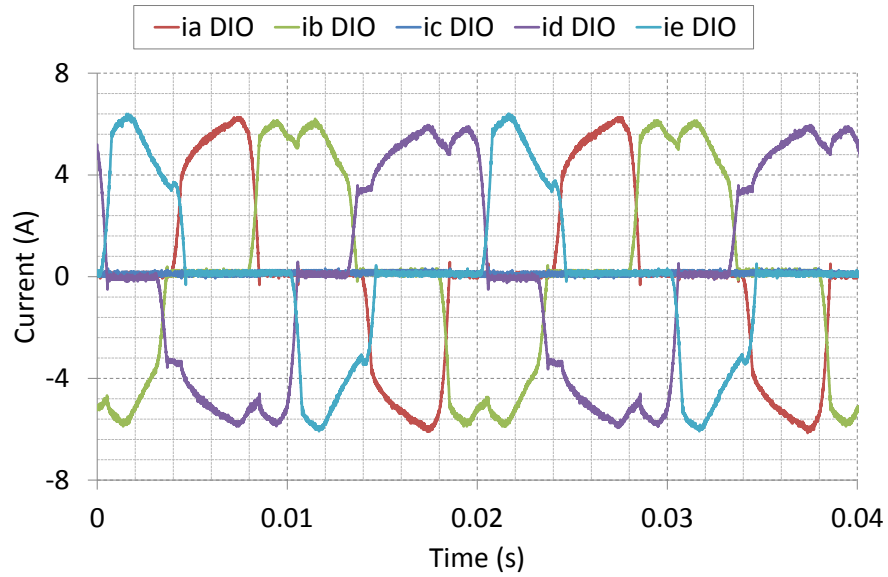


Figure 5.75: AC Currents for Five-phase Fully-pitched Star-connected Generator with Open-circuit Phase Fault

Increasing the current drawn from the generator, observed in *Figure 5.74*, increases the percentage of DC voltage ripple. The AC voltage shows considerable third, fifth and seventh harmonic, distorting the waveform. The near full pk-pk DC ripple voltage exceeds the MIL-STD-704F specifications, however, this particular topology is operating above its rating.

The five-phase, polygon-connected generator with an open-circuit phase fault shows, in *Figure 5.77*, very similar characteristics to that of the three-phase, delta-connected generator. The current drawn from the generator, presented in *Figure 5.76*, no longer shows the circulating harmonic currents observed in *Figure 5.41* but current sharing between phases is now unequal which will lead to the production of pulsating torque. The phase grouping shows a similar trend to that seen in the three-phase generator, which is explained in Appendix 7.9.2. The peak of the AC generator current is approximately double of that observed in the healthy generator case.

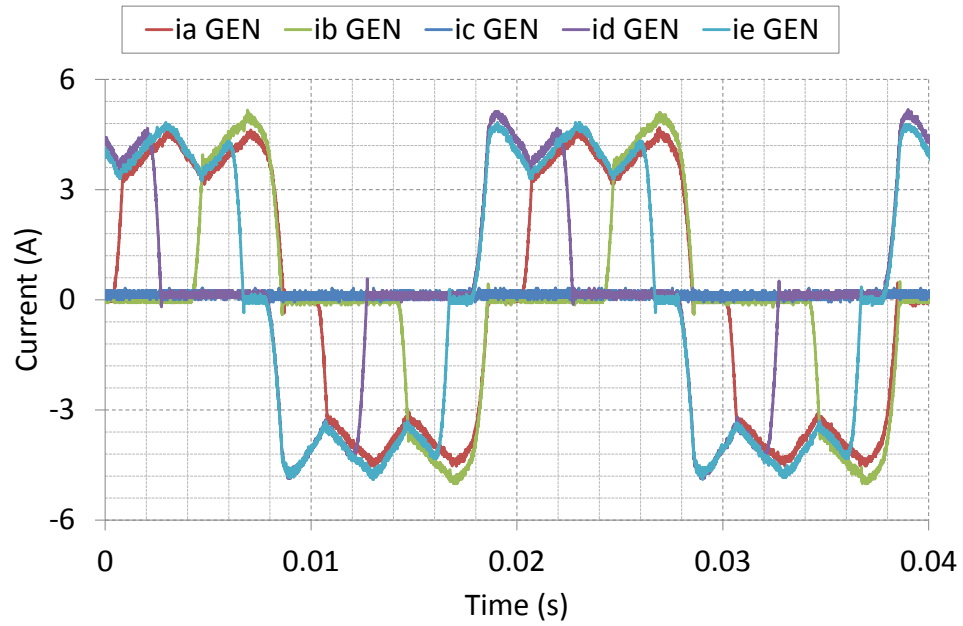


Figure 5.76: AC Generator Currents for Five-phase Fully-pitched Polygon-connected Generator with Open-circuit Phase Fault 58 Ω Load

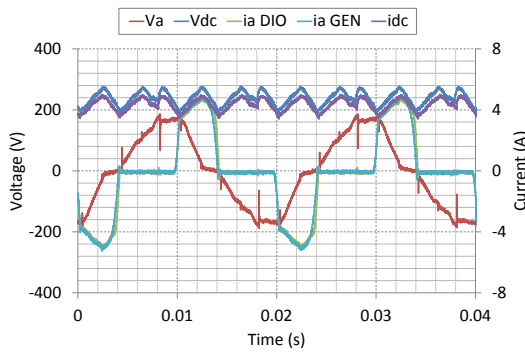


Figure 5.77: Five-phase Fully-pitched Polygon-connected Generator Open-circuit Phase Fault 58 Ω Load

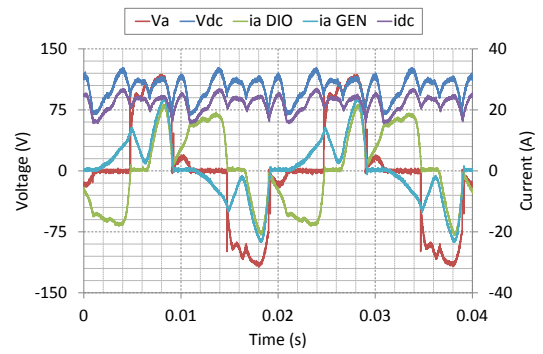


Figure 5.78: Five-phase Fully-pitched Polygon-connected Generator Open-circuit Phase Fault 5 Ω Load

Increasing the current on the DC side, shown in Figure 5.78, causes the expected prolonged zero periods shown in Section 5.5.3 and the deterioration of the DC characteristics.

The lightly loaded fully-pitched, polygon-connected generator with an open-circuit diode device fault condition is depicted in Figure 5.79. The AC behaviour is similar to the three-phase case presented in Figure 5.68 with circulating harmonic currents of a higher order present in the healthy generator windings. The DC voltage ripple is much better, being 25 % less in magnitude.

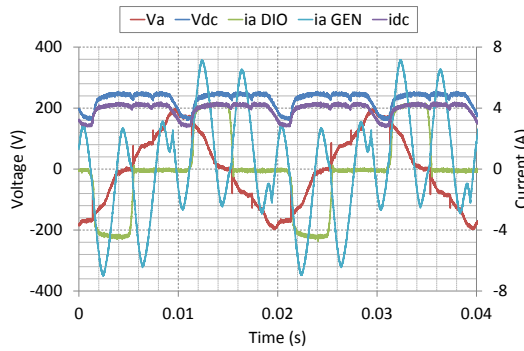


Figure 5.79: Five-phase Fully-pitched Polygon-connected Diode Open-circuit 58 Ω Load

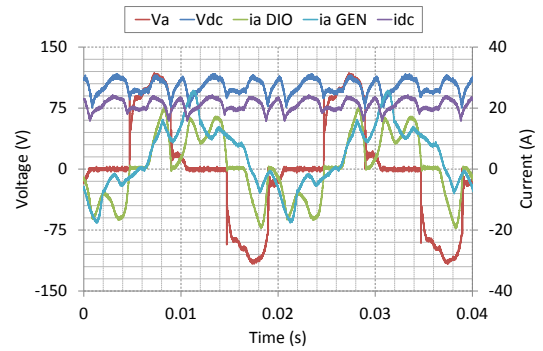


Figure 5.80: Five-phase Fully-pitched Polygon-connected Diode Open-circuit 5 Ω Load

Increasing the current drawn by the DC load distorts the AC voltage shown in *Figure 5.80* to the same effect as described previously. The generator currents have a much lower peak magnitude when compared with the three-phase case in *Figure 5.70* showing a lesser de-rating in the event of fault conditions.

It can be observed in *Table 5.18* that the five-phase, polygon-connected generator offers the best AC and DC side performance. The current drawn from the generator is lower, except in the heavily loaded case where the difference is not significant. The pk-pk DC ripple is also much lower for the polygon-connection with the percentage of the average being over 50 % lower under heavy system loading.

Table 5.18: Five-phase Fully-pitched Generator Open-circuit Phase and Diode Device Faults

			V_{AC}	i_{AC}	V_{DC}	i_{DC}	V_{DC}	V_{DC} Ripple
			(V_{pk})	(A_{pk})	(V_{pk})	(A_{pk})	(V_{pk-pk})	(% of AVG)
Star-connected	Gen/Dio	58 Ω	198.4	6.33	361.6	6.17	172.8	56.4
	O/C	5 Ω	94.4	23.6	129.6	26.0	110.4	115.3
Polygon-Connected	Gen	58 Ω	185.6	4.91	278.4	4.66	89.6	37.5
	O/C	5 Ω	118.4	24.0	126.4	24.9	59.2	58.1
Polygon-Connected	Dio	58 Ω	198.4	6.98	252.8	4.06	92.8	40.5
	O/C	5 Ω	118.4	25.8	117.2	24.4	43.2	42.7

The results contained in *Table 5.18* highlight the improvement in rectifier DC side performance when using a polygon-connected generator and having an open-circuit diode device fault present. Both connection topologies show a considerable improvement over the three-phase generator under open-circuit diode faults in the previous section. The AC quantities are comparable between the star- and polygon-connection, with the latter configuration drawing higher peak currents under both load conditions. The DC ripple,

however, is greatly reduced in the polygon-connection, particularly when comparing the two topologies under higher DC loading conditions.

As with the three-phase results, the five-phase, short-pitched test results are contained in Section 7.9.4.

5.6.4 15-phase Generator

Similar to the five-phase generator, the AC voltage rating of the generator is reduced, in this case, to $3/15^{\text{th}}$ of its original value as the number of coils per phase is reduced. The locations of the open-circuit faults are depicted in *Figure 5.81*.

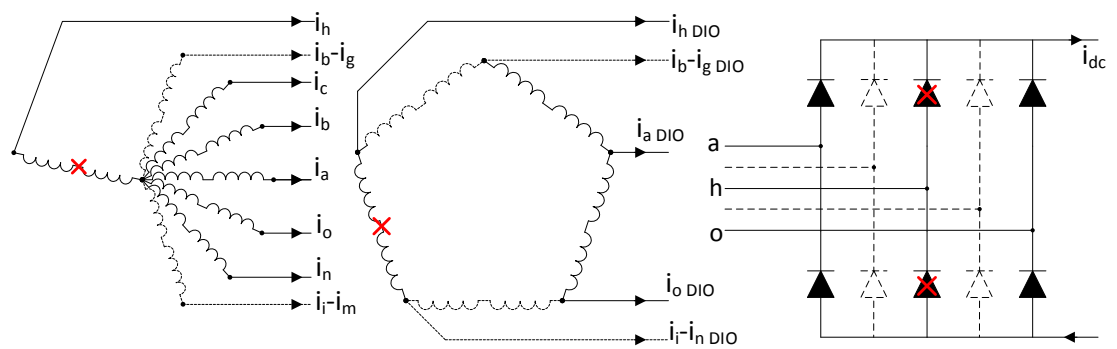


Figure 5.81: 15-phase Generator Connection Topologies and Open-circuit Fault Locations

The open-circuit generator fault for the fully-pitched, star-connected generator is presented in *Figure 5.82* and *Figure 5.83* for the different load conditions. With a low current, the generator performance is very similar to normal operating conditions. The AC current in adjacent phases is affected by the open-circuited phase conducting no current. This causes the preceding phase to conduct for longer as the voltage falls to below the value of the next phase before commutation occurs, demonstrated in *Figure 5.82*. The ripple on the DC side shows some degree of distortion but the change in pk-pk ripple magnitude is small when compared with the three- and five-phase cases.

When the current drawn from the generator is increased, shown in *Figure 5.83*, adjacent phases conduct at the same time but with unequal current sharing, giving a number of current pulses leading up to the main current transfer. The phases adjacent to the fault have an increased duty, covering the missing phase. The open-circuited phase affects the DC ripple, giving a pk-pk ripple that is almost twice the magnitude of that observed in the lightly loaded generator-rectifier system.

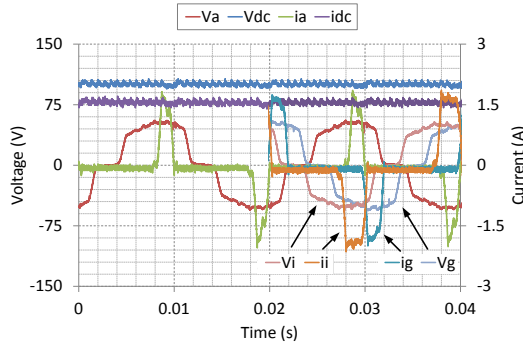


Figure 5.82: 15-phase Fully-pitched Star-connected Generator Open-circuit Phase Fault 58 Ω Load

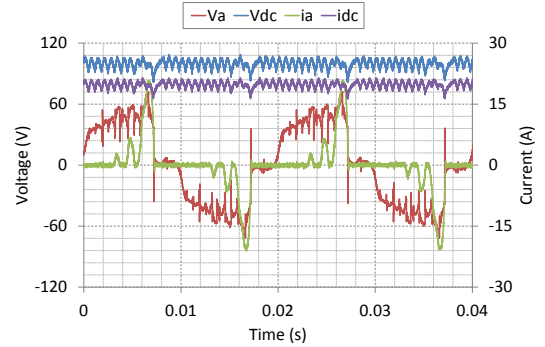


Figure 5.83: 15-phase Fully-pitched Star-connected Generator Open-circuit Phase Fault 5 Ω Load

The polygon-connected generator in Figure 5.84 changes the AC generator behaviour under open-circuit phase fault conditions compared to the star-connected case. The AC generator current drawn has a comparatively high peak value but has a lower time harmonic content. However, the phases closer to the fault (i_i GEN, for example) have a shorter duty which show higher time harmonic components. Similar to the five-phase, polygon-connected generator, the AC voltage is held at zero for periods during commutation under heavy loading as the voltage is equal in magnitude across a number of phases.

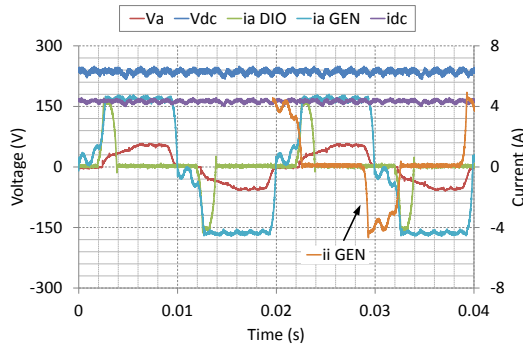


Figure 5.84: 15-phase Fully-pitched Polygon-connected Generator Open-circuit Phase Fault 58 Ω Load

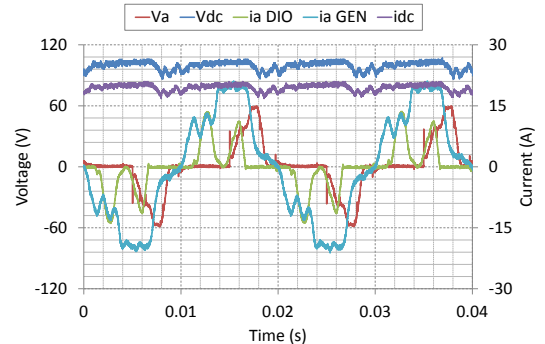
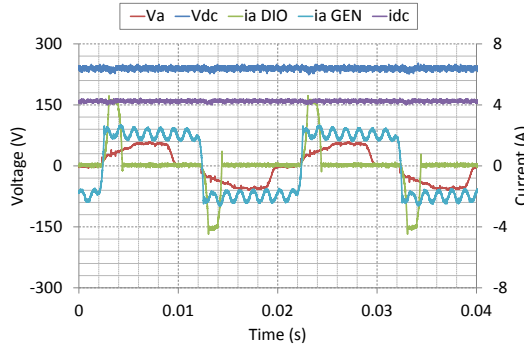


Figure 5.85: 15-phase Fully-pitched Polygon-connected Generator Open-circuit Phase Fault 5 Ω Load

Reducing the resistive load to 5 Ω , the results are shown in Figure 5.85. The AC generator peak voltage does not reduce in the higher loaded 15-phase generator as in the three- and five-phase topologies. The DC voltage ripple increases but due to the high phase number and the behaviour of the generator, the comparative ripple magnitude remains better than those achieved using a star-connection. The AC generator currents have varying duties and peak magnitudes in the remaining healthy phases, which will reduce the rating of the generator under the open-circuit phase fault condition.

Observing the diode open-circuit condition, shown in *Figure 5.86*, under light loading conditions, the generator performance is similar to its normal operation. The current drawn from the generator is consistent across all phases. However, the AC diode currents show a longer duty for the phases adjacent to the faulted diode. The DC side performance shows reduced ripple voltage magnitude, similar to the generator open-circuit phase condition, and is almost 3 % less as a percentage of the average for a higher pk-pk ripple voltage compared with that of the star-connected system, highlighted in *Table 5.19*.



*Figure 5.86: 15-phase Fully-pitched Polygon-connected Generator Open-circuit Diode
58 Ω Load*

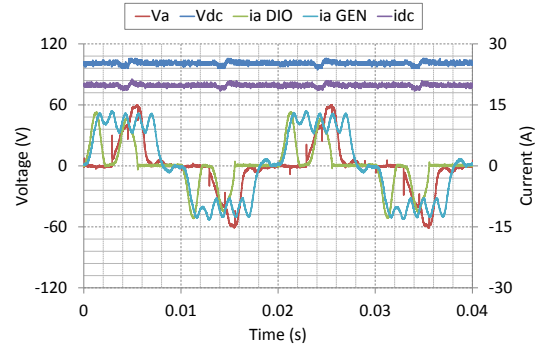


*Figure 5.87: 15-phase Fully-pitched Polygon-connected Generator Open-circuit Diode
5 Ω Load*

Increasing the current drawn on the DC side illustrated in *Figure 5.87*, leads to the behaviour of the generator resembling that observed in *Figure 5.62*.

Table 5.19: 15-phase Fully-pitched Generator Open-circuit Phase and Diode Device Faults

			V_{AC}	i_{AC}	V_{DC}	i_{DC}	V_{DC}	V_{DC} Ripple
			(V_{pk})	(A_{pk})	(V_{pk})	(A_{pk})	(V_{pk-pk})	(% of AVG)
Star-connected	Gen/Dio	58 Ω	59.5	1.86	107.2	1.71	14.4	14.3
	O/C	5 Ω	78.1	20.8	108.8	21.5	27.2	27.3
Polygon-Connected	Gen	58 Ω	58.2	4.80	249.6	4.58	31.9	13.6
	O/C	5 Ω	58.9	21.1	107.2	21.0	20.8	20.9
Polygon-Connected	Dio	58 Ω	58.9	2.69	252.8	4.44	28.8	12.0
	O/C	5 Ω	60.2	13.6	105.6	21.3	11.2	11.1

The results in *Table 5.19* show a difference in behaviour for the star- and polygon-connected 15-phase generator, particularly when compared with the three- and five-phase machines. The short duty current pulse of the star-connection has a high harmonic content which will contribute to losses in the generator. The pk-pk ripple magnitudes are comparable between the two connection configurations, highlighting the benefits of

utilising an increased phase number machine. The polygon-connection offers the best method for reducing the DC ripple magnitude.

The short-pitching of the 15-phase machine was selected to reduce the THD but seventh and ninth circulating harmonic currents can be seen to have a significant effect on the generator current, observed previously in *Figure 5.29*. The polygon-connected generator shows a significant change in voltage and current waveforms, shown in *Figure 5.88*, compared with the fully-pitched generator, even under light load conditions. The AC voltage and generator current do not exhibit a smooth transient, showing oscillatory behaviour which overlaps with the adjacent phases, suggesting the presence of circulating harmonic currents. The DC side voltage and current show a number of disturbances per cycle as a result of the small differences in the AC phase voltages. This can also be observed for the higher load conditions in *Figure 5.89*.

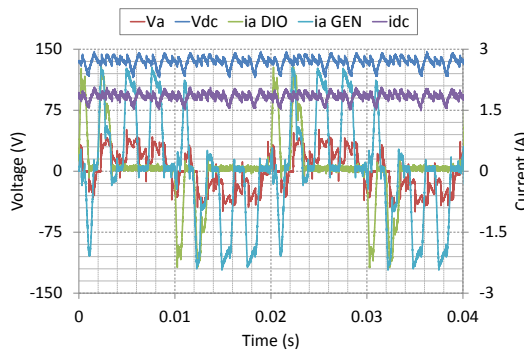


Figure 5.88: 15-phase Short-pitched Polygon-connected Generator Open-circuit Phase Fault 58 Ω Load

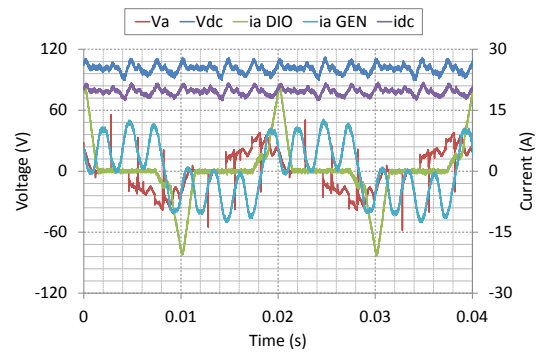


Figure 5.89: 15-phase Short-pitched Polygon-connected Generator Open-circuit Phase Fault 5 Ω Load

Carrying out a FFT on the generator currents in *Figure 5.88* and *Figure 5.89* shows a high harmonic content in both cases, depicted in *Figure 5.90*. The lightly loaded system shows excessive seventh, 11th and 13th harmonic currents flowing. The seventh harmonic in particular is greater in magnitude than the fundamental, measuring approximately 109 %. As the load current drawn to the DC side is increased from 2 A to approximately 20 A, the dominant harmonic currents are lower in frequency. The third harmonic is approximately 38 % of the fundamental and the seventh is now 79 %. This highlights the problems with short-pitching the stator windings to cancel specific harmonic components or to minimise THD in high phase number machines.

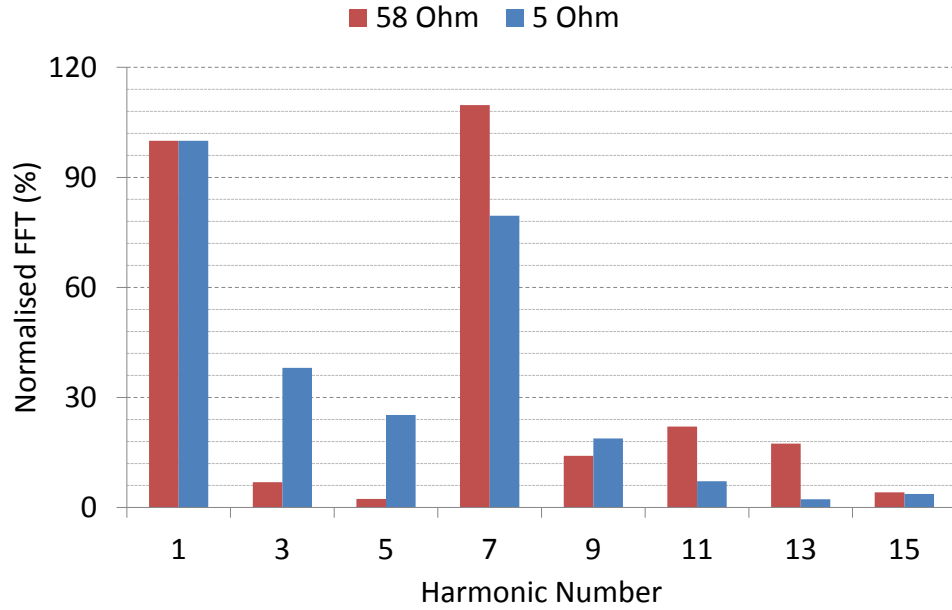


Figure 5.90: Harmonic Content of 15-phase Short-pitched Polygon-connected Generator Currents with Open-circuit Phase Faults

Further short-pitched results for the star- and polygon-connected 15-phase generator-rectifier system are contained in Appendix 7.9.5.

5.6.5 Summary of Comparison of Fault Tolerance in Star- and Polygon-connected Generators

The investigation into the effects of connection topology on fault tolerance in this section has shown that, in the three-phase, star-connected case, the DC power quality is not acceptable when an open-circuit fault is sustained in any part of the generator-rectifier system. The delta-connected generator shows a much better DC voltage waveform in the event of a generator phase fault but similar behaviour on the DC side to that of the star-connected configuration for a diode fault and is still not acceptable in terms of DC voltage ripple. Circulating currents are, however, present in the generator in the delta-connected case which are not an issue in the star-connection.

The five-phase generator presented improved performance compared with the three-phase generator-rectifier. The DC ripple was much lower in all but one of the cases, with the three-phase, delta-connected generator with an open-circuit phase fault offering a better DC ripple voltage than the five-phase generator under light loading. The shorter period of the current drawn from the star-connected generator cases will result in a higher harmonic content, increasing the losses within the generator compared with the polygon-connected generator. Both connection topologies showed that In the event of a generator phase or diode device open-circuit fault, the on-time of the diodes changes. Under high

load conditions, this would require de-rating of the generator to ensure that the losses in the phases do not cause thermal damage to the windings.

The 15-phase machine has shown distinct advantages for a generator-rectifier system supplying a DC electrical power network under fault conditions, regardless of connection method. Taking the fully-pitched case presented as an example, the voltage ripple on the DC side is approximately 85 % and 70 % lower when compared with the three- and five-phase generators, respectively. It has been observed that the polygon configuration performs better overall for AC and DC characteristics under both open-circuit fault conditions. Similar to the five-phase topology, both connection methods have a change in diode device on-time as a result of the open-circuit fault. This results in the uneven distribution of current in the remaining healthy phases and requires generator de-rating at higher loads.

The open-circuit fault conditions researched have focused on a single open-circuit phase or diode device fault in the system. For a star-connected system, further faults occurring in the generator would require machine de-rating but would not present a significant problem in terms of the continued operation of the generator. In the polygon-connected system, further diode device failures to open-circuit would be maintainable. However, subsequent open-circuit phase faults sustained in non-adjacent locations would require significant de-rating. The unequal current sharing could lead to significant torque ripple. The torque ripple is beyond the scope of this project but is of importance for a fault tolerant generator on-board an aircraft. Therefore, it is highlighted as an area for further research.

5.7 Summary

The experimental results have been presented to validate the simulation and allow the performance of different windings topologies, connection methods and load conditions to be evaluated.

The simulation model, for the normal operating conditions, showed good matches throughout Section 5.2.3, highlighting the validity of the simulation for healthy cases. However, in the higher phase cases where open-circuit faults were introduced, the ideal dynamic circuit model showed different AC and DC quantities to those achieved in testing. Saturation and stray load losses, along with other parasitic effects, were not considered in

the simulation and, for high phase numbers, the difference in switching voltages were small. For these reasons, the simulation is less accurate for the fully-pitched topology than short-pitched but it still shows the general trends. This is also true of the higher load cases where multiple diode conduction was predicted but the magnitudes and number of conduction periods were less well approximated. In the laboratory environment, differences in terminal resistances led to a change in switching behaviour which was not reflected in the simulation, culminating in a different DC ripple characteristic. The simulation provides a useful tool to analyse and compare system performance for different generator phase numbers under normal operation and with open-circuit faults.

Short-pitching the generator stator windings showed an improvement in generator performance under normal operating conditions for both star- and polygon-connected machines. The polygon-connection requires short-pitching to remove the circulating harmonic currents that are present in the fully-pitched windings. However, the 15-phase generator showed adverse performance from short-pitching in *Figure 5.90*, where lower order circulating harmonic currents weren't cancelled, even under open-circuit phase faults. This highlights the importance of the winding design for multiphase machines.

Loading the generator highlighted the distinct differences in the generator behaviour for different DC loads. Under high DC current demands, the three- and five-phase, star-connected generators were operated in a region outside of their rated capability. The polygon-connected generators were comparable across phases for the load conditions applied and showed the change in phase relationship for the circulating harmonic currents that were present in the fully-pitched winding.

The method of connection of the machine allowed the comparison of fault performance for high phase number machines. The star-connected topology exhibited the same degradation in the AC and DC waveforms, regardless of the location of the open-circuit fault. As phase number increased, the fault handling capability of the system showed that the need for filter capacitance, to remain within tolerable DC ripple limits, was reduced. The 15-phase generator was marginally outside of MIL-STD-704F specification, requiring filter capacitance in the event of a fault but at reduced size, weight and cost. Single phase faults are sustainable under light loads. However, as loading increases and the equal current sharing diminishes, the de-rating of the generator will increase.

6

Conclusions and Future Work

6.1 Introduction.....	174
6.2 Review of Presented Work.....	174
6.3 Contribution to Knowledge	176
6.4 Further Work.....	178
6.5 Publications	181

6.1 Introduction

This project has focused on the development of an electrical generation system to provide an aircraft DC power network. This thesis has met the project aim of investigating the effects that phase number, connection topology and winding pitch have on the behaviour of an AC synchronous generator connected to a diode rectifier. The work carried out through the finite element and dynamic simulation modelling has been validated by the experimental testing using the purpose-built test-rig.

This chapter evaluates the work contained within this thesis, identifying key findings with respect to the aims and objectives set out in Chapter 1, and determines prospective future work, discussed in Section 6.4.

6.2 Review of Presented Work

This section provides a brief summary of the work that has been presented in each chapter of this thesis.

Chapter 2 contained a review of previous research on multiphase machines. The majority of the literature focused on the benefits of multiphase motors, in particular induction machines. As a result of this literary survey, this thesis evaluates the wound-field

multiphase synchronous machine as a generator for the production of DC power using an uncontrolled rectifier.

Chapter 3 outlined the simulation modelling techniques undertaken to quantify and qualify the generator-rectifier system behaviour. Mathematical analysis, using ideal scenarios for ease of calculation, was used to verify the simulation. It also allowed general trends to be identified in DC voltage ripple and current harmonic content as phase number increased and connection topology changed. The equations that were outlined in Section 3.5.3 provided a good match in most cases. Differences could be attributed to the idealistic assumptions in the analysis; these could be accounted for in the simulation. Further detail was added to the simulation model from the information provided by the FEA. This completed the first of the objectives set out in Section 1.2, which was the development of a generator-rectifier simulation model.

Chapter 4 detailed the finite element analysis that was carried out based on the electromagnetic characteristics of the generator. Open-circuit voltages were investigated as the phase number increased and the pitching of the windings was changed. This was used in the dynamic circuit simulation model for the representation of harmonic effects. Other assumptions made in the simulation modelling on saliency and inductance scaling were shown to be valid. Finally, core losses were evaluated for a five-phase generator connected to an uncontrolled rectifier. This was conducted for both the star- and polygon-connected generator when fully- and short-pitched under static conditions. The results were compared with the standard three-phase generator-rectifier system, highlighting an approximate average 50 % saving in stator core losses for the five-phase machine at $2/3^{\text{rds}}$ rated current and 25 % at full rated current. The polygon-connected generator also offered similar reductions of over 28 % at $2/3^{\text{rds}}$ rated current and 19 % at full rated current, when compared with the star-connection. This chapter accomplished the second objective from Section 1.2 in ascertaining the losses incurred and the harmonic content of the back-emf in the windings.

Chapter 5 provided the full experimental results for normal operating conditions as well as investigating open-circuit faults within the generator and the rectifier. The connection topologies offered different behaviour when open-circuit faults were imposed. The star-connected generator showed no significant difference in behaviour with respect to the location of the open-circuit fault. The polygon-connected generator provided a distinct advantage compared to the star configuration for an open-circuit generator phase fault.

However, this topology still suffered from circulating harmonic currents with an open-circuit diode fault that affected the losses induced in the generator.

Some harmonic components could be removed through the short-pitching of the generator windings. This provided a more sinusoidal back-emf developed at the generator terminals in most cases. The simulation model provided accurate representation of the experimental generator-rectifier system for the short-pitched case. Extension of the simulation to include back-emf harmonics improved simulation accuracy for the fully-pitched configuration. This correctly predicted the presence of harmonics but with some error in the phase relationship. Referring back to the objectives set-out in Section 1.2, the construction of the test-rig is detailed in Appendix 7.1. The remaining two objectives are addressed through the work carried out in Chapter 5, in the validation of the simulation model through comparison with experimental results and the investigation into open-circuit effects on the star- and polygon-connected generators.

6.3 Contribution to Knowledge

This project has addressed the design, modelling and analysis of a reconfigurable multiphase synchronous generator-rectifier system. Key findings are summarised here to provide an overview of the significant findings and contribution to the field.

6.3.1 Effects of an Increase in Phase Number

The increase in generator phase number, when connected to a diode rectifier, has been observed to have significant benefits in the production of DC power. A key advantage of this technology is the reduction in DC side pk-pk ripple voltage, which under normal operating conditions can be as low as 2.5 %, as a percentage of the average DC waveform for the 15-phase generator compared with 20 % for the three-phase generator. This is well within the MIL-STD-704F tolerances and would require no filter capacitance to be present, reducing system costs and also DC fault current. Analytical expressions developed in Chapter 3, along with the simulation models, provided a method of predicting voltage ripple for an arbitrary number of phases. The finite element modelling showed that core losses were reduced for the five-phase generator when compared with the three-phase machine for both connection topologies.

Further effects of increasing the phase number can be observed through the change in commutation effects. The uncontrolled diode switching results in the commutation taking

up a greater proportion of the time and multiple diodes conducting simultaneously, this leads to a reduction in voltage on the DC side.

6.3.2 Connection Topology

The connection topology has a distinct effect on the generator output characteristics under normal operating conditions. Short duty, high peak currents were drawn from the star-connected generator. In the five- and 15-phase generator, this resulted in high time-harmonic content, increasing core losses. However, under high current loading, for high phase numbers, the peak AC current drawn from the generator reduced as a result of current conduction occurring simultaneously in a number of other phases. The polygon-connected generator showed much longer duty waveforms with constant current conduction in the lightly loaded cases. However, circulating currents in the fully-pitched windings led to increased copper losses, particularly in the three- and five-phase machines.

Under heavy loading, the two connection topologies showed different behaviour also. The reduction in AC voltage under high load conditions was shown to be attributed to excessive loading, highlighted in Section 5.5, taking the machine beyond its rated output. As the phase number increased, it was observed that the peak DC voltage characteristics worsened for the star-connected generator but remained relatively consistent for the polygon configuration.

6.3.3 Winding Configuration

The pitching of the stator windings was seen to reduce the harmonic content of the generator voltage as intended, for most cases. The short-pitching was chosen based on the minimisation of THD content. For the delta- and polygon-connection, short-pitching reduced the circulating harmonics in the three- and five-phase generators. However, it can be observed in Section 5.6.4 that this was not the case for the 15-phase machine, which had lower order circulating harmonic currents present in the short-pitched windings. Therefore, careful consideration of the pitch angle must be made to mitigate the required harmonic content. Short-pitching provided a better match with the simulation results due to the better approximation of the sinusoidal back-emf. It also provided a reduction in core losses, particularly in the polygon-connected generator, observed in Section 4.7.

6.3.4 Open-circuit Faults

Open-circuit faults were investigated and simulated, for both the generator and rectifier, to ascertain which connection topology provided the best fault mitigation. The polygon-

connection showed a better generator utilisation under open-circuit diode device faults due to the generator remaining in a healthy condition. The star-connection was subjected to the same current path being removed regardless of the fault location and, therefore, the generator incurred greater losses as a result of a single open-circuit fault. The three-phase delta-connection provided a current path to the rectifier in the event of an open-circuit phase fault, but for a diode device fault it then acted like a star-connected system. The open-circuit behaviour of the 15-phase, short-pitched, polygon-connected generator was interesting as the small difference in voltage between phases led to multiple commutation of adjacent diode legs. As a result, the ripple voltage and generator currents were not as expected.

Investigating the redundancy of the system, through open-circuit fault conditions, revealed that the three-phase generator-rectifier system performance was very poor under phase or diode device faults. The five-phase system showed significant improvement. However, the 15-phase generator showed minimal impact under open-circuit fault conditions with the polygon-connection offering a better ripple reduction for both light and heavy loading. The load sharing between the remaining healthy phases provided a reduction in the requirement for machine de-rating in the presence of an open-circuit fault.

6.4 Further Work

The work presented in this thesis covers the project objectives set out in the introduction. Recommendations are made here for the potential work to be carried out to further the development and understanding of the areas to which this project applies.

6.4.1 Controllable Switching

It has been observed that the uncontrolled switching of diode devices can result in significant distortion in the AC generator currents and poor DC power quality. For the star-connected generator, as the phase number increases the commutation angle of the diode devices also increases and the DC voltage drops significantly under increased load conditions. This imposes limitations on the generator performance for high phase number machines as multiple diodes conduct simultaneously.

The ability to control the switching events will allow full control of generator currents. The control strategy can also act to enhance the system performance in the event of an open-circuit fault by controlling the switching of the phases adjacent to the fault. For example,

evenly distributing the current across the remaining healthy phases will minimise the DC voltage ripple.

A further benefit to controlled switching is the possibility of bi-directional power flow. The Rolls-Royce Trent 1000 engine on-board the Boeing 787 no longer has a pneumatic access point through which to start the engine [71]. Instead this is done electrically using the starter/generator. The multiphase machine proposed will have a higher torque output for the same volume machine [72], therefore, will be able to be utilised to start the engine.

6.4.2 High Frequency Operation

The experimental test-rig was limited, by design, to 50 Hz operation; this is acceptable for a standalone test unit. However, aircraft generators are mechanically powered from the gas turbine engine, which may have high spool speeds reduced through a mechanical gearbox. The speed ranges provide between 380 – 760 Hz AC output [13] in modern aircraft, which for a two-pole machine would be between approximately 20,000 – 45,000 rpm. The two-pole rotor could be exchanged for a four-pole type but it would still need to be driven at a significantly higher speed to produce a frequency output within the range of modern aircraft. The dynamic circuit model developed could be used to simulate the high frequency operation with relevant adjustments made to the parameters.

The higher frequency operation will have an effect on the diode commutation for high phase number machines. It was observed that the commutation time for the 15-phase machine with a constant current load on the DC side was significant, leading to a reduction in DC side voltage. Controlled switching may then become particularly beneficial in limiting the time for which the switching device is closed, reducing losses in the generator and improving power quality on the DC side.

6.4.3 Saturation Effects

The simulation results did not account for the effects that magnetic saturation has on the dynamic model performance. The characteristic of the machine material has a significant bearing on the behaviour of the back-emf and generator current developed. Where the material is used in its non-linear region, the dynamic circuit model will incorrectly predict the generator outputs. Further testing could be carried out, involving the change in the open-circuit characteristic of the generator as the field excitation is increased. Saturation will cause the back-emf developed to increase less for a greater field as the permeability of the stator material is reduced. Time-stepped FEM, discussed in Section 6.4.4, could also be

used and would show, in its solution, the regions of the generator that are most affected by saturation.

6.4.4 Time-stepping Finite Element Modelling

The best method of modelling the generator behaviour is through FEM. The FEA carried out in Chapter 4 was performed to provide a static solution for known generator conditions, such as two phases conducting current to the diode rectifier in a star-connected system, for example. Time-stepped FEM allows the software to evaluate the internal distribution of the flux within the generator at one point in time before it changes. If the correct material properties are input into the model parameters, saturation effects will be taken into account. The effects of pitching the windings could also be more accurate since the model will account for the change in rotor field interaction with the stator over time. Furthermore, the 15-phase core losses could be more readily assessed. However, the process of time-stepped FEM is computationally intensive and requires accurate and detailed machine parameters to produce the correct solution.

6.4.5 Representative DC Loads

The DC loads investigated in Chapter 5, were chosen to observe the generator under two distinct conditions. However, for aircraft applications, the DC distribution system wouldn't be subject to a single resistive load and would instead have a number of loads with varying characteristics. For example, motor loads would most likely have a power electronic converter attached to the DC load side, which would appear as a constant current demand. The combination of loads for a flight profile would affect the DC distribution network and, consequently, the power drawn from the generator.

6.4.6 Torque Ripple

The torque ripple was not investigated in this project. However, with the validation of the dynamic circuit model and the installation of a torque transducer on the experimental test-rig, it is possible to simulate and measure torque ripple under normal operating and open-circuit fault conditions. Extending the open-circuit fault analysis to non-adjacent faults occurring in the polygon-connected generator will provide an insight into the machine performance under significant stress with the unequal current sharing in phases affecting the torque transferred through to prime mover.

6.5 Publications

Conference presentation and publications are listed here:

S. Jordan and J. Apsley, "*Diode Rectification of Multiphase Synchronous Generators for Aircraft Applications*," in IEEE Energy Conversion Congress and Exposition, Phoenix, USA, 2011, pp. 3208-3215.

S. Jordan and J. Apsley, "*Experimental Validation of Multiphase Synchronous Generators for Diode Rectified DC Power Networks on Civil Aircraft*," in More-electric Aircraft Conference, Bordeaux, France, 2012

S. Jordan and J. Apsley, "*Open-circuit Fault Analysis of Diode Rectified Multiphase Synchronous Generators for DC Aircraft Power Systems*," in IEEE International Electric Machines and Drives Conference, Chicago, USA, 2013, pp. 992-997.

References

- [1] G. Neidhöfer, "The Evolution of the Synchronous Machine," *Engineering Science and Education Journal*, vol. 1, 1992.
- [2] P. C. Krause, O. Wasynczuk, and S. D. Sudhoff, *Analysis of Electric Machinery and Drive Systems*, 2nd ed.: John Wiley & Sons Ltd, 2002.
- [3] A. J. Mitcham and J. J. A. Cullen, "Permanent Magnet Generator Options for the More Electric Aircraft," in *International Conference on Power Electronics, Machines and Drives*, 2002, pp. 241-245.
- [4] Air Transport Action Group, "Beginner's Guide to Aviation Efficiency," 2010.
- [5] M. J. Provost, "The More Electric Aero-engine: a General Overview from an Engine Manufacturer," in *International Conference on Power Electronics, Machines and Drives*, 2002, pp. 246-251.
- [6] D. C. White and H. H. Woodson, *Electromechanical Energy Conversion*. New York: John Wiley & Sons, Inc., 1959.
- [7] E. Levi, "Multiphase Electric Machines for Variable-speed Applications," *IEEE Transactions on Industrial Electronics*, vol. 55, 2008.
- [8] F. Terrien, S. Siala, and P. Noy, "Multiphase Induction Motor Sensorless Control for Electric Ship Propulsion," in *International Conference on Power Electronics, Machines and Drives*, 2004, pp. 556-561.
- [9] A. Emadi, M. Eshani, and J. M. Miller, *Vehicular Electric Power Systems: Land, Sea, Air and Space Vehicles*. New York: Marcel Dekker, 2004.
- [10] European Commission, "European Aeronautics: A Vision for 2020," 2001.
- [11] C. R. Avery, S. G. Burrow, and P. H. Mellor, "Electrical Generation and Distribution for the More-Electric Aircraft," in *42nd International Universities Power Engineering Conference Brighton*, 2007, pp. 1007 - 1012.
- [12] The Boeing Company, "Cleaner, Healthier Air", http://www.newairplane.com/787/design_highlights/#/passenger-experience/cleaner-air [accessed: 13th February 2013]
- [13] I. Moir and A. Seabridge, *Aircraft Systems*, 3rd ed.: John Wiley & Sons Ltd, 2008.
- [14] B. Rebbechi, M. Burchill, and G. Coco, *An Investigation of F/A-18 AMAD Gearbox Driveshaft Vibration*: DSTO Aeronautical and Maritime Research Laboratory, 1997.
- [15] Liebherr Aerospace, "Power Optimised Aircraft", http://www.dlr.de/rm/en/desktopdefault.aspx/tabid-3837/5985_read-8790/ [accessed: 29th June 2010]
- [16] M. Hirst, A. McLoughlin, P. J. Norman, and S. J. Galloway, "Demonstrating the More-electric Engine: A Step Towards the Power Optimised Aircraft," *IET Electric Power Applications*, vol. 5, pp. 3 - 13, 2011.
- [17] M. Sinnet, "787 No-bleed Systems: Saving Fuel and Enhancing Operational Efficiencies," in *Boeing Commercial Aeromagazine*, 2007, pp. pp 6-11.
- [18] G. Klaus, W. Nick, H. W. Neumuller, G. Nerowski, and W. McCown, "Advances in the Development of Synchronous Machines with High-temperature Superconducting Field Winding at Siemens AG," in *IEEE Power Engineering Society General Meeting*, 2006, pp. 1 - 7.
- [19] H. Saravanamuttoo, G. Rogers, H. Cohen, and P. Straznicky, *Gas Turbine Theory*, 6th ed. Harlow: Prentice Hall, 2009.
- [20] C. G. Hodge and D. J. Mattick, "The Electric Warship," *Institute of Marine Engineers Transactions*, vol. 108, 1996.

- [21] C. G. Hodge and D. J. Mattick, "The Electric Warship Then, Now and Later," in *International Naval Engineering Conference*, Hamburg, 2008, pp. 1 - 9.
- [22] A. J. Sørensen and A. K. Ådnanes, "Reconfigurable Marine Control Systems and Electrical Propulsion Systems for Ships," *ASNE Reconfiguration and Survivability Symposium*, 2005.
- [23] A. Ouriua, L. Domasck, and J. H. Beno, "Electric Ship Power System Integration Analyses through Modeling and Simulation," in *IEEE Electric Ship Technologies Symposium*, 2005, pp. 70 - 74.
- [24] J. G. Ciezki and R. W. Ashton, "Selection and Stability Issues Associated with a Navy Shipboard DC Zonal Electric Distribution System," *IEEE Transactions on Power Delivery*, vol. 15, pp. 665-669, 2000.
- [25] S. Williamson, S. Smith, and C. Hodge, "Fault Tolerance in Multiphase Propulsion Motors," *Marine Engineering and Technology*, vol. 4, 2004.
- [26] J. M. Apsley, "Derating of Multiphase Induction Machines Due to Supply Imbalance," *IEEE Transactions on Industry Applications*, vol. 46, pp. 798-805, 2010.
- [27] M. Bash, R. R. Chan, J. Crider, C. Harianto, J. Lian, J. Neely, S. D. Pekarek, S. D. Sudhoff, and N. Vaks, "A Medium Voltage DC Testbed for ship power system research," in *IEEE Electric Ship Technologies Symposium*, 2009, pp. 560-567.
- [28] G. K. Singh, "Multi-phase Induction Machine Drive Research," *Electric Power Systems Research*, vol. 61, 2002.
- [29] L. Parsa, "On Advantages of Multi-phase Machines," *IEEE Industrial Electrical Conference*, pp. 1574-1579, 2005.
- [30] P. M. Tuohy, A. C. Smith, and M. Husband, "Induction Rim-drive for a Marine Propulsor," in *5th IET International Conference on Power Electronics, Machines and Drives* 2010, pp. 1-6.
- [31] C. F. Taylor, *Internal Combustion Engine in Theory and Practice* vol. 2: Combustion, Fuels, Materials, Design: MIT Press, 1985.
- [32] C. C. Chan and Y. S. Wong, "The State of the Art of Electric Vehicles Technology," in *Power Electronics and Motion Control Conference*, Xi'an, 2004, pp. 46 - 57.
- [33] P. de Haan, M. G. Mueller, and A. Peters, "Does the Hybrid Toyota Prius Lead to Rebound Effects? Analysis of Size and Number of Cars Previously Owned by Swiss Prius Buyers," *Ecological Economics*, vol. 58, 2006.
- [34] M. Esani, Y. Gao, and A. Emadi, *Modern Electric, Hybrid Electric, and Fuel Cell Vehicles*, 2nd ed. Boca Raton: CRC Press, 2010.
- [35] I. Petrov and J. Pyrhonen, "Performance of Low Cost Permanent Magnet Material in PM Synchronous Machines," *IEEE Transactions on Industrial Electronics*, 2012.
- [36] E. Levi, *Polyphase Motors: A Direct Approach to Their Design*. New York: John Wiley & Sons Ltd., 1984.
- [37] E. Levi, R. Bojoi, F. Profumo, H. A. Toliyat, and S. Williamson, "Multiphase Induction Motor Drives - A Technology Status Review," *IET Electrical Power Applications*, 2007.
- [38] M. Mezzarobba, L. Spangaro, and A. Tassarolo, "Experimental Evaluation of Damper Circuit Influence on the Performance of Multiphase Synchronous Generators Feeding Multiple Rectifiers," in *International Conference on Power Engineering, Energy and Electrical Drives*, 2011, pp. 1 - 6.
- [39] K. Gopakumar, V. T. Ranganthan, and S. R. Bhat, "Split phase Induction motor operation from PWM voltage source inverter," *IEEE Transactions on Industrial Applications*, pp. 927 - 932, 1993.
- [40] A. Tassarolo, "Analysis of Split-Phase Electric Machines with Unequally-Loaded Stator Windings and Distorted Phase Currents," in *International Conference on Electrical Machines*, 2010, pp. 1-7.

- [41] G. Sulligoi, A. Tassarolo, V. Benucci, M. Baret, A. Rebora, and A. Taffone, "Modeling, Simulation, and Experimental Validation of a Generation System for Medium-Voltage DC Integrated Power Systems," *IEEE Transactions on Industry Applications*, vol. 46, pp. 1304-1310, 2010.
- [42] A. G. Jack, B. C. Mecrow, and J. A. Haylock, "A Comparative Study of Permanent Magnet and Switched Reluctance Motors for High-performance Fault-tolerant Applications," *IEEE Transactions on Industry Applications*, vol. 32, pp. 889-895, 1996.
- [43] A. Damiano, G. Gatto, I. Marongiu, A. Serpi, and A. Perfetto, "A Multiphase PM Synchronous Generator Wind Turbine Control for Internal Medium Voltage DC Distribution System," in *International Symposium on Power Electronics, Electrical Drives, Automation and Motion 2012*, pp. 1256-1262.
- [44] N. E. A. M. Hassanain and J. E. Fletcher, "Steady-state Performance Assessment of Three- and Five-phase Permanent Magnet Generators Connected to a Diode Bridge Rectifier Under Open-circuit Faults," *IET Renewable Power Generation*, vol. 4, pp. 420-427, 2010.
- [45] Z. Zhang, Y. Yan, S. Yang, and Z. Bo, "Development of a New Permanent-Magnet BLDC Generator Using 12-Phase Half-Wave Rectifier," *IEEE Transactions on Industrial Electronics*, vol. 56, 2009.
- [46] Department of Defense, "Aircraft Electrical Power Characteristics MIL-STD-704F," Department of Defense Interface Standard, 1991.
- [47] N. Bianchi, *Electrical Machine Analysis Using Finite Elements*. Boca Raton: CRC Press, 2005.
- [48] N. Mohan, T. M. Undeland, and W. P. Robbins, *Power Electronics: Converters, Applications and Design*, 3rd ed.: John Wiley & Sons Ltd, 2003.
- [49] C. Ong, *Dynamic Simulation of Electric Machinery*: Prentice Hall, 1998.
- [50] I. Boldea, *The Electric Generators Handbook: Synchronous Generators* vol. 1: CRC Press, 2006.
- [51] R. H. Park, "Two-Reaction Theory of Synchronous Machines," *AIEE Transactions*, vol. 48, pp. 716-730, 1929.
- [52] N. N. Schulz, M. Lin, and A. K. Srivastava, "A Generic Digital Model of Multiphase Synchronous Generator for Shipboard Power System," in *Electric Ship Technologies Symposium*, Arlington, VA, USA, 2007, pp. 348-355.
- [53] P. Kundur, *Power System Stability and Control*: McGraw-Hill, 1994.
- [54] D. Izquierdo, A. Barrado, C. Raga, M. Sanz, and A. Lazaro, "Protection Devices for Aircraft Electrical Power Distribution Systems: State of the Art," *IEEE Transactions on Aerospace and Electronic Systems*, vol. 47, pp. 1538-1550, 2011.
- [55] P. J. Norman, S. J. Galloway, G. M. Burt, D. R. Trainer, and M. Hirst, "Transient Analysis of the More-electric Engine Electrical Power Distribution Network," in *4th IET Conference on Power Electronics, Machines and Drives*, 2008, pp. 681-685.
- [56] D. Izquierdo, R. Azcona, F. del Cerro, C. Fernandez, and B. Delicado, "Electrical Power Distribution System (HV270DC), for Application in More Electric Aircraft," in *Applied Power Electronics Conference and Exposition*, 2010, pp. 1300-1305.
- [57] R. Todd and A. J. Forsyth, "DC-bus Power Quality for UAV Systems During Generator Fault Conditions," in *5th IET International Conference on Power Electronics, Machines and Drives*, 2010, pp. 1-6.
- [58] W. Shanshan and L. Yongdong, "Application and Challenges of Power Electronics for Variable Frequency Electric Power System of More Electric Aircraft," in *International Conference on Electrical Machines and Systems*, 2011, pp. 1-4.

- [59] T. Clark, F. J. Chivite-Zabalza, A. J. Forsyth, and M. Barnes, "Analysis and Comparison of Diode Rectifier Units Suitable for Aerospace Applications," in *4th IET Conference on Power Electronics, Machines and Drives*, 2008, pp. 602-606.
- [60] K. Ki-Man, P. Sang-Hoon, L. Jung-Hyo, J. Chul-ho, and W. Chung-Yuen, "Mode Change Method of Bi-directional DC/DC Converter for Electric Vehicle," in *IEEE 8th International Conference on Power Electronics*, 2011, pp. 2687-2693.
- [61] M. E. El-Hawary, *Electrical Energy Systems*. Boca Raton, FL: CRC Press, 2000.
- [62] A. E. Fitzgerald, Charles Kingsley, Jr., and S. D. Umans, *Electric Machinery*, 6th ed. New York: McGraw-Hill, 2003.
- [63] P. L. Alger, *Induction Machines Their Behavior and Uses*: Gordon and Breach Science, 1995.
- [64] I. Batarseh, *Power Electronic Circuits*: John Wiley & Sons Ltd, 2004.
- [65] A. Thom and C. J. Apelt, *Field Computations in Engineering and Physics*. London: Van Nostrand Reinhold, 1961.
- [66] D. L. Logan, *A First Course in the Finite Element Method*, 5th ed.: Global Engineering, 2011.
- [67] D. Meeker, "Femm", <http://www.femm.info/wiki/HomePage> [accessed: 2nd November 2009]
- [68] M. G. Say, *Alternating Current Machines*, 5th ed.: John Wiley & Sons Ltd, 1992.
- [69] Collaboration for Nondestructive Testing, "Copper and Copper Alloys", 2001, http://www.ndt-ed.org/GeneralResources/MaterialProperties/ET/Conductivity_Copper.pdf [accessed: 5th January 2012]
- [70] AK Steel, "Selection of Electrical Steels for Magnetic Cores ", 2007, http://www.aksteel.com/pdf/markets_products/electrical/Mag_Cores_Data_Bulletin.pdf [accessed: 13th February 2012]
- [71] Rolls-Royce, "Trent 1000 Optimised for Boeing 787 Dreamliner Family," Rolls-Royce Technical Publications, 2010.
- [72] L. Parsa and H. A. Toliyat, "Fault-tolerant five-phase permanent magnet motor drives," in *Industry Applications Conference, 2004. 39th IAS Annual Meeting. Conference Record of the 2004 IEEE*, 2004, pp. 1048-1054 vol.2.
- [73] D. Hanselman, *Brushless Permanent Magnet Motor Design*, 2nd ed.: The Writers' Collective, 2006.
- [74] Standard Instruments, "High Accuracy Tachometers", 2005, http://www.standardinst.com/frames/tacho_2.html [accessed: 12th November 2011]
- [75] IEEE Standards Board, "IEEE Guide: Test Procedures for Synchronous Machines," The Institute of Electrical and Electronic Engineers Inc., 1996.

Appendices

Appendix

7.1 Construction of Experimental	
Test-rig.....	187
7.2 Winding Factors.....	194
7.3 Calculation of Equivalent Circuit	
Parameters	199
7.4 Characterisation and Testing of a Three- Phase Synchronous Generator	201
7.5 Parameters for Synchronous	
Generator	212
7.6 Simulation Model	213
7.7 State-space Matrices	218
7.8 Experimental and Simulation Results...	219
7.9 Further Experimental Results	220

7.1 Construction of Experimental Test-rig

The experimental test-rig, schematically depicted in Section 5.2, comprises a DC drive machine, a synchronous generator and a power electronic converter. The machines were placed in a back to back arrangement to enable the rotors of the machines to couple and provide a suitable input to the synchronous generator, shown in *Figure 7.1*.

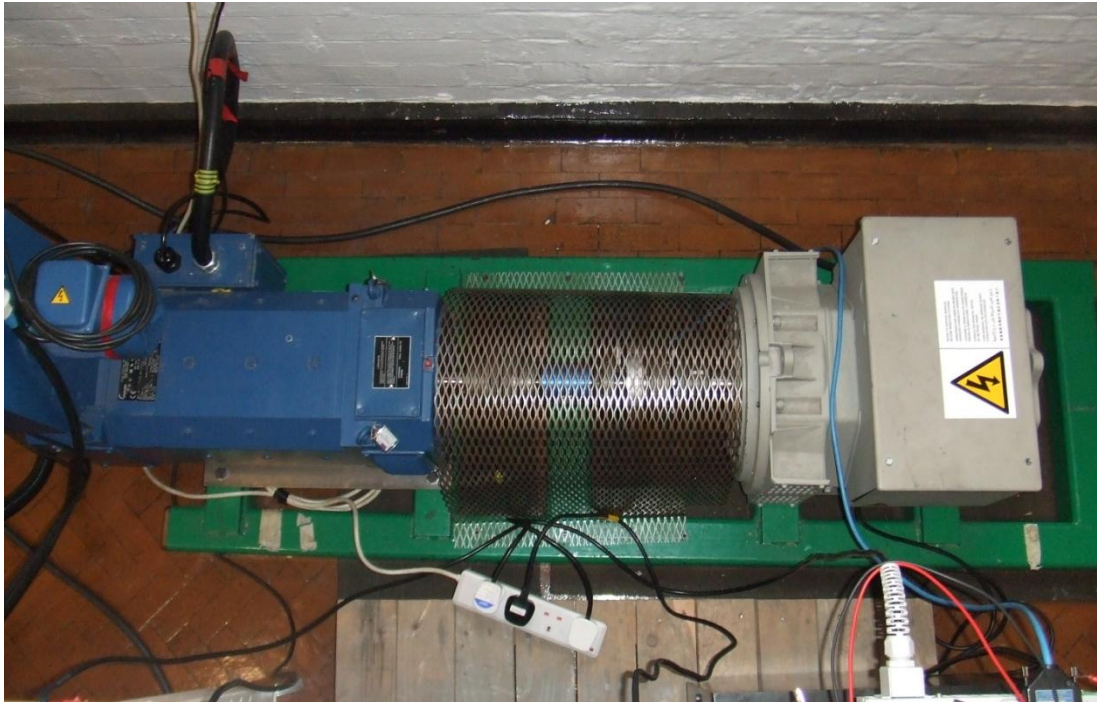


Figure 7.1: DC Machine Connected to Synchronous Generator

A standard three-phase, off-the-shelf, BCI162G model was used for parameter extraction and datasheet validation testing. A second BCI162G generator was rewound for multiphase operation.



Figure 7.2: Original BCI162G Generator Stator

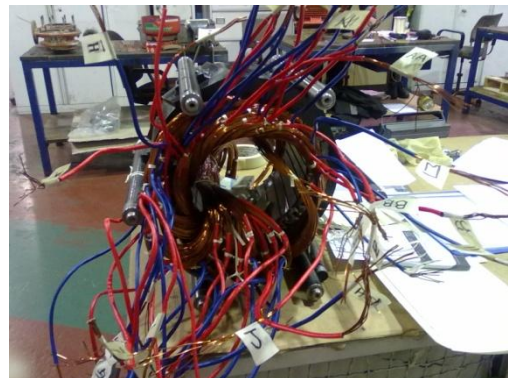


Figure 7.3: Modified BCI162G Generator Stator (Under Construction)

The rewind took several months which allowed the full characterisation of the three-phase generator, the modification of the rotor and the expansion to the test-rig to include a wiring cabinet.

The original rotor used a brushless excitation system which was controlled by an AVR unit, supplied with the generator. In order to control and measure the voltages and currents used to produce the field and provide the correct voltage output for the multiphase generator, the exciter was removed and replaced with slip rings and brushes.

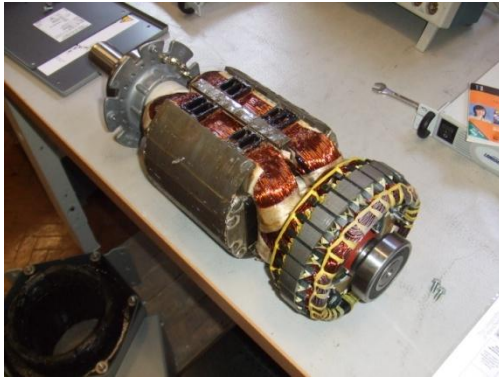


Figure 7.4: Original Rotor with Brushless Excitation



Figure 7.5: Modified Rotor with Slip Rings

The machine was tested for accuracy before being varnished. These tests involved establishing the correct coil position in the stator, the correct number of parallel turns and that the insulation between coils was sufficient.



Figure 7.6: Testing of Rewound BCI162G Generator



Figure 7.7: Rewound Stator Housed in Original Casing with Spigot for Brushes

The carbon brushes were inserted into brush holders that were mounted onto a spigot and placed inside the body of the generator, in the area that the exciter stator previously occupied.



Figure 7.8: Protective Insert to Prevent Damage to Stator Laminations

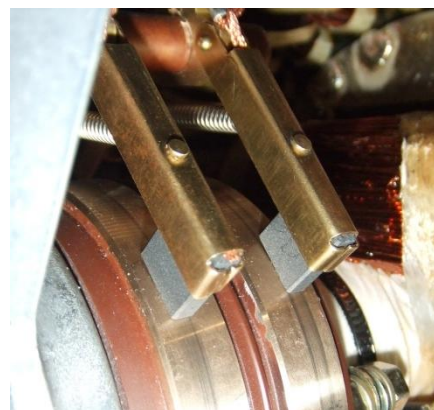


Figure 7.9: Brushes in Situ

Once the rotor had been fitted, the cooling fan could be replaced with modification due to the change in end-winding size. The fan clearance was adjusted to prevent catching the end-windings and balanced to ensure steady operation.



Figure 7.10: Cooling Fan Placement in Generator



Figure 7.11: Clearance between Fan and Windings

The machine was be fully reassembled in the original housing, the machine volume and casing remained unchanged.



Figure 7.12: Front of Rewound Generator



Figure 7.13: Rear of Rewound Generator with DC Input Lead to Brushes

The cabinet used to house the terminals of the multiphase synchronous generator was attached to the end of the test-rig bed plate. This also housed the power electronics.



Figure 7.14: Multiphase Synchronous Generator in Situ



Figure 7.15: External Wiring Cabinet for Multiphase Terminals and Power Electronics

The rectifier was connected to a resistive load bank and the measurement devices were connected to a LeCroy Oscilloscope for data capture.

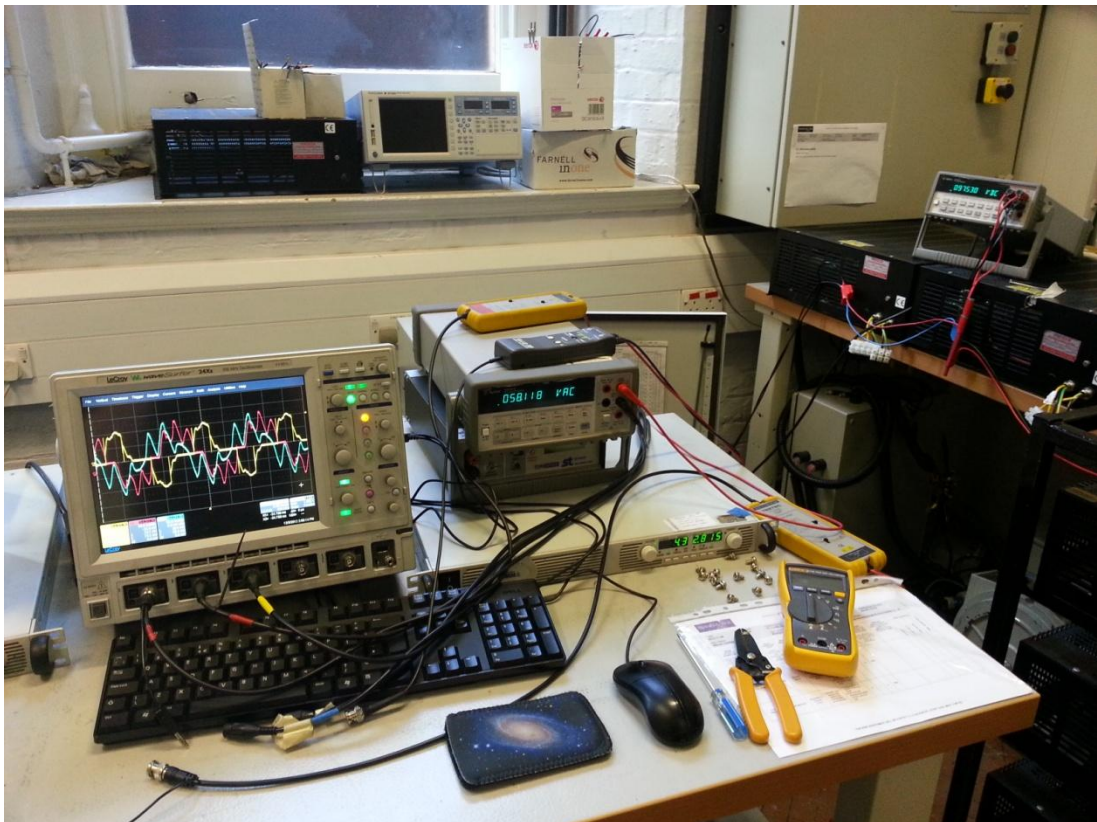
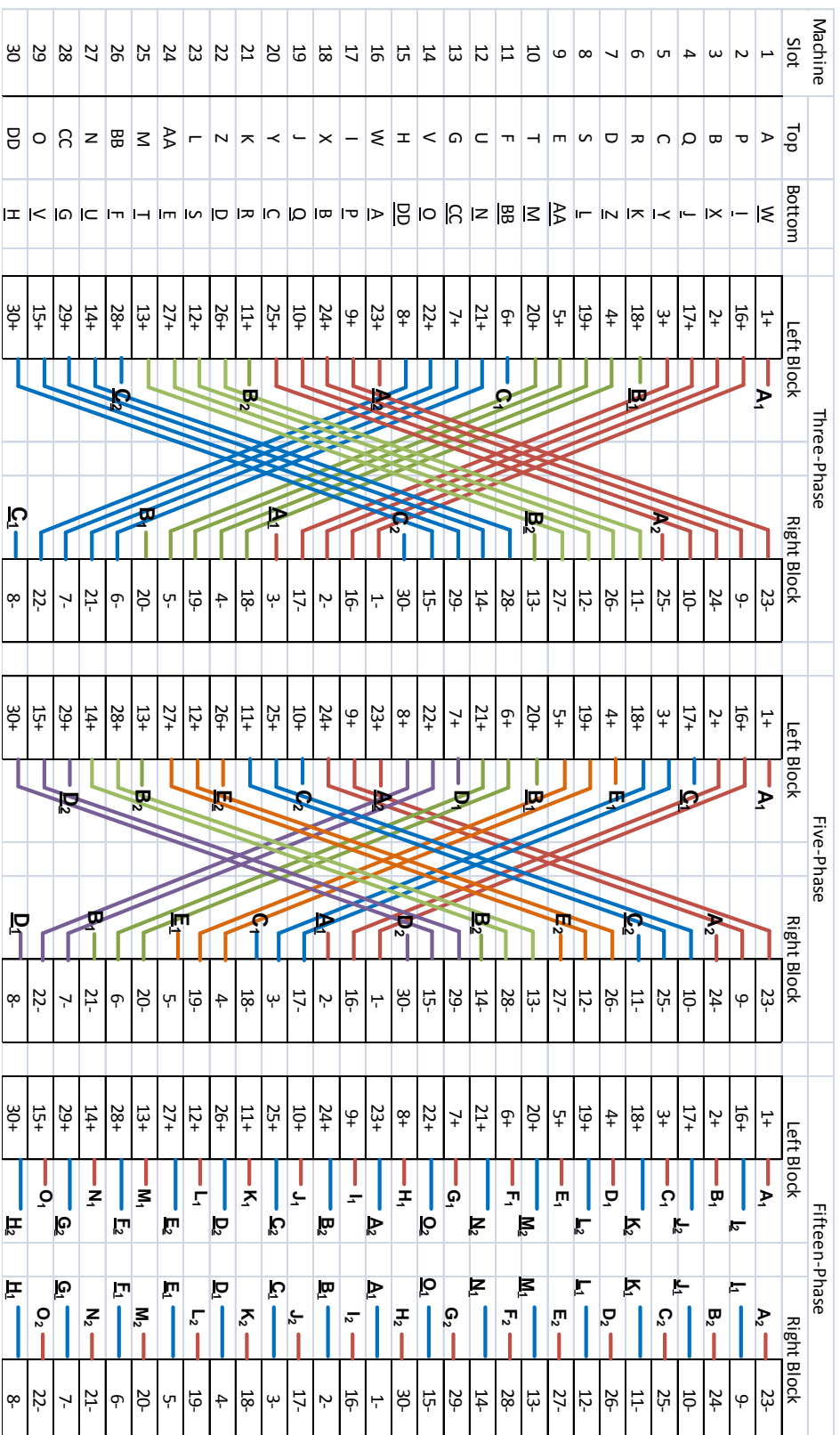


Figure 7.16: Experimental Test-rig in Operation

Fully-pitched



Numbers correspond to lettering of phase windings not stator slot position

Cabinet Wiring Diagram

7.2 Winding Factors

The winding factors for the machine show the harmonics magnitudes for the expected winding distribution when short-pitched. The following tables show the expected magnitudes for the harmonic developed in a simple distributed winding, a fully-pitched winding and the proposed short-pitched winding. These are calculated from Equation (49) which was taken from [62]:

$$k_{wn} = \frac{\sin\left(\frac{m_c n \beta}{2}\right)}{m_c \sin\left(\frac{n \beta}{2}\right)} \cos\left(\frac{n \alpha_s}{2}\right) \quad (49)$$

where k_{wn} is the harmonic scaling magnitude, m_c is the number of coils per phase belt, n is the harmonic number, β is the slot angle and α_s is the short-pitch angle.

7.2.1 Three-Phase Winding Factor

Coils per phase belt	m_c	5
Slot angle	β	12° (0.209 radians)
Short-pitch angle	α_s	= $k\beta$ (where k is an integer value)

Table 7.1: Three-phase Winding Factors

Harmonic number (n)	Simple distributed winding (1/n)	Winding factor k_{wn} for short-pitch angle $\alpha_s = 0^\circ$	Winding factor k_{wn} for short-pitch angle $\alpha_s = 60^\circ$
1	1.0000	0.9567	0.8285
3	0.3333	0.6472	0.0000
5	0.2000	0.2000	-0.1732
7	0.1429	-0.1494	0.1294
9	0.1111	-0.2472	0.0000
11	0.0909	-0.1095	-0.0948
13	0.0769	0.1022	0.0885
15	0.0667	0.2000	0.0000

7.2.2 Five-Phase Winding Factor

Coils per phase belt	m_c	3
Slot angle	β	12° (0.209 radians)
Short-pitch angle	α_s	$= k\beta$ (where k is an integer value)

Table 7.2: Five-phase Winding Factors

Harmonic number (n)	Simple distributed winding (1/n)	Winding factor k_{wn} for short-pitch angle $\alpha_s = 0^\circ$	Winding factor k_{wn} for short-pitch angle $\alpha_s = 36^\circ$
1	1.0000	0.9854	0.9372
3	0.3333	0.8727	0.5129
5	0.2000	0.6667	0.0000
7	0.1429	0.4030	-0.2369
9	0.1111	0.1273	-0.1211
11	0.0909	-0.1128	0.1072
13	0.0769	-0.2757	0.1621
15	0.0667	-0.3333	0.0000

7.2.3 Fifteen-Phase Winding Factor

Coils per phase belt	m_c	1
Slot angle	β	12° (0.209 radians)
Short-pitch angle	α_s	$= k\beta$ (where k is an integer value)

Table 7.3: 15-phase Winding Factors

Harmonic number (n)	Simple distributed winding (1/n)	Winding factor k_{wn} for short-pitch angle $\alpha_s = 0^\circ$	Winding factor k_{wn} for short-pitch angle $\alpha_s = 36^\circ$
1	1.0000	1.0000	0.9511
3	0.3333	1.0000	0.5878
5	0.2000	1.0000	0.0000
7	0.1429	1.0000	-0.5878
9	0.1111	1.0000	-0.9511
11	0.0909	1.0000	-0.9511
13	0.0769	1.0000	-0.5878
15	0.0667	1.0000	0.0000

7.2.4 Rotor Winding Factor

$$\begin{aligned}\hat{B} &= \frac{4\mu_0}{\pi g} \left(\frac{k_{wr} N_f}{p} \right) I_f^r \\ 0.85 &= \frac{4 \cdot 4\pi \times 10^{-7}}{\pi \cdot 0.0012} \left(\frac{k_{wr} 390}{2} \right) 5 \\ 0.85 &= 1.33 \times 10^{-3} \left(\frac{k_{wr} 390}{2} \right) 5 \\ k_{wr} &= 0.6538\end{aligned}$$

where, \hat{B} is the peak flux density taken from an air-gap contour, μ_0 is the permeability of free space, g is the air-gap length, k_{wr} is the rotor winding factor, N_f is the number of rotor windings, p is the number of poles and I_f^r is the rotor field current (magnitude assumed based on stator referred simulation levels) [62].

7.2.5 Current Density

The current density within the stator slot can affect the performance of the generator. The generator is currently air cooled, due to the current density being within acceptable limits, i.e. less than the quoted value of 6 A/mm² [50, 73].

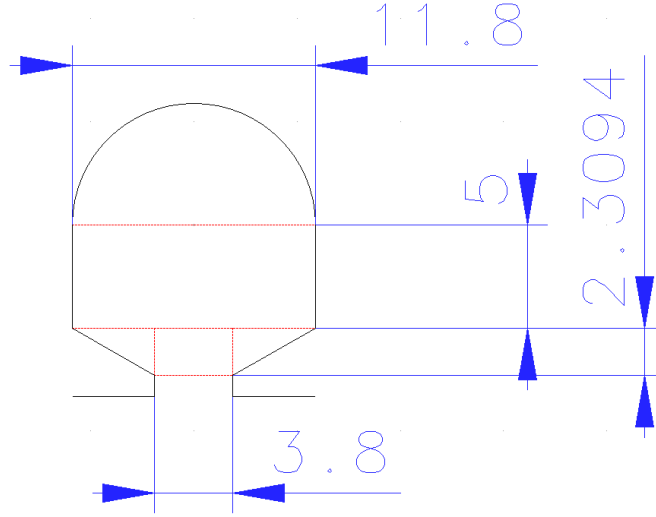


Figure A. 1: Stator Slot

6 strands of 0.85 mm thickness conductor in parallel provides a 5.1 mm² copper cross-sectional area. There were 8 turns per coil giving a total copper area of 40.8 mm² for one-layer winding in the old machine. Manufacturer quoted data shows a fill factor of 83.7 %, which can be deemed excessive and assumes that the enamel thickness is included. The rewound machine has 7 coils which gives a copper area of 35.7 mm². Fully-pitched with both coils carrying maximum current, the current density is given by Equation (50).

$$J = \frac{A_{slot} \cdot N_{ss} \cdot k_{fill}}{6 \cdot W_A \cdot I_n} \quad (50)$$

where A_{slot} is the useful copper slot area, N_{ss} is the number of stator slots, k_{fill} is the copper winding fill factor, W_A is the turns per path per phase and I_n is the rated current.

$$J = \frac{71.4 \times 30 \times 0.837}{6 \times 1.667 \times 76} = 2.359 \text{ A/mm}^2$$

This uses the winding factor from the manufacturer datasheet which would appear to be an overestimation of the copper fill factor. A lower fill factor will reduce the current density and the generator will still remain in acceptable limits. The generator, therefore, requires no special cooling techniques.

7.3 Calculation of Equivalent Circuit Parameters

The generator is supplied with a datasheet, providing parameters gained from testing the unit; these include synchronous, transient and sub-transient reactance values for both the d and q axes as well as generalised information regarding the brushless exciter. This section shows how the equivalent circuit parameters were determined from the datasheet values. As a result of the limited information provided, the brushless exciter, at this stage, is not fully modelled and the complexity of the system prevents characterising it through testing, field coil parameters were the only values used.

The provision of the d and q axis synchronous reactances, depicted in the equivalent circuit form in *Figure 7.17*, and the leakage reactance allowed the simple calculation of the magnetising reactance illustrated in Equation (51).

$$\begin{aligned} X_{md} &= X_d - X_l \\ X_{mq} &= X_q - X_l \end{aligned} \quad (51)$$

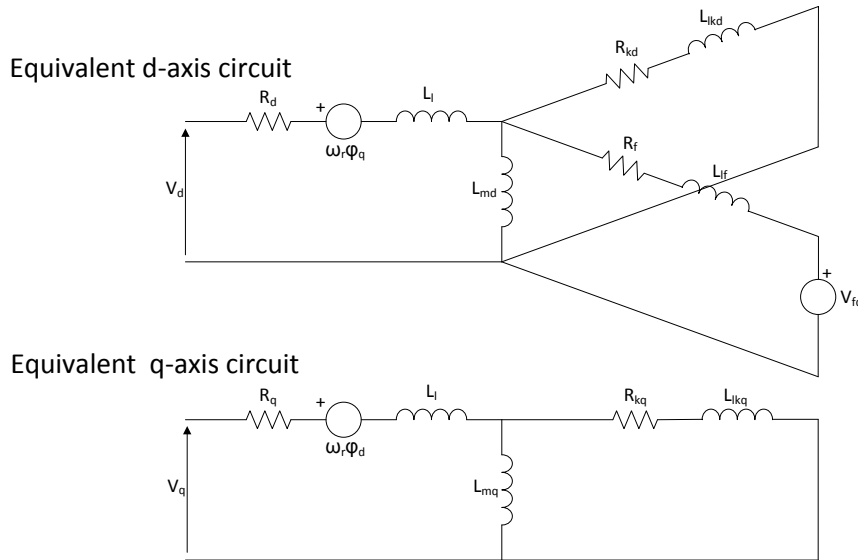


Figure 7.17: Equivalent circuit of a synchronous generator [53]

From these, further d-q axis parameters could be calculated such as the damper and field winding resistances and reactances, in per unit and Standard International (SI) units. The d and q axis damper winding leakage reactances are calculated in Equation (52), taken from [53]. Power system generators rely on two damper windings on the q-axis where smaller generators, as in this case, need only one damper winding placed on the q-axis.

Assumptions made in calculating the inductance values are that resistances are assumed small enough to be neglected and associated time constants allow for separate calculation.

$$X_{lkd} = \frac{(X_d'' - X_l) X_{md} X_{lf}}{X_{md} X_{lf} - [(X_d'' - X_l)(X_{md} + X_{lf})]}$$

$$X_{kd} = X_{lkd} + X_{md}$$
(52)

$$X_{lkq} = \frac{X_{mq} (X_q'' - X_l)}{X_{mq} + X_l - X_q''}$$

$$X_{kq} = X_{lkq} + X_{mq}$$

The parameters shown in Equation (52) are in per unit notation, conversion from per unit to SI units is highlighted in Equation (53).

$$X_{kd(SI)} = X_{kd(pu)} \cdot Z_{base}$$
(53)

where

$$Z_{base} = \frac{(V_{base})^2}{S_{base}}$$

The resistances can be found in a similar manner, however, they require information about the transient and sub-transient time constants for calculation, as the field resistance calculation illustrates in Equation (54).

$$R_{f(SI)} = \frac{X_{lf} + \left(\frac{(X_{md} X_{lf})}{X_{md} + X_{lf}} \right)}{T_d' \omega_{base}} \cdot Z_{base}$$
(54)

Extending this to the damper winding resistances gives Equation (55).

$$R_{kd(SI)} = \frac{X_{lkd} + \left(\frac{(X_{md} X_l X_{lf})}{(X_{md} X_l) + (X_{md} X_{lf}) + (X_l X_{lf})} \right)}{T_d'' \omega_{base}} \cdot Z_{base}$$
(55)

$$R_{kq(SI)} = \frac{X_{lkq} + \left(\frac{(X_{mq} X_l)}{X_{mq} X_l} \right)}{T_q'' \omega_{base}} \cdot Z_{base}$$

7.4 Characterisation and Testing of a Three-Phase Synchronous Generator

7.4.1 Introduction

Cummins Generator Technologies specialise in the manufacture and distribution of high quality brushless AC generators for commercial and industrial applications. The BCI162G is a self-excited three-phase, two-pole, salient rotor synchronous generator rated to produce 20 kW with a terminal voltage of 380 V_{L-L RMS} in series-star configuration. The supplied datasheet, see Appendix 7.5, provides detailed information regarding the stator and rotor parameters.

In establishing the datasheet as being accurate, the parameters contained within can be utilised in the mathematical modelling of the BCI162G synchronous generator and compared with experimentally obtained data. The pre-processor script for the model in Chapter 3 was altered accordingly to include the datasheet parameters before configuring the model to simulate the required test. In order to verify that the mathematical model developed was accurate, a standard synchronous generator model was used from the SimPowerSystems library to directly compare the simulation outputs.

Conducting open-circuit tests establishes the machine performance aspects, internal voltage magnitudes, for example, and provides information about the excitation of the machine [62]. Short-circuit testing infers the behaviour of the current carrying paths, providing information with regard to leakage impedances and losses associated with the current loading of the machine, I^2R and stray load losses.

The test platform comprises the three-phase synchronous generator being driven by a DC machine capable of rotating at 3000 rpm, synchronous speed. The speed of the DC machine was controlled by altering the rotor field voltage locally, allowing slip testing to be carried out. Measurement of the rotor speed was obtained from a Standard Instruments ST-6236B digital tachometer which has a measuring accuracy of 0.05 % [74]. The speed was measured on the DC machine side of the shaft which was coupled to the synchronous generator through a torque sensor and torque coupling. The coupling is fixed with a clutch mechanism to disengage the two shafts if peak torque is exceeded. Since the peak torque was not achieved, it can be assumed that the speed at both ends of the shaft is consistent. Noise present within the measurement of the voltage and current may lead to the results being over estimated. The resolution of the Tektronics oscilloscope used is good for short

transients. However, in order to capture the full waveform as it peaks and troughs results in a lower resolution and the inclusion of noise becomes more evident.

7.4.2 Slip Test

Conducting slip tests enables the evaluation of d- and q-axis synchronous reactance parameters through the relationship between the stator current and voltage [75]. The stator is supplied with a reduced voltage through a variable transformer in order to prevent saturation within the stator core. The field winding of the synchronous generator is open-circuited so that there is no external excitation imposed on the rotor. Under slip conditions the stator interacts with the rotor damper windings, however, it is important to retain the slip at a low value. This reduces the magnitude of the currents driven around the damper windings, allowing their effects to be neglected in the calculation of the d-q synchronous reactances. If this is not the case then the synchronous parameters will be underestimated.

Since the machine is driven at a rotational speed, ω_r , and the stator is supplied with voltages of a fixed frequency, ω_{r0} , a difference arises between the stator field and the rotor field as an emf is developed in the rotor winding. The saliency of the rotor causes the stator field to fluctuate in a periodic motion. This gives rise to peaks and troughs in the sinusoidal currents and voltages at the stator terminals, providing information on the synchronous reactances, highlighted in Equation (56).

$$X_d = \frac{E_{aMAX}}{I_{aMIN}} \quad X_q = \frac{E_{aMIN}}{I_{aMAX}} \quad (56)$$

The mathematical model can be configured to reflect this testing by introducing a proportional integral control loop to the field winding, driving the current to zero and, therefore, simulating the open-circuit condition imposed in the practical experimentation. The speed reference is configured to ensure that the machine runs at below synchronous speed, enabling the damper interaction in the simulation model. The same voltage was applied to the simulation model as in the experiment with a reduced voltage – 40 % rated voltage – preventing saturation of the stator iron. The simulated results are shown in *Figure 7.18*.

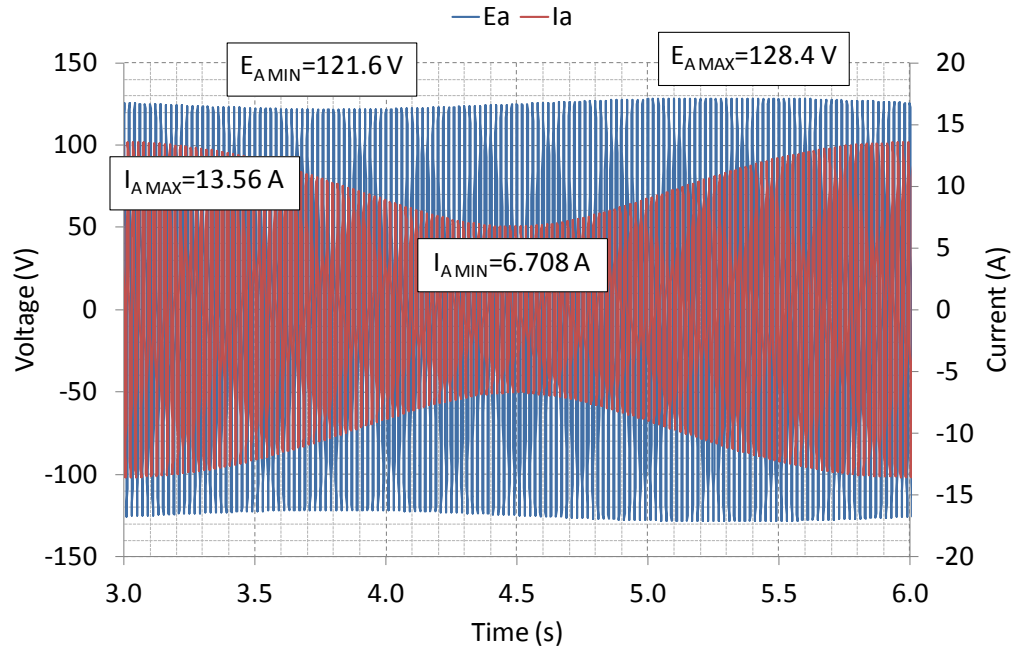


Figure 7.18: Simulated slip test at 2990 rpm

The test was repeated across a number of speeds down to 1 % of the synchronous speed.

Using the measured stator currents in the finite element model, with an unexcited rotor for different rotor positions, allowed the parameters gained in the experimentation to be verified. The results, displayed in Figure 7.19, support the experimental data rather than that gathered from the datasheet. The generator is acting in a state which is not representative of its intended application where it would run at synchronous speed with rotor excitation present.

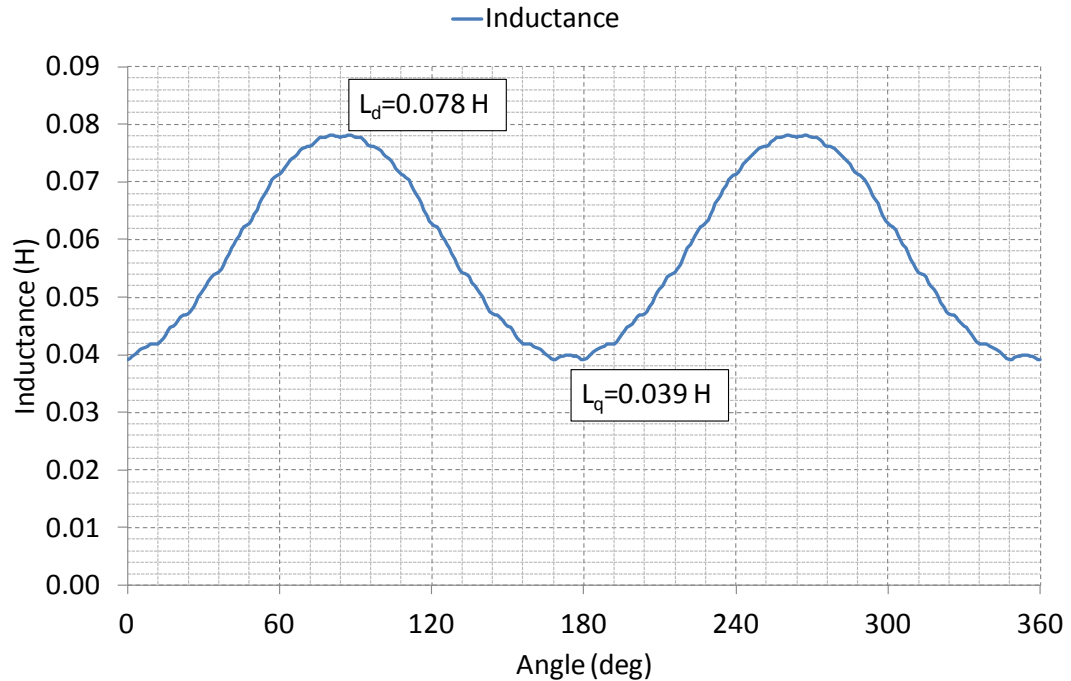


Figure 7.19: Finite Element Simulated Inductances (Unexcited Rotor)

Since the experimental values have been verified by the finite element analysis, it is important to establish how this new data affects the simulation of the slip test when the experimental values for this generator are implemented. Together with the short-circuit parameters detailed in Section 7.4.3, the d- and q-axis synchronous reactances can be applied along with the respective time constants obtained.

The standard three-phase SimPowerSystems model was used to verify that the experimental parameters used in the dynamic circuit model for the slip test conditions. The average d- and q-axis inductance is 0.0794 H and 0.0345 H, respectively. This can be observed for both the SimPowerSystems and standard dynamic circuit model. Extrapolating the data to find the no-slip case gives a value of 0.0763 H and 0.0345 H, respectively. Comparing this data to those from experimental testing, the average d- and q-axis inductance across the slip test speed range is 0.0745 H and 0.0352 H, respectively. The simulation results, performed using experimental parameters, represent a 6.6 % deviation from the experimentally measured values for the d-axis inductance and 2 % for the q-axis value.

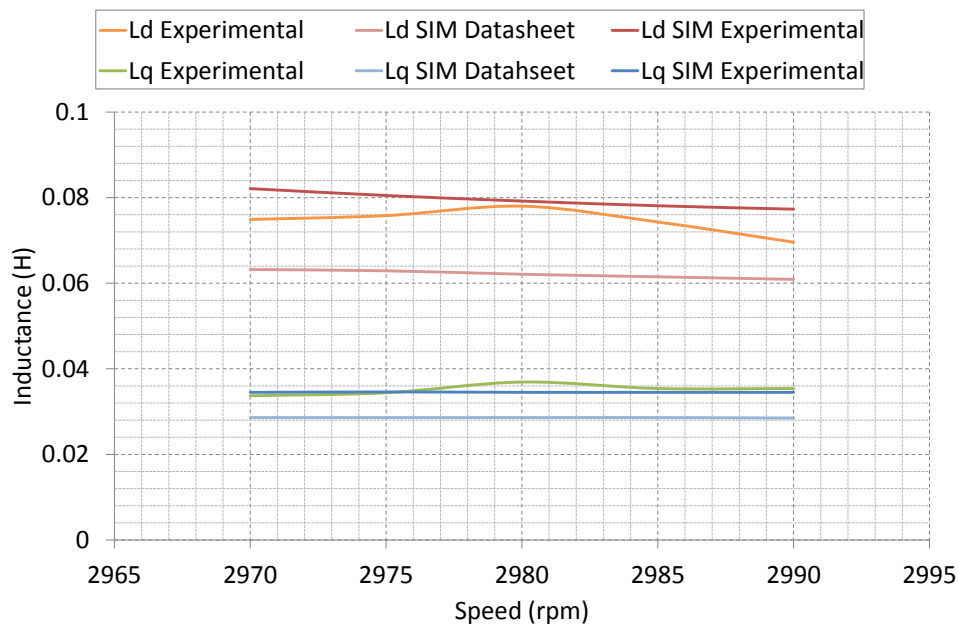


Figure 7.20: d - q axis Inductances for Slip Test

It is clear from *Figure 7.20* that the datasheet parameters are not consistent to describe the behaviour of the machine used in experimental testing. The simulation of the parameters derived from the experimental testing showed a much better agreement. This could be due to differences in the construction of the generator during the manufacturing process resulting in variations in the parameters that invalidate the parameters contained within the datasheet.

7.4.3 Short-circuit Test

Open-circuit testing, such as the slip tests performed, provides only a fraction of the information contained within the datasheet. Conducting the short-circuit tests will provide d -axis reactances and transient time constants based on the machine performance when subjected to a short-circuit fault across all three phases. The methodology for conducting this type of test was sourced from the IEEE standards [75].

The mechanical and thermal stress on the machine can be considerable and it was therefore decided to limit the terminal voltage at which the test was conducted. As a safety precaution the DC machine driving the shaft connected to the synchronous machine is fitted with a torque limiter ensuring that no excessive load could be transferred through the rotor shaft. The synchronous generator was supplied with a low voltage DC input to the field winding of the brushless exciter, bypassing the automatic voltage regulator (AVR). Synchronous speed was maintained by varying the field winding voltage supplied to the DC machine, ensuring that the machine returned to synchronous speed for the steady-state

fault condition after the initial transient. The short-circuit test set-up is depicted in *Figure 7.21*.

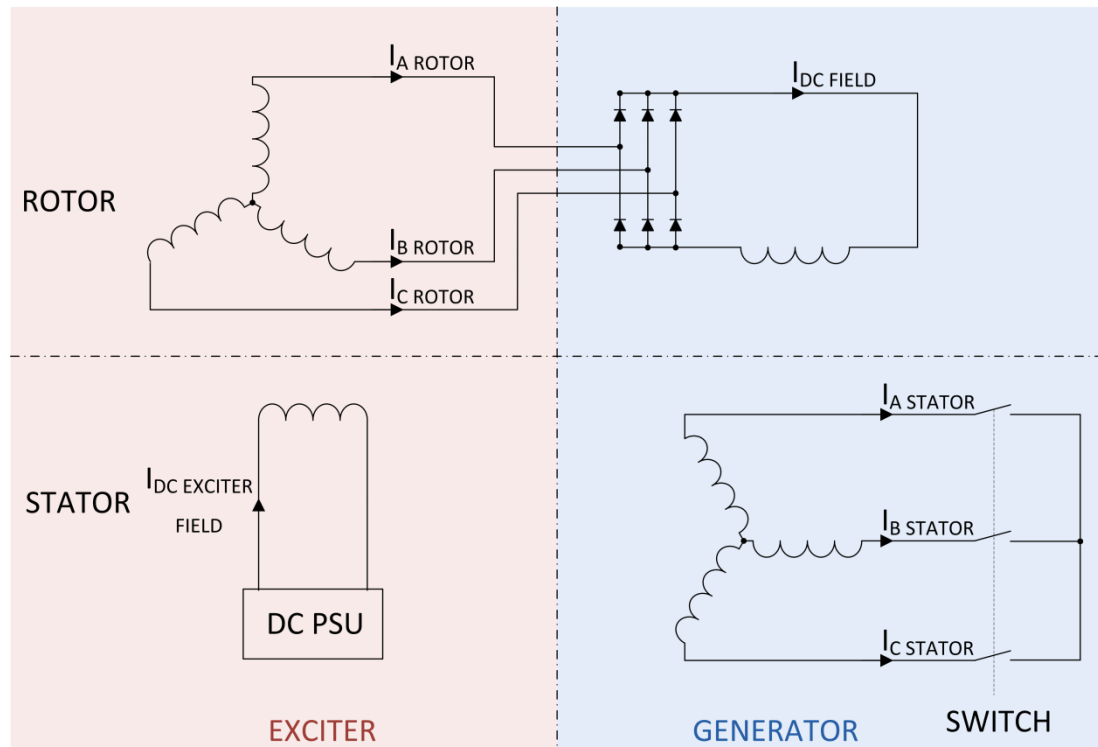


Figure 7.21: Diagram of Short-circuit Test Conditions Applied to a Synchronous Generator

The synchronous generator terminal voltage was increased in 50 V steps from the initial 150 V_{L-L RMS}, up to 250 V_{L-L RMS}. The output waveform gave an exponential decay which can be used to determine the magnitude of the time constants governing the machine behaviour. The d- and q-axis sub-transient time constants cannot be found in this instance as they occur too fast to be detected in a machine of this size. Such time constants can be found in large-scale synchronous generators used in power systems, as discussed in [53], since they are designed to have a low resistance, hence a slower transient response to short-circuit fault conditions.

Running the machine over the range of terminal voltages described, the peak short-circuit current magnitudes and steady-state values can be compared with those obtained from the simulation results using the nominal datasheet parameters, shown in *Table 7.4*. Using the averaging function within Excel the noise included within the experimental transient data acquisition can be accounted for to a degree, particularly in the steady-state fault condition.

Table 7.4: Experimental and Simulation Short-circuit Transient Currents

Terminal Voltage	Experimental Peak Transient Current	MATLAB Simulink Peak Transient Current*	Experimental Steady-State Current	MATLAB Simulink Steady-State Current*
(V)	(A _{pk})	(A _{pk})	(A _{pk})	(A _{pk})
150	108	85	10	6.67
200	134	113.1	11	8.89
250	144	141	12	11.11

* Nominal Datasheet Parameters

The discrepancy in the peak values could be due to the instance of time at which the short-circuit fault is invoked. The position of the rotor at that instant will have an effect on the emf induced in the stator winding aligned with rotor flux. The switching of the short-circuit fault in laboratory conditions occurs at arbitrary times. However, it was carried out a number of times to ensure that there was not a significant variation of the peak current magnitudes.

The transient behaviour of the simulation with datasheet parameters does not coincide with the behaviour seen from the test generator. The sinusoidal exponential decay observed in the experimental testing is not replicated by the simulation, as shown in *Figure 7.22* and *Figure 7.23*, respectively.

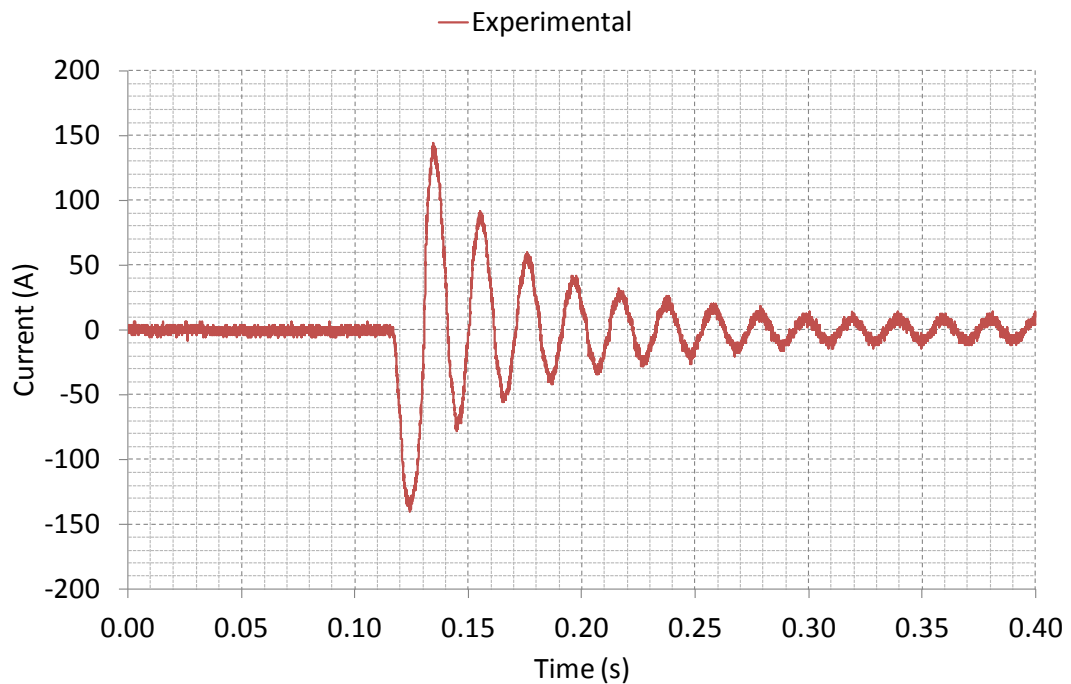


Figure 7.22: Experimental Short-circuit Current Transient at 250 V_{L-L}

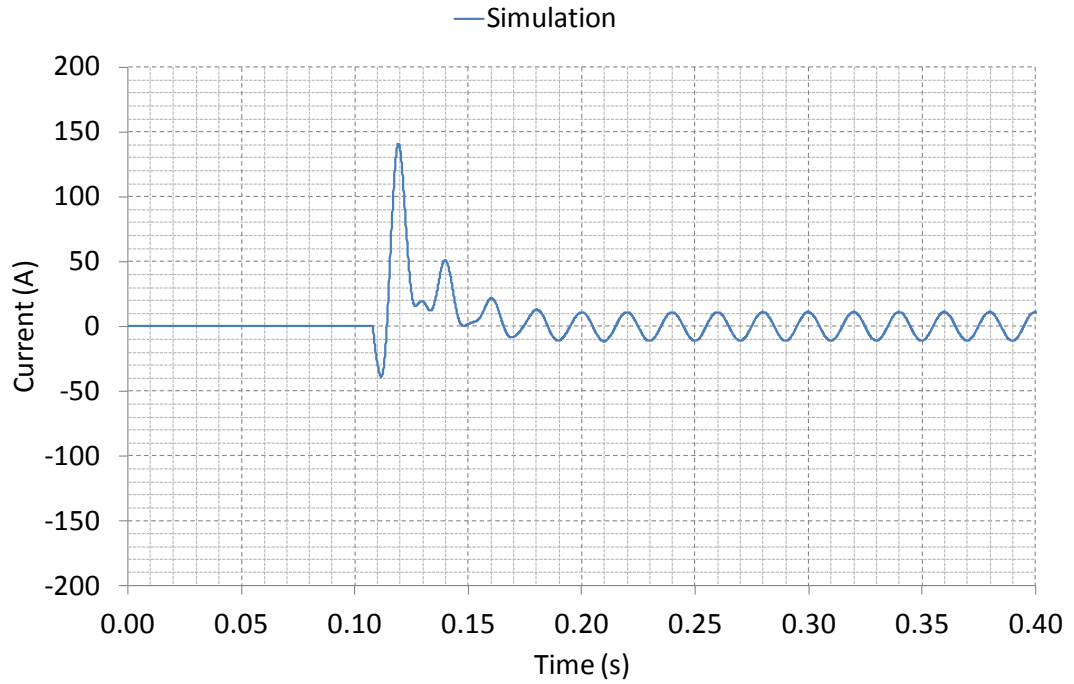


Figure 7.23: Simulation (Datasheet Parameters) Short-circuit Current Transient at 250 V_{L-L}

It is clear from these two figures that there is a discrepancy in the behaviour of the generator when simulated with the datasheet parameters. Referring back to *Table 7.4*, the steady-state current is comparable at rated voltage, which would indicate that the d-axis synchronous reactance agrees with that quoted by the datasheet. The SimPowerSystems model gave the same response as that depicted in *Figure 7.23*, signifying that the model was acting correctly for the parameters given.

Implementing the reactances and time constants gained from the open-circuit and short-circuit experimental testing it is possible to assess the validity of the information contained within the datasheet. The field resistance, R_f , used in the simulation model is shown in Equation (57).

$$R_{f(SI)} = \frac{X_{lf} + \left(\frac{(X_{md} X_{lf})}{X_{md} + X_{lf}} \right)}{T_d' \omega_{base}} \cdot Z_{base} \quad (57)$$

where X_{lf} is the field leakage reactance, X_{md} is the d-axis magnetising reactance, T_d' is the d-axis transient time constant, ω_{base} is the line frequency and Z_{base} is the per unit base impedance.

Implementing these changes, the resulting AC short-circuit transient current waveform is depicted in *Figure 7.24*, highlighting the distinct difference in performance due to the parameters entered into the simulation. The field voltage required to achieve the maximum test line-to-line RMS terminal voltage was greatly reduced as a result of the value for the field resistance, R_f , being changed.

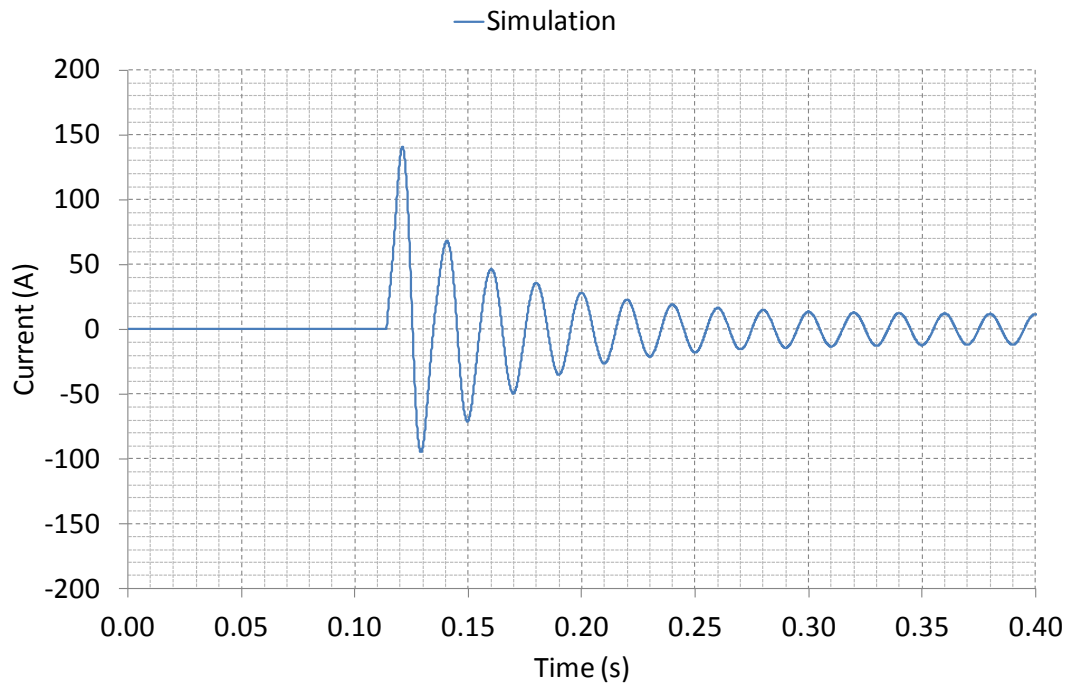


Figure 7.24: Simulation Short-circuit Current Transient from Experimental Parameters

The behaviour of the simulation with experimental parameters is much more consistent with the machine transient behaviour in *Figure 7.22*. The parameters gained from the short-circuit testing are drawn through the consideration of each separate stage of the short-circuit response. The initial transient governs the sub-transient reactance, followed by the transient reactance and finally the steady-state synchronous reactance. As previously discussed, the d- and q-axis sub-transient time constants cannot be found. However, the d-axis transient time constant can be obtained from the time at which the short-circuit condition was invoked up to the time at which the peak magnitude falls to $1/e$ its original value. The transient time quoted in the datasheet for the d-axis transient time constant is 0.012 seconds. The experimental data, with the exponential envelope, gave a much slower transient time constant value of 0.0468 seconds. The calculation method is illustrated in *Figure 7.25*.

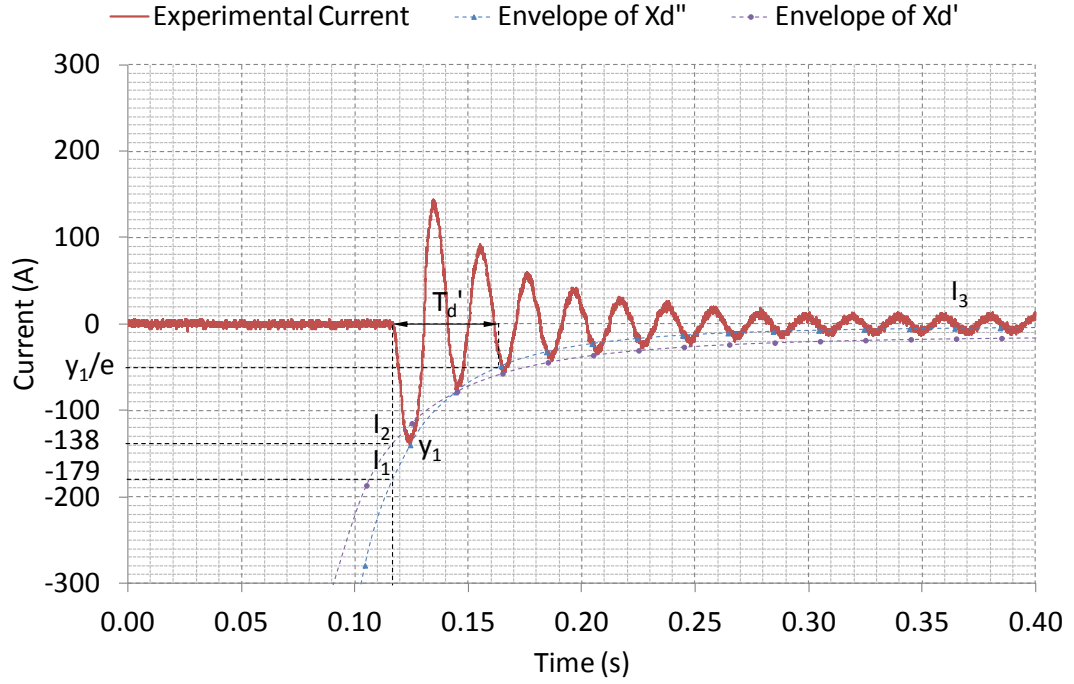


Figure 7.25: Calculation of Parameters from Short-circuit Response

The current values marked, in Figure 7.25, denote the value of current at the instant of the short-circuit event based on the envelope of the sub-transient (blue dashed line) and transient (purple dashed line) value. The synchronous reactance is based on the steady-state short-circuit fault envelope which, since it is in a steady-state, is the maximum (or minimum) value. The initial peak current, y_1 , determines the transient time constant, as discussed above.

$$\begin{aligned}
 X_d'' &= \frac{V}{I_1} = \left(\frac{\sqrt{2} \times 250}{\sqrt{3}} \right) / 179 = 1.1404 \Omega \\
 X_d' &= \frac{V}{I_2} = \left(\frac{\sqrt{2} \times 250}{\sqrt{3}} \right) / 138 = 1.4792 \Omega \\
 X_d &= \frac{V}{I_3} = \left(\frac{\sqrt{2} \times 250}{\sqrt{3}} \right) / 14 = 14.5803 \Omega
 \end{aligned} \tag{58}$$

The values, calculated in Equation (58), are in SI units. The pre-processor script used in MATLAB to initialise the variables for the mathematical model uses per unit values, requiring the simple division of the SI unit values by the base impedance, Z_{base} . A list of the new experimental values obtained for the BCI162G generator can be found in Appendix 7.5.

7.4.4 Summary

Slip testing showed that there were significant differences in the synchronous parameters provided in the datasheet and those obtained from conducting the relevant testing. Further characterisation was conducted to find more parameters in order to calculate the remaining necessary information for the accurate modelling of the dynamic circuit behaviour.

Transient effects were investigated through short-circuit testing. This allowed for the extraction of sub-transient and transient reactances and time constants. The synchronous reactance calculated from this test, however, is much lower than that quoted in the datasheet. It also differs from the experimental slip test calculations which were consistently above the quoted data. The verification of the slip results with finite element modelling, configured to reflect the currents in the machine, would suggest that these are the best values to utilise for further simulation work regarding the generator at reduced rotor excitation, ensuring the machine has not entered saturation. The measured parameters improve the match between simulated generator response under short-circuit fault conditions and experimental results, as highlighted in *Figure 7.24*.

7.5 Parameters for Synchronous Generator

			Three-phase		Five-phase	15-Phase
			Datasheet	Experimentally Derived*	†	†
Voltage	V	V	380	332.5	199.5	66.5
Rated Apparent Power	S	kVA	25	21.875	21.875	21.875
Base Impedance	Z	Ω	5.779	5.054	3.032	1.016
Stator Resistance	R_s	Ω	0.353	0.432	0.259	0.086
d-axis Synchronous Reactance	X_d	p.u.	3.184	4.419	4.419	4.419
d-axis Transient Reactance	X_d'	p.u.	0.322	0.443	0.443	0.443
d-axis Sub-transient Reactance	X_d''	p.u.	0.203	0.183	0.183	0.183
q-axis Synchronous Reactance	X_q	p.u.	1.586	2.165	2.165	2.165
q-axis Sub-transient Reactance	X_q''	p.u.	0.358	0.183	0.183	0.183
Leakage Reactance	X_l	p.u.	0.131	0.126	0.126	0.126
Transient Time Constant	τ_d'	s	0.012	0.056	0.056	0.056
Sub-transient Time Constant	τ_d''	s	0.003	0.017	0.017	0.017

* De-rated for 7 turns rather than 8

† Inductances will be scaled by per unit base impedance for five- and 15-phase generators

7.6 Simulation Model

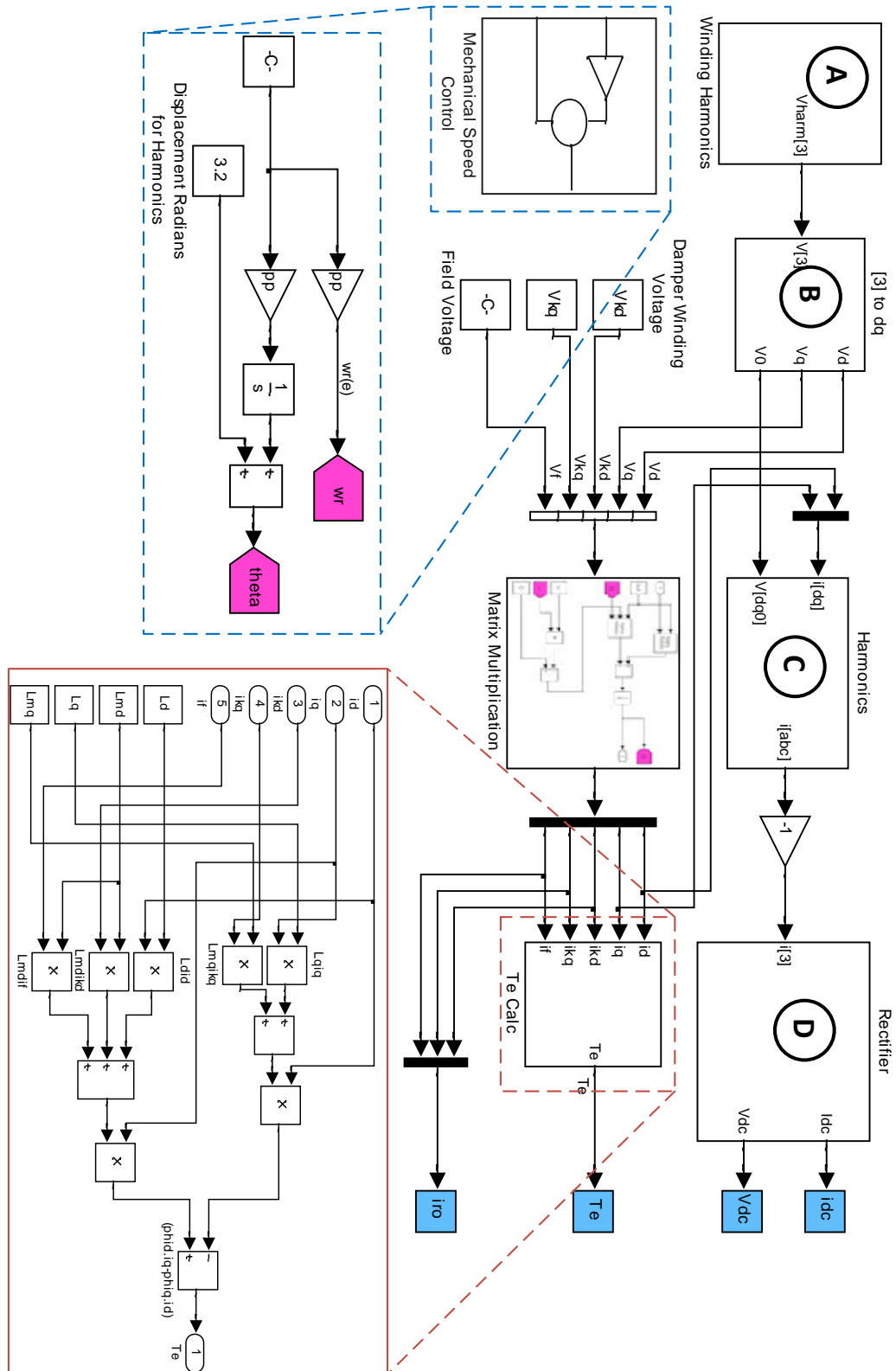


Figure 7.26: MATLAB Simulink Model Overview

A. Winding Harmonic Voltages

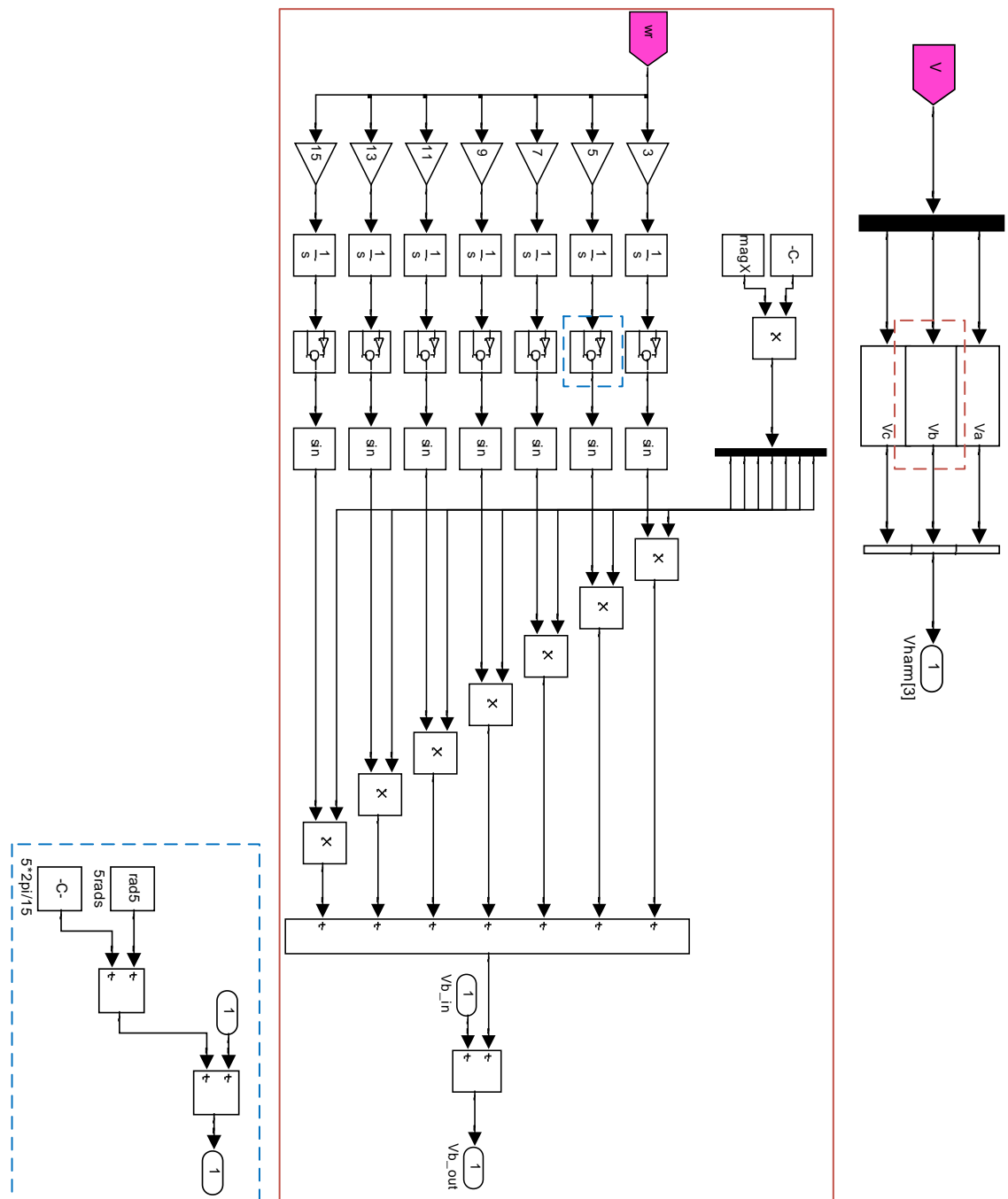


Figure 7.27: Harmonic Voltages from Winding Factors

B. Park Transform

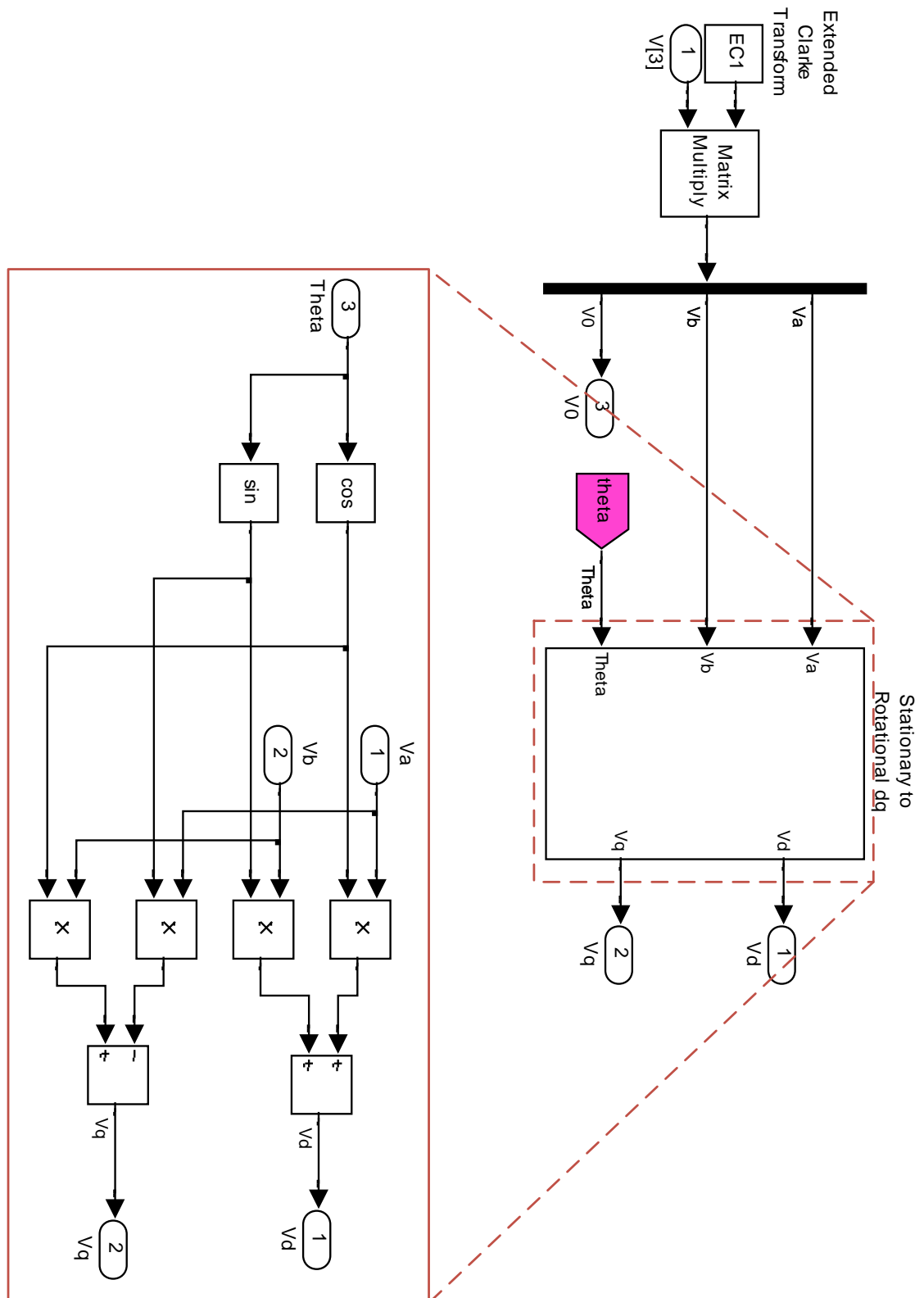


Figure 7.28: Park Transform

C. Higher Order d-q Harmonics and Zero-sequence Recombined with Fundamental Currents (Three-phase)

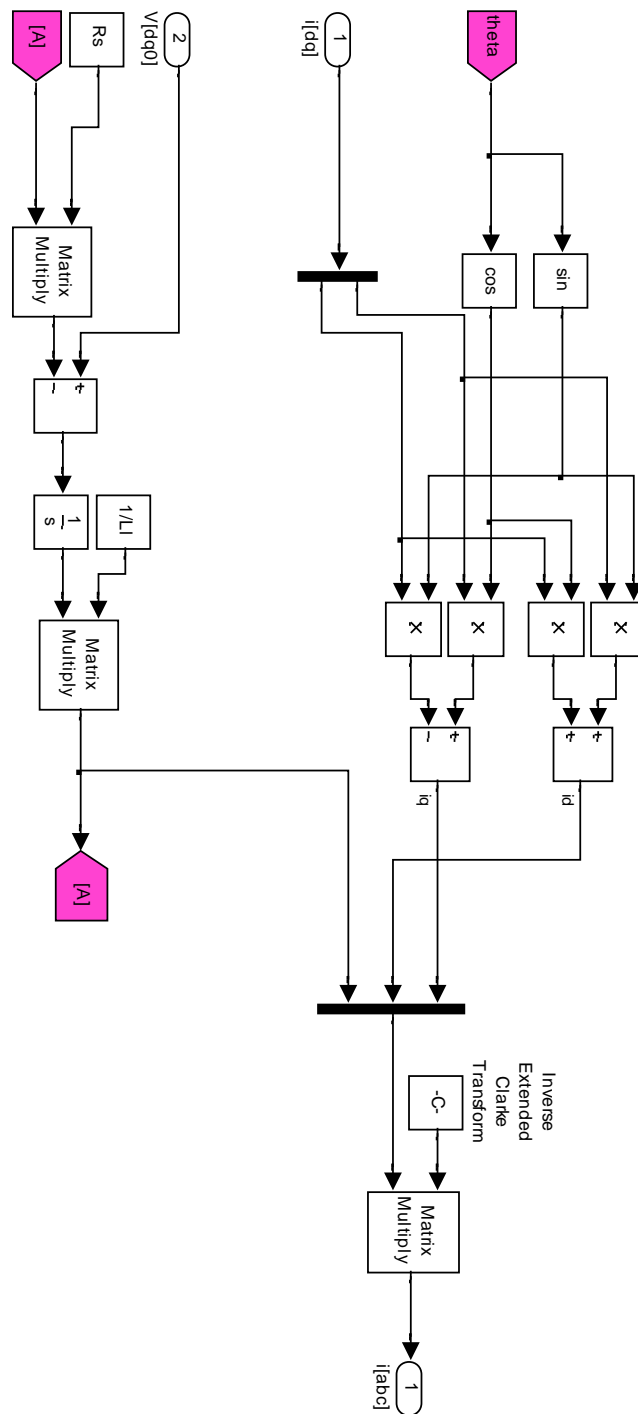


Figure 7.29: Recombination of Fundamental d-q Values with Higher Order d-q Harmonic Pairs and Zero-sequence Components

D. Rectifier Block (Three-phase)

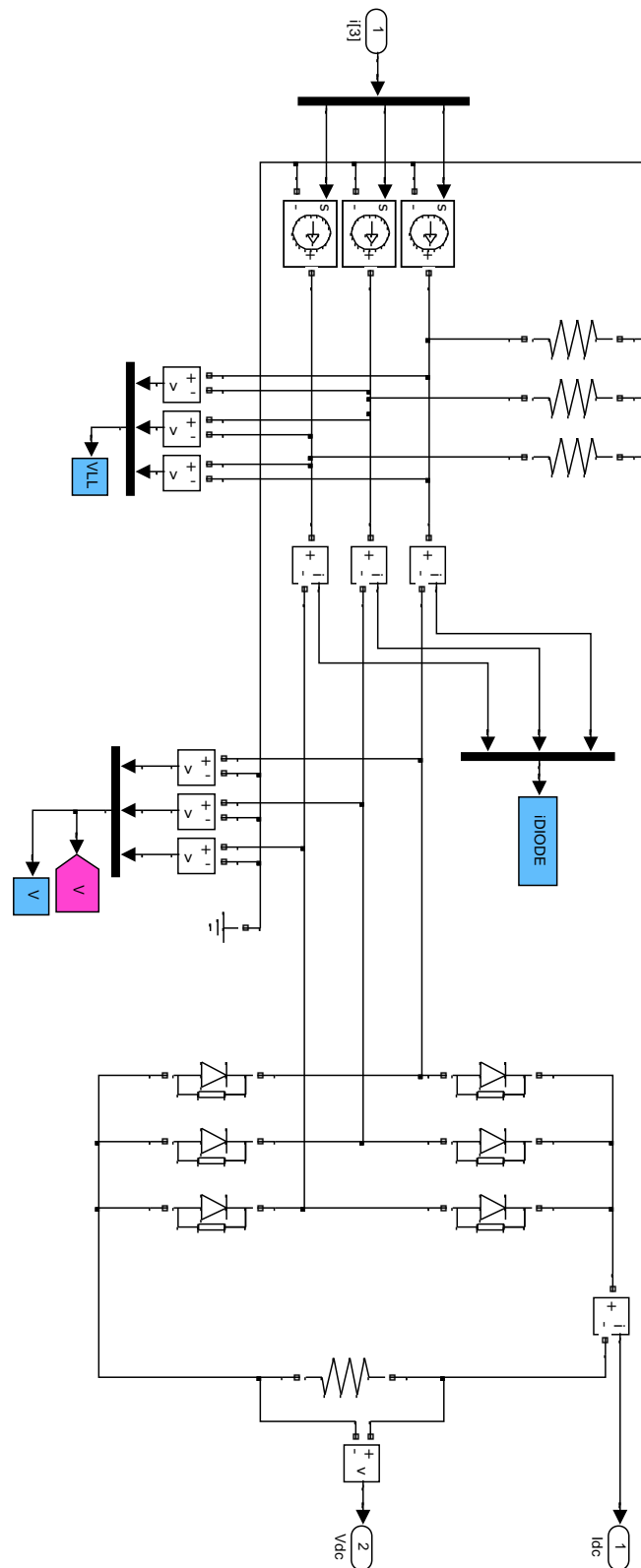


Figure 7.30: Rectifier with SimPowerSystems Diode Models

7.7 State-space Matrices

Formation of A and B matrices

$$[A] = \begin{bmatrix} R_D & 0 & 0 & 0 & 0 \\ 0 & R_Q & 0 & 0 & 0 \\ 0 & 0 & R_{kd} & 0 & 0 \\ 0 & 0 & 0 & R_{kq} & 0 \\ 0 & 0 & 0 & 0 & R_f \end{bmatrix} + \omega_r^e \begin{bmatrix} 0 & -L_Q & 0 & -L_{mq} & 0 \\ L_D & 0 & L_{md} & 0 & L_{md} \\ 0 & 0 & 0 & 0 & 0 \\ 0 & 0 & 0 & 0 & 0 \\ 0 & 0 & 0 & 0 & 0 \end{bmatrix}$$

$$[B] = \begin{bmatrix} L_D & 0 & L_{md} & 0 & L_{md} \\ 0 & L_Q & 0 & L_{mq} & 0 \\ L_{md} & 0 & L_{kd} & 0 & L_{md} \\ 0 & L_{mq} & 0 & L_{kq} & 0 \\ L_{md} & 0 & L_{md} & 0 & L_f \end{bmatrix}$$

7.8 Experimental and Simulation Results

Table 7.5: Short-pitched Results

			Normal Operation				Generator Open-circuit				Diode Open-circuit				
			V_{ac} (V _{pk})	i_{ac} (A _{pk})	V_{dc} (V _{pk})	Avg of V_{dc} ripple (%)	V_{ac} (V _{pk})	i_{ac} (A _{pk})	V_{dc} (V _{pk})	Avg of V_{dc} ripple (%)	V_{ac} (V _{pk})	i_{ac} (A _{pk})	V_{dc} (V _{pk})	Avg of V_{dc} ripple (%)	
			Ω												
Three-phase	STAR	E	58	297.589	8.319	492.781	27.70	281.589	8.479	479.982	165.18	307.188	8.799	486.381	166.15
		S	58	279.552	8.327	482.891	19.63	-	-	-	-	285.921	8.661	502.340	155.72
		E	5	50.558	15.994	77.437	26.05	51.198	23.679	113.596	178.12	51.838	24.319	116.796	181.07
		S	5	47.293	13.209	66.042	6.28	-	-	-	-	62.553	23.391	116.955	156.19
	DELTA	E	58	287.989	5.269	294.389	28.24	287.989	4.864	291.189	30.97	300.788	5.119	294.389	179.98
		S	58	308.294	5.290	306.788	36.63	285.053	4.888	288.443	47.79	381.187	6.611	383.391	162.41
		E	5	115.196	23.359	113.596	28.62	119.995	23.039	116.796	45.28	167.994	33.279	158.394	163.93
		S	5	116.152	22.906	114.531	45.34	104.732	26.231	131.57	78.55	173.498	35.192	175.956	158.31
Five-phase	STAR	E	58	180.793	5.759	329.587	13.59	188.793	6.079	329.587	61.71	191.993	5.919	335.987	61.73
		S	58	172.533	5.599	324.756	5.61	-	-	-	-	171.111	5.584	323.950	46.54
		E	5	71.677	22.079	109.437	22.62	68.797	26.239	132.795	91.20	67.197	26.239	132.795	89.76
		S	5	72.720	25.156	125.776	9.97	-	-	-	-	68.484	25.217	126.760	45.90
	POLY-ON	E	58	251.154	4.671	265.590	11.37	180.793	4.608	265.580	13.99	179.193	4.544	268.790	47.49
		S	58	178.723	4.862	281.937	10.09	171.248	4.593	267.365	16.11	167.440	4.502	261.090	48.47
		E	5	113.596	21.119	110.396	18.74	113.596	23.339	110.396	34.09	110.396	19.199	110.396	32.43
		S	5	87.373	23.091	115.455	25.89	86.974	22.555	113.503	57.86	86.989	22.560	113.256	57.88
15-phase	STAR	E	58	57.171	2.208	108.878	4.84	57.598	1.952	110.396	12.25	55.678	1.952	111.996	12.13
		S	58	52.394	1.707	99.010	3.80	-	-	-	-	58.737	1.817	105.334	22.56
		E	5	62.718	23.319	115.196	14.92	67.837	22.399	107.196	27.36	68.477	19.871	108.796	27.09
		S	5	62.927	22.239	111.358	2.82	-	-	-	-	55.539	19.695	98.876	17.42
	POLY-ON	E	58	59.518	5.170	259.190	7.70	51.198	2.560	147.194	23.77	57.598	2.240	107.196	14.22
		S	58	61.142	4.304	249.520	2.06	40.613	1.836	137.224	5.57	33.295	1.967	114.116	4.36
		E	5	40.958	11.649	90.358	7.29	55.678	20.799	113.596	25.35	49.918	20.159	107.196	14.46
		S	5	31.809	21.164	107.189	6.47	33.639	20.956	105.954	19.78	37.173	24.225	121.812	19.60

Table 7.6: Fully-pitched Results

			Normal Operation				Generator Open-circuit				Diode Open-circuit				
			V_{ac} (V _{pk})	i_{ac} (A _{pk})	V_{dc} (V _{pk})	Avg of V_{dc} ripple (%)	V_{ac} (V _{pk})	i_{ac} (A _{pk})	V_{dc} (V _{pk})	Avg of V_{dc} ripple (%)	V_{ac} (V _{pk})	i_{ac} (A _{pk})	V_{dc} (V _{pk})	Avg of V_{dc} ripple (%)	
			Ω												
Three-phase	STAR	E	58	345.587	8.480	486.381	24.85	319.988	8.799	505.581	170.67	297.589	8.639	486.381	171.36
		S	58	277.855	8.141	472.126	16.66	-	-	-	-	274.113	8.323	482.688	155.06
		E	5	105.596	14.719	70.397	18.30	89.597	21.119	102.396	186.06	95.996	21.439	108.796	198.03
		S	5	45.483	13.007	65.038	8.76	-	-	-	-	54.943	21.572	107.860	158.93
	DELTA	E	58	275.189	4.607	271.990	20.24	291.189	5.183	297.589	34.79	265.590	4.672	265.590	161.01
		S	58	276.050	4.732	274.441	13.68	291.276	4.995	289.666	36.10	274.974	4.760	276.110	162.16
		E	5	119.995	28.159	118.395	46.21	145.594	30.398	148.794	125.16	175.993	33.918	172.793	178.70
		S	5	119.388	23.550	117.772	19.54	139.161	27.504	139.203	67.830	171.321	34.669	173.344	156.01
Five-phase	STAR	E	58	188.793	6.008	339.187	22.76	198.392	6.332	361.586	56.39	188.793	5.920	342.387	58.29
		S	58	155.228	5.150	298.650	9.56	-	-	-	-	191.651	5.827	339.087	47.28
		E	5	103.996	23.179	115.196	29.72	94.396	23.579	129.595	115.33	94.396	23.039	127.995	116.87
		S	5	67.135	22.576	112.877	12.01	-	-	-	-	80.069	25.353	126.761	54.50
	POLY-ON	E	58	195.193	4.540	248.278	7.88	185.593	5.140	278.389	37.53	198.392	4.736	252.790	40.50
		S	58	180.663	4.117	238.775	10.88	155.408	4.635	322.607	56.96	162.849	4.510	261.605	54.57
		E	5	121.595	19.672	125.195	24.79	118.395	21.439	126.395	58.13	118.395	19.539	117.196	42.66
		S	5	82.793	20.804	104.020	31.04	93.894	24.603	123.015	72.30	78.802	23.510	117.548	69.32
15-phase	STAR	E	58	56.958	1.984	106.063	8.72	59.518	1.856	107.196	14.34	61.438	2.080	111.996	13.95
		S	58	54.852	1.821	105.530	0.82	-	-	-	-	54.906	1.823	105.671	7.24
		E	5	67.837	22.079	125.563	99.89	78.077	20.799	108.796	27.32	76.157	20.479	108.796	28.92
		S	5	51.414	18.220	94.865	3.39	-	-	-	-	65.511	23.884	119.415	17.89
	POLY-ON	E	58	58.238	4.746	246.391	9.52	58.238	4.544	249.590	13.55	58.878	4.608	252.790	11.99
		S	58	68.896	4.328	251.338	2.06	68.825	4.347	252.083	4.98	69.379	4.399	262.736	7.55
		E	5	58.878	12.320	100.479	2.25	58.878	13.600	107.196	20.93	60.158	13.280	105.596	11.08
		S	5	40.743	23.269	116.342	10.42	37.308	20.069	102.551	24.84	40.589	23.334	116.666	20.72
E = Experimental							S = Simulated								

E = Experimental

S = Simulated

7.9 Further Experimental Results

7.9.1 Introduction

This section provides an explanation of the generator and rectifier circuit behaviour with an open-circuit phase. Supplementary experimental test results are also included. These results support the trends identified in Chapter 5 but do not add new information to the content discussed in the thesis.

7.9.2 Explanation of Circuit Behaviour

Investigating the delta-connected generator behaviour under an open-circuit phase fault, depicted in *Figure 7.31* and results presented in *Figure 5.67*, shows the effect of the missing generator current path. The generator current contribution from the b -phase ($i_{B\text{ GEN}}$) is zero, observed in *Figure 7.34*. However, the ab - and bc -phase diode currents exist due to the voltage developed between the generator terminals from phases a and c switching on the diodes $+D_{ab}$, $-D_{ab}$, $+D_{bc}$ and $-D_{bc}$ respectively. Since the windings are connected together, a current path exists to create the diode line currents for the missing phase. The numbers in the diagram of *Figure 7.32* correspond to the system states at the end of the period in *Figure 7.33* and *Figure 7.34*. The commutation occurs midway through the period.

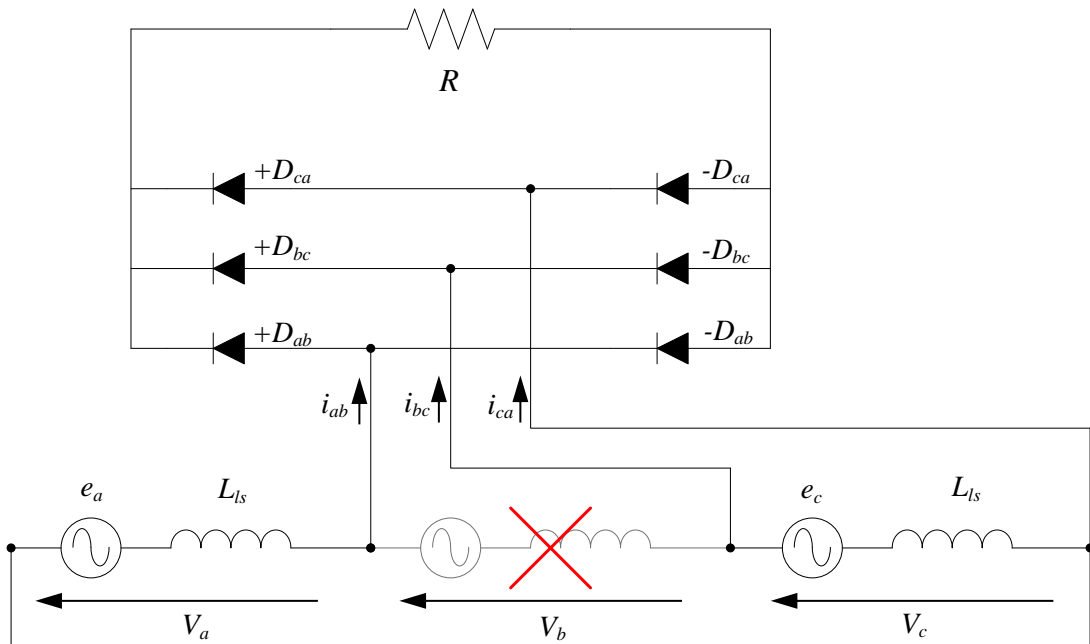


Figure 7.31: Three-phase Open-circuit Diagram

The switching patterns of the diodes in the presence of the open-circuit phase fault are presented in *Figure 7.32* along with a description of each numbered stage.

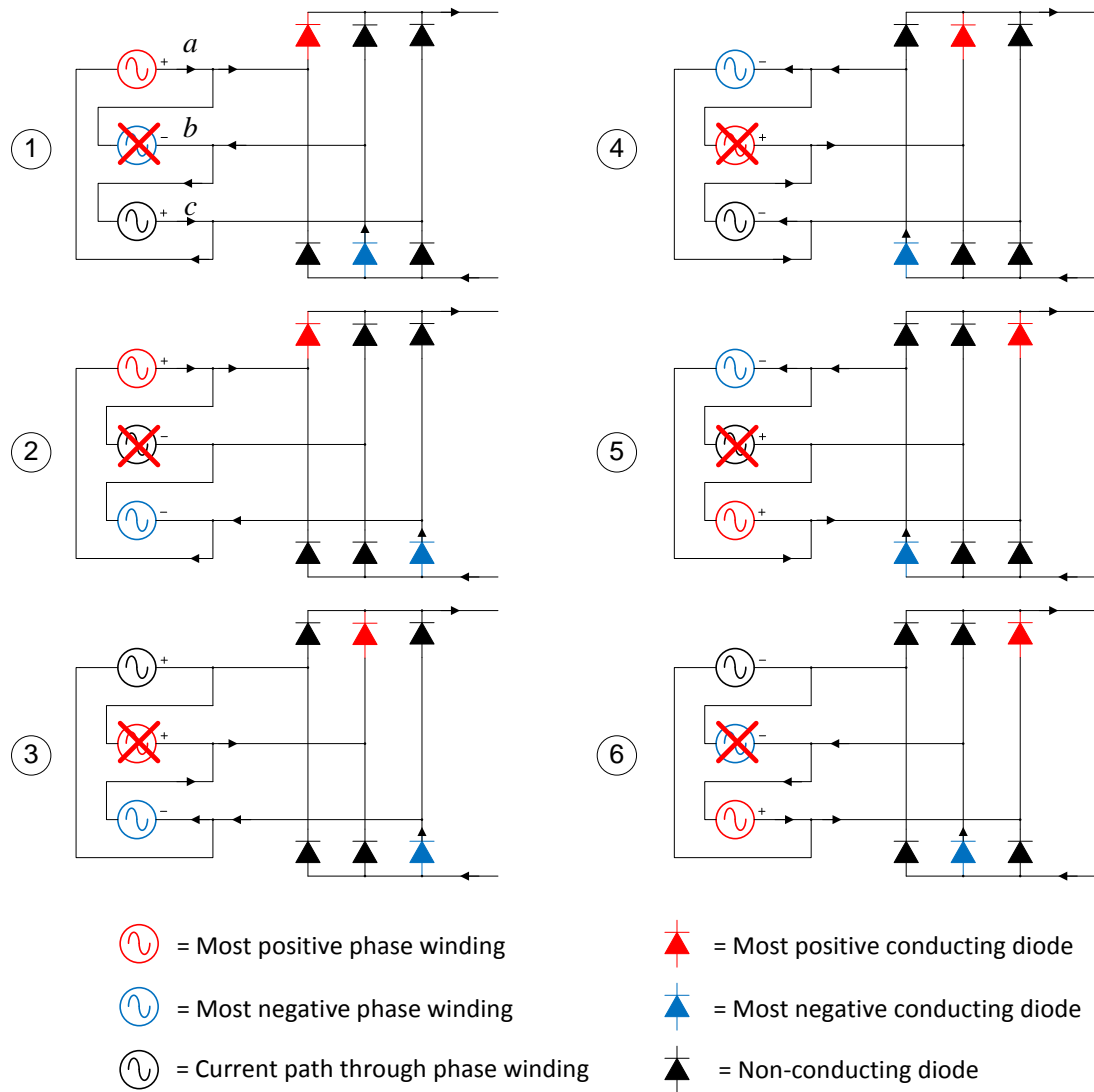


Figure 7.32: Formation of Diode Current Path

1. At the start of this period, the voltage V_c is falling and voltage V_a is rising. Positive current flows through the c -phase diode line and returns through the b -phase diode line; the negative voltage V_b , which is the inverse sum of V_a and V_c , holds diode $-D_{bc}$ on. Only the c -phase of the generator conducts. As V_a increases, the voltage impressed across the diode $+D_{ab}$ turns the device on, allowing current to flow to the DC side. The voltage V_b , being at its lowest magnitude, creates this return path through $-D_{bc}$. Therefore, the a -phase and c -phase generator windings both conduct positive current, shown in Figure 7.34.

2. The voltage V_a is still at maximum and therefore $+D_{ab}$ remains switched on. The commutation to diode $-D_{ca}$ creates the return current path. At this point, current only flows through the a -phase generator winding.
3. The extended duty of voltage V_a falls below V_b resulting in diode $+D_{bc}$ turning on. At the end of the commutation event, only negative c -phase current flows from the DC side, through the c -phase winding and back through the b -phase diode line.
4. The positive voltage V_b remains impressed across diode $+D_{bc}$ whilst V_a now reaches a minimum. The diode $-D_{ca}$ turns off and diode $-D_{ab}$ begins to conduct. Return current now flows in a negative direction through the a -phase winding and continues through the c -phase winding, forming the diode line current i_{bc} .
5. Voltage V_c reaches maximum, commutating from diode $+D_{bc}$ to $+D_{ca}$. The return current path is formed through the a -phase winding.
6. The voltage V_b reaches its most negative and turns on the lower leg diode, $-D_{bc}$, to create the return path from the DC side. Only c -phase positive current is drawn from the generator as a result.

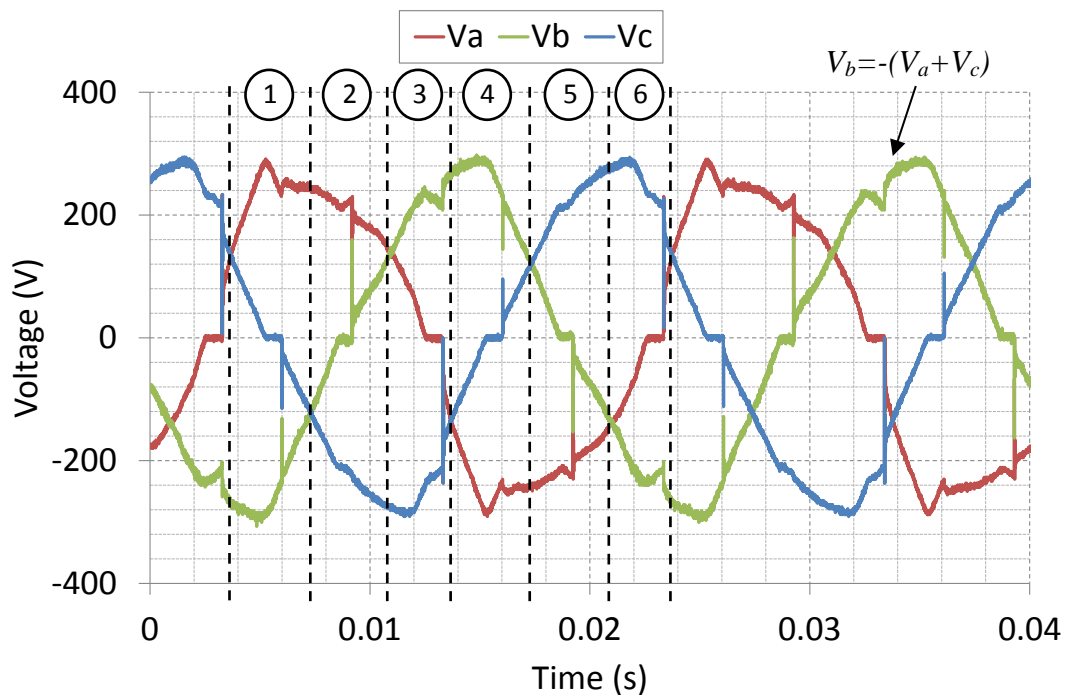


Figure 7.33: Delta-connected Generator Voltage for 58 Ω Load

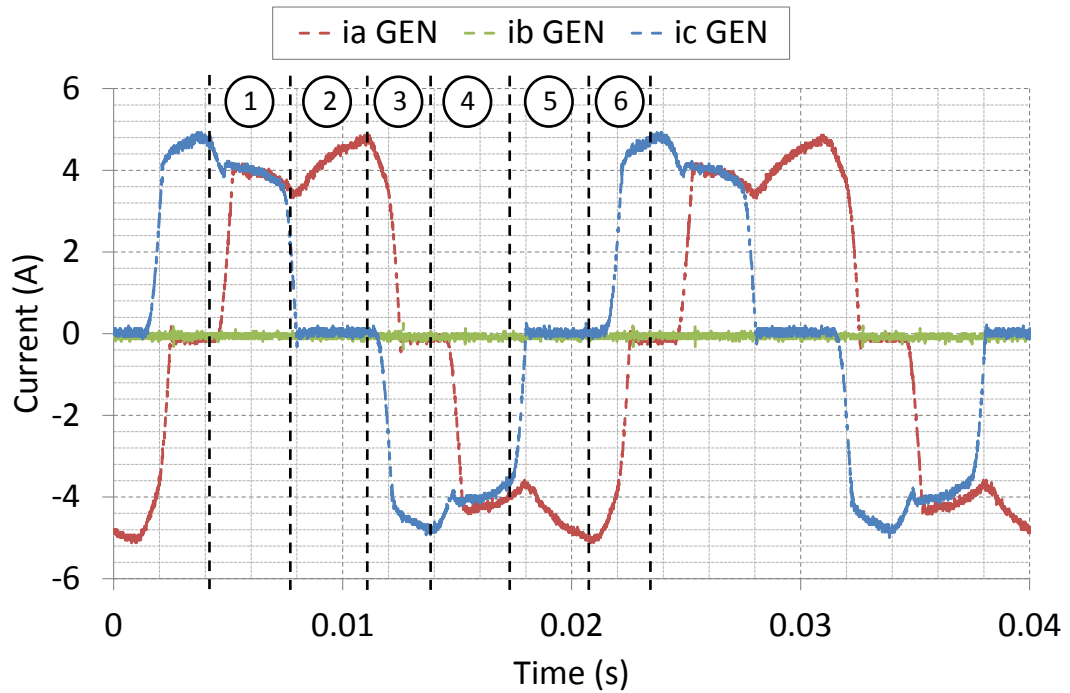


Figure 7.34: Delta-connected Generator Current with Open-circuit Phase Fault for 58 Ω Load

At points 2, 3, 5 and 6 of the cycle, all of the current is transferred to the DC side from either the a - and c -phase windings solely but there are also periods, in 1 and 4, where the current measured travels through both healthy phase windings, highlighted in Figure 7.35.

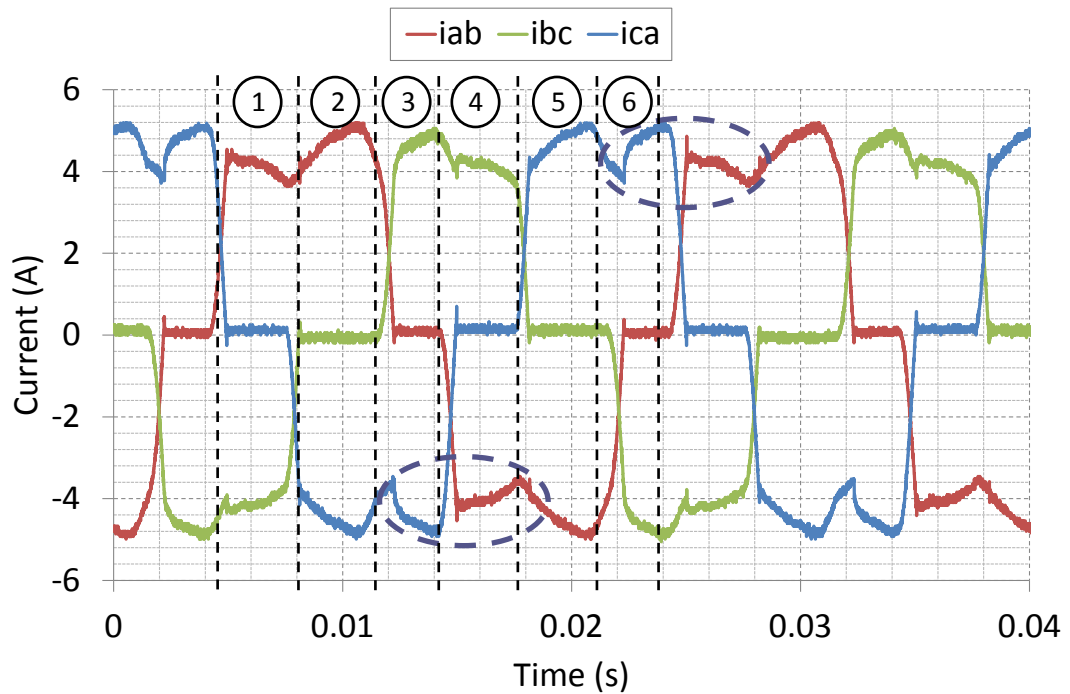


Figure 7.35: Diode and Generator Current with Open-circuit Phase Fault

The open-circuit conditions will present themselves in the same way as for the fully-pitched machine topology. The results for the star-connected system for a fault occurring in either the generator or diode leg are shown in *Figure 7.36*.

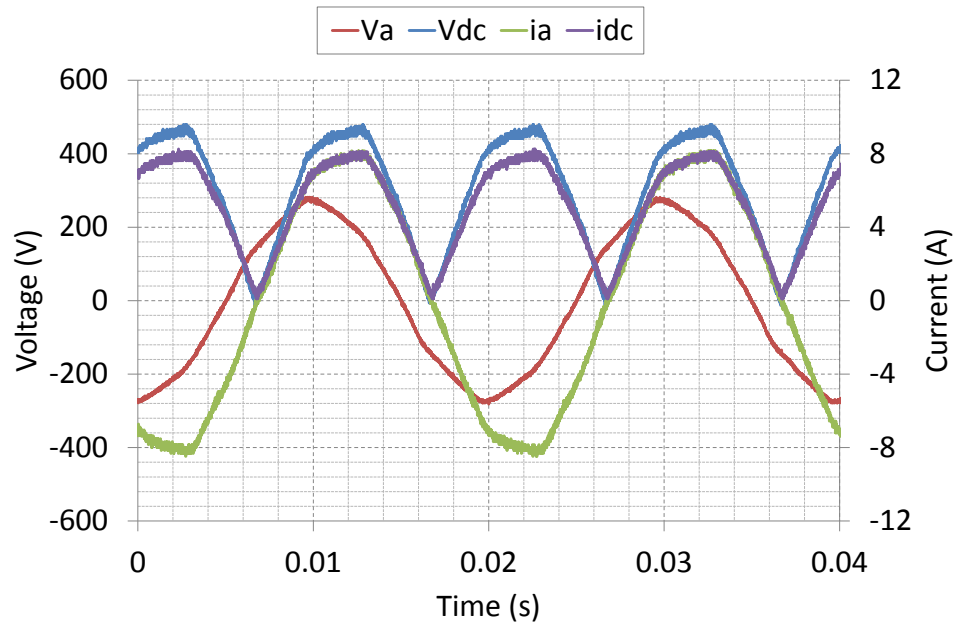


Figure 7.36: Short-pitched Star-connected Generator Open-circuit Phase Fault 58 Ω Load

The rectifier is acting as a H-bridge, since the current path that has been removed in the star-connected system also removes the corresponding diode leg. The presence of the open-circuit phase fault causes the voltage of the b -phase diode leg to float. At point x , V_{ca} is increasing to a maximum. The a -phase voltage must, therefore, be at a lower magnitude, allowing the diode to conduct, forming the return path. At point y , V_{ca} has reached its maximum value, and maximum AC current is drawn from the generator phase before the remaining healthy phases commutate to the next conduction mode. The neutral reference point, against which the phase voltage is determined, changes in magnitude as the line-to-line voltages fluctuate; therefore, the voltages referenced to the b -phase are ignored in *Figure 7.37*.

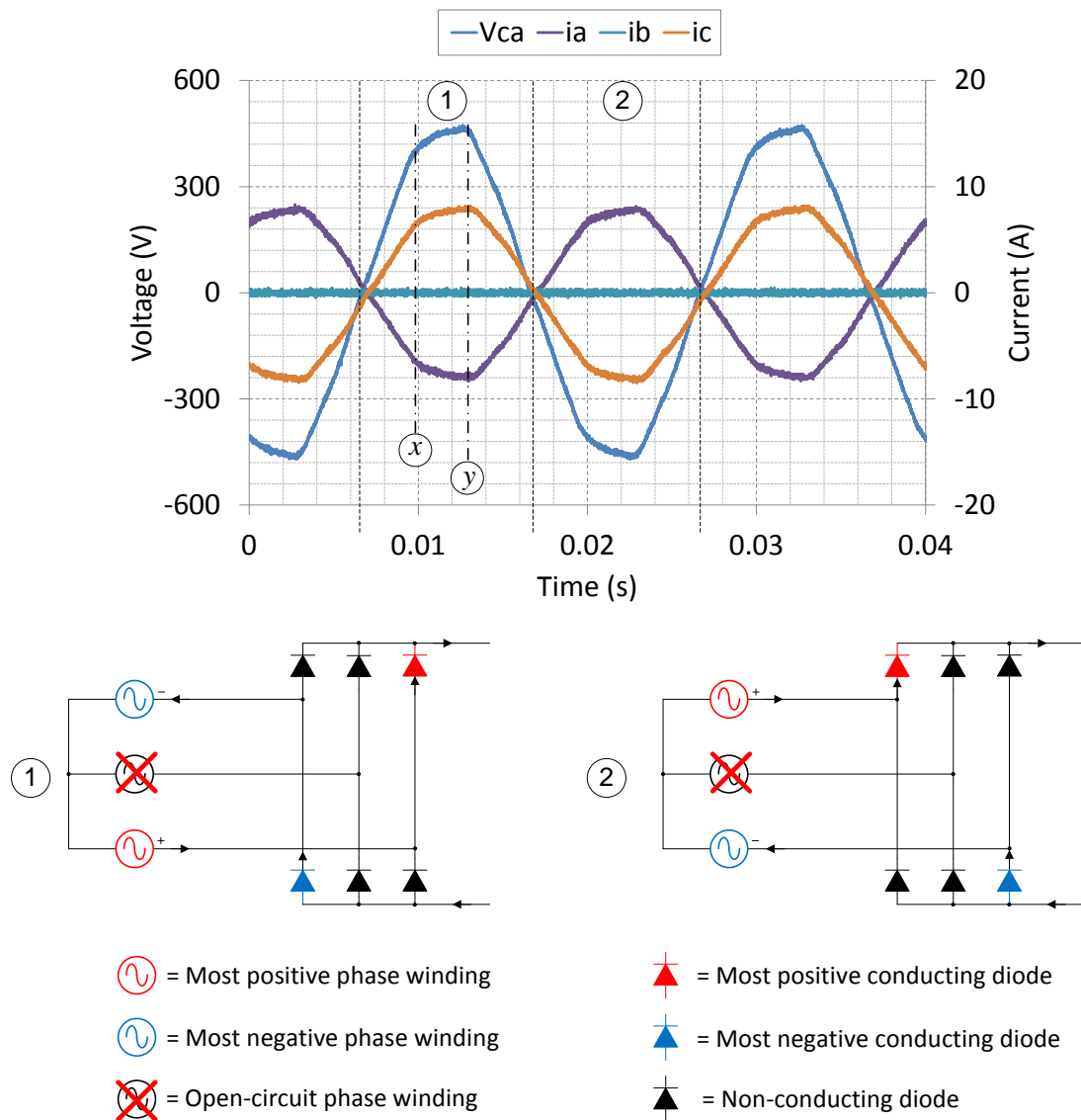


Figure 7.37: Star-connected Generator b -phase Open-circuit AC Voltage and Current

The three-phase analysis can be extended to the five- and 15-phase generator-rectifier behaviour for a single open-circuit phase fault under lightly loaded conditions for both the star- and delta-connected machines.

7.9.3 Three-phase Short-pitched Generator

The behaviour of the three-phase, short-pitched generator, presented here, is very similar to the fully-pitched generator results that are described in Chapter 5. The discussion that accompanies the fully-pitched results throughout Chapter 5 is sufficient to describe the behaviour here, where differences are outlined.

The combined results, shown in *Figure 7.38*, are similar to those observed in the fully-pitched case. The fifth harmonic that was dominant in the AC voltage due to the rectifier has been removed.

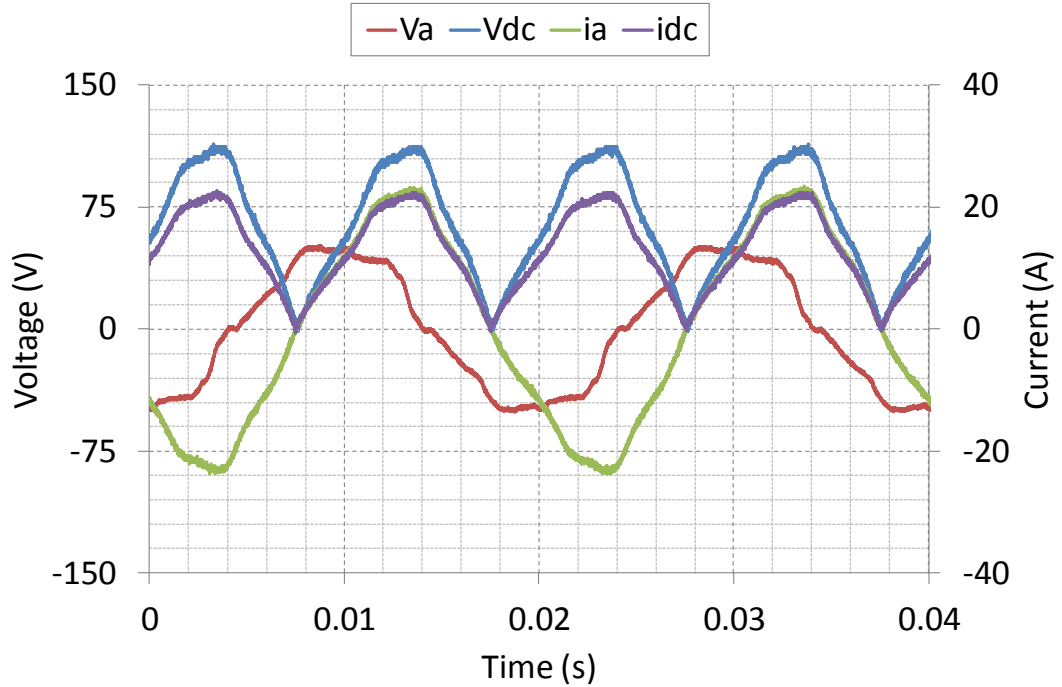


Figure 7.38: Three-phase Short-pitched Star-connected Generator Open-circuit Phase Fault 5 Ω Load

The short-pitched, delta-connected generator under normal operating conditions shows the current waveform expected from the analysis carried out in Chapter 3, highlighted in *Figure 7.39*. The current drawn from the generator contains fifth harmonic to distort the waveform.

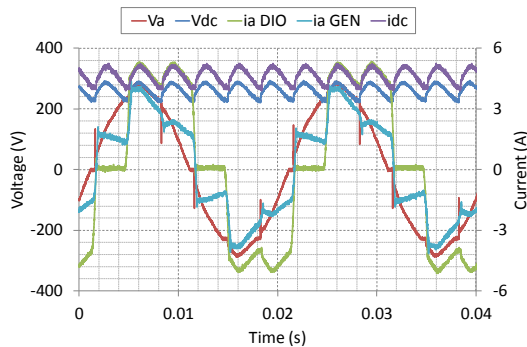


Figure 7.39: Three-phase Short-pitched Delta-connected Generator AC and DC Voltage and Current 58 Ω Load

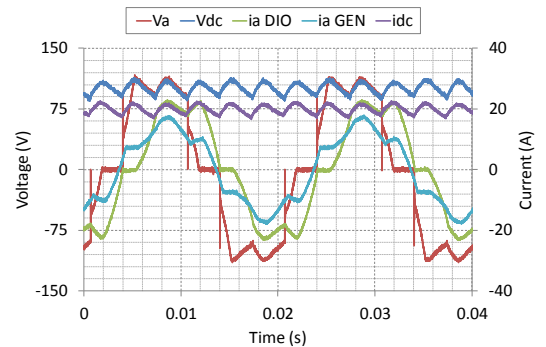
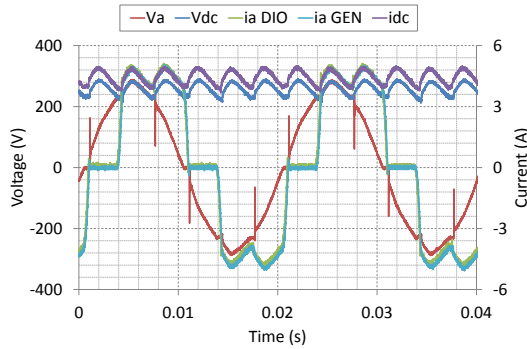


Figure 7.40: Three-phase Short-pitched Delta-connected Generator AC and DC Voltage and Current 5 Ω Load

The 5 Ω resistive load leads to a reduction in peak AC voltage and peak DC voltage. The short-circuit characteristic of the machine causes the voltage drops across the stator impedance to reduce the output voltage, discussed earlier in Section 5.5.1.

The behaviour observed in *Figure 7.41* is similar to that discussed in *Figure 5.67*. The AC voltage shows a more sinusoidal characteristic giving a smoother DC ripple despite the open-circuit phase fault.

The diode open-circuit fault, depicted in *Figure 7.42*, creates the 100 Hz ripple frequency, seen in *Figure 5.68*, but no longer exhibits the same AC behaviour. The circulating harmonic currents in the delta-connected windings have been removed through short-pitching, giving a more sinusoidal generator current.



*Figure 7.41: Three-phase Short-pitched Delta-connected Generator Open-circuit Phase Fault
58 Ω Load*

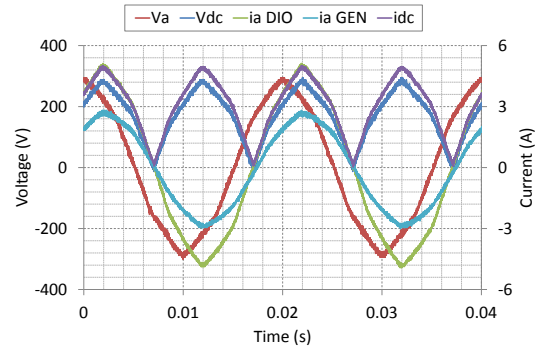


*Figure 7.42: Three-phase Short-pitched Delta-connected Generator Open-circuit Diode Fault
58 Ω Load*

The data presented in *Table 7.7* highlights the benefits of the delta-connected generator in maintaining DC power quality under open-circuit phase faults.

Increasing the load current drawn for both fault conditions is shown in *Figure 7.43* and *Figure 7.44*. The behaviour is very similar to the lightly loaded systems. The results are presented in *Table 7.7*.

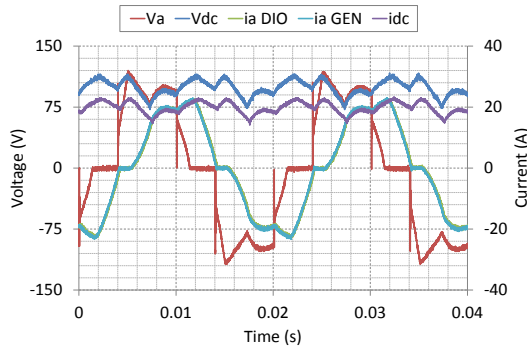


*Figure 7.43: Three-phase Short-pitched Delta-connected Generator Open-circuit Phase Fault
5 Ω Load*

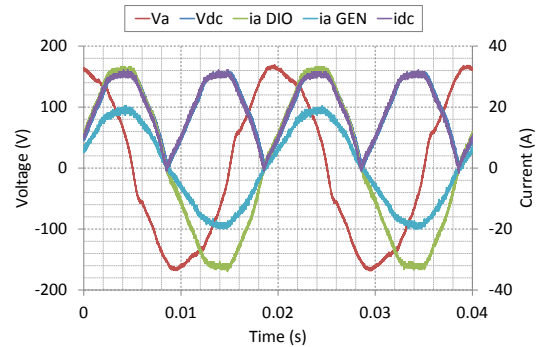


*Figure 7.44: Three-phase Short-pitched Delta-connected Generator Open-circuit Diode Fault
5 Ω Load*

Table 7.7: Three-phase Short-pitched Star- and Delta-connected Generator Open-circuit Faults

			V_{AC} (V_{pk})	i_{AC} (A_{pk})	V_{DC} (V_{pk})	i_{DC} (A_{pk})	V_{DC} (V_{pk-pk})	V_{DC} Ripple (% of AVG)
Star-	Gen/Dio	58 Ω	281.6	8.48	479.9	8.26	492.8	165.2
connected	O/C	5 Ω	51.2	23.7	113.6	22.7	115.2	178.1
Delta-	Gen	58 Ω	287.9	5.03	291.2	5.01	80.0	31.0
Connected	O/C	5 Ω	120.0	23.0	116.8	23.4	44.8	45.3
Delta-	Dio	58 Ω	300.8	2.82	294.4	5.02	307.2	179.9
Connected	O/C	5 Ω	167.9	20.5	158.4	32.2	161.6	163.9

The results in *Table 7.7* show that for a short-pitched, three-phase synchronous generator a diode open-circuit fault has a significant impact on the system regardless of the connection method. The diode rectifier becomes an effective H-bridge, limiting the performance of the DC side and drawing current from the generator – in the star-connected case – that is π radians out of phase in the two remaining healthy windings. This gives the high pk-pk ripple magnitude observed in *Table 7.7*, underlining the problems of using a three-phase generator for the provision of DC power.

7.9.4 Five-phase Short-pitched Generator

Comparing the short-pitched results with that of the fully-pitched generator, the results observed in *Figure 7.45* show the same trends as seen in *Figure 5.73*.

Again, with an increased load current drawn to the DC side, *Figure 7.46* shows similarity with the fully-pitched generator, depicted in *Figure 5.74*. The ripple magnitude is reduced as a result of the increased AC voltage duty for the remaining healthy phases, allowing for a prolonged conduction of current.

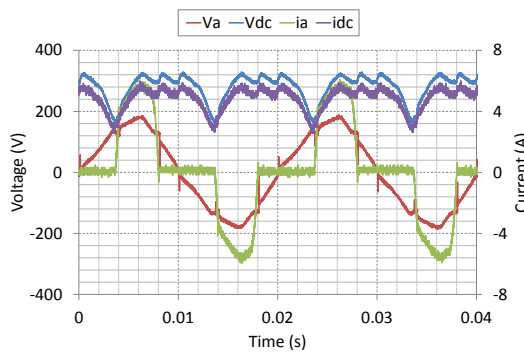


Figure 7.45: Five-phase Short-pitched Star-connected Generator Open-circuit Phase Fault 58 Ω Load

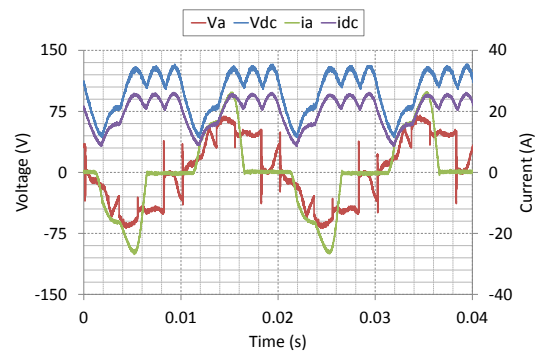


Figure 7.46: Five-phase Short-pitched Star-connected Generator Open-circuit Phase Fault 5 Ω Load

The short-pitched polygon-connected generator is presented in *Figure 7.47*, with the higher loading shown in *Figure 7.48*.

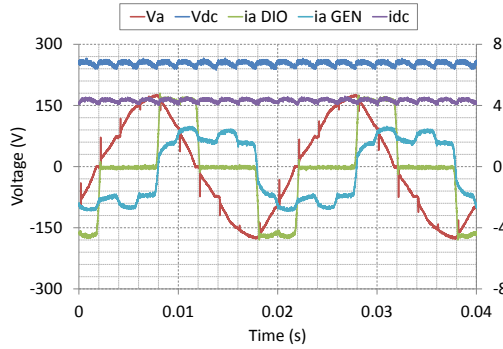


Figure 7.47: Five-phase Short-pitched Polygon-connected AC and DC Voltage and Current 58 Ω Load

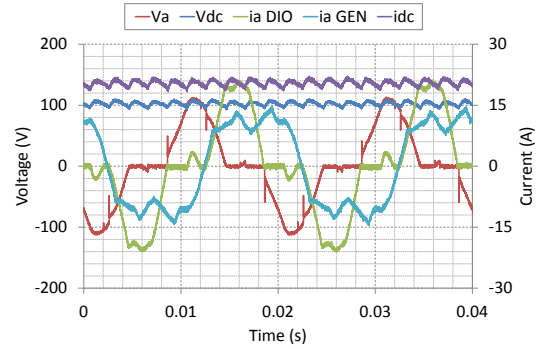


Figure 7.48: Five-phase Short-pitched Polygon-connected AC and DC Voltage and Current 5 Ω Load

The generator current in *Figure 7.47* shows the removal of the circulating harmonics that were discussed in *Figure 5.41*. The higher current loading results depicted in *Figure 7.48*, show similar trends, however, the AC voltage now resembles waveform observed in the fully-pitched topology of *Figure 5.58*. Unlike the polygon-connected, short-pitched generator, in the fully-pitched topology, the diode line current starts to exhibit overlap in the diode devices that are conducting current, shown in *Figure 7.49*. Only one diode is in a non-conducting state during this period. This has no effect on the performance of the generator since the current drawn from the generator to form the diode line current is different.

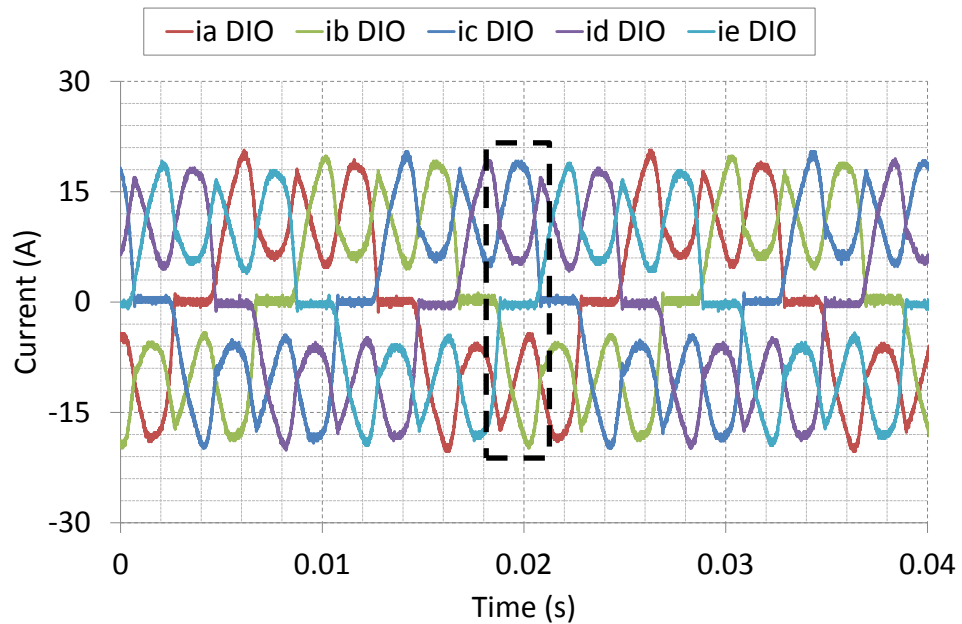


Figure 7.49: Five-phase Fully-pitched Polygon-connected Generator Diode Current 5 Ω Load

The polygon-connected generator with an open-circuit phase fault, shown in *Figure 7.50*, behaves much in the same manner as the healthy generator condition. The peak voltage and current magnitudes are near identical. However, the DC voltage ripple magnitude is 2.6 % larger, as a percentage of the average voltage. The AC current drawn from the generator is considerably different. Two of the phases are consistent with the diode line currents, where the other two remaining healthy phases show a similar behaviour but extended over a longer period, observed in *Figure 7.50*.

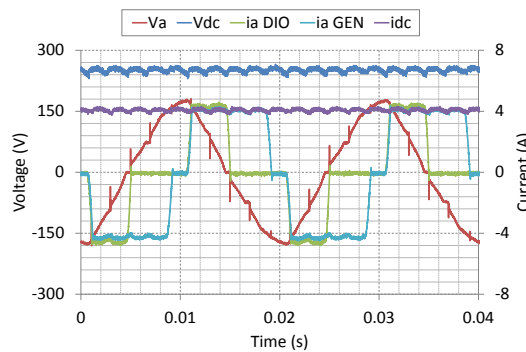


Figure 7.50: Five-phase Short-pitched Polygon-connected Generator Open-circuit Phase Fault 58 Ω Load

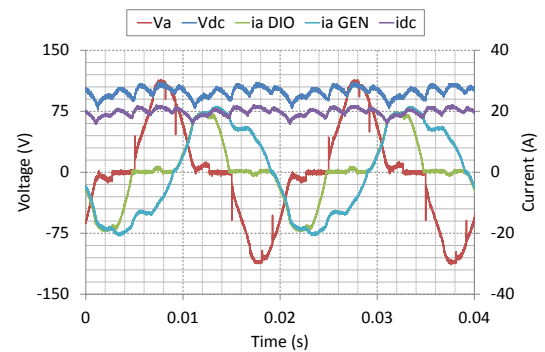


Figure 7.51: Five-phase Short-pitched Polygon-connected Generator Open-circuit Phase Fault 5 Ω Load

The higher current case, in *Figure 7.51*, again underlines the distortion of the AC generator characteristics. The DC voltage and current ripple is affected by this, resulting in a higher percentage ripple but offering better performance than the star-connected case.

The results of implementing a diode open-circuit fault can be seen in *Figure 7.52* and *Figure 7.53*.

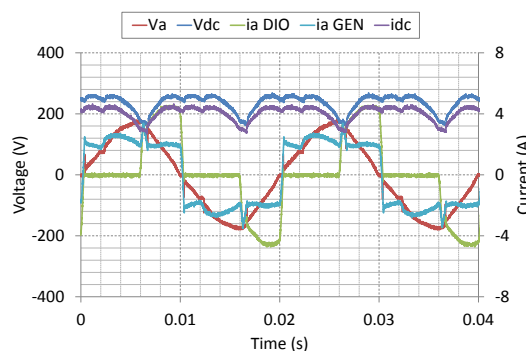


Figure 7.52: Five-phase Short-pitched Polygon-connected Diode Open-circuit 58 Ω Load

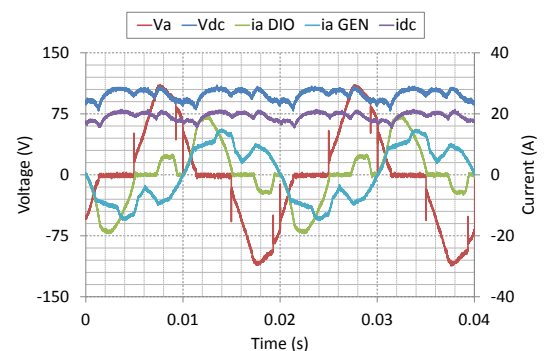


Figure 7.53: Five-phase Short-pitched Polygon-connected Diode Open-circuit 5 Ω Load

The lightly loaded case, in *Figure 7.52*, shows a marked difference in the AC current drawn from the generator compared with *Figure 5.79*. The short-pitching has a considerable effect on the way in which the current is distributed through the phases to form the diode current.

The effect of increasing the current drawn to the DC side shown in *Figure 7.53*, exhibits similar behaviour to the fully-pitched results, depicted in *Figure 5.80*. The AC generator current shows a different waveform shape due the removal of the circulating harmonic currents distorting the output.

The full results for the short-pitched generator under fault conditions are contained in *Table 7.8*.

Table 7.8: Five-phase Short-pitched Star- and Polygon-connected Generator Open-circuit Faults

			V_{AC}	i_{AC}	V_{DC}	i_{DC}	V_{DC}	V_{DC} Ripple
			(V_{pk})	(A_{pk})	(V_{pk})	(A_{pk})	(V_{pk-pk})	(% of AVG)
Star-	Gen/Dio	58 Ω	188.8	6.08	329.6	6.00	172.8	61.7
connected	O/C	5 Ω	68.8	26.2	132.8	26.2	91.2	91.5
Polygon-	Gen	58 Ω	180.8	4.34	265.6	4.32	14.0	14.0
Connected	O/C	5 Ω	113.6	21.1	110.4	21.8	33.6	34.1
Polygon-	Dio	58 Ω	179.2	3.39	268.8	4.65	112.0	47.5
Connected	O/C	5 Ω	110.4	15.0	110.4	21.4	32.0	32.4

7.9.5 15-phase Short-pitched Generator

The star-connected configuration, depicted in *Figure 7.54*, offers minimal degradation under light loading conditions which matches the fully-pitched performance shown in *Figure 5.82*.

With a higher resistive loading, shown in *Figure 7.55*, the AC current shows the same trends as the fully-pitched generator observed in *Figure 5.83*. The fully-pitched case had a number of conduction periods where the short-pitched current waveform only has two, resulting in a higher peak current drawn from the generator.

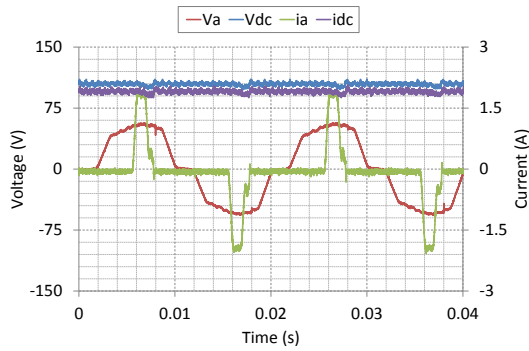


Figure 7.54: 15-phase Short-pitched Star-connected Generator Open-circuit Phase Fault 58 Ω Load

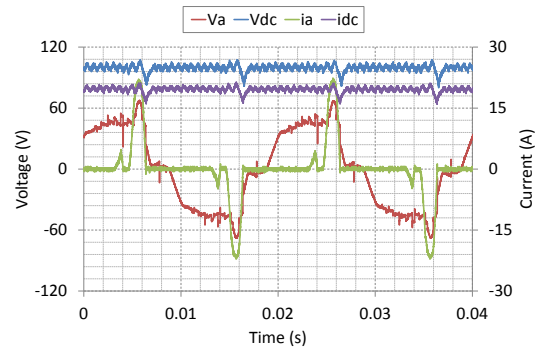


Figure 7.55: 15-phase Short-pitched Star-connected Generator Open-circuit Phase Fault 5 Ω Load

The data for the 15-phase short-pitched generator under normal operating conditions are presented for comparison in *Table 7.9*.

The diode open-circuit condition, shown in *Figure 7.56*, has a similar effect on the generator behaviour as the open-circuit phase fault. The same harmonic behaviour exists for the generator current. However, in the healthy generator, the magnitudes of the key contributing harmonic components have been reduced. On the DC output side, the pk-pk ripple is greater than under normal operating conditions but shows minimal interruption for the diode device fault, unlike the open-circuit phase fault case.

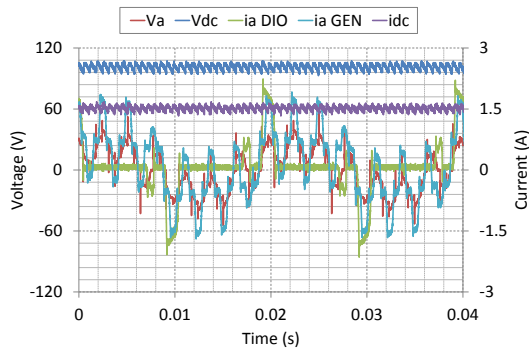


Figure 7.56: 15-phase Short-pitched Polygon-connected Generator Open-circuit Diode Fault 58 Ω Load

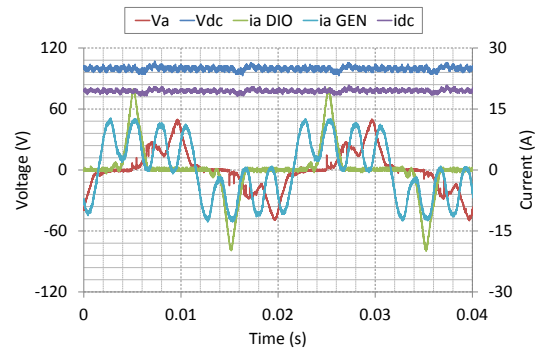


Figure 7.57: 15-phase Short-pitched Polygon-connected Generator Open-circuit Diode Fault 5 Ω Load

The higher load condition, depicted in *Figure 7.57*, shows very similar AC behaviour as the generator open-circuit phase case shown in *Figure 5.89*. However, the DC output is much improved and shows the single fault in the waveform with a much reduced pk-pk ripple. In both loading cases, the peak DC voltage and the pk-pk ripple is the same, however, due to the fault being more obvious in the 5 Ω resistive load case, the average is reduced giving a different ripple magnitude percentage, highlighted in *Table 7.9*.

Table 7.9: 15-phase Short-pitched Generator Open-circuit Diode Fault

			V_{AC} (V_{pk})	i_{AC} (A_{pk})	V_{DC} (V_{pk})	i_{DC} (A_{pk})	V_{DC} (V_{pk-pk})	V_{DC} Ripple (% of AVG)
Star-	Gen/Dio	58 Ω	57.6	1.95	110.4	2.08	12.8	12.3
connected	O/C	5 Ω	67.8	22.4	107.2	21.4	27.2	27.4
Polygon-	Gen	58 Ω	51.2	2.59	147.2	2.06	32.0	23.8
Connected	O/C	5 Ω	55.7	12.8	113.6	21.9	25.6	25.4
Polygon-	Dio	58 Ω	57.6	1.92	107.2	1.68	14.4	14.2
Connected	O/C	5 Ω	49.9	12.8	107.2	20.8	14.4	14.5

The results shown in *Table 7.9* underline the benefits of using a high phase number generator to continue operation under open-circuit fault conditions. The star-connected system has a worse generator performance with regards to the current drawn, showing a much higher peak value under heavy loading. The pk-pk ripple almost doubles for the star-connected generator compared with the polygon-connection.